

# PE&RS

August 2019

Volume 85, Number 8

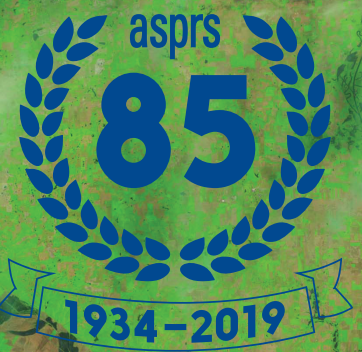
PHOTOGRAMMETRIC ENGINEERING & REMOTE SENSING The official journal for imaging and geospatial information science and technology

— Illinois River

Mississippi River

Missouri River —

St. Louis



# PECORA 21 • ISRSE 38

## *Continuous Monitoring of Our Changing Planet: From Sensors to Decisions*



# Save the Date

**October 6-11, 2019**

Baltimore, MD • Marriott Waterfront

<https://www.asprs.org/event/pecora21-isrse38>





joint meeting of the 21st William T. Pecora Memorial Remote Sensing Symposium (Pecora 21) and the 38th International Symposium on Remote Sensing of Environment (ISRSE-38) will convene in

Baltimore, Maryland, USA from October 6 – 11, 2019. The combined conference will be hosted by NASA, NOAA and the USGS, with an overarching theme of *“Continuous Monitoring of Our Changing Planet: from Sensors to Decisions.”*

## Keynote Speakers

### Gilberto Câmara

Dr. Gilberto Câmara is a Brazilian researcher in Geoinformatics, Spatial Analysis, Land Use Change, and Nature-Society Interactions, from Brazil’s National Institute for Space Research (INPE). Dr. Câmara is currently Secretariat Director for the Group on Earth Observations (GEO).

### Michael Freilich\*

Dr. Michael Freilich is an accomplished oceanographer, microwave remote sensing expert, educator, and science administrator who directed NASA’s Earth Science Division from November 2016 through February 2019.

### Stephen Volz

Dr. Volz has 26 years of professional experience in aerospace. He is a leader in the international Earth observation community, serving as the NOAA Principal to the Committee on Earth Observation Satellites (CEOS). Dr. Volz is currently the NOAA Assistant Administrator for Satellite and Information Services.

\*Sponsored by *Remote Sensing*.



## Conference Location

### Baltimore Marriott Waterfront

Attendees can book their reservations at the Baltimore Marriott Waterfront by calling 1-877-212-5752. A very limited number of rooms are reserved in the room block at this special rate.

## Exhibiting

Contact Bill Spilman, Innovative Media Solutions, to discuss your companies exhibiting needs.

(877) 878-3260 toll-free • (309) 483-6467  
bill@innovativemediasolutions.com

## Special Presentation Sessions

- The Challenges of Integration for Arctic Monitoring
- Using Remotely Sensed Data to Map Forest Structure and Attributes
- Space Agencies Outlook
- Communicating Science Across the Earth Observation Life Cycle
- National Land Cover Database 2016, Offering New Change Insights Across the Conterminous United States
- Copernicus—Europe’s eyes on Earth: Sustainable and Continuous Monitoring of our Environment
- Global Hyperspectral Imaging Spectral-library of Agricultural-Crops (GHISA) in Support of NASA’s Surface Biology and Geology (SBG) mission
- Climate Science – Challenges and Opportunities for Fulfilling Global Multilateral Agreements
- Mapping and Monitoring Surface Change: Landslides and Subsistence
- Copernicus Serving Sustainable Development Goals
- Biodiversity and Conservation Case Studies
- Large Area Land Change Mapping and Monitoring Investigations
- Sustainable Land Imaging and the Future of Moderate-Resolution Land Observation
- Women in Remote Sensing
- Earth Observation and Remote Sensing Education Initiatives
- Toward the Assessment and Modeling of a Functional Relationship of Land Cover and Land Use A Possible New Path forward – the LCHML (Land Characterization Metal-Language) A New Proposed ISO Standard
- Open Data Cube: A New Data Technology for Enhancing the Use of Satellite Data to Address Sustainable Development Goals
- Bathymetry and Near-Shore Investigations
- How No-cost Landsat Data is Reshaping College Level Remote Sensing Courses (AmericaView Special Session)-Land Change Monitoring Assessment and Projection (LCMAP): New Land Change Science Research and Development
- New Generation of NOAA Operational Satellites to support Land, Arctic, and Coastal Waters Applications
- Advances in Soil Moisture and Condition Measurement and Monitoring
- A Conversation on the Landsat Program and its Data Policy
- Investigations in Support of Human Welfare
- Satellite Interoperability
- NASA Harvest and Other Recent Advances in Remote Sensing of Agricultural Applications and Food Security
- Collaboration in the Diverse Geospatial Workforce: How Early Career Professionals Can Bring Innovations to the Technical Community
- Case Studies in Flood Monitoring and Management
- UAS: Changing the Future of Remote Sensing
- Earth Observation and Agricultural Statistics – Agricultural and Agri-environmental Monitoring for SDG 2: Zero Hunger
- Processing Strategies for Big Data
- Remote Sensing Investigations of Wetlands and Near-Shore Issues
- New Technology and Techniques to Increase Scientific and Applications Access to Satellite Earth Observations
- Applications of Earth Observations for Disaster Assessments and Management
- Plus many more!

## ANNOUNCEMENTS

**Dewberry**, a privately held professional services firm, announced that Mark Safran, CP, GISP; Mike Sutherland; and Al Karlin, Ph.D., CMS-L, GISP have joined the firm's geospatial and technology services (GTS) group.

Mark Safran is an associate vice president and senior program manager based in Fairfax, and has more than 30 years of experience in program management and business development with a focus on spatial technologies. In his new role, he is responsible for the oversight of major GTS programs. He serves on the council of the American Geographical Society and is also a member of the U.S. Geospatial Intelligence Foundation (USGIF), American Society of Photogrammetry and Remote Sensing (ASPRS), Management Association of Private Photogrammetric Surveyors, National States Geographic Information Council (NSGIC), and past president of the San Francisco Bay Area chapter of the Urban and Regional Information Systems Association (URISA).

Senior Geospatial Analyst Mike Sutherland, based in Denver, has 10 years of experience and most recently worked for the Cooperative Institute for Research and Environmental Sciences (CIRES) for the National Oceanic and Atmospheric Administration (NOAA) at the University of Colorado Boulder. As a senior geospatial analyst at Dewberry, Sutherland is responsible for quality control of lidar projects, coastal and topobathymetric domain staff training, and data processing workflow development and refinement. Sutherland is a member of ASPRS.

Based in Tampa, Senior GIS Professional Dr. Alvan Karlin brings with him more than 20 years of experience in the geospatial and remote sensing industry, where he recently worked as a senior GIS scientist for the Southwest Florida Water Management District. He has published numerous research articles and presented at conferences globally, and is an adjunct professor of biology at the University of Tampa. Karlin is actively involved in the Florida statewide lidar mapping project, which covers more than 32,000 square miles of ground. Karlin has been an active member of ASPRS for more than 25 years and has served on various committees during his time. He has also participated on various GIS Certification Institute committees.

"We are thrilled to welcome Mark, Mike, and Al to our geospatial team," states Dewberry Vice President and Director of Remote Sensing Amar Nayegandhi, CP, CMS, GISP. "They each have a strong background in geospatial technologies, which will directly serve our clients by providing the best possible technical and management expertise to support their needs."

**GeoCue Group Inc.** unveiled its new True View™ line of drone sensors at an invitation only industry event on June 25th in Nashville, Tennessee. True View sensors offer surveyors an innovative lidar + dual oblique mapping camera configuration integrated in a single lightweight payload for

use on commercial drone platforms. True View allows for fast, easy automated generation of true 3D colorized point clouds, oblique imagery and orthophotos from a single flight.

The first sensor of the product line, the True View 410, was displayed at the reveal along with full workflow processing in the companion True View Evo processing software. The True View 410 is the industry's first integrated LIDAR/camera fusion platform designed from the ground up to generate high accuracy 3D colorized LIDAR point clouds. Featuring dual GeoCue Mapping Cameras, a Quanergy M8 Ultra laser scanner and Applanix Position and Orientation System (POS), the result is a true 3D imaging sensor. With its wide 120° fused field of view, the True View 410 provides high efficiency 3D color mapping with vegetation penetration in a payload package with a mass of about 2 kg.

Demonstrations of True View Evo full post-processing workflow software (included with the sensor) were provided. The audience witnessed the creation of stunning 3D colorized point clouds with processing time from sensor to final product of less than 15 minutes for a 50-acre site. The visualization of colorized vertical surfaces demonstrated the value of the dual oblique cameras and true 3D mapping of LIDAR points to images.

Contact GeoCue at 1-256-461-8289 or [info@geocue.com](mailto:info@geocue.com) for detailed system information.

**SPECTRAL EVOLUTION** has moved operations to expanded facilities in Haverhill, Massachusetts. "This move provides us with an expanded space to meet our growing business requirements and allow us to service customers more effectively," said Dennis Witz, Spectral Evolution's President. The new facility is conveniently located near Interstate I-495 highway. The telephone and fax numbers remain the same. Our new address is Spectral Evolution, 26 Parkridge Road, Suite 104, Haverhill, MA, 01835, Tel: 978-687-1833, Fax: 978-945-0372.

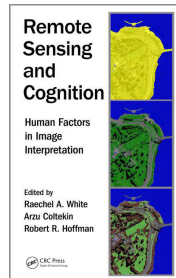
## CALENDAR

- 17-18 September, **GIS IN THE ROCKIES**, Denver, Colorado. For more information, visit <http://gisintherockies.org>.
- 18-20, **NCAUG Conference**, Wilmington, North Carolina. For more information, visit [www.ncaug.com/conference](http://www.ncaug.com/conference).
- 23-26 September, **2019 JACIE/ECCOE Workshop**, Reston, Virginia. For more information, visit <https://www.usgs.gov/land-resources/eros/calval/upcoming-jacie-workshop>.
- 28 September – 2 October, **GIS-PRO 2019**, New Orleans, Louisiana. For more information, visit [www.urisa.org/gispro2019](http://www.urisa.org/gispro2019).

## FEATURES



**533** ARE WE SINKING?—Results of Absolute Gravity Changes in Louisiana  
 By Clifford J. Mugnier



**535** Book Review—*Remote Sensing and Cognition – Human Factors in Image Interpretation*

### COLUMNS

**537** Grids and Datums  
 This month we look at Tuvalu.

### ANNOUNCEMENTS

**529** Pecora 21/ISRSE 38 Symposium  
**540** Headquarters News  
**541** New ASPRS Members  
 Join us in welcoming our newest members to ASPRS.

### DEPARTMENTS

**530** Industry News  
**530** Calendar  
**539** Ad Index  
**572** ASPRS Sustaining Members  
**584** Who's Who in ASPRS  
**612** ASPRS Media Kit

## PEER-REVIEWED ARTICLES

### 543 Roof-Cut Guided Localization for Building Change Detection from Imagery and Footprint Map

Jinqi Gong, Xiangyun Hu, Shiyang Pang, and Yujun Wei

A graph-based model to locate rooftops and demolished buildings based on older footprint maps is introduced.

### 559 Contextual Global Registration of Point Clouds in Urban Scenes

Xuming Ge and Bo Wu

A contextual global registration of partially overlapping point clouds in urban scenes is presented. The approach extracts feature points, establishes correspondence candidates using a contextual rule-based method which is pruned by a new penalization strategy.

### 573 Pavement Marking Retroreflectivity Estimation and Evaluation using Mobile Lidar Data

Erzhao Che, Michael J. Olsen, Christopher E. Parrish, and Jaehoon Jung

Pavement marking visibility is automatically evaluated based on retroreflectivity using mobile lidar sensors such as the Leica Pegasus. The paper introduces a calibration approach to perform the task. Various configurations to quantitatively assess the accuracy of the proposed approach are discussed.

### 585 Total Vertical Uncertainty (TVU) Modeling for Topo-bathymetric Lidar Systems

Firat Eren, Jaehoon Jung, Christopher E. Parrish, Nicholas A. Forfinski-Sarkozi and Brian R. Calder

Authors propose a comprehensive total vertical uncertainty (TVU) model for topo-bathymetric lidar systems. The TVU model consists of a combination of analytical uncertainty propagation for the subaerial portion and Monte Carlo simulation models for the subaqueous portion. Tests on a topo-bathymetric lidar datasets show that the approach captures the variability of uncertainty with depth while providing conservative estimates of uncertainty.

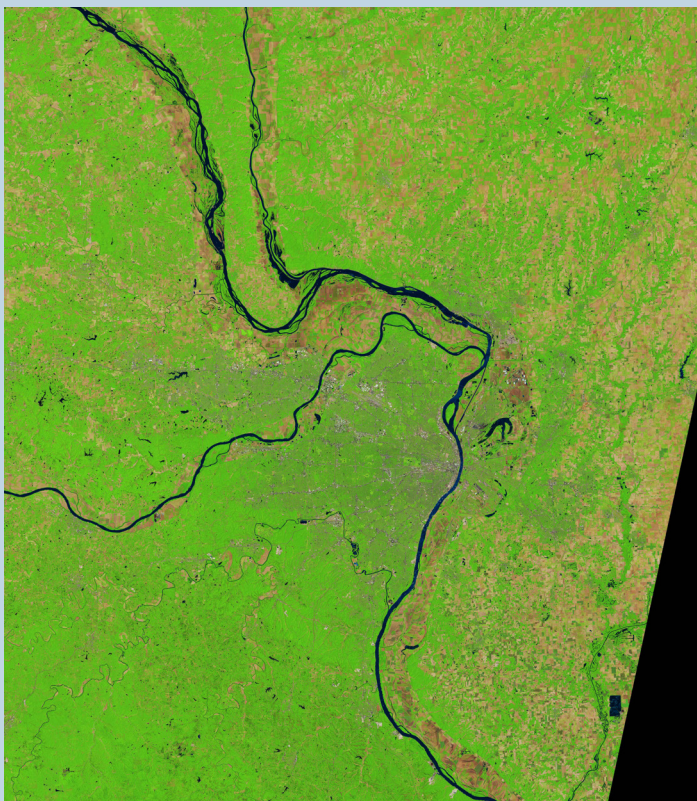
### 597 Exploiting Cosegmentation and Geo-Eco Zoning for Land Cover Product Updating

Ling Zhu, Yang Sun, Ruoming Shi, Yixuan La, and Shu Peng

An incremental updating method for land cover maps based on image cosegmentation and a geo-eco zoning rule database is presented. Cosegmentation of images is first used to extract changed pixels which is then improved by using the geo-eco zoning rule database to detect and remove spurious changes.

See the Cover Description on Page 532

# COVER DESCRIPTION



On May 9, 2019, the U.S. Advanced Hydrologic Prediction Service reported that 313 river gauges across the United States were above flood stage. All but five of those gauges were in the heartland of the United States, mostly within the Mississippi River watershed.

Thirty-two U.S. river gauges were above major flood stage, and 18 of them were within 200 miles of St. Louis, Missouri. Rock Island, Illinois, set a new local high-water record on May 2 at 22.70 feet. The Mississippi River crested at 41.33 feet at St. Louis on May 6—not a record, but a major flood nonetheless.

Towns along the main stem of the Mississippi in Iowa and Illinois have reported some level of flooding for the past six weeks, and recent water levels reached the top five highest on record for most stations. While flood waters have crested and started to recede in many areas, new locations to the south could approach flood stage in the next week as the pulse of water flows toward the Gulf of Mexico.

The Operational Land Imager (OLI) on Landsat 8 caught a rare opening in the spring cloud cover to observe the flooding along the Mississippi River near St. Louis. These false-color images were acquired on May 7, 2019, cover image, and June 5, 2018, above, (for comparison in the same season). The images were composed from a combination of infrared and visible light (OLI bands 6-5-4) in order to better distinguish water that is out of the river banks and on the floodplains.

The latest flood crests came after several heavy rainstorms in late April and early May doused the already saturated ground of the Midwest and Plains states. Beyond the Mississippi River, flash flooding has been a problem in Kansas, Missouri, Nebraska, Arkansas, Oklahoma, and Texas. Snow fell in the Upper Midwest on May 8, and more rain is expected across the Mississippi basin later this week.

This spring flooding was predicted by U.S. government climatologists and weather forecasters. In a national hydrological assessment released in March by the National Oceanic and Atmospheric Administration, forecasters noted: "The potential for major flooding due to well-above-normal precipitation, snowmelt, saturated soils, and frozen ground is high compared to its historical average across the Upper Mississippi River and Red River of the North basins."

For more information visit, <https://landsat.visibleearth.nasa.gov/view.php?id=145029>.

NASA Earth Observatory images by Lauren Dauphin, using Landsat data from the U.S. Geological Survey. Story by Mike Carlowicz.



THE IMAGING  
& GEOSPATIAL  
INFORMATION  
SOCIETY

## PHOTOGRAMMETRIC ENGINEERING & REMOTE SENSING

### JOURNAL STAFF

Publisher ASPRS  
Editor-In-Chief Alper Yilmaz  
Assistant Editor Jie Shan  
Assistant Director — Publications Rae Kelley  
Electronic Publications Manager/Graphic Artist  
Matthew Austin

*Photogrammetric Engineering & Remote Sensing* is the official journal of the American Society for Photogrammetry and Remote Sensing. It is devoted to the exchange of ideas and information about the applications of photogrammetry, remote sensing, and geographic information systems. The technical activities of the Society are conducted through the following Technical Divisions: Geographic Information Systems, Photogrammetric Applications, Lidar, Primary Data Acquisition, Professional Practice, and Remote Sensing Applications. Additional information on the functioning of the Technical Divisions and the Society can be found in the Yearbook issue of *PE&RS*.

Correspondence relating to all business and editorial matters pertaining to this and other Society publications should be directed to the American Society for Photogrammetry and Remote Sensing, 425 Barlow Place, Suite 210, Bethesda, Maryland 20814-2144, including inquiries, memberships, subscriptions, changes in address, manuscripts for publication, advertising, back issues, and publications. The telephone number of the Society Headquarters is 301-493-0290; the fax number is 225-408-4422; web address is [www.asprs.org](http://www.asprs.org).

**PE&RS.** *PE&RS* (ISSN0099-1112) is published monthly by the American Society for Photogrammetry and Remote Sensing, 425 Barlow Place, Suite 210, Bethesda, Maryland 20814-2144. Periodicals postage paid at Bethesda, Maryland and at additional mailing offices.

**SUBSCRIPTION.** For the 2019 subscription year, ASPRS is offering two options to our *PE&RS* subscribers — an e-Subscription and the print edition. E-subscribers can plus-up their subscriptions with printed copies for a small additional charge. Print and Electronic subscriptions are on a calendar-year basis that runs from January through December. We recommend that customers who choose both e-Subscription and print (e-Subscription + Print) renew on a calendar-year basis. The new electronic subscription includes access to ten years of digital back issues of *PE&RS* for online subscribers through the same portal at no additional charge. Please see the Frequently Asked Questions about our journal subscriptions.

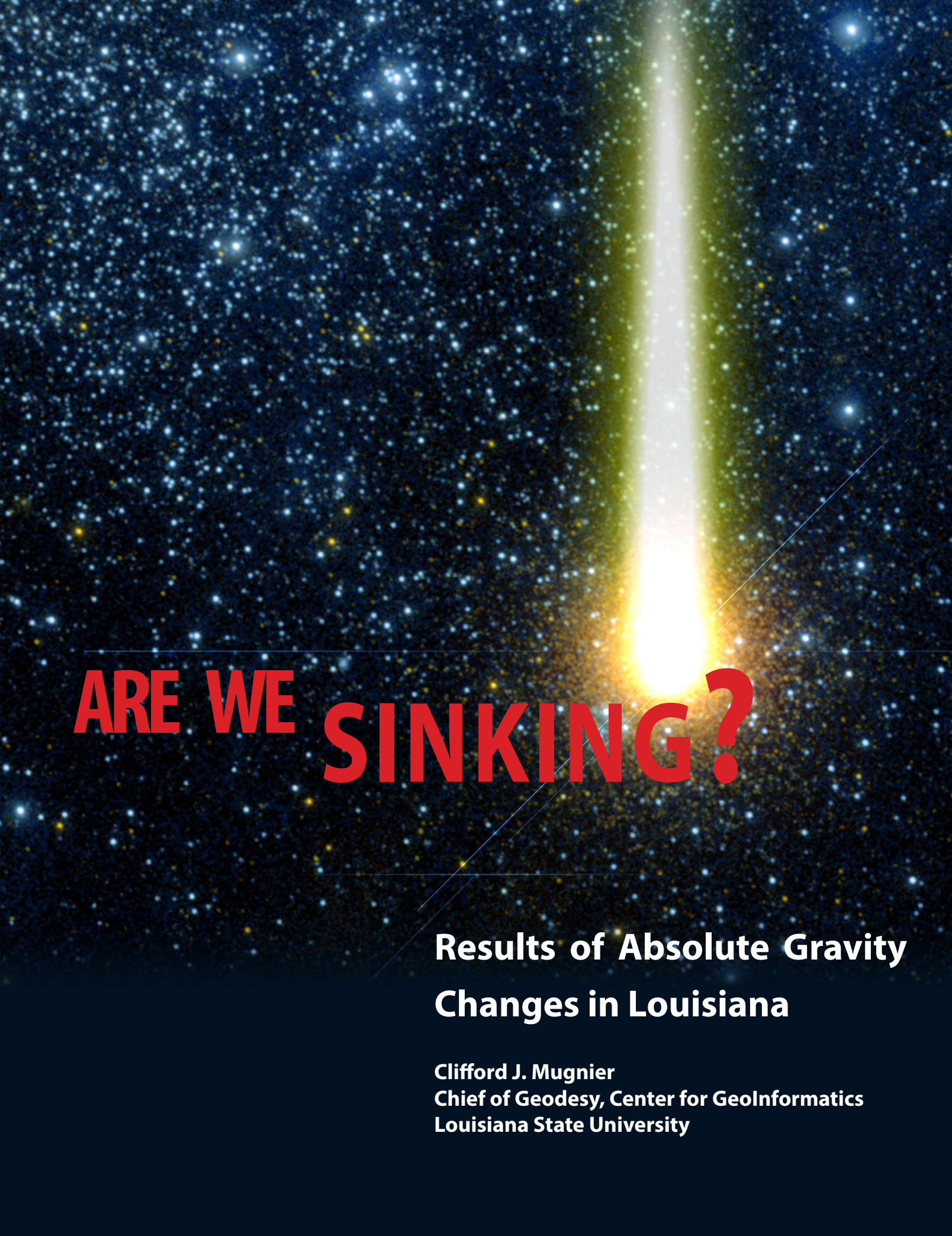
The rate of the e-Subscription (digital) Site License Only for USA and Foreign: 1000.00 USD; e-Subscription (digital) Site License Only for Canada\*: 1049.00 USD; Special Offers: e-Subscription (digital) Plus Print for the USA: 1365.00 USD; e-Subscription (digital) Plus Print Canada\*: 1424.00 USD; e-Subscription (digital) Plus Print Outside of the USA: 1395.00 USD; Printed-Subscription Only for USA: 1065.00 USD; Printed-Subscription Only for Canada\*: 1124.00 USD; Printed-Subscription Only for Other Foreign: 1195.00 USD. \*Note: e-Subscription/Printed-Subscription Only/e-Subscription Plus Print for Canada include 5% of the total amount for Canada's Goods and Services Tax (GST #135123065). **PLEASE NOTE: All Subscription Agencies receive a 20.00 USD discount.**

**POSTMASTER.** Send address changes to *PE&RS*, ASPRS Headquarters, 425 Barlow Place, Suite 210, Bethesda, Maryland 20814-2144. CDN CPM #40020812)

**MEMBERSHIP.** Membership is open to any person actively engaged in the practice of photogrammetry, photointerpretation, remote sensing and geographic information systems; or who by means of education or profession is interested in the application or development of these arts and sciences. Membership is for one year, with renewal based on the anniversary date of the month joined. Membership Dues include a 12-month electronic subscription to *PE&RS*. Or you can receive the print copy of *PE&RS* Journal which is available to all member types for an additional fee of 60.00 USD for shipping USA, \$65 USD for Canada, or 75.00 USD for international shipping. Dues for ASPRS Members outside of the U.S. will now be the same as for members residing in the U.S. Annual dues for Regular members (Active Member) is 150 USD; for Student members 50 USD for USA and Canada 58 USD; 60 USD for Other Foreign members. A tax of 5% for Canada's Goods and Service Tax (GST #135123065) is applied to all members residing in Canada.

**COPYRIGHT 2019.** Copyright by the American Society for Photogrammetry and Remote Sensing. Reproduction of this issue or any part thereof (except short quotations for use in preparing technical and scientific papers) may be made only after obtaining the specific approval of the Managing Editor. The Society is not responsible for any statements made or opinions expressed in technical papers, advertisements, or other portions of this publication. Printed in the United States of America.

**PERMISSION TO PHOTOCOPY.** The appearance of the code at the bottom of the first page of an article in this journal indicates the copyright owner's consent that copies of the article may be made for personal or internal use or for the personal or internal use of specific clients. This consent is given on the condition, however, that the copier pay the stated per copy fee of 3.00 USD through the Copyright Clearance Center, Inc., 222 Rosewood Drive, Danvers, Massachusetts 01923, for copying beyond that permitted by Sections 107 or 108 of the U.S. Copyright Law. This consent does not extend to other kinds of copying, such as copying for general distribution, for advertising or promotional purposes, for creating new collective works, or for resale.



# **ARE WE SINKING?**

## **Results of Absolute Gravity Changes in Louisiana**

**Clifford J. Mugnier  
Chief of Geodesy, Center for Geolnformatics  
Louisiana State University**

The first observation of absolute gravity in Louisiana at the one micro gal level of precision was at the University of New Orleans in 1989 by the National Geodetic Survey. Since then, four additional observations through 2018 have shown a cumulative apparent subsidence of 147mm in 29 years (-5mm/yr). In 2002, the Commander, New Orleans District Corps of Engineers requested assistance of what is now the National Geospatial-Intelligence Agency (NGA) to perform an absolute gravity observation campaign throughout the State of Louisiana at many of the LSU Center for GeoInformatics (C4G) GPS Continuously Operating Reference Station (CORS) sites. A second observation campaign was completed by NGA this year. Cumulative apparent elevation changes are:

Baton Rouge	negligible	Lake Charles	-16 mm	Ruston	-9 mm
Old River	-34 mm	Sicily Island	+8 mm	Hammond	negligible
Thibodeaux	+7 mm	LUMCON	-20 mm	Shreveport	negligible
Oakdale	negligible	Rayville	+13 mm	Natchitoches	+17mm
Lafayette	negligible	Boothville	-13 mm	Alexandria	-49 mm

Changes in the absolute value of gravity at a location can be a result of uplift/subsidence as well as variations in ground water and tectonic motion. In a generally homogenous sedimentary basin such as Louisiana, it's likely some combination of subsidence and ground water. LSU now has a three-person permanent gravity survey crew that is traveling to all C4G CORS sites state-wide as well as to tide gauges collocated with CORS sites throughout the northern rim of the Gulf of Mexico for the observation of absolute gravity and for deflection of the vertical. These observations are expected to contribute to the knowledge of the surface motions of the State as well as to form the basis of a new quasi-geoid model for Louisiana in collaboration among NGA, NGS, and LSU.

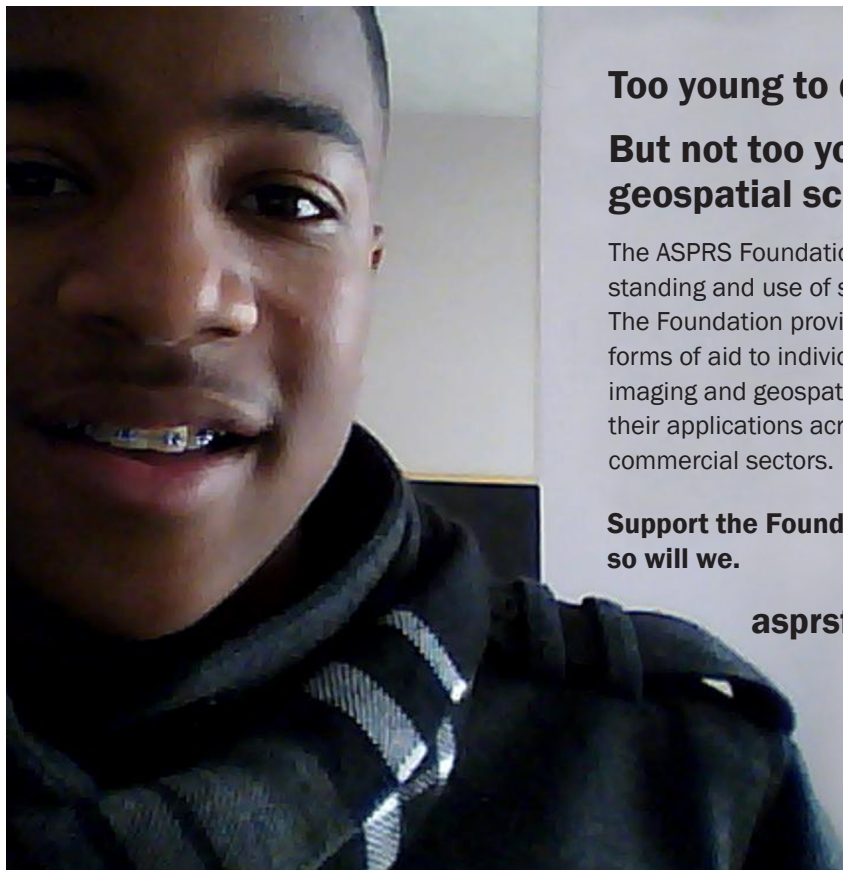
This is a follow-up to “*Are We Sinking?— National Geospatial-Intelligence Agency Visits LSU Campus to Measure Subsidence*” which was originally published in the January 2019 issue of *PE&RS*.

## Too young to drive the car? Perhaps! But not too young to be curious about geospatial sciences.

The ASPRS Foundation was established to advance the understanding and use of spatial data for the betterment of humankind. The Foundation provides grants, scholarships, loans and other forms of aid to individuals or organizations pursuing knowledge of imaging and geospatial information science and technology, and their applications across the scientific, governmental, and commercial sectors.

**Support the Foundation, because when he is ready  
so will we.**

[asprsfoundation.org/donate](https://asprsfoundation.org/donate)



Reluctantly subversive and at the same time pleasingly fresh, this succinct and extremely readable excursion into the human aspects of geospatial interpretation comes at a time when spectacular results from AI-driven, automated sensor data capture, and analysis appear to be an everyday expectation.

The quality of this compilation is affirmed by the glowing reviews on its back cover. The book is slightly over 175 pages, including a preface and eight chapters. This work provides an insight into the psychological, philosophical, and sometimes anatomic/physiologic, aspects of human perception and understanding of images as rendered by geospatial software and hardware.

“*Remote Sensing and Cognition*” makes its opportune appearance now that technological advances thrust us into a “must-be-3 (or more)-D-or-else” geospatial data visualization paradigm. As “mixed reality” or XR, as it is known, i.e., Virtual Reality plus Augmented Reality plus, based experiences are quickly disrupting and forcefully extending the capabilities of everyday analytical workflows. This volume provides an opportunity to explore what still makes image interpretation a uniquely human endeavor.

In assembling a group of experts from diverse fields, the editors try to elucidate how geocognition and cognitive GIScience works, focusing on the most basic aspect associated with remote sensing; i.e. the interpretation of images (“e.g. photographs, digital images, and sensor data rendered on a display”).

Chapter 1—Cognitive and Perceptual Processes in Remote Sensing Image Interpretation by Robert R. Hoffman, sets the stage for subsequent chapters by examining the core issues of what constitutes expert interpretation and how knowledge and reasoning serve the expert.

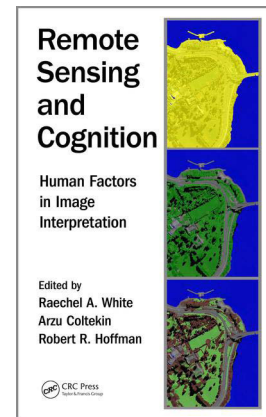
What constitutes “human spatial knowledge?” That is the question addressed in Chapter 2—Characteristics of Geospatial Photographs in Constructing Human Spatial Knowledge by Pyry Kettunen.

The influence of perspective on both art and military reconnaissance are explored in the context of cognitive GIScience in Chapter 3—Intersectional Perspectives on the Landscape Concept: Art, Cognition and Military Perspectives by Raechel A. White.

The dichotomy in the perceptual framework in analyzing terrestrial and “from above” scenes is presented in Chapter 4—Head in the Clouds, Feet on the Ground: Applying Our Terrestrial Minds to Satellite Perspectives by Ryan V. Ringer and Lester C. Loschky.

Chapter 5—Eye-Tracking Evaluation of Non-Photorealistic Maps of Cities and Photo-Realistic Visualization of an Extinct Village by Stanislav Popelka examines the results of geovisualization modalities by exposing participants in a study to 2D and 3D stimuli from map portals.

Chapter 6—Designing Geographic Information for Moun-



## Remote Sensing and Cognition – Human Factors in Image Interpretation

Raechel A. White, Arzu Coltekin, and Robert R. Hoffman, Editors

CRC Press, Taylor and Francis Group, LLC 2018, xiv and 175 pp., black and white and color figures, tables, index. ISBN-13 978-1-4987-8156-5. Hardback: \$141.98; Kindle: \$33.86.

Reviewed by Demetrio P. Zourarakis, Ph.D., GISP, CMS, CGP-GIS.

tains: Mixed Methods Research by Raffaella Balzarini and Nadine Mandran, presents results from exposing human subjects to different mountain area views and diverse cartographic products in order to detect differences in geocognition patterns and the quality and quantity of extracted information.

The essence of what constitutes geointelligence is analyzed in Chapter 7—The Human Factors of Geospatial Intelligence by Laura D. Strater, Susan P. Coster, Dennis Bellafiore, Stephen P. Handwerk, Gregory Thomas, and Todd S. Bacastow; the constraints and possibilities posed by Goal-Directed Task Analysis are presented.

The potential for true encapsulation of expert knowledge involved in the process of image classification via geo-semantics and geo-ontologies is postulated in Chapter 8—Employing Ontology to Capture Expert Intelligence within GEOBIA: Automation of the Interpretation Process by Sachit Rajbhandari, Jagannath Aryal, Jon Osborn, Arko Lucieer, and Robert Musk.

Photogrammetric Engineering & Remote Sensing  
Vol. 85, No. 8, August 2019, pp. 535–536.  
0099-1112/19/535–536

© 2019 American Society for Photogrammetry  
and Remote Sensing

doi: 10.14358/PERS.85.8.535

The message one could extract from reading this book is that regardless of how complex the ecosystem of hardware and software arrays used to render geospatial images may be, at the end of the day, the only meaningful understanding of remotely sensed data is that one performed by a human being.

As the golden era of machine learning and computer vision is being ushered in, works like this one reminds us that human intelligence usually resides on this side of the screen, and ultimately requires human perception and brain for it to work. This book is a welcome addition to our remote sensing body of knowledge and essential for anybody who seeks an understanding of the “wetware”-based mechanisms and architecture that allow for this to happen.

**ASPRS is proud to partner with CRC Press, Taylor & Francis Group.** We are excited to feature *Remote Sensing and Cognition – Human Factors in Image Interpretation* and other essential books in GIS and Mapping for a discount price to ASPRS members. Visit the ASPRS Bookstore at [www.asprs.org](http://www.asprs.org). Don't forget to apply code **ASP25** to **SAVE 25% on entire purchase\* + FREE Shipping**. Can't find what you're looking for? Visit [crcpress.com](http://crcpress.com) to shop and save on all of their books.

\*Valid for online orders only and excludes eBooks.

## *Sponsor One Rising Star Today and Make a Difference for Tomorrow*

### **SPONSORSHIP AND MENTORSHIP**

ASPRS' Rising Star program is established to advance geospatial science through a sponsorship and mentorship program for early career professional and student members.

#### **SPONSORS**

ASPRS Corporations, Regions, Member Groups, and Individual Members are all eligible to sponsor a Rising Star or multiple Rising Stars.

#### **COSTS**

- Membership: \$150 annual membership fees for the Rising Star
- Time and Travel Expenses up to \$1000 per year including time and travel for the Rising Star to attend the ASPRS Annual Conference and participate in ASPRS Technical Division activity throughout the year.

#### **BENEFITS**

- Listing in *PE&RS* Journals for the entire time of sponsorship to include Sponsor Name and the list of the Rising Star members supported by each sponsor.
- Feature Article – One Rising Star will be featured with a *PE&RS* Highlight Journal Article every three months.

#### **RISING STARS**

Be a part of setting the direction of the geospatial profession by contributing your expertise and energy, by guiding industry and professional practice standards, specifications, and by leading, training, and encouraging others to appreciate and apply new mapping and remote sensing technologies.

[HTTP://WWW.ASPRS.ORG/RISING-STAR-PROGRAM](http://www.asprs.org/rising-star-program)

## *Meet Our Rising Stars!*

**Chris Stayte**

*Sponsored by Woolpert, Inc.*

**Corey Ochsman**

*Sponsored by Woolpert, Inc.*

**Collin Hutcheson**

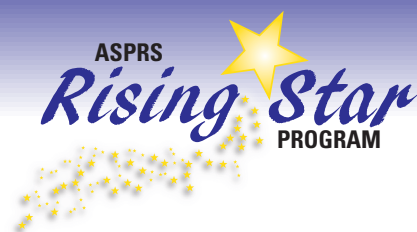
*Sponsored by Merrick & Company*

**Charles Krugger**

*Sponsored by Stahl Sheaffer Engineering, LLC*

**Kristine Taniguchi-Quan, Ph. D.**

*Sponsored by Pacific Southwest Region of ASPRS*





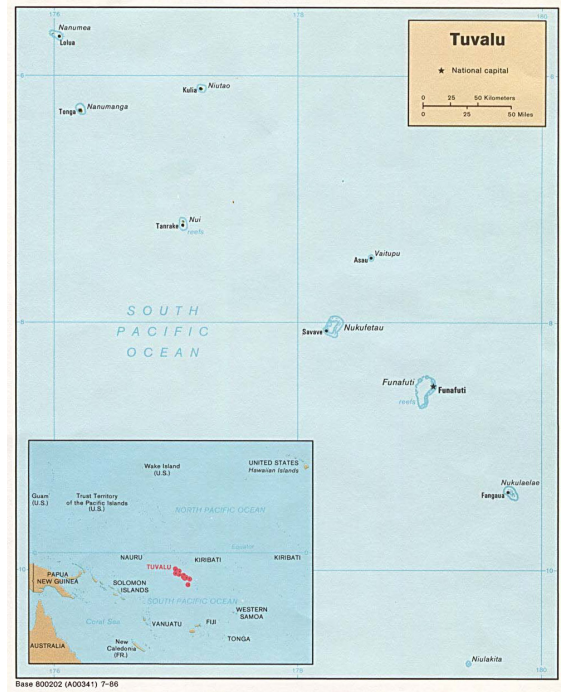
# & GRIDS & DATUMS

# TUVALU

BY Clifford J. Mugnier, CP, CMS, FASPRS

The Grids & Datums column has completed an exploration of every country on the Earth. For those who did not get to enjoy this world tour the first time, *PE&RS* is reprinting prior articles from the column. This month's article on Tuvalu was originally printed in 2001 but contains updates to their coordinate system since then.

**T**uvalu comprises a chain, 580 kilometers long, of nine coral atolls in the Pacific Ocean just west of the International Date Line. The total land area of the densely populated group is only 26 sq km (10 sq mi); however, the islands occupy 1.3 million sq km (500,000 sq mi) of ocean between Kiribati and the Samoas. Five of the islands are low-lying coral atolls; the highest point on these (and the highest point in Tuvalu) is just 4.6m (15 ft) above sea level. The remaining four islands are pinnacles of land that rise up from the sea bed. On the islands, there are many reefs and salt-water ponds while the island of Nanumea hosts a fresh-water pond; rare for an atoll. Made mostly of eroded coral, Tuvalu has poor soil, no streams or rivers, and few remaining outcrops of forest. Coconut palms grow in abundance across all the islands, but otherwise there is only enough soil to support subsistence agriculture for about three-quarters of the population. All other food is imported. Water needs are met by catchment and storage facilities because the porous, low-lying atolls are unable to hold ground water. The only land animals are the Polynesian rat, chickens, dogs, and pigs — all introduced species. Niulakita has no lagoon, but has a swamp at its center. Because it has never had a permanent population, the southernmost island was not taken into account in the naming of the Tuvalu group. Tuvalu means “eight standing together.” The climate is tropical, with an average temperature of 30°C (87°F) and little seasonal variation. The wet season is between October and March, and 350 cm (12 ft) of rain falls in a normal year. Cyclone (hurricane) activity is rare; there have been only four severe hits this century (but all since 1972).



Physiographically, Tuvalu belongs in Micronesia, but culturally, the islands belong to Polynesia. Language, traditions, and artifacts indicate that Polynesians from Tonga and Samoa in the southeast arrived in the island group early in the 14th century. In 1597, Don Alvaro de Mendaña y Neyra cruised through the coral atolls of Tuvalu. Further European contact came in the late 18th century, and the last of the islands were charted by 1826. They were named the Ellice Islands after the British member of parliament who owned the ship that first landed on Funafuti Atoll in 1819. In 1892, the islands became part of the Gilbert and Ellice Islands protectorate and, in 1916, became a Crown Colony. During WWII the U.S. used Tuvalu's northernmost atoll, Nanumea, as a base to repel the Japanese who were threatening the Gilbert Islands. Wrecks of air and sea craft remain on the island.

From the 1960s through 1977, Tuvaluans embarked on

Photogrammetric Engineering & Remote Sensing  
Vol. 85, No. 8, August 2019, pp. 537–539.  
0099-1112/19/537–539

© 2019 American Society for Photogrammetry  
and Remote Sensing

doi: 10.14358/PERS.85.8.537

steady constitutional development. In 1974, the Polynesian Ellice Islanders voted to separate from the Micronesian Gilberts. They reverted to their precolonial name of Tuvalu and attained independence on 01 October 1978.

Hydrographic surveys were under-taken by the USS Sumner in 1943, the USS Hydro in 1944, and by the H.M.S. Cook from 1959-1963. Between 1962 and 1966 the HIRAN trilateration of the southwest Pacific was undertaken by the U.S. Air Force. A number of primary stations were established. These were originally expressed in terms of the WGS 60 Datum, the Australian National Datum of 1966, as well as being converted to the Fiji Datum of 1956 (*PE&RS*, October, 2000). The British Directorate of Overseas Surveys (DOS) carried out survey work between 1968 and 1973, expressing their values in terms of local astronomic datums for individual islands. Some stations were linked to the HIRAN survey and hence were expressed in terms of Fiji 56. In 1974, the Royal Military Survey of the U.K. decided that where possible island areas should be positioned on WGS 72; hence, where possible the Fiji 56 datums were converted to the WGS 72 Datum using cartesian shifts. In addition, shifts have been established between the local astro datums and Fiji 56 for some of the islands, but other values are held only in local datum terms for some island areas. In 1984 and 1985, the Australians carried out "Operation ANON." This provided 16 Doppler fixes to many points in the Tuvalu Group, yielding coordinates in terms of the WGS 72 Datum. The primary objective was to provide the government of Tuvalu with sufficient survey data to enable them to determine base points for the definition of their Exclusive Economic Zone.

The survey work for Operation ANON in 1984 and 1985 used 11 points from earlier surveys by the Australians. Because all field work was carried out on the WGS 72 Datum, the points were converted to the WGS 84 Datum using the standard NIMA WGS72 to WGS84 transformation:  $\Delta X = 0$  m,  $\Delta Y = 0$  m,  $\Delta Z = 4.5$  m,  $k = 0.219$  ppm, and  $R_z = 0.554''$ .

On Nanumea, the northernmost of Tuvalu's atolls, the origin of the Nanumea Sodano Astro Datum of 1966 at Laken Island is  $\Phi_0 = 05^\circ 39' 04.59''$  S,  $\Lambda_0 = 176^\circ 04' 31.09''$  East of Greenwich, and the ellipsoid of reference is the International 1924 where  $a = 6,378,388$  m, and  $1/f = 297$ . The vertical datum is based on readings of the tide levels made on the ocean side (at the seaward end of the LST wreck) and in the lagoon (at NME 25), and these two staff gauges were connected by height traversing and also to the Post Office. From the Nanumea Sodano Astro Datum to the WGS84 Datum,  $\Delta X = +225$  m,  $\Delta Y = -114$  m, and  $\Delta Z = -148$  m; the accuracy of this transformation is estimated to be  $\pm 2$  meters in each of Eastings and Northings. The Nanumea TM Local Grid is based on the Transverse Mercator projection where the Latitude of Origin is at the equator ( $\phi_0 = 0^\circ$ ), the Central Meridian  $\lambda_0 = 176^\circ 06'$  E, the False Easting = 45 km, and the False Northing = 8,000 km. The Scale Factor at Origin is unity ( $m_0 = 1.0$ ).

On the island of Nanumaga, the origin of the NMG 1 Astro Datum of 1974 is  $\Phi_0 = 06^\circ 17' 15.04''$  S,  $\Lambda_0 = 176^\circ 18' 52.86''$  East of Greenwich, and the ellipsoid of reference is the International 1924. The vertical datum is based on heights observed as part of the traversing. They have been related to mean sea level by two days of readings on a staff gauge set up in the boat channel. Two tide poles were erected on the reef opposite the Government flagstaff, and continuous observations were obtained for 2.5 days. From the NMG 1 Astro Datum of 1974 to the WGS84 Datum,  $\Delta X = +204$  m,  $\Delta Y = -31$  m, and  $\Delta Z = +113$  m; the accuracy of this transformation is estimated to be between  $\pm 2$  m and  $\pm 26$  m in each of Eastings and Northings. The Nanumaga TM Local Grid is based on the Transverse Mercator projection where the Latitude of Origin is at the equator ( $\phi_0 = 0^\circ$ ), the Central Meridian  $\lambda_0 = 176^\circ 19'$  E, the False Easting = 35 km, and the False Northing = 7,000 km. The Scale Factor at Origin is unity ( $m_0 = 1.0$ ).

On the atoll of Nukufetau, the location of the WWII airfield on Motulalo Island, the origin of the NFT 1 Astro Datum of 1974 is  $\Phi_0 = 08^\circ 01' 40.28''$  S,  $\Lambda_0 = 178^\circ 18' 48.37''$  East of Greenwich, and the ellipsoid of reference is the International 1924. From the NFT 1 Astro Datum of 1974 to the WGS84 Datum,  $\Delta X = +200$  m,  $\Delta Y = -83$  m, and  $\Delta Z = +96$  m; the accuracy of this transformation is estimated to be  $\pm 7$  m in Eastings and  $\pm 21$  m in Northings. The Nukufetau TM Local Grid is based on the Transverse Mercator projection where the Latitude of Origin is at the equator ( $\phi_0 = 0^\circ$ ), the Central Meridian  $\lambda_0 = 178^\circ 22'$  E, the False Easting = 40 km, and the False Northing = 6,000 km. The Scale Factor at Origin is unity ( $m_0 = 1.0$ ).

On the solitary coral island of Niulakita, I guess that the origin of the Niulakita Astro Datum of 1965 is  $\Phi_0 = 10^\circ 47' 21.6059''$  S,  $\Lambda_0 = 179^\circ 27' 51.7081''$  East of Greenwich, and the ellipsoid of reference is the International 1924. From the Niulakita Astro Datum of 1965 to the WGS84 Datum,  $\Delta X = +184$  m,  $\Delta Y = -465$  m, and  $\Delta Z = +119$  m; the accuracy of this transformation is estimated to be  $\pm 10$  m in Eastings and  $\pm 19$  m in Northings. The Niulakita TM Local Grid is based on the Transverse Mercator projection where the Latitude of Origin is at the equator ( $\phi_0 = 0^\circ$ ), the Central Meridian  $\Phi_0 = 179^\circ 28'$  E, the False Easting = 15 km, and the False Northing = 3,000 km. The Scale Factor at Origin is unity ( $m_0 = 1.0$ ). A century ago workers excavated guano here for commercial fertilizer. Later an Australian company used the island as a coconut plantation, and in 1944 the British government purchased the island and gave it to overpopulated Niutao, which relocated a few families there.

On the atoll of Niutao, the origin of the NTO 1 Astro Datum of 1973 is  $\Phi_0 = 06^\circ 06' 29.25''$  S,  $\Lambda_0 = 177^\circ 19' 59.16''$  East of Greenwich, and the ellipsoid of reference is the International 1924. The vertical Datum at NTO 2 is based on a personal estimate of probable mean sea level! From the NTO 1 Astro Datum of 1973 to the WGS84 Datum,  $\Delta X = +219$  m,  $\Delta Y = -198$  m, and  $\Delta Z = -92$  m; the accuracy of this transformation is es-

timated to be  $\pm 15$  m in Eastings and  $\pm 4$  m in Northings. The Niutao TM Local Grid is based on the Transverse Mercator projection where the Latitude of Origin is at the equator ( $\phi_0 = 0^\circ$ ), the Central Meridian  $\lambda_0 = 177^\circ 20' \text{ E}$ , the False Easting = 30 km, and the False Northing = 5,000 km. The Scale Factor at Origin is unity ( $m_0 = 1.0$ ).

The atoll of Nukulaelae is the easternmost of the Tuvalu islands and was the first island to accept Christianity. Because of rising sea level, Nukulaelae is threatened by salt water seeping into the taro swamps. For Nukulaelae, the origin of the Nukulaelae Astro Datum of 1965, actually on Fanagua Island, is unknown, but the ellipsoid of reference is the International 1924. From the Nukulaelae Astro Datum of 1965 to the WGS84 Datum,  $\Delta X = +254$  m,  $\Delta Y = -238$  m, and  $\Delta Z = -234$  m; the accuracy of this transformation is estimated to be  $\pm 13$  m in Eastings and  $\pm 14$  m in Northings. The Nukulaelae TM Local Grid is based on the Transverse Mercator projection where the Latitude of Origin is at the equator ( $\phi_0 = 0^\circ$ ), the Central Meridian  $\lambda_0 = 179^\circ 50' \text{ E}$ , the False Easting = 25 km, and the False Northing = 2,000 km. The Scale Factor at Origin is unity ( $m_0 = 1.0$ ).

On the atoll of Vaitupu, the educational center of Tuvalu, I guess that the origin of Vaitupu Atoll Datum is at point VTZ 1 Astro:  $\Phi_0 = 07^\circ 29' 24.710'' \text{ S}$ ,  $\Lambda_0 = 178^\circ 41' 52.31'' \text{ East}$  of Greenwich, and the ellipsoid of reference is the International 1924. From the Vaitupu Island Datum to the WGS84 Datum,  $\Delta X = +193$  m,  $\Delta Y = +61$  m, and  $\Delta Z = +201$  m; the accuracy of this transformation is estimated to be  $\pm 23$  m in Eastings and  $\pm 26$  m in Northings. The Vaitupu TM Local Grid is based on the Transverse Mercator projection where the Latitude of Origin is at the equator ( $\phi_0 = 0^\circ$ ), the Central Meridian  $\lambda_0 = 178^\circ 41' \text{ E}$ , the False Easting = 10 km, and the False Northing = 1,000 km. The Scale Factor at Origin is unity ( $m_0 = 1.0$ ).

On the capital atoll of Funafuti, the coordinates of the origin of the UF5 Astro Datum of 1973 are unknown but the ellipsoid of reference is the International 1924. The vertical datum is based on an automatic tide gauge situated on the main jetty at Fongafale, and 48-hour readings were obtained. The gauge is run by the University of Hawaii. From the UF5 Astro Datum of 1973 to the WGS84 Datum,  $\Delta X = +189$  m,  $\Delta Y = +783$  m, and  $\Delta Z = +256$  m. The Funafuti TM Local Grid is based on the Transverse Mercator projection where the Latitude of Origin is at the equator ( $\phi_0 = 0^\circ$ ), the Central Meridian  $\lambda_0 = 179^\circ 08' \text{ E}$ , the False Easting = 50 km, and the False Northing = 9,000 km. The Scale Factor at Origin is unity ( $m_0 = 1.0$ ).

The only Micronesian community in Polynesian Tuvalu is on Nui. Nui is 255 km northwest of Funafuti Island. On the atoll of Nui, the coordinates of the origin of the Nui As-

tro Datum of 1965 are  $\Phi_0 = 07^\circ 13' 40.09'' \text{ S}$ ,  $\Lambda_0 = 177^\circ 09' 47.26'' \text{ East}$  of Greenwich and the ellipsoid of reference is the International 1924. The vertical datum is based on ocean and lagoon tide levels read over four weekends. The ocean staff gauge was off the Maneapa and the lagoon gauge was at the Government station. The two gauges were connected by height traverse to the local control and to the Post Office for height of the Meteorological Service mercury barometer. From the Nui Astro Datum of 1965 to WGS84 Datum,  $\Delta X = +259$  m,  $\Delta Y = +217$  m, and  $\Delta Z = -246$  m. The Nui TM Local Grid is based on the Transverse Mercator projection where the Latitude of Origin is at the equator ( $\phi_0 = 0^\circ$ ), the Central Meridian  $\lambda_0 = 177^\circ 09' \text{ E}$ , the False Easting = 20 km, and the False Northing = 4,000 km. The Scale Factor at Origin is unity ( $m_0 = 1.0$ ).

Thanks to Jane Resture for details of local culture. Thanks for all technical details of the complex coordinate systems of Tuvalu go entirely to Karen French, Geodetic Branch, Defence Geographic Centre of the British Military Survey.

## UPDATE

The Pacific Islands Geospatial and Surveying Strategy 2017-2027 is a 10-year regional plan for developing geospatial and surveying capacity. The Tuvalu Geodetic Survey Project 2016—Phase I was supported by Government funding and consisted of 4 weeks for field surveys on 3 islands: Vaitupu, Nukufetau, and Funafuti.

In 2017, completion of Phase II of the Geodetic Survey for the four northern Islands (Nanumea, Nanumaga, Niutao and Nui) included Geodetic survey, Cadastral survey, Topo survey, UAV/Drone survey, Tide Monitoring to establish mean sea level or MSL, lowest astronomical tide or LAT, and highest astronomical tide or HAT on these 4 islands.

2018 saw completion of the last Phase III of the Geodetic Project on Nukulaelae, Niulakita and on Funafuti again.

[http://ggim.un.org/meetings/GGIM-committee/7th-Session/side\\_events/2%20-%20Faatasi%20Malologa.pdf](http://ggim.un.org/meetings/GGIM-committee/7th-Session/side_events/2%20-%20Faatasi%20Malologa.pdf)

<https://tuvalutrustfund.tv/wp-content/uploads/2018/03/2018-TUVALU-NATIONAL-BUDGET.pdf>

The contents of this column reflect the views of the author, who is responsible for the facts and accuracy of the data presented herein. The contents do not necessarily reflect the official views or policies of the American Society for Photogrammetry and Remote Sensing and/or the Louisiana State University Center for GeoInformatics (C<sup>4</sup>G).

This column was previously published in *PE&RS*.

---

## Ad Index

Geomni, Inc.

Geomni.net/psm

Cover 4

## JOURNAL STAFF

### Editor-In-Chief

Alper Yilmaz, Ph.D., PERSeditor@asprs.org

### Associate Editors

Rongjun Qin, Ph.D., qin.324@osu.edu

Michael Yang, Ph.D., michael.yang@utwente.nl

Petra Helmholtz, Ph.D., Petra.Helmholtz@curtin.edu.au

Bo Wu, Ph.D., bo.wu@polyu.edu.hk

Clement Mallet, Ph.D., clemallet@gmail.com

Vasit Sagan, Ph.D., Vasit.Sagan@slu.edu

Jose M. Pena, Ph.D., jmpena@ica.csic.es

Xin Huang, Ph.D., huang\_w hu@163.com

Prasad Thenkabail, Ph.D., pthenkabail@usgs.gov

Ruisheng Wang, Ph.D., ruishwang@ucalgary.ca

Desheng Liu, Ph.D., liu.738@osu.edu

Valérie Gouet-Brunet, Ph.D., valerie.gouet@ign.fr

Yury Vizilter, Ph.D., viz@gosniias.ru

Dorota Iwaszczuk, Ph.D., dorota.iwaszczuk@tum.de

Qunming Wang, Ph.D., wqm11111@126.com

Filiz Sunar, Ph.D., fsunar@itu.edu.tr

Norbert Pfeifer, Ph.D., np@ipf.tuwien.ac.at

Jan Dirk Wegner, Ph.D., jan.wegner@geod.baug.ethz.ch

Hongyan Zhang, Ph.D., zhanghongyan@whu.edu.cn

Zhenfeng Shao, Ph.D., shaozhenfeng@whu.edu.cn

### Assistant Editor

Jie Shan, Ph.D., jshan@ecn.purdue.edu

### Contributing Editors

#### Grids & Datums Column

Clifford J. Mugnier, C.P., C.M.S., cjmce@lsu.edu

#### Book Reviews

Sagar Deshpande, Ph.D., bookreview@asprs.org

#### Mapping Matters Column

Qassim Abdullah, Ph.D., Mapping\_Matters@asprs.org

#### Sector Insight

Lucia Lovison-Golob, Ph.D., lucia.lovison@sat-drones.com

#### Project Management Column

Raquel Charrois, PMP, CP, CMS, PMP@asprs.org

### ASPRS Staff

#### Assistant Director — Publications

Rae Kelley, rkelley@asprs.org

#### Electronic Publications Manager/Graphic Artist

Matthew Austin, maustin@asprs.org

#### Circulation Manager

Priscilla Weeks, pweeks@asprs.org

#### Advertising Sales Representative

Bill Spilman, bill@innovativemediasolutions.com

## ASPRS ANNOUNCES NEW LOGO!

The American Society for Photogrammetry and Remote Sensing, The Imaging and Geospatial Information Society, is pleased to announce the unveiling of the latest version of our Association logo which can be viewed in the header of this announcement.

The new logo is the work of our talented Graphics Artist, Matthew Austin, who also serves as our Electronic Publishing Manager.



THE IMAGING  
& GEOSPATIAL  
INFORMATION  
SOCIETY

## JOIN ASPRS IN WELCOMING OUR NEWEST SUSTAINING MEMBER!

### Extensis

1008 Western Ave Ste 200

Seattle, WA 98104-1092

303-815-2254

[www.extensis.com](http://www.extensis.com)



Celebrating 25 years in business, Extensis® is a leading developer of solutions that help organizations increase the return on investment and value of their digital assets, fonts, and large imagery. Used by more than 100,000 professionals and 5,000 companies across the globe, Extensis' solutions accelerate workflows so customers can achieve their goals faster. In its growing product line, Extensis has incorporated all legacy LizardTech software packages including GeoExpress and Express Server which have been relied upon by geospatial users for years to fully access and exploit the value of their geospatial data sets. These products are utilized extensively in applications related to state and local governments, natural resource management, national defense & intelligence, environmental monitoring, infrastructure development, land records archiving, AEC, and location-based services.

Founded in 1993, Extensis is headquartered in Portland, Oregon, with offices in Seattle, New York, the United Kingdom, France, Germany and Australia. To learn more about Extensis full suite of solutions for digital asset management, font asset management, image asset management, and image compression, visit <https://www.extensis.com/> or follow Extensis on Twitter @extensis .



## JOIN US AT PECORA 21 / ISRSE 38!

**P**ecora 21 / ISRSE 38 will play host to a range of remote sensing experts and scientists from federal agencies, non-governmental organizations, universities, and industry. The technical program will focus on both science and operational applications, emerging challenges and opportunities in working with Earth observations, and the role of partnerships in addressing scientific research, technical advancements and societal solutions.

Every three-years, NASA, NOAA, USGS, and ASPRS come together to host the William T. Pecora Memorial Remote Sensing Symposium. This year we have broken with tradition and are hosting Pecora in collaboration with ISRSE 38, the International Symposium on Remote Sensing of Environment, making this year's symposium a truly international event.

This exceptional event was developed specifically for remote sensing experts and scientists from federal agencies, non-governmental organizations, universities, and industry. I have attended almost every event since I first joined ASPRS in 1979 and I look forward to the scientific session each time to learn about the latest advances in imaging science, to socialize with friends, and to energize my career. I would be thrilled to have you as an exhibitor and sponsor, October 6-11, 2019!

Baltimore Marriott Waterfront is the perfect location to host Pecora 21 / ISRSE 38. Situated within a few hours driving distance of most major East Coast metro areas, the Baltimore Marriott Waterfront showcases an excellent Harbor East location, perfect for work and play. Dine with meeting colleagues at more than 50 nearby restaurants or venture out of the hotel to explore this historic city's finest attractions, including the National Aquarium and Maryland Science Center.

Participating in Pecora and ISRSE-38 offers you opportunities to connect with other industry professionals. Barbara Ryan, Pecora Committee Chairperson, shared, "With the Pecora and ISRSE communities joining forces, I am optimistic that attending, and exhibiting in Baltimore, will provide a really unique opportunity to showcase, to a large and diverse clientele, the vital role that the commercial sector plays in producing data, information, products and services, indeed key contributions along the entire value-chain."

You don't want to miss this incredible opportunity! The Pecora 21 / ISRSE 38 prospectus is located at <https://pecora.asprs.org/exhibitor-information/>. To participate as an exhibitor, sponsor and advertiser, please contact Bill Spilman at [bill@innovativemediasolutions.com](mailto:bill@innovativemediasolutions.com) or call him at 309-483-6467.

I hope to see you this October in Baltimore!  
Tommy Jordan, ASPRS President

## NEW ASPRS MEMBERS

ASPRS would like to welcome the following new members!

### **At Large**

Yakubu Issaka

### **Columbia River**

Madison Hope Fung

Tyler James Newton

### **Heartland**

James Kaufmann

### **Intermountain**

Bryan Ford

### **Mid-South**

Barry Guidry

Clayton Cockerham

Grady Owens

Christina Saltus

Lonie James Upton

### **New England**

Dominic Leonard Filiano

Russell F. Schimmer

### **North Atlantic**

Adam Grant

### **Pacific Southwest**

Robert L. Lafica, CP

Johnny Spiva, II

### **Potomac**

Ron Mahabir

Keith Owens

FOR MORE INFORMATION ON ASPRS  
MEMBERSHIP, VISIT

[HTTP://WWW.ASPRS.ORG/JOIN-NOW](http://www.asprs.org/join-now)

*Your path to success in the  
geospatial community*

# ASPRS BOOKSTORE

visit [asprs.org](http://asprs.org)

available at  


## Digital Elevation Model Technologies & Applications, 3rd Ed

Co-Editors: David F. Maune, PhD, CP, CFM, PSM, PS, GS, SP and Amar Nayegandhi, CP, CMS-Remote Sensing  
**List Price:** \$100 | **ASPRS Members:** \$80  
**ASPRS Student Members:** \$50<sup>†</sup>  
*Also available for Amazon Kindle*  
**Amazon Kindle Price\*\*:** \$85

## Landsat's Enduring Legacy: Pioneering Global Land Observations From Space

Landsat Legacy Project Team  
ISBN: ISBN 1-57083-101-7 · Hardcover · 586 pages · 2017 · Stock #4958  
**List Price:** \$95 | **ASPRS Members:** \$65  
**Student Members:** \$60  
**Amazon Price\*:** \$100

## Manual of Airborne Topographic Lidar

Editor: Michael S. Renslow  
ISBN: 1-57083-097-5 · Hardcover · 528 pages · 2012 · Stock #4587  
**List Price:** \$150 | **ASPRS Members:** \$95  
**Student Members:** \$75  
**Amazon Price (hardcover)\*:** \$135  
*Also available for Amazon Kindle*  
**Amazon Kindle Price\*\*:** \$110

## Manual of Photogrammetry, Sixth Edition

Editor: J. Chris McGlone  
ISBN: 1-57083-099-1 · Hardcover · 1372 pages · 2013 · Stock #4737  
**List Price:** \$175 | **ASPRS Members:** \$125  
**Student Members:** \$98  
**Amazon Price\*:** \$175

## Glossary of the Mapping Sciences

Co-published by ASPRS, ACSM and ASCE  
ISBN: 1-57083-011-8  
563 pp · Paperback · 1994 · Stock #5021  
**List Price:** \$50 | **ASPRS Members:** \$35  
**Student Members:** \$25 | **Amazon Price\*:** \$50

## Hyperspectral Remote Sensing for Forestry

Paul Treitz, Valerie Thomas, Pablo J. Zarco-Tejada, Peng Gong, and Paul J. Curran  
ISBN: 1-57083-093-2  
107 pp · Softcover · 2010 · Stock #4584  
**List Price:** \$26 | **ASPRS Members:** \$21  
**Student Member:** \$21 | **Amazon Price\*:** \$26

## Manual of Geographic Information Systems

Editor: Marguerite Madden, PhD  
Foreword: Jack Dangermond, Esri  
ISBN: 1-57083-086-X · Hardcover · 1352 pages + DVD · July 2009 · Stock #4650  
**List Price:** \$53 | **ASPRS Members:** \$40  
**Student Members:** \$xxxxxxx  
**Amazon Price\*:** \$55

## Meeting Environmental Challenges with Remote Sensing Imagery

Editors: Rebecca Dodge & Russ Congalton  
Published by American Geosciences Institute; Publishing Partners: AmericaView, USGS Land Remote Sensing Program, ASPRS  
ISBN: 978-0-922152-94-0 · 82 pp · Softcover · 2013 · Stock #4589  
**List Price:** \$7.50 | **ASPRS Members:** \$6  
**Bulk Orders (3 or more copies):** \$4.50 each  
**Amazon Price\*:** \$9.95

## MANUAL OF REMOTE SENSING, 3<sup>RD</sup> EDITION (A SERIES)

### Earth Observing Platforms & Sensors

Volume 1.1  
Volume Editor: Mark Jackson  
ISBN: 1-57083-089-4  
550 pp · Hardcover · 2009 · Stock #4582  
**List Price:** \$95 | **ASPRS Members:** \$75  
**Student Members:** \$55 | **Amazon Price\*:** \$95

### Remote Sensing of Human Settlements

Volume 5  
Editor-in-Chief: Andrew B. Rencz  
Volume Editors: Merrill K. Ridd & James D. Hipple  
ISBN: 1-57083-077-0  
747+ pp · Hardcover · 2005 · Stock # 4576  
**List Price:** \$99 | **ASPRS Members:** \$80  
**Student Members:** \$60  
**Amazon Price\*:** \$69.99

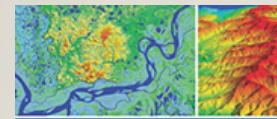
### Remote Sensing of the Marine Environment

Volume 6  
Editor-in-Chief: Andrew B. Rencz  
Volume Editor: James F.R. Gower  
ISBN: 1-57083-080-0 · 360 pp · Hardcover · 2006 · Stock # 4578  
**List Price:** \$95 | **ASPRS Members:** \$75  
**Student Members:** \$50 | **Amazon Price\*:** \$95

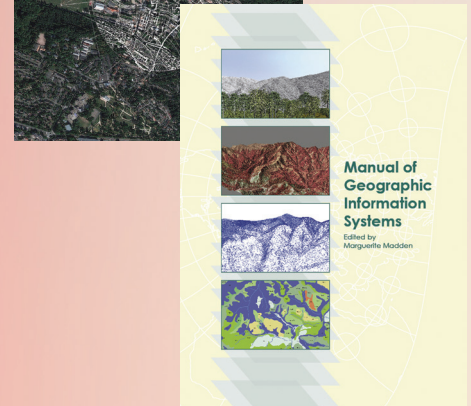
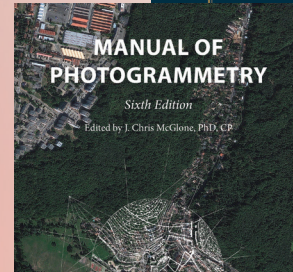
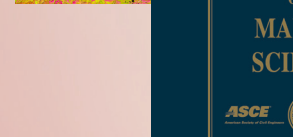
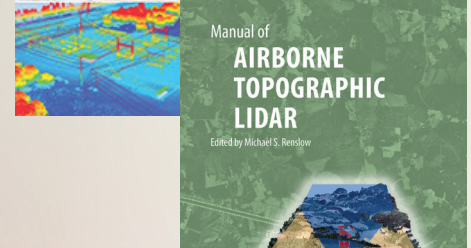
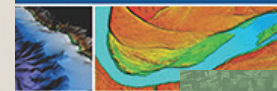
\*Member discounts are not available when ordering directly from Amazon.

\*\*Member discounts are not available on Amazon Kindle e-books,

<sup>†</sup>Students must order via the ASPRS Bookstore & a copy of your valid student ID must be submitted to be eligible for student pricing.



Digital Elevation Model Technologies and Applications: The DEM Users Manual, 3<sup>rd</sup> Edition  
Edited by David F. Maune, PhD, CP and Amar Nayegandhi, CP, CMS



# Roof-Cut Guided Localization for Building Change Detection from Imagery and Footprint Map

Jinqi Gong, Xiangyun Hu, Shiyan Pang, and Yujun Wei

## Abstract

Identification and monitoring of buildings are of considerable practical value in three-dimensional (3D) reconstruction of building models and urbanization monitoring. Especially for the change detection of buildings with composite structures and relief displacements, heterogeneous appearance and positional inconsistencies are two outstanding issues. In this work, a novel roof-cut approach is developed using graph-based model to locate rooftops and demolished buildings through the use of imagery and preexisting building footprint maps. The building region, boundary, and rooftop contour constraint terms were first formulated by multiple cues derived from both data sources. Next, roof-cut segmentation was performed by gathering all terms required for high-quality unsupervised rooftop extraction. Finally, the positional displacement statistics of similar adjacent buildings were collected to accurately estimate the rooftop location and achieve building demolition detection with the overlap ratio index. Experimental results indicated the effectiveness and generality of the proposed roof-cut algorithm for aerial and satellite images.

## Introduction

### Retroreflectivity

Automatic building change detection from satellite and aerial images is a relevant research area in the remote sensing field, as the results are required for a range of applications such as urbanization monitoring, identification of illegal or unauthorized buildings, land use change detection, and digital map updating (Akçay and Aksoy 2010). Similarly, information about the change of buildings can be useful for aiding municipalities with long-term residential area planning and the analysis on the condition of damaged buildings after natural disasters, supporting rescue activities and reconstruction measures (Sofina and Ehlers 2017).

Conventional methods proceed with effective selection of discriminative features according to the defined criteria of buildings and comparison of features to achieve change detection from remotely sensed images of the same scene obtained at different times (Tiede *et al.* 2011; Taskin Kaya *et al.* 2011; Voigt *et al.* 2011). Image-image comparison vary between pixel-oriented methods and object-oriented methods, and between spectral characteristics-based methods and artificial intelligence-based methods (Bouziani, Goïta, and He 2010). Pixel-oriented methods mainly use techniques based on algebraic operations (Singh 1989), transformation (Coppin

and Bauer 1996) and classification (Lunetta and Elvidge 1999) to recognize change information. However, when applied to high-resolution remotely sensed images, there may appear to be a large amount of small pseudo changes because of the increased high-frequency components (Chen *et al.* 2012). Furthermore, pixel-based methods strongly depend on geometric registration and radiometric correction (Hussain *et al.* 2013), thus they have limited accuracies and are commonly used to detect abrupt changes from low- or medium-resolution images (Hechteltjen, Thonfeld, and Menz 2014). Object-oriented methods evolving from the concept of object-based image analysis (Thomas *et al.* 2014) can not only employ the spectral, texture, and transformed values, but also exploit extra information about the shape features and spatial relations of objects by image segmentation techniques. As image objects are used as the basic units in object-oriented methods, they are more suitable for handling high-resolution remotely sensed images and can achieve better performance (Myint *et al.* 2011; Sellaoui *et al.* 2013; Hussain *et al.* 2013; Xiao *et al.* 2017). However, it is difficult to obtain a globally optimal segmentation, thus geometric inconsistency is usually unavoidable. In addition, due to the complexity and diversity of remotely sensed images, variable characteristics of buildings with potentially infinite spatial layouts is hardly described and the accuracy of the change detection suffers when only image data are used.

Many modern approaches have focused on the integration of high-resolution remotely sensed image and geographic information system (GIS) technologies. The GIS data in these studies were applied to select training areas for image classification, finding differences for change detection, and providing initial approximations for object detection and boundary cues for three-dimensional (3D) reconstruction (Jolly and Gupta 2000; Vosselman 2008; Durieux, Lagabrielle, and Nelson 2008). Suveg and Vosselman (2004) integrate the aerial image analysis with information from large-scale two-dimensional GIS databases and domain knowledge to get the possible locations of the building. Chesnel, Binet, and Wald (2008) used ancillary data that agreed with the reference image, and automatically searched for the damaged buildings in the postcrisis image using the correlation between the homologous pixels inside the building roof outline. For the updating of geodatabases in urban environment, Mourad, Goïta, and He (2010) proposed an object-oriented approach allowing the analysis of the objects which are characterized by different attributes to detect various types of building change. In this process, the existing knowledge was used to improve image processing and change detection. Automatic detection and classification of damaged buildings by integrating high-resolution satellite images and vector maps was proposed by Samadzadegan and Rastiveisi (2008). This approach located buildings from vector

Jinqi Gong, Xiangyun Hu, and Yujun Wei are with the School of Remote Sensing and Information Engineering, Wuhan University, Wuhan 430079, China (huxy@whu.edu.cn).

Xiangyun Hu and Shiyan Pang are with the Collaborative Innovation Center of Geospatial Technology, Wuhan University, Wuhan 430079, China.

Shiyan Pang is with the School of Resource and Environmental Sciences, Wuhan University, Wuhan 430079, China.

Photogrammetric Engineering & Remote Sensing  
Vol. 85, No. 8, August 2019, pp. 543–558.  
0099-1112/19/543–558

© 2019 American Society for Photogrammetry  
and Remote Sensing  
doi: 10.14358/PERS.85.8.543

maps and evaluated their condition by measuring and comparing textural features. Based on the understanding that the rooftops of intact buildings usually have a certain degree of homogeneity, and damaged buildings highlight heterogeneous areas, Shi and Hao (2013) used a postevent satellite image and the preevent GIS data to detect earthquake-collapsed buildings.

The application of vector-based information from GIS enables object-oriented change analysis and the use of additional prior knowledge, to some extent reducing false alarms due to radiometric- and geometric-related factors. However, most of these methods are sensitive to an unexpected appearance of heterogeneity due to objects located on building roofs, such as pipes, air vents, antennas, etc., thereby causing erroneous detection, as shown in Figure 1a. Moreover, differences in production mode lead to positional inconsistencies between the image and the vector map (Guo *et al.* 2015), making change detection harder to manipulate, as shown in Figure 1b. In vector maps, the buildings are generally stored as polygonal features representing existing building footprints, which depict the land covered by the union of all parts of the building so that an inventory of building stock can be maintained. On aerial or satellite photographs, the displacement of image due to variation in relief of the terrain is known as relief displacement or height distortion (Figure 1c). Even if an image is geometrically corrected with a digital elevation model, relief displacement cannot be completely removed as the height of ground objects is not considered. In particular, high-rise building rooftops in high-resolution remotely sensed images seriously deviate from the ground, appearing as large relief displacements, and huge differences among multitemporal images may be observed. The use of true-ortho rectification (Zhou *et al.* 2005) may solve the positional displacement problem, but it requires a high-resolution digital surface model and additional processing.

Given this context, taking into account heterogeneous appearances and positional inconsistencies is necessary, particularly when detecting changes in buildings with composite structures and relief displacements. Therefore, in this work, we propose a roof-cut method to locate rooftops and demolished changes in buildings by combining remotely sensed images and building footprint maps. The main contribution of this paper lies in the following two aspects:

- A novel roof-cut approach is proposed to locate rooftops with shape prior. The method integrates multiple cues to facilitate the stability of localization, and it is resistant to heterogeneous appearances and the relief displacements.
- The proposed framework is general and it can be applied to distinguish whether buildings had been demolished while quickly and accurately providing information on building roofs. The method has been validated with large and complex urban scenes.

This article is organized as follows. The section “Problem, Definition, and Solution” gives the definition and solution of the problem being address. The section “Methodology” presents the proposed method. The experiment and discussion of the obtained results are presented in the sections “Experimental Results” and “Discussion”, respectively. Finally, conclusions from an analysis of the obtained experimental results are presented in the last section.

### Problem, Definition, and Solution

Our ultimate goal is to use the footprint polygon to find the corresponding matching rooftop for building demolition detection in high-resolution remotely sensed images. In this study, graph cut (Boykov and Jolly 2001), which adopts a max-flow/min-cut algorithm (Boykov and Kolmogorov 2004) to find the solution by constructing a weight map, is improved with the shape prior, and a novel framework integrating multiple image features and accounting for footprint vector information, which we named roof-cut, is proposed to enable segmentation for implementation of rooftop localization. Similar to the graph cut algorithm, the objective of roof-cut is to assign a label to each pixel by minimizing the energy function:

$$E(M) = E^{region}(M) + E^{boundary}(M) + E^{contour}(M) \quad (1)$$

where  $E^{region}(M)$  represents the region term that can help find the potential building region, which is expressed as follows:

$$E_{region}(M) = \sum_{p \in P} D_p(I_p) \quad (2)$$

where  $P$  is the set of all the pixels (e.g., nodes in the graph), and  $D_p(I_p)$  represents the cost for assigning pixel  $p$  to label  $I_p$ . It measures how well pixels fit into the object/background models, and the object/background models could be known beforehand or modeled from the seeds provided by the user.

$E^{boundary}(M)$  denotes the boundary term, which is mainly used to penalize inconsistency in building rooftop labeling, e.g.,

$$E^{boundary}(M) = \sum_{\{p,q\} \in N} V_{\{p,q\}}(I_p, I_q) \quad (3)$$

where  $N$  is the set of all pixel pairs in the neighborhood (e.g., edges in the graph),  $p$  and  $q$  are two neighbor points, and  $V_{\{p,q\}}(I_p, I_q)$  defines the cost of assigning the labels  $I_p$  and  $I_q$  to the pixel pairs  $p$  and  $q$ , respectively.

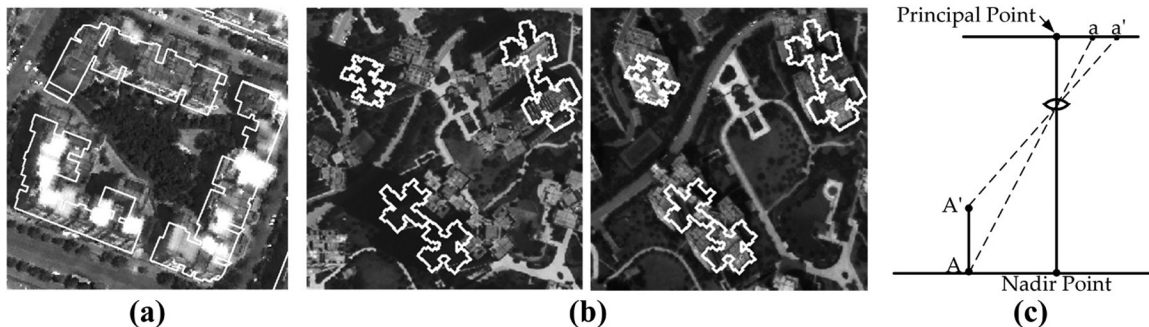


Figure 1. Underlying problems in vector-based change analysis: (a) Composite building rooftops with multiple colors, (b) high-rise inclination buildings with large relief displacements, and (c) illustration of relief displacement.

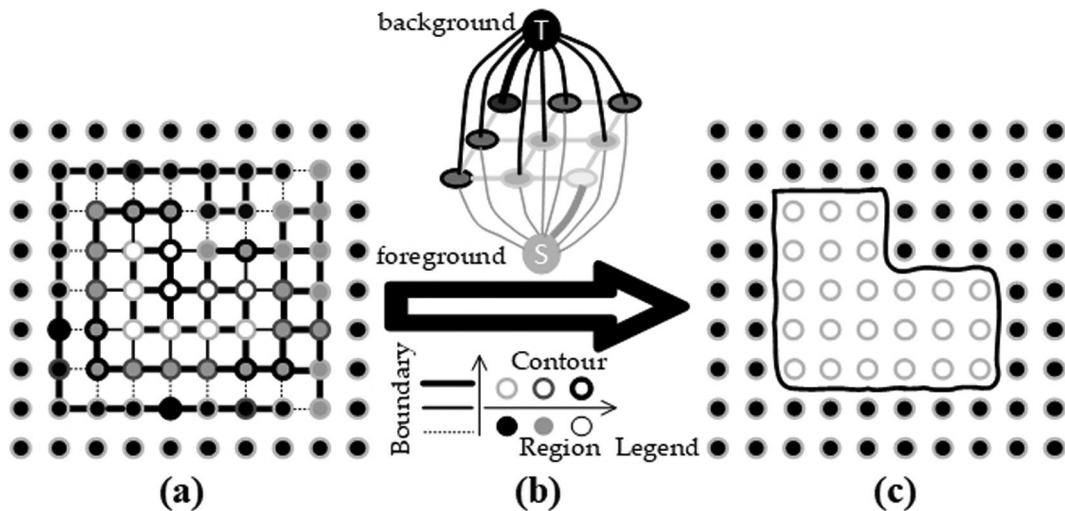


Figure 2. Workflow of roof-cut segmentation: (a) Graph model composed of region, boundary, and contour terms, (b) legend illumination, and (c) the segmentation result.

$E^{contour}(M)$  represents the contour term and maximizes shape matches between the input contour and the footprint polygon, which is defined as:

$$E^{contour}(M) = \sum_{\{p,q\} \in N} S_{\{p,q\}}(l_p, l_q) \quad (4)$$

where  $S_{\{p,q\}}(l_p, l_q)$  penalizes the discrepancy between the labels  $l_p$  and  $l_q$  corresponding to the pixel pairs  $p$  and  $q$ , respectively, under the shape constraint.

Each term in this cost function represents a corresponding property of the desired output labeling. By gathering region, boundary and contour terms, the minimum cut is performed via the max-flow/min algorithm for high quality unsupervised extraction of building rooftops. The basic workflow of roof-cut is shown in Figure 2.

Figure 2a represents the graph model created using all terms and Figure 2b is the legend illumination. The filled circle is the building region saliency, and the color is whiter, the saliency is stronger. The line denotes the similarity between a pixel pair, and the thicker the line, the greater the similarity. The hollow circle is the contour weight, and the deeper the black, the higher the weight value. Figure 2c is the segmentation result.

## Methodology

In this section, we introduce the main steps of roof-cut guided localization for building change detection from imagery and footprint maps. The processing chain for the proposed framework is shown in Figure 3 and consists of the following four steps: (1) data preprocessing (section “Data Preprocessing”), (2) feature extraction to generate the building region term (section “Building Region Term”) and calculate the boundary term (section “Boundary Term”), (3) shape constraint to build a rooftop contour term (section “Building Rooftop Contour Term”), and (4) rooftop localization and building change detection (section “Rooftop Localization and Building Change Detection”).

### Data Preprocessing

#### Merging and Simplification of Footprint Polygon Features

So that the prior shape was more suitable for rooftops, the original polygon features stored in the building footprint map

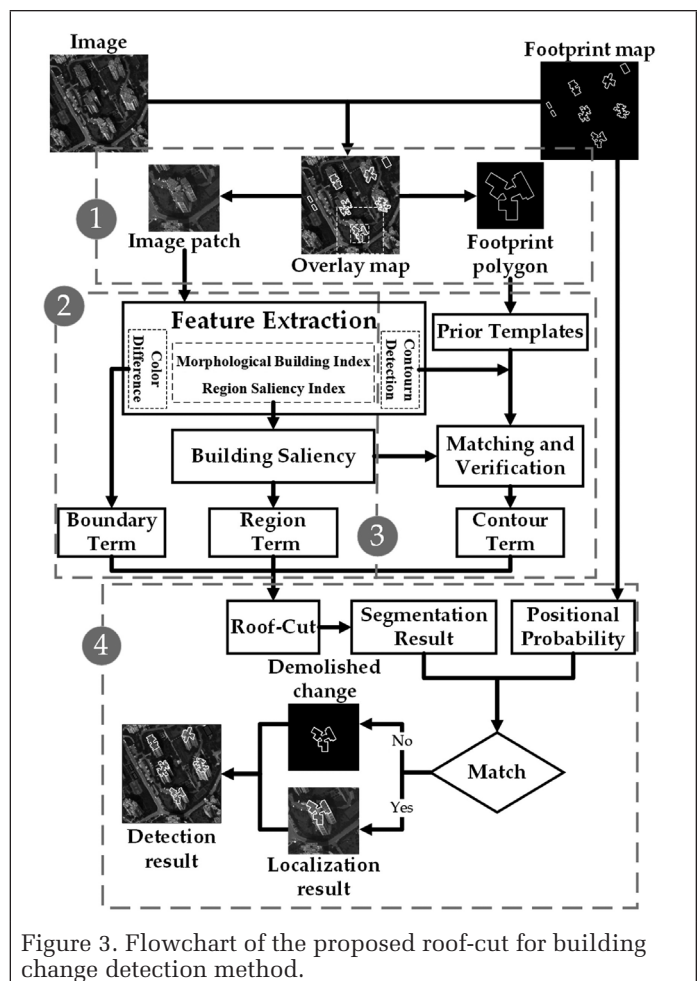


Figure 3. Flowchart of the proposed roof-cut for building change detection method.

were merged and simplified. Merging combines intersecting polygon features into a single feature, as shown in Figures 4a and 4b. The fundamental principle for polygon simplification is that any redundant vertices and very short line segments in the original footprint polygon must be filtered out to form a smooth polygon that contains the original detailed building shape. In the first case, four extreme points in the merged

polygon feature are identified from bounding box to partition the polygon. As shown in Figure 4c, the black rectangle is the bounding box, the black marks are the four extreme points, and the gray marks are vertices. Then, the line path connecting two extreme points (e.g., leftmost to top, or top to rightmost) was simplified using the Douglas-Peucker algorithm with 1.0 m as the distance threshold (Douglas and Peucker 1973; Hershberger and Snoeyink 1992), as shown in Figure 4d.

#### Image Patch Creation

According to the geographical scope of the building footprint polygon extended by a defined threshold (e.g., 40 m), we clipped the corresponding patch from the original image as the input to perform rooftop localization and change detection.

#### Generating the Building Region Term and the Boundary Term

##### Building Region Term

Normally, in remotely sensed images, buildings exhibit relatively high reflectance (brightness) and stand out from their surroundings as spatially adjacent shadows, leading to high local contrast. Therefore, we used brightness as the initial input to calculate the morphological building index (MBI). Meanwhile, global contrast differences were compared to

define the region saliency index (RSI) by using color histogram and position from the input image. Then, a building saliency map is obtained by combining MBI and RSI, to initiate the labeling mask for the building region term and generate a building proposal, where bright means brighter and the saliency is stronger than the surrounding features, as shown in Figure 5.

MBI is defined by depicting the characteristics of buildings based on a morphological transformation with a set of multi-scale and multidirectional linear structural elements (Huang, Zhang, and Zhu 2013). MBI is able to indicate the presence of buildings in high-resolution remotely sensed images (Wen, Huang, and Zhang 2015), which helpful for locating the roof-top of buildings. The brief formulation is as follows:

- (1) Calculating brightness image. The maximum value is the brightness obtained from the multispectral bands for each pixel:

$$b(i) = \max_{1 \leq k \leq K} (band_k(i)) \quad (5)$$

where  $band_k(i)$  is the digital number value of the  $i$ th pixel for the  $k$ th band, and  $K$  is the number of bands.

- (2) Constructing differential top-hat profiles (DTP). Top-hat transformation is able to detect bright structures. Moreover,

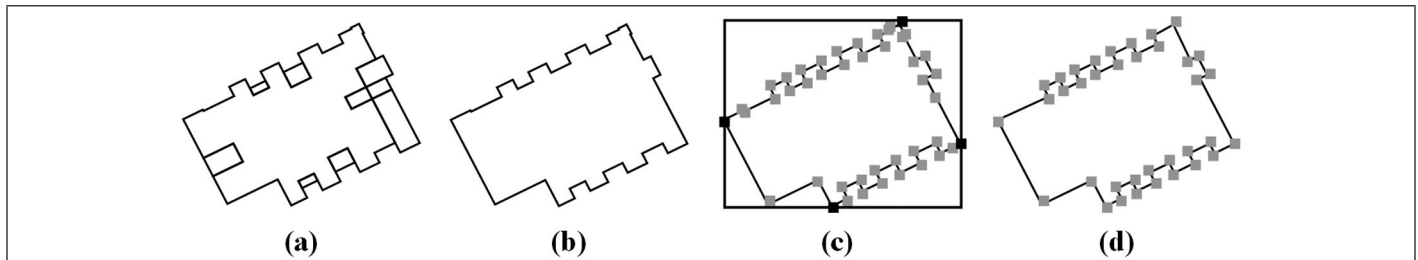


Figure 4. Merging and simplification of vector data: (a) Original footprint polygon, (b) merged polygon, (c) four extreme points identified on the bounding box and vertices of the merged polygon, and (d) the simplification result.

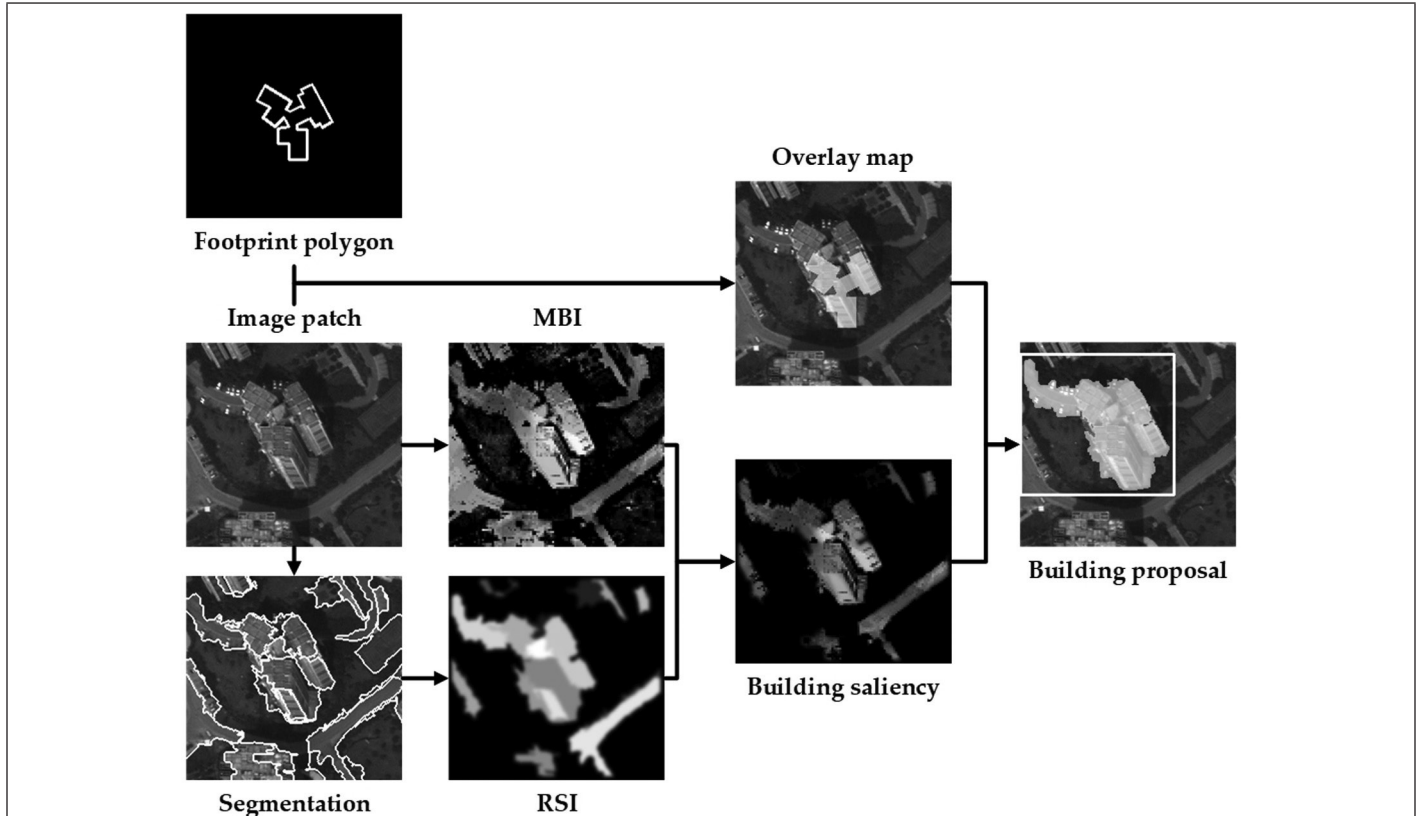


Figure 5. Building saliency map and proposal generation.

the rooftops of buildings in remotely sensed images have high local contrast compared with the surrounding regions. Therefore, DTP were constructed to represent the spectral-structural characteristics of buildings with a set of multi-scale and multidirectional linear structural elements (SE).

$$DTP(d, s) = |TH_b(d, s + \Delta s) - TH_b(d, s)| \quad (6)$$

where  $TH_b(d, s)$  represents the top-hat in the reconstruction of the brightness  $b$  with the direction  $d$  and size  $s$  of the linear SE, and  $\Delta s$  is the increasing interval of the size.

(3) Calculating MBI. MBI is defined as:

$$MBI = \frac{\sum_d \sum_s DTP(d, s)}{D \times S} \quad (7)$$

where  $D$  and  $S$  are the total number of directions and sizes, respectively. In this study, four directions were considered (e.g., 45°, 90°, 135°, and 180°), and  $S$  was determined by the sizes of buildings and  $\Delta s$  (e.g.,  $s_{min} = 5m$ ,  $s_{max} = 55m$ , and  $S = 11$ ).

Saliency has been widely used in many applications, and its computing is important for detecting the region of interest (Hou, Wang, and Liu 2016). In remotely sensed images, buildings have significant differences from the surrounding regions, which inspires us to adopt the contrast analysis method (Cheng *et al.* 2011), region contrast (RC), to define RSI. In RC, the input image was first segmented into regions by using a simple and fast graph-based algorithm (Felzenszwalb and Huttenlocher 2004). Then, the region property descriptor for each segment was built by extracting its color histogram and position. In addition, a spatial weighting term was introduced as spatial information to increase the effects of closer regions and decrease the effects of regions farther away. Specifically, we defined the spatially weighted region contrast based saliency of any region  $r_i$  as RSI:

$$RSI = w_s(r_i) \sum_{r_j \neq r_i} e^{-\frac{D_s(r_i, r_j)}{\sigma_s^2}} w(r_j) D_r(r_i, r_j) \quad (8)$$

where  $w(r_i)$  is the weight of region  $r_i$ , defined by the number of pixels in  $r_i$ ;  $D_r(r_i, r_j)$  and  $D_s(r_i, r_j)$  are the contrast and spatial distance between two regions  $r_i$  and  $r_j$ , respectively;  $\sigma_s$  controls the strength of spatial distance weighting, and  $w_s(r_i)$  is a spatial prior weighting term similar to center bias (Jiang *et al.* 2011). The spatial distance  $D_s(r_i, r_j)$  is the Euclidean distance between the center of region  $r_i$  and the center of region  $r_j$ . The contrast distance is:

$$D_r(r_i, r_j) = \sum_{p=1}^{n_i} \sum_{q=1}^{n_j} f(c_{i,p}) f(c_{j,q}) D(c_{i,p}, c_{j,q}) \quad (9)$$

where  $f(c_{k,p})$  is the frequency of the  $p$ th color  $c_{k,p}$  among all  $n_k$  colors in the  $k$ th region  $r_k$ , and  $D(c_{i,p}, c_{j,q})$  is the color difference. The color differences between dominant colors was further emphasized by using  $f(c_{k,p})$  as the weight for this color. In our study, we used  $\sigma_s^2 = 0.4$  and  $w_s(r_i) = e^{-9d_i}$  with pixel coordinates normalized to  $[0, 1]$ , and  $d_i$  is the average distance between pixels in region  $r_i$  and the center of the image.

MBI and RSI were normalized to  $[0, 1]$ , and a building saliency map was generated by the operation  $MBI \times RSE$ . Here, Otsu's method was employed to divide MBI and building saliency maps; we combined their binarization results to determine salient regions representing the foreground, and regions with a low MBI and RSI were labeled as background. Thereafter, we used two Gaussian mixtures with  $GK = 5$  components to build full foreground and background color appearance models for assigning labels to each pixel, similar to the approach used by Rother, Kolmogorov, and Blake (2004), for interactive image segmentation. Finally, the region term is:

$$D_p(I_p) = \begin{cases} -\ln(\Pr(I_p; \beta_1, \mu_1, \Sigma_1)), & \text{if } I_p = 1 \\ -\ln(\Pr(I_p; \beta_0, \mu_0, \Sigma_0)), & \text{otherwise} \end{cases} \quad (10)$$

where  $\Pr(x; \beta, \mu, \Sigma)$  is how well a pixel color  $x$  fits a Gaussian mixture model with component weights  $\beta$ , means  $\mu$  and covariance matrices  $\Sigma$ . Note that subscripts to Gaussian mixture parameters in Equation 10 indicate either a foreground or background model.

For efficient computation, in the building saliency map, we chose the maximum connected regions containing the original footprint polygon as the building proposal, as shown in Figure 5.

#### Boundary Term

The boundary term is a penalty term describing the discontinuity between neighborhood pixels. A segmentation boundary occurs when two neighboring pixels are assigned different labels. Most nearby pixels are expected to have the same label; therefore, no penalty is assigned if neighboring pixels have the same label, and a penalty is assigned otherwise. This boundary term penalty usually depends on the red-green-blue (RGB) difference between pixels, which is small in regions of high contrast (Papadopoulos *et al.* 2017). We define this boundary term as used in (Rother, Kolmogorov, and Blake 2004):

$$V_{\{p,q\}}(I_p, I_q) = \exp\left(-\frac{I_p - I_q^2}{2\sigma^2}\right) \cdot \frac{1}{d(p,q)} \quad (11)$$

where  $I_k$  represents the pixel color,  $d(p, q)$  is the Euclidean distance between pixels  $p$  and  $q$ , and  $\sigma^2$  is a scale parameter, which is set as suggested by Rother, Boykov, and Blake (2004):

$$\sigma^2 = I_p - I_q^2 \quad (12)$$

where  $\langle \cdot \rangle$  denotes the average value over the whole image.

#### Building Rooftop Contour Term

Generally, although the building rooftop often deviates from the ground in an image due to the relief displacement, a coincidence between them still exists in the aspect of the contour shape and some obvious vertical lines are also formed. Therefore, the footprint polygon can be considered as a shape prior to impose a contour constraint on the region. In the process of building the rooftop contour term, we calculated the coincidence between the prior shape from the vector data and the detected contours in the remotely sensed image to estimate the rooftop contour integrity by contour matching (CM). Moreover, vertical lines were verified to improve the robustness and effectiveness of the process, especially for high-rise buildings with large relief displacements.

During CM calculation, according to the simplified building polygons, we first constructed distance and direction

templates to provide prior information for each point to stabilize the contour constraint. Meanwhile, the corresponding image is used to perform contour extraction. Then, at a certain position, we used weighted voting to count the score of each contour point under the constraint of the prior templates. Thus, the CM value is calculated as the ratio of the weighted voting sum of the detected pixels to the number of pixels expected for the intact building.

#### Constructing Prior Templates

A distance prior template assigns a corresponding weight of each point through distance transform to the simplified footprint polygon, as shown in Figures 6a and 6b. Given a point  $P$  close to the edge of a building polygon, its distance weight ( $dw$ ) is computed as follows:

$$dw = \begin{cases} 1 - d / D_{max}, & \text{if } d < D_{max} \\ 0, & \text{otherwise} \end{cases} \quad (13)$$

where  $d$  is the distance to the nearest boundary pixel and  $D_{max}$  is the maximum distance allowed ( $D_{max} = 2.5\text{m}$  in our experiments). Thus,  $dw$  progressively decreases from the centerline to both sides and it is between 0 and 1.

A direction prior template is a template representing the directions for the points in the buffer around the simplified polygon, and the direction at a point is perpendicular to the corresponding edge of the simplified polygon. In Figure 6c, the shaded area indicates valid direction constraint template, and the buffer distance is set to 2.5 meters. In the paper, the angle values are within the range of  $[0:180]$  that is classified into six intervals for the coding computation (Figure 7).

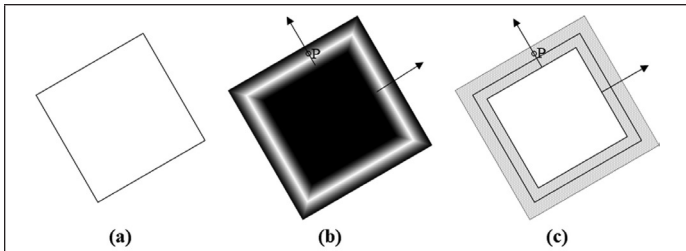


Figure 6. Contour constraint construction: (a) original polygon, (b) distance prior, and (c) direction prior template.

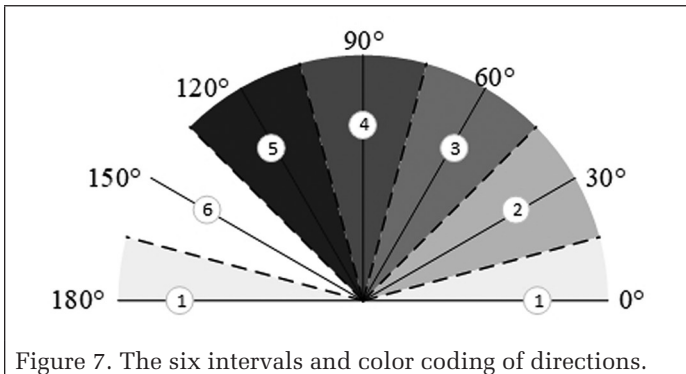


Figure 7. The six intervals and color coding of directions.

#### Edge and Line Detection

A contour is defined as a set of edges forming a coherent boundary, curve, or line, so edge and line detection are applied to obtain contours in remotely sensed images. Given an image, we compute an edge response for each pixel using the Structured Edge Detector (SED) because the learning-based approach performs well and efficiently when predicting object boundaries. Local straight lines are another obvious characteristic of

buildings that are visible in remotely sensed images. Among the many line detection methods available, the line segment detector (LSD) method is considered state of the art (Gioi 2010). LSD finds line segments based on the method presented by Burns, Hanson, and Riseman (1986) and validates the line segments using a contrario model introduced by Desolneux, Moisan, and Morel (2000). By doing so, accurate subpixel results are obtained quickly without parameter tuning. After SED and the LSD algorithm are applied to the image, the gradient orientation is calculated for each detected contour pixel:

$$\theta = \begin{cases} \tan^{-1}(G_y / G_x) + \pi, & \text{if } \tan^{-1}(G_y / G_x) < 0 \\ \tan^{-1}(G_y / G_x), & \text{otherwise} \end{cases} \quad (14)$$

where  $G_x$  and  $G_y$  are the derivatives for the horizontal and vertical directions, respectively. In accordance with the direction-prior template, the obtained angle values are mapped to six codes.

#### Calculation of Contour Matching

After the above measures are taken, the prior templates are used in the bounding box of the building proposal where the detected contour part is to be matched. When the direction-prior template moved to a certain position in the box, we voted on the pixel on the raster contour with the same code of contour orientation and recorded the value corresponding to the same distance-prior template as the voting weight. Therefore, the contour matching degree at this position is:

$$CMD = \frac{\sum_{i=1}^n dw(i)}{C} \quad (15)$$

where  $C$  is the circumference of the simplified footprint polygon, and  $dw(i)$  indicates the weight value corresponding to the distance prior template for the  $i$ th eligible contour point. CMD is the similarity between the building footprint shape from the vector data and the detected contours at each position of the moving track. Based on these measurement results, we calculated the contour weight of each point corresponding to the template at the current position through the

$$CW(p_i \in T) = \begin{cases} CMD, & \text{if } CMD \geq \varphi \text{ and } p_i \in M \\ 0, & \text{else if } CMD \geq \varphi \\ -\infty, & \text{otherwise} \end{cases} \quad (16)$$

where  $\varphi$  denotes the contour integrity within the range of  $(0,1)$ ,  $T$  and  $M$  represent a set of points corresponding to the template and the masked workspace, respectively (e.g., the gray buffer and the masked black in the matching results of Figure 8). When completing all matching in the building proposal, the maximum value of every point is selected as the final contour weight  $CW(i) = \max(CW_z(i))$ , where  $Z$  is the number of the matching. As we can see from the results in Figure 8, the polling points marked in black are more on the rooftop.

#### Vertical Line Verification

To maximize the effects of contour matching, especially for buildings with high slope angles, when the template moves along the building proposal boundary, we connected the corresponding nodes of the polygons between the footprint and current positions to verify vertical lines. First, straight lines from LSD were marked in the building proposal if their orientation angles were approximate to the angle of the connected line between the footprint and template in the movement. As

shown in Figure 9a, gray is the buffer of the connected line and white lines are masked since their orientation angles are approximate to the connected line's angle. In this study, we defined the buffer distance of the connected lines as 1 meter, and a differential angle less than  $5^\circ$  was considered appropriate. Then, when a straight line was encompassed by any buffer of the connected lines and its each endpoint was restricted near the corresponding endpoint of the connected line, we retained it as a vertical line. The tolerances of the distance between the endpoints was set to 2.5 meters. In Figures 9b and 9c, the white line surrounded by a gray buffer is eliminated since its endpoint is far from the corresponding endpoint of the connected line, and white lines covered by black buffer are preserved. Finally, the length and orientation of the preserved vertical lines are measured to obtain the offsets from original position of the footprint.

Given the length and orientation of the vertical line, the migrated contours are obtained by subtracting the offset  $\Delta f$  from the original position of the building footprint vector. Then, the migrated contours are used to further refine contour matching, and the contour weight is adjusted as follows:

$$CW(\mathbf{p}_0 - \Delta f) := \lambda CW(\mathbf{p}_0) \quad (17)$$

where  $\mathbf{p}_0$  represents a set of points corresponding to the original position,  $:=$  denotes the assignment operator, and  $\lambda \geq 1$  controls the strength of the migrated contour point weighting. In this work, we used  $\lambda=5$  to maximize the number of credible points used.

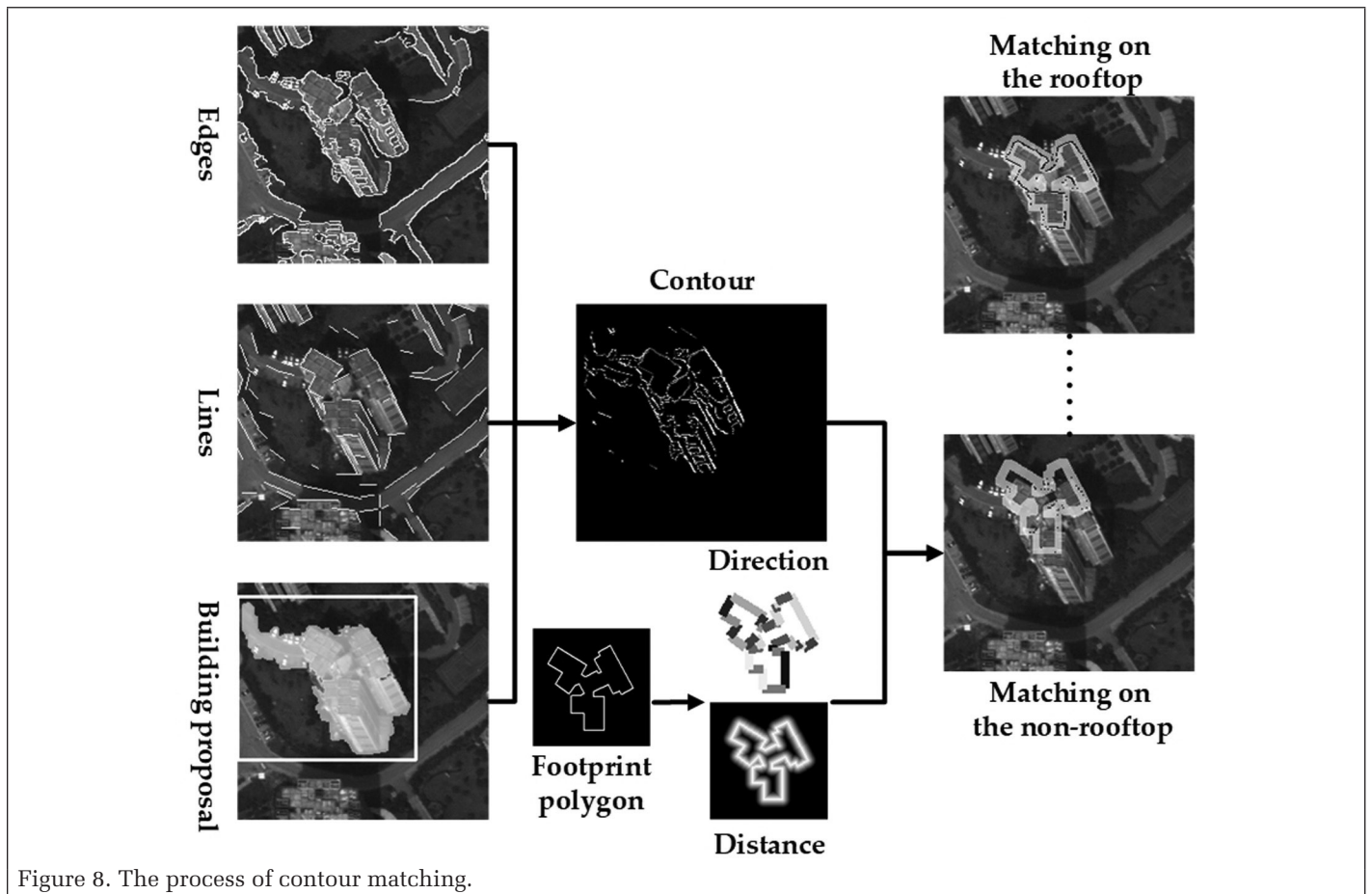


Figure 8. The process of contour matching.

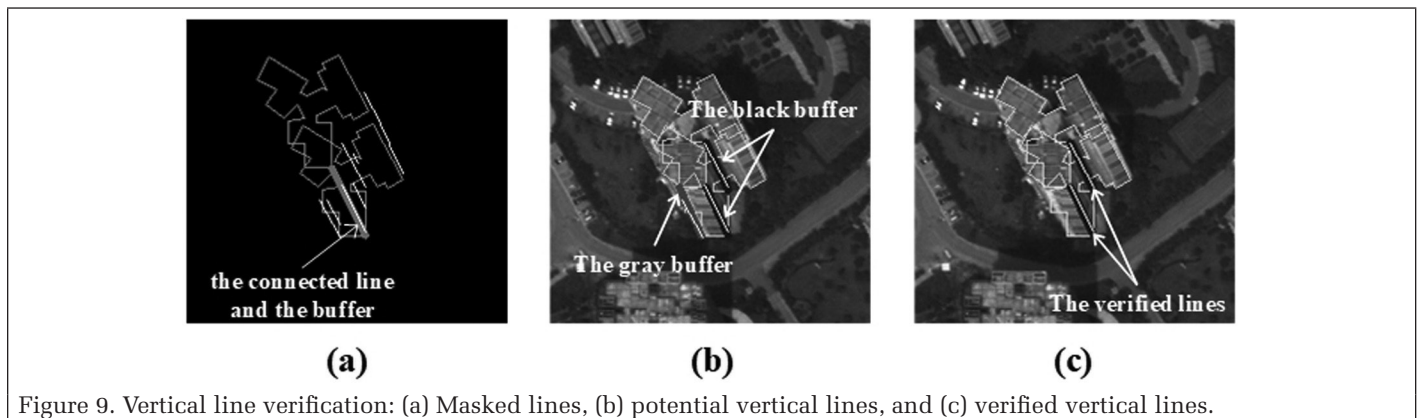


Figure 9. Vertical line verification: (a) Masked lines, (b) potential vertical lines, and (c) verified vertical lines.

### Roof-top Contour Constraint Term

According to the adjusted contour weight from the above steps, we built the rooftop contour constraint term:

$$S_{\{p,q\}}(I_p, I_q) = \exp(-\max(CW_p, CW_q)) \quad (18)$$

where  $CW_k$  represents the pixel color. With this formula, the greater the weight of pixel  $p$  or  $q$ , the smaller the contour constraint term between them. In this case, the points in the rooftop contour are broken via energy minimization.

### Roof-top Localization and Building Change Detection

#### Roof-Cut Segmentation

Through the use of roof-cut, we divided the images into foreground and background representing the rooftop and other components, respectively. As shown in Figure 10b, the initial segmented rooftop retained a certain shape of the footprint polygon but was coarse. Therefore, we relied on our initial labeling mask and its evolution over each resegmentation iteration to refine the roof-cut result; a maximum of three iterations was performed in our experiments. After each iteration, we use dilation and erosion on the current segmentation result to obtain a new trimap for the next roof-cut iteration. As shown in Figures 10c and 10d, the region outside the dilated region is set as the background, the region inside the eroded region is set as the foreground, and the remaining areas are set as unknown in the trimap. The segmentation results obtained through three iterations (Figure 10e) perfectly reflect the rooftop contour, and demolished buildings can be detected (third row in Figure 10e). Furthermore, considering the accurate rooftop localization required in many applications and partial destruction in a building, using the segmentation result as the estimated reference, rooftop corresponding to the building footprint polygon is located to achieve an exact match and the change state of the building is judged by the positional displacement statistics of similar adjacent buildings and the overlap ratio index (ORI).

#### Accurate Rooftop Localization and Building Change Detection

On a local scale, such as a community, buildings are quite similar in terms of height, contour shape, and structure. Therefore, the positional displacement between the building rooftop in remotely sensed images and the footprint polygon

in the map in a neighborhood can be assumed as consistent. Based on this assumption, displacement distribution probability (DDP) was predicted using the positional displacement statistics of similar adjacent buildings.

First, we constructed the adjacency graph to represent the neighborhood relationship among buildings based on the shape similarity index (SSI) and the area ratio index (ARI), as calculated by Shi and Hao (2013). In this study, the SSI denotes the shape similarity between the current building polygon and the adjacent one, and the ARI indicates the ratio of the total number of pixels in the two polygons. Next, statistical analyses of the positional discrepancies of similar buildings adjacent to the current building were performed according to the adjacency graph. Then, for each building polygon, the DDP was computed within the statistics based on the distribution of the offset directions  $d_s$  and the probability of the shifting distance  $d_r$ , as follows:

$$DDP = d_s \times d_r \quad (19)$$

$$d_s = \frac{n_i}{\sum n_i}, \quad i = 1, 2, 3, 4 \quad (20)$$

$$d_r(x_p, y_p) = 1 - \min \left( \frac{\min_{1 \leq h \leq H} \left( \sqrt{(x_p - x_q(h))^2 + (y_p - y_q(h))^2} \right)}{r}, 1 \right) \quad (21)$$

where  $n_i$  is the number of similar adjacent buildings in each of the four quadrants in the local range from the view of the offset directions,  $(x_p, y_p)$  is an arbitrary coordinate point,  $(x_q, y_q)$  is the migrated coordinates predicted by the position offsets of similar adjacent buildings,  $H$  is the total number of similar adjacent buildings, and  $r$  is the radius of the local circle window, (e.g.,  $r = 2.5$  m), as shown in the positional displacements of adjacent similar buildings of Figure 11.

Finally, on the premise that the segmented result is similar to the building footprint polygon, ORI is calculated at each point when the building footprint polygon moves on the map obtained by roof-cut segmentation, which is the ratio of the total number of overlapping pixels and the total number of

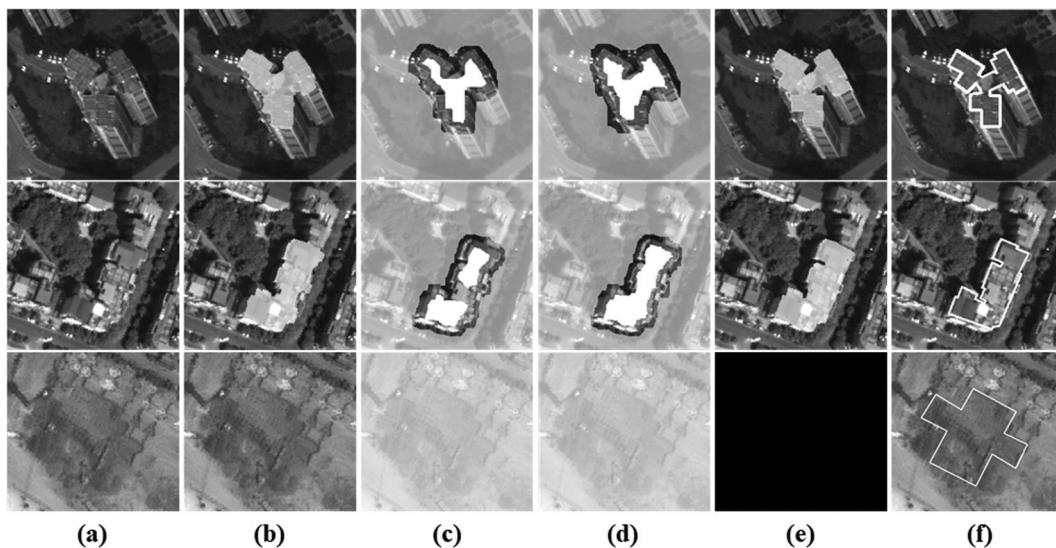


Figure 10. Demonstration of roof-cut: (a) original image patch, (b) initial segmentation, (c) trimap after first iteration, (d) trimap after second iteration, (e) final segmentation, and (f) overlay map. In the trimaps (c–d), foreground is white, background is gray, and unknown regions are left unchanged.

pixels in the footprint polygon, as shown in Figure 11. We masked positions where ORI is maximum and acceptable (e.g., greater than 0.75) as initial candidates and updated these candidates by searching for the maxima of  $DDP \times ORI$ ; the initial candidates were maintained when  $DDP \times ORI = 0$ . The building was considered a demolished change if no marker was found, and the center of the K-means cluster was selected as the best location if more than one candidate was obtained. Thus, we calculated the displacement between the best location and the centroid of the original footprint polygon to guarantee that their shapes are identical.

## Experimental Results

### Study Site and Dataset Description

To verify the effectiveness and applicability of the proposed method, three datasets composed of aerial or satellite images were collected with a valid area of approximately 6.3 km<sup>2</sup>, 2.3 km<sup>2</sup>, and 18 km<sup>2</sup> respectively, as shown in Figure 12. The three datasets were located in the urban area of Chongqing, China. As a typical mountain city, the relief displacements of buildings usually vary considerably with location and cannot be eliminated by geo-rectification in the images. The dataset 1 (aerial image, 7464×7629 pixels) was acquired on April 15, 2013 with three multispectral bands and a resolution of 0.5 m. The dataset 2 and 3 (satellite images, 3641×3904 and 12 595×9529 pixels) were a fusion of panchromatic and

multispectral images (RGB) with a 0.5 m resolution generated by WorldView-2 in October 2014. These images covered a typical urban environment with schools, residential areas, commercial districts, and industrial areas. The buildings are differently distributed and vary in size and structure and there are some demolished buildings because they are temporary, illegal, or pending reconstruction.

The building footprint maps were obtained from building investigations and included 2661, 1984, and 10 277 vector objects for the dataset 1, 2, and 3, respectively. Although the vector data were assigned to the same latitude/longitude reference system as images, they were inaccurate with some positional inconsistencies that occurred randomly. The references were prepared in advance for each vector object by manually moving the building footprint polygon and finding the demolished building, which are used to evaluate the accuracy of the localization and detection.

### Building Rooftop Localization and Change Detection Results

After completing pre-processing, there were 893, 831, and 4736 simplified building footprint polygons in the dataset 1, 2, and 3, respectively. In this study, the contour integrity  $\phi$  is set to 0.5 and 0.3 in aerial and satellite image, respectively, and roof-cut was implemented to locate the rooftops and detect the demolished changes. The selection and setting of the main parameters are discussed in the section “Parameter Selection”. As shown in Figure 13, cyan portions indicate

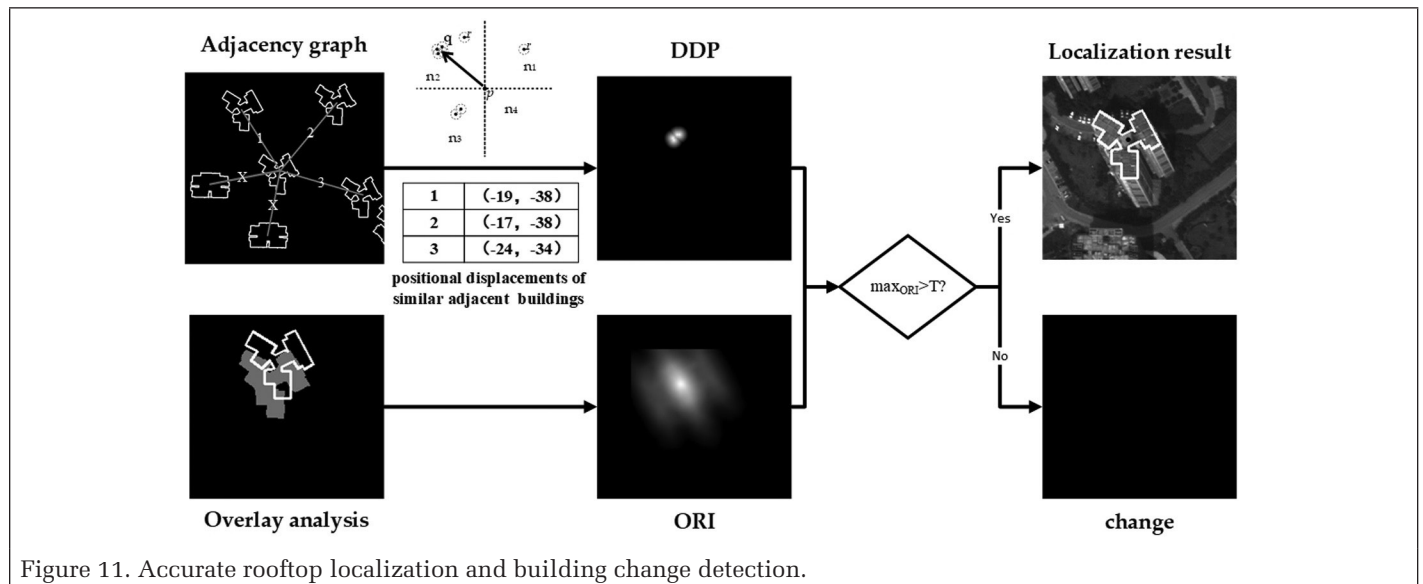


Figure 11. Accurate rooftop localization and building change detection.

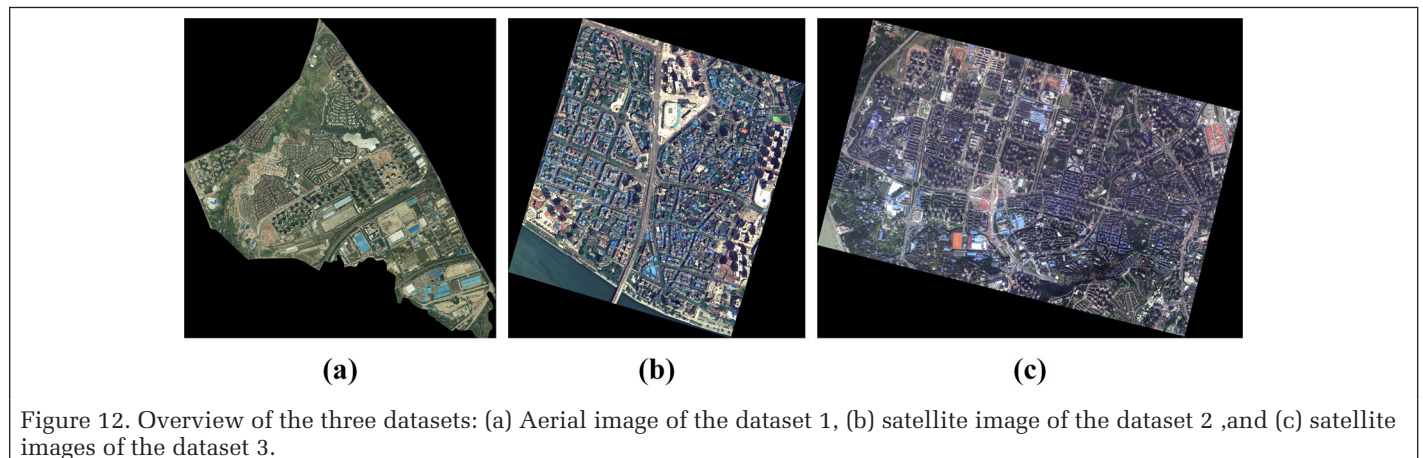


Figure 12. Overview of the three datasets: (a) Aerial image of the dataset 1, (b) satellite image of the dataset 2, and (c) satellite images of the dataset 3.

correct localization, blue portions imply demolished building detection, and yellow regions denote incorrect results.

To observe the results in much more details, Figure 14 shows the localization and detection results of seven typical regions with different types of buildings and scenes. The detail areas A–D and E–G spring from the dataset 1 and 2, respectively. The left column shows the original footprint maps and references of the buildings displayed in black and white, respectively. The middle and right columns show the results of rooftop localization and building change detection, respectively; here, white portions indicate correct localization

and demolished building detection, black portions with single outline imply the missing, and black regions with double contour denote incorrect results.

The subset A is an industrial area mainly composed of low-rise buildings with uneven distribution and vary in size and structure, where there are some demolished temporary buildings. The subregion B is a residential area of three communities, where some temporary low-rise sheds disappear with the completion of building project. In each community, the buildings are uniformly distributed and are quite similar, with certain differences between them. In A and B, the

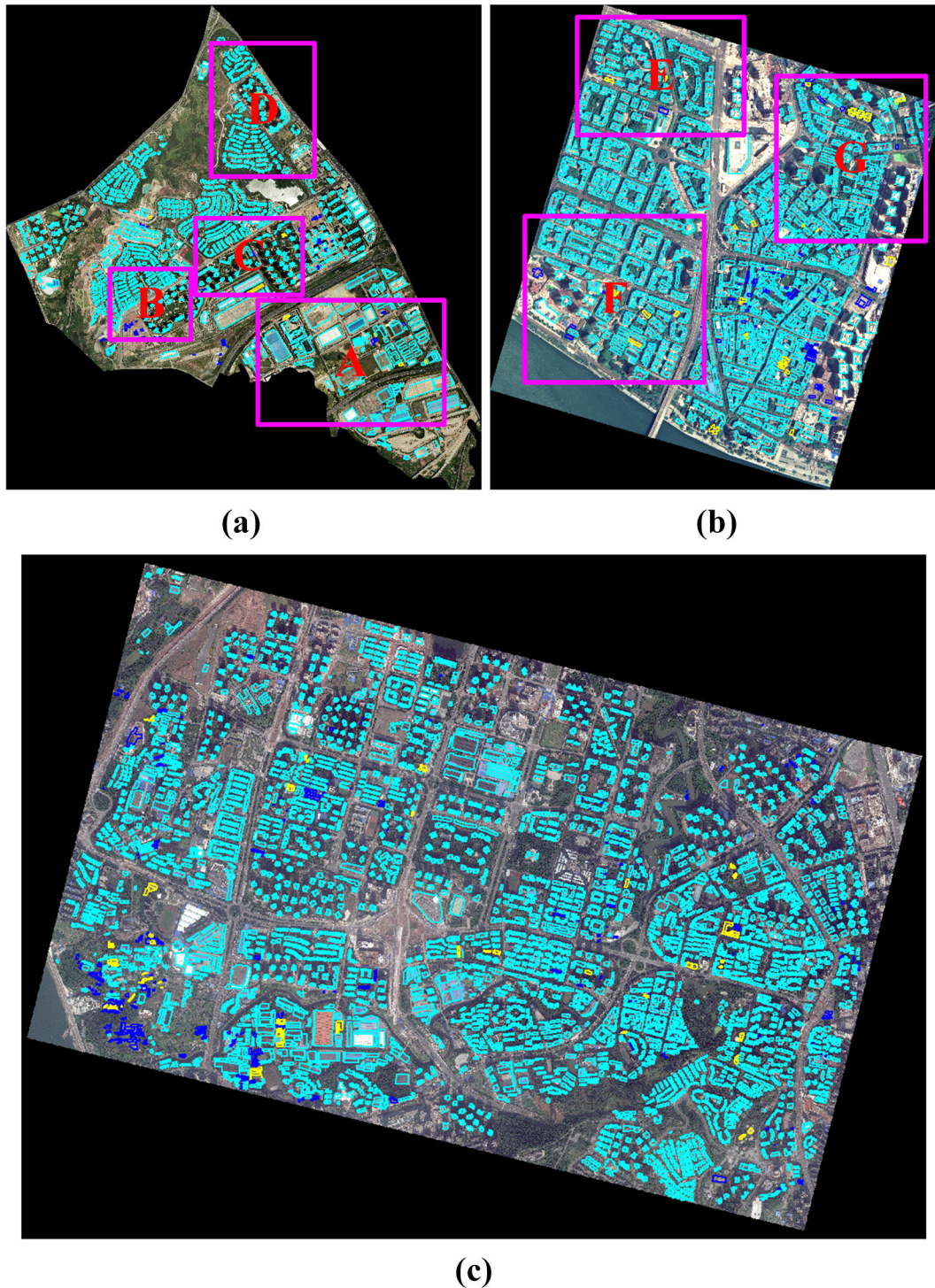


Figure 13. Results of rooftop localization and building demolition detection using the roof-cut method.

buildings have low relief displacements, the rooftops are homogeneous, and the geometric displacements are consistent. In the two regions of C and D, the buildings are also uniformly distributed and have a certain resemblance to the periphery. For the subarea C, most buildings are high-rise with large

relief displacements and their rooftops are homogeneous, but the geometric displacements are partly inconsistent due to the influence of image splicing. In addition, there are some demolished buildings for pending reconstruction. Conversely, both low-rise buildings with minimal relief displacements and high-rise buildings with large relief displacements are present in the subarea D. The rooftop of each building varies, but the geometric displacements are relatively consistent with the surroundings. The subsets E–G are commercial districts and residential areas, where buildings are mostly complex and different in size, structure, and distribution, their rooftops are heterogeneous and some illegal buildings are demolished. As for the relief displacements, the buildings are small in the enlarged region E and vary greatly in F and G.

Notably, the chosen regions are quite representative and highly challenging, and the results indicate that the presented approach is robust and suitable. Most buildings are successfully located, and their positions are accurate. Moreover, the demolished buildings are also well detected. These findings are also verified in the following quality assessments.

#### Quality Assessments

In addition to visual illustration, in this quality assessment, we evaluated the object-level performance by counting the truly ( $TL/TD$ ), falsely ( $FL/FD$ ), and missing ( $ML/MD$ ) localization and detection, and then calculated the precision ( $PL/PD$ ), recall ( $RL/PD$ ), and F-score ( $F_1^L/F_1^D$ ) measures (Özdemir *et al.* 2010) of the localization and detection, respectively, which are respectively defined as:

$$PL = \frac{TL}{TL + FL} \quad (22)$$

$$RL = \frac{TL}{TL + ML} \quad (23)$$

$$F_1^L = \frac{2PL \cdot RL}{PL + RL} \quad (24)$$

$PD$ ,  $RD$ , and  $F_1^D$  are calculated by  $TD$ ,  $FD$ , and  $MD$  with the same formulas, respectively.

#### Rooftop Localization Assessment

In the rooftop localization assessment, we used an overlapping threshold of 90% to determine the number of  $TL$  and  $ML$  as previously described (Ok, Senaras, and Yuksel 2013). The overlap ratio was computed in terms of the number of pixels and a located building rooftop was labeled as  $TL$  if at least 90% of the rooftop overlapped with a reference building rooftop.  $FL$  denoted the number of demolished buildings mislabeled as rooftop.  $F_1^L$  measured the overall

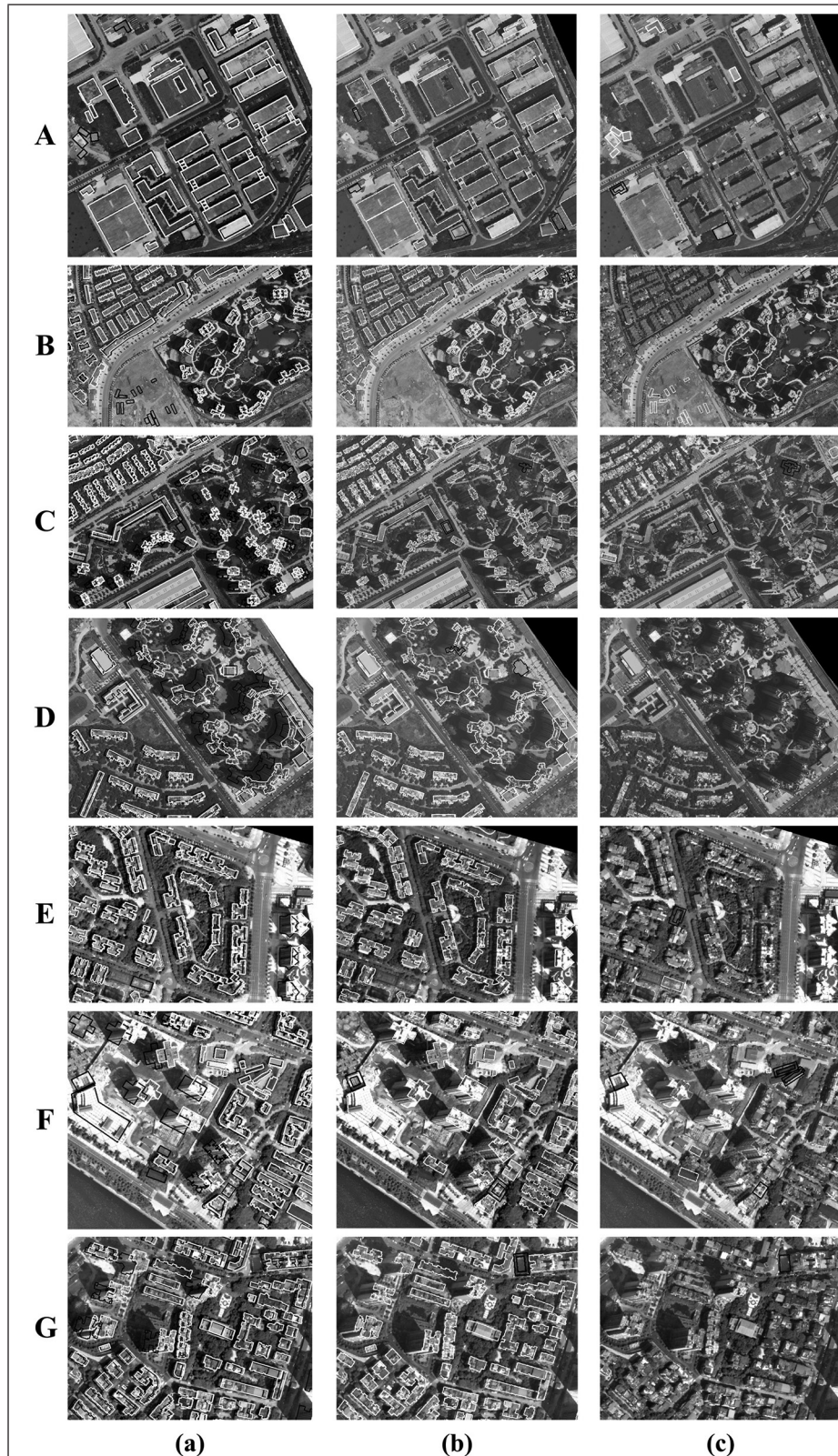


Figure 14. Amplified details of seven typical regions: (a) the references, (b) rooftop localization, and (c) change detection results of the enlarged subsets.

performance through the weighted harmonic of precision and recall. The detailed evaluation results are depicted in Table 1.

Table 1. The object-level performance of building rooftop localization.

Analyzed Data	No. of Correctly Located Buildings		No. of Wrongly Located Buildings		PL (%)	RL (%)	$F_1^L$ (%)
	TL	FL	ML				
Aerial Image							
dataset 1	813	4	19	99.51	97.71	98.60	
Satellite Image							
dataset 2	705	8	35	98.87	95.27	97.04	
dataset 3	4046	39	161	99.04	96.17	97.58	
Aerial Image							
A	98	1	4	98.98	96.07	97.51	
B	133	0	2	100.00	98.51	99.25	
C	90	1	2	98.90	97.82	98.36	
D	99	0	3	100.00	97.05	98.50	
Satellite Image							
E	63	0	3	100.00	95.45	97.67	
F	110	2	5	98.21	95.65	96.91	
G	91	2	5	97.84	94.79	96.29	

For region A, B, and E, where the buildings are mainly low-rise with minimal relief displacements, the overall performance of rooftop location was over 97%. In region A, 98 rooftops were located out of a total of 102, resulting in a recall of 96.07%. Owing to the weak saliency, four rooftops were out of accurate localization. The reason that one demolished building was falsely located as rooftop was that the demolished region still remained the building shape and had a contrast with the surround, thus leading to 98.98% performance in precision. In region B, 133 out of 135 rooftops were extracted correctly, resulting in 98.51% performance in completeness. There were two inexactly located rooftops because of the shape difference between the rooftop contour and the footprint polygon. In region E, due to the severe distortion of the rooftops and the serious shelter of neighboring objects, three inaccurately located rooftops out of 66 arose, resulting in a completeness of 95.45%. In region C, 39 low-rise buildings and 53 high-rise buildings were present, with large relief displacements and different geometric displacements in the mosaic region. Among these buildings, 90 rooftops were located correctly, providing a recall of 97.82%. There were two rooftops located inexactly, which were caused by the weak saliency and the shadow occlusion. One rooftop was located falsely because a basketball court built in the region had the same shape with the original footprint polygon, resulting in 98.90% performance in precision. Region D, F, and G are highly complex districts, where the buildings have a rooftop with multiple colors and vary considerably in terms of size, structure, distribution, and displacement, the overall performance of rooftop location was over 96%. A total of 99 out of 102 rooftops were located correctly, and three inaccurately located rooftops resulted from the shape scaling and deformation, resulting in a recall of 97.05% in region D. In region F, 110 out of 115 buildings were identified and located correctly, resulting in 95.65% performance in overall completeness. In region G, 91 rooftops were located accurately and five rooftops were out of accurate localization, providing a recall of 94.79%. In terms of rooftop localization, among all the three datasets, the proposed approach had 98.60% and 97.04% performance in overall accuracy for aerial image of the dataset 1

and satellite image of the dataset 2, respectively. Meanwhile, based on our test over a large urban scene with about 18 square kilometers and 4736 buildings, our algorithm achieved 97.58% accuracy. In the dataset 3, various scene complexities with many building types challenge the algorithm, and the result turns out the applicability.

#### Building Change Detection Assessment

In the building change detection assessment, *TD* represented true positives and corresponded to the number of buildings correctly labeled as change in both ground reference and detection result. *FD* represented false positives and corresponded to the number of buildings mislabeled as change. *MD* represented false negatives and corresponded to the number of buildings mislabeled as no change. The detailed evaluation results are depicted in Table 2.

Table 2. The evaluation results of building change detection.

Analyzed Data	No. of Correctly Located Buildings		No. of Wrongly Located Buildings		PL (%)	RL (%)	$F_1^L$ (%)
	TL	FL	ML				
Aerial Image							
dataset 1	57	8	4	87.69	93.44	90.47	
Satellite Image							
dataset 2	83	14	8	85.56	91.20	88.29	
dataset 3	490	77	39	86.42	92.63	89.41	
Aerial Image							
A	8	2	1	80.00	88.88	84.21	
B	15	0	0	100.00	100.00	100.00	
C	6	1	1	85.71	85.71	85.71	
D	0	0	0	-	-	-	
Satellite Image							
E	8	1	0	88.88	100.00	94.11	
F	14	3	2	82.35	87.50	84.84	
G	12	2	2	85.71	85.71	85.71	

Figure 14c and Table 2 illustrate the detected building changes and the results of evaluation, respectively. According to Table 2, in region A, eight demolished buildings were detected correctly out of a total of nine, resulting in 88.88% performance in overall completeness. There was one demolished building falsely located as a rooftop, thus leading to one missing of change. Two buildings were wrongly classified as demolition by the reason that the buildings had neither saliency nor a clearer contour, leading to a precision of 80%. In region B, all 15 change buildings were found and there was no mistake, resulting in 100% performance in recall and correctness. In region C, of seven buildings in the reference, six buildings were detected correctly as change, providing a recall of 85.71%. One missing change was caused by the reason that the demolished building was falsely located as rooftop. Meanwhile, there was one falsely detected as change, which were caused by the shadow occlusion, leading to 85.71% performance in correctness. In region E, all eight demolitions were correctly identified, resulting in a completeness of 100%. There was one mislabeled change, which was caused by the serious shelter of surrounding trees. In region F, 14 out of 16 buildings were detected correctly and three buildings were falsely detected as change, leading to 87.50%, 82.35%, and 84.84% in overall completeness, correctness, and accuracy, respectively. In region G, 12 demolished buildings were found correctly out of 14 buildings in the reference, providing a recall of 85.71%. In the building change detection on the

three datasets, the proposed approach had 90.47%, 88.29%, and 89.41% performance in overall accuracy, respectively. In dataset 1, 57 buildings are successfully labelled as changed, eight are wrongly labelled as changed and four changed buildings are missed. In dataset 2, 83 buildings are successfully labelled as changed, 14 are wrongly labelled as changed and eight changed buildings are missed. In dataset 3, 490 buildings are successfully labelled as changed, 77 are wrongly labelled as changed and 39 changed buildings are missed. As shown in Figure 13 and Figure 14, the main reason for buildings wrongly labelled as changes is that the shapes of footprint polygon are not accurate and the peripheral environment factors seriously obscure some useful features of the buildings. The reason for missing changed buildings is that although some buildings do not present in images, their edge intensities, and contrast saliency are still strong, so the localization in this circumstance is out of operation.

Based on the above analysis, in region A, the main reason of wrong result was that the peripheral building was very similar to the current building and had stronger saliency and a clearer contour. Figure 15a shows that the rooftop was identified as being located on the peripheral building. In particular, when the demolished region still remained the building shape and had a contrast with the surround, the disappearance is undetected, resulting in missed demolition detection, as shown in Figure 15b. In region B, D, and G, some shape differences were observed between the rooftop contour and the footprint polygon, and contour matching failed, leading to the migration of localization and even pseudo change (Figure 15c). In region C, E, and F, the mistakes resulted from the building being seriously covered by a shadow cast by other nearby buildings or trees, complicating the ability to successfully obtain building proposals and detect contours, and increasing the falsely demolished building change detection (Figure 15d).

## Discussion

### Parameter Selection

The parameters in this work involve polygon simplification, MBI, RSI, building saliency, prior template construction, edge detection, contour matching, vertical line verification, number of iterations  $N_r$ , and DDP. Considering that this study focuses on rooftop extraction by roof-cut, we mainly discuss the parameter selection of the contour integrity  $\varphi$ , the migrated weight  $\lambda$ ,  $N_r$ , and the convergence tolerance  $\tau$ ; all other parameters are determined by experience and relevant references. We now provide insights into how to select and tune the parameters of the proposed algorithm. We also provide recommended settings that should give good results when working with a variety of data.

### Contour Integrity and Migrated Weight

Using test areas C and G as an example, Tables 3 and 4 present the statistics of the contour constraint with different  $\varphi$  and  $\lambda$ , respectively. Table 3 shows that  $\varphi$  ranges from 0.1 to 0.7 and Table 4 shows that  $\lambda$  ranges from 1.0 to 7.0. For the region C, when  $\varphi = 0.5$  and  $\lambda = 5.0$ , the precision of detection is the highest. For the region G, when  $\varphi = 0.3$  and  $\lambda = 5.0$ , the precision of detection is the highest. The large floating of the overall accuracy as  $\varphi$  changes in Table 3 is obvious. Table 4 shows that  $\lambda = 5.0$  and  $\lambda = 7.0$  achieve the same maximum precision, which demonstrates that overall accuracy approaches stability with increasing  $\lambda$ . Comparing regions C and G, we can conclude that  $\varphi$  and  $\lambda$  exert a common effect on high-rise buildings with relief displacements while low-rise buildings with a heterogeneous appearance are only sensitive to  $\varphi$ . Thus, in the results presented in this paper, we chose a constant  $\lambda = 5$  to achieve visually appealing results. In addition, the contour integrity  $\varphi$  was set to 0.5 in the aerial image and 0.3 in the satellite images.

Table 3. Statistics of the contour constraint with different  $\varphi$ .

Analyzed Data	$(\varphi, \lambda)$	Located Buildings (Wrong Localization)/ Detected Buildings (Wrong Detection)	Q (%)
C	(0.1, 5.0)	96 (12)/3 (0)	87.87
	(0.3, 5.0)	94 (6)/5 (1)	92.92
	(0.5, 5.0)	92(2)/7(1)	96.96
	(0.7, 5.0)	79 (0)/20 (13)	86.86
G	(0.1, 5.0)	104 (16)/6 (0)	85.45
	(0.3, 5.0)	96 (5)/14 (2)	93.63
	(0.5, 5.0)	81 (2)/29 (17)	82.72
	(0.7, 5.0)	69 (1)/41 (28)	73.63

Table 4. Statistics of the contour constraint with different  $\lambda$ .

Analyzed Data	$(\varphi, \lambda)$	Located Buildings (Wrong Localization)/ Detected Buildings (Wrong Detection)	Q (%)
C	(0.5, 1.0)	90 (9)/9 (3)	87.87
	(0.5, 3.0)	91 (5)/8 (2)	92.92
	(0.5, 5.0)	92(2)/7(1)	96.96
	(0.5, 7.0)	92(2)/7(1)	96.96
G	(0.3, 1.0)	95 (6)/15 (3)	91.81
	(0.3, 3.0)	95 (5)/15 (3)	92.72
	(0.3, 5.0)	96 (5)/14 (2)	93.63
	(0.3, 7.0)	96 (5)/14 (2)	93.63

Parameter  $\varphi$  depends on the detection level of edges and lines, and will affect the constraint of the shape prior. Figure 16b illustrates the segmentation result without the contour constraint, and Figures 14c, 14d, and 14e are obtained when

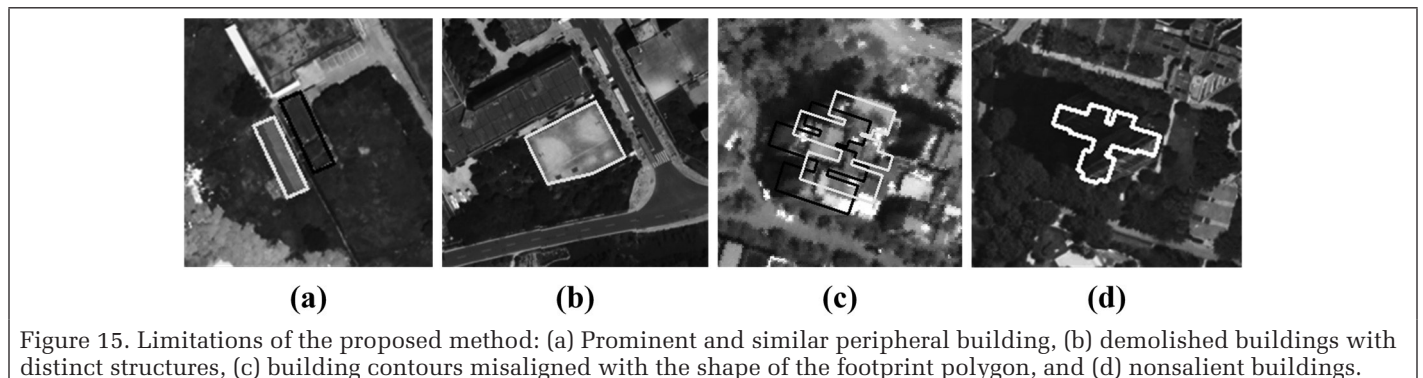


Figure 15. Limitations of the proposed method: (a) Prominent and similar peripheral building, (b) demolished buildings with distinct structures, (c) building contours misaligned with the shape of the footprint polygon, and (d) nonsalient buildings.

$\varphi = 0.2, 0.5, \text{ and } 0.7$ , respectively. The results show that  $\varphi$  should be large enough to achieve the desired contour constraint effect but small enough to avoid over-constraint. A value of  $\varphi \in [0.25, 0.55]$  generally provides good results when working with a variety of data. However, this parameter should be adjusted per dataset according to the edge and line detection effect.

Parameter  $\lambda$  should ideally be chosen as a function of the displacement level; the effect of this parameter can be clearly observed when it is applied to high-rise buildings with relief displacements. As shown in Figure 17, the result goes from the footprint to becoming almost identical to the rooftop as  $\lambda$  increases. Incorrect segmentation may easily be performed for high-rise buildings due to the impact of the contour matching when  $\lambda = 1$  (Figure 17b). The vertical line is used to emphasize the effects of matching-point weighting on the rooftop when  $\lambda > 1$ . As  $\lambda$  increases, the constraint effect is improved to a certain extent (Figures 15c and 15d).

In view of the above discussion, it is drawn that the proposed model can effectively solve the problems we are dealing with by the direct combination, since the shape prior is introduced to impose the contour constraint on the

segmentation process and it is adjustable by the parameters of the contour integrity and migrated weight.

#### Number of Iterations and Convergence Tolerance

Parameters  $N_i$  and  $\tau$  affect the quality of the estimated reference rooftop and the processing speed. In this work, roof-cut iterations are ceased when the change in pixels between the footprint polygon and the segmented region falls below a user-specified tolerance or a maximum  $N_i$  is reached. Figure 18 shows the segmentation effects of different iteration numbers. The contour is crude after initial segmentation (Figure 18b), and good results are obtained after three iterations (Figure 18c), which yield no obvious difference from the results obtained after five iterations (Figure 18d). In general,  $N_i \in [3, 6]$  and  $\tau \in [40, 80]$  work well.

#### Advantages and Disadvantages of the Proposed Algorithm

The results of this work are promising for challenging regions with complex scenes, and the proposed method presents several advantages. First, the proposed method correctly locates the rooftop and demolished building changes even in regions where buildings vary considerably in size, structure, projection, and displacement. In particular, this method yields very good localization results for high-rise buildings by reducing

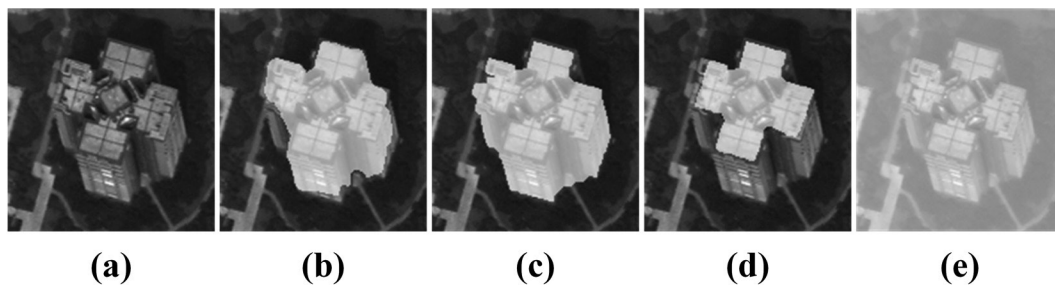


Figure 16. Segmentation results with different contour integrities  $\varphi$ : (a) Original image; (b) the result without the contour constraint; and the results when (c)  $\varphi = 0.2$ , (d)  $\varphi = 0.5$ , and (e)  $\varphi = 0.7$ .

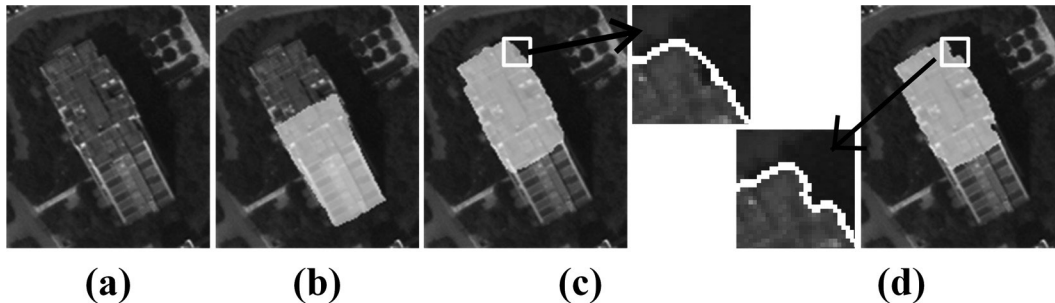


Figure 17. Segmentation results with different migrated weights  $\lambda$ : (a) Original image; the results when (b)  $\lambda = 1$ , (c)  $\lambda = 3$ , and (d)  $\lambda = 5$ .

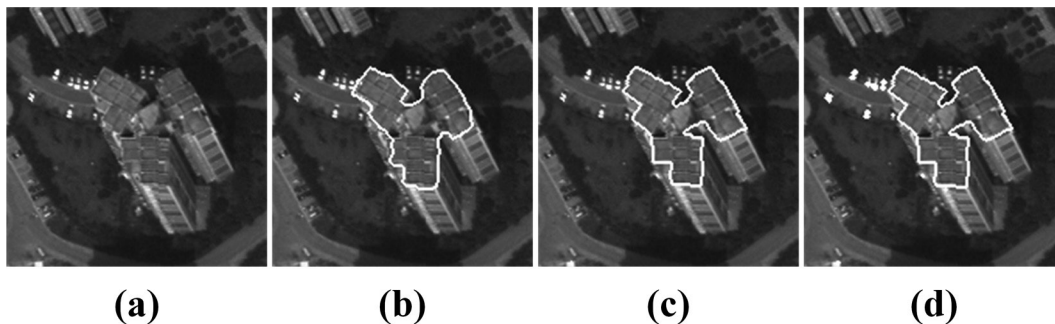


Figure 18. Segmentation results with different iterations  $N_i$ : (a) Original image and results obtained when (b)  $N_i = 1$ , (c)  $N_i = 3$ , and (d)  $N_i = 5$ .

the false change caused by large relief displacements. The second advantage of the proposed method is that it is suited for heterogeneous buildings and, thus, improves the accuracy of change detection. Even when a building has a roof with multiple colors, the rooftop is successfully located. In general, the proposed method can effectively distinguish whether buildings had been demolished while quickly and accurately providing information on building roofs.

Given its many benefits, this approach, however, also presents some limitations that must be minimized or overcome. First, compared with peripheral objects, buildings show a slight saliency, challenges may be encountered. For example, obtaining the building proposal and attempting to detect contours are almost impossible when a building is extensively covered by the shadow cast by other nearby buildings or trees. Similarly, when peripheral buildings are very similar to the current building and have stronger saliency, especially in the demolished region, rooftops may be inappropriately identified on these buildings, leading to missed demolition detection. Second, the rooftop contour is occasionally seriously misaligned with the original shape of the building footprint polygon, i.e., shape distortions, including extreme scaling, rotation, and deformation, may occur between the rooftop and building footprint polygon. Matching the rooftop using prior knowledge of vector data is fairly difficult and may result in poor performance and even pseudo changes.

## Conclusions

In this paper, a roof-cut approach was developed to locate rooftops for building change detection by combining the analysis of two different data types: remotely sensed images and building footprint vector information. The proposed method is effective and robust for accurate rooftop localization and building demolition detection using aerial and satellite images. Moreover, roof-cut integrates multiple cues to facilitate more stable convergence for building rooftop extraction via the graph model with knowledge of the shape prior, and it is resistant to heterogeneous appearances and the positional inconsistencies caused by relief displacements. However, the presented algorithm does not detect new buildings or rooftops that are completely or seriously occluded by trees or shade due to the limited saliency and contour of the relevant buildings. In addition, the contour constraint term is sensitive to severe shape distortions between the rooftop and building footprint polygon, causing localization offsets and false change information.

For future studies, the following approaches could be considered: an assistant active contour model for migration correction, using 3D building change detection approaches combined with deep learning-based change detection, and application of an algorithm for shadow elimination in an image enhancement step.

## Acknowledgments

This work was partially supported by the National Key Research and Development Program of China (Project No. 2016YFB0501403) and National Natural Science Foundation of China (Project No. 41771363 and 41701389).

## References

Akçay, H. G. and S. Aksoy. 2010. Building detection using directional spatial constraints. Pages 1932–1935 in *Proceedings of the 2010 IEEE International Geoscience and Remote Sensing Symposium*, held in Honolulu, HI, 25–30 July 2010.

Thomas B. H., G. K. Maggi, L. Stefan and H. Peter. 2014. Geographic object-based image analysis—Towards a new paradigm. *ISPRS Journal of Photogrammetry and Remote Sensing* 87: 180–191.

Bouziani, M., K. Goïta and D. C. He. 2010. Automatic change detection of buildings in urban environment from very high spatial resolution images using existing geodatabase and prior knowledge. *ISPRS Journal of Photogrammetry and Remote Sensing* 65: 143–153.

Boykov, Y. and M.-P. Jolly. 2001. Interactive graph cuts for optimal boundary and region segmentation of objects in N–D images. Pages 105–112 in *Proceedings of the Eighth IEEE International Conference on Computer Vision*, held in Vancouver, B.C., Canada, 7–14 July 2001.

Boykov, Y. and V. Kolmogorov. 2004. An experimental comparison of min-cut/max-flow algorithms for energy minimization in vision. *IEEE Transactions on Pattern Analysis and Machine Intelligence* 26: 1124–1137.

Burns, J. B., A. R. Hanson and E. M. Riseman. 1986. Extracting straight lines. *IEEE Transactions on Pattern Analysis and Machine Intelligence* 8 (4): 425–455.

Cheng, M. M., G. X. Zhang, N. J. Mitra, X. Huang and S. M. Hu. 2011. Global contrast based salient region detection. *Computer Vision and Pattern Recognition* 37: 409–416.

Chen, G., G. J. Hay, L. M. T. Carvalho and M. A. Wulder. 2012. Object-based change detection. *International Journal of Remote Sensing* 33: 4434–4457.

Chesnel, A. L., R. Binet and L. Wald. 2008. Urban damage assessment using multimodal QuickBird images and ancillary data: The Bam and the Boumerdes earthquakes. In *Proceedings of the 6th International Workshop on Remote Sensing for Disaster Management Applications*, held in Pavia, Italy, 11–12 September 2008.

Coppin, P. R. and M. E. Bauer. 1996. Digital change detection in forest ecosystems with remote sensing imagery. *Remote Sensing Reviews* 200 (2): 161–161.

Croitoru, A. and Y. Doytsher. 2004. Right-angle rooftop polygon extraction in regularized urban areas: Cutting the Corners. *Photogrammetric Record* 19 (108): 311–341.

Desolneux, A., L. Moisan and J. M. Morel. 2000. Meaningful alignments. *International Journal of Computer Vision* 40 (1): 7–23.

Dollar, P. and C. L. Zitnick. 2015. Fast edge detection using structured forests. *IEEE Transactions on Pattern Analysis and Machine Intelligence* 37 (8): 1558–1570.

Peucker, T. and D. H. Douglas. 1973. Algorithms for the reduction of the number of points required to represent a digitized line or its caricature. *Classics in Cartography* 10 (2): 112–122.

Durieux, L., E. Lagabrielle and A. Nelson. 2008. A method for monitoring building construction in urban sprawl areas using object-based analysis of Spot 5 images and existing GIS data. *ISPRS Journal of Photogrammetry and Remote Sensing* 63 (4): 399–408.

Elmerabet, Y., C. Meurie, Y. Ruichek, A. Sbihi and R. Touahni. 2015. Building roof segmentation from aerial images using a line-and region-based watershed segmentation technique. *Sensors* 15 (2): 3172–3203.

Felzenszwalb, P. F. and D. P. Huttenlocher. 2004. Efficient graph-based image segmentation. *International Journal of Computer Vision* 59 (2): 167–181.

Gioi, R. G. V., J. Jakubowicz, J. M. Morel and G. Randall. 2010. LSD: A fast line segment detector with a false detection control. *IEEE Transactions on Pattern Analysis and Machine Intelligence* 32 (4): 722–732.

Guo, Z., S. Du, M. Li and W. Zhao. 2015. Exploring GIS knowledge to improve building extraction and change detection from VHR imagery in urban areas. *International Journal of Image and Data Fusion* 7 (1): 42–62.

Hecheltnen, A., F. Thonfeld and G. Menz. 2014. Recent advances in remote sensing change detection—A review. *Land Use and Land Cover Mapping in Europe* 18: 145–178.

- Hershberger, J. and J. Snoeyink. 1992. Speeding up the Douglas-Peucker line-simplification algorithm. Pages 134–143 in *Proceedings of the International Symposium on Spatial Data Handling*.
- Hou, B., Y. Wang and Q. Liu. 2016. A saliency guided semi-supervised building change detection method for high resolution remote sensing images. *Sensors* 16 (9): 1377.
- Huang, X., L. Zhang and T. Zhu. 2013. Building change detection from multitemporal high-resolution remotely sensed images based on a morphological building index. *IEEE Journal of Selected Topics in Applied Earth Observations and Remote Sensing* 7 (1): 105–115.
- Hussain, M., D. Chen, A. Cheng, H. Wei and D. Stanley. 2013. Change detection from remotely sensed images: from pixel-based to object-based approaches. *ISPRS Journal of Photogrammetry and Remote Sensing* 80 (2): 91–106.
- Jiang, H., J. Wang, Z. Yuan, T. Liu, N. Zheng and S. Li. 2011. Automatic salient object segmentation based on context and shape prior. Pages 9–9 in *British Machine Vision Conference*, Vol. 6.
- Jolly, M. P. D. and A. Gupta. 2000. Color and texture fusion: Application to aerial image segmentation and GIS updating. *Applications of Computer Vision* 18 (10): 2–7.
- Katartzis, A. and H. Sahlí. 2007. A stochastic framework for the identification of building rooftops using a single remote sensing image. *IEEE Transaction on Geoscience & Remote Sensing* 46 (1): 259–271.
- Li, H. Y., H. Q. Wang and C.B. Ding. 2006. A new solution of automatic building extraction in remote sensing images. Pages 3790–3793 in *Proceedings of the IEEE International Conference on Geoscience and Remote Sensing Symposium*, held in Denver, CO, 31 July–4 August 2006.
- Lunetta, R. S. and C. D. Elvidge. 1999. Remote sensing change detection. *Environmental Monitoring Methods and Applications*.
- Nosrati, M. S. and P. Saeedi. 2010. A novel approach for polygonal rooftop detection in satellite/aerial imageries. Pages 1709–1712 in *Proceedings of the IEEE International Conference on Image Processing*, held in Cairo, Egypt, 7–10 November 2010.
- Myint, S. W., P. Gober, A. Brazel, S. Grossman-Clarke and Q. Weng. 2011. Per-pixel vs. object-based classification of urban land cover extraction using high spatial resolution imagery. *Remote Sensing of Environment* 115 (5): 1145–1161.
- Ok, A. O., C. Senaras and B. Yuksel. 2013. Automated detection of arbitrarily shaped buildings in complex environments from monocular VHR optical satellite imagery. *IEEE Transactions on Geoscience and Remote Sensing* 51 (3): 1701–1717.
- Özdemir, B., S. Aksoy, S. Eckert, M. Pesaresi and D. Ehrlich. 2010. Performance measures for object detection evaluation. *Pattern Recognition Letters* 31 (10): 1128–137.
- Papadopoulos, D. P., J. R. R. Uijlings, F. Keller and V. Ferrari. 2017. Extreme clicking for efficient object annotation. Pages 4940–4949 in *Proceedings of the IEEE International Conference on Computer Vision*, held in Venice, Italy, 22–29 October 2017.
- Rother, C., V. Kolmogorov and A. Blake. 2004. “GrabCut”: Interactive foreground extraction using iterated graph cuts. *ACM Siggraph* 23 (3): 309–314.
- Samadzadegan, F., H. Rastiveisi and W. G. Viii. 2008. Automatic detection and classification of damaged buildings, using high resolution satellite imagery and vector data. *Journal of Food Science* 78 (7): 1049–1056.
- Sellaouti, A., A. Hamouda, A. Deruyver and C. Wemmert. 2013. Template-based hierarchical building extraction. *IEEE Geoscience and Remote Sensing Letters* 11 (3): 706–710.
- Shi, W. and M. Hao. 2013. A method to detect earthquake-collapsed buildings from high-resolution satellite images. *Remote Sensing Letters* 4 (12): 1166–1175.
- Singh, A. 1989. Digital change detection techniques using remotely-sensed data. *International Journal of Remote Sensing* 10: 989–1003.
- Sofina, N. and M. Ehlers. 2017. Building change detection using high resolution remotely sensed data and GIS. *IEEE Journal of Selected Topics in Applied Earth and Observations and Remote Sensing* 9 (8): 3430–3438.
- Suveg, I. and G. Vosselman. 2004. Reconstruction of 3D building models from aerial images and maps. *ISPRS Journal of Photogrammetry and Remote Sensing* 58: 202–224.
- Taskin, K. G., N. Musaoglu and O. K. Ersoy. 2011. Damage assessment of 2010 Haiti earthquake with post-earthquake satellite image by support vector selection and adaptation. *Photogrammetric Engineering and Remote Sensing* 10 (77): 1025–1035.
- Tiede, D., S. Lang, P. Füreder, D. Hölbling, C. Hoffmann and P. Zeil. 2011. Automated damage indication for rapid geospatial reporting. *Photogrammetric Engineering and Remote Sensing* 77 (9): 933–942.
- Voigt, S., T. Schneiderhan, A. Twele, M. Gähler, E. Stein and H. Mehl. 2011. Rapid damage assessment and situation mapping: learning from the 2010 Haiti earthquake. *Photogrammetric Engineering and Remote Sensing* 77 (9): 923–931.
- Vosselman, G. 2008. Fusion of laser scanning data, maps, and aerial photographs for building reconstruction. *IEEE International Geoscience and Remote Sensing* 1: 85–88.
- Wen, D., X. Huang, L. Zhang and J. A. Benediktsson. 2015. A novel automatic change detection method for urban high-resolution remotely sensed imagery based on multiindex scene representation. *IEEE Transactions on Geoscience and Remote Sensing* 54 (1): 609–625.
- Xiao, P., M. Yuan, X. Zhang, X. Feng and Y. Guo. 2017. Cosegmentation for object-based building change detection from high-resolution remotely sensed images. *IEEE Transactions on Geoscience and Remote Sensing* PP (99): 1–17.
- Zhou, G., W. Chen, J. A. Kelmelis and D. Zhang. 2005. A comprehensive study on urban true orthorectification. *IEEE Transactions on Geoscience and Remote Sensing* 43 (9): 2138–2147.

# Contextual Global Registration of Point Clouds in Urban Scenes

Xuming Ge and Bo Wu

## Abstract

*This paper presents an innovative and powerful approach for contextual global registration of partially overlapping point clouds in urban scenes. First, a fast and robust strategy for extraction of feature points from large-scale scanning scenes is proposed and used to represent the scanning scene. Correspondences are then established using a contextual rule-based method at the two-dimensional and three-dimensional levels. A penalization strategy is then introduced to generate dense corresponding sets between two overlapping point clouds. Finally, a three-stage optimal strategy is implemented to efficiently match these point clouds. The proposed approach highlights the following aspects: (1) The designed voting-based feature extraction method can efficiently and robustly represent a scanning scene in a complex environment with a huge database; (2) The contextual information enables the generation of more reliable correspondences beyond the geometric features; (3) The novel penalization strategy and the three-stage optimal method benefit the approach to achieve tight alignment at a lower computational cost. State-of-art baseline algorithms from the field of photogrammetry are used to evaluate the performance of the proposed method in the comprehensive experiments. The presented approach outperforms other methods in registration accuracy and computational cost.*

## Introduction

The registration is particularly challenging when the pairwise scanning scenes only partially overlap and when no initial alignment values are given. Point cloud registration should overcome three key challenges: (1) the huge amount of data (Theiler *et al.* 2014), (2) the strong variations in point densities caused by the line-of-sight scanning principle in long-distance measurements (Dong *et al.* 2018), and (3) the large numbers of outliers and noise in complex scanning scenes (Zai *et al.* 2017). To overcome these challenges, extensive studies have been performed to extend the original registration strategies or design novel frameworks to strengthen the capabilities of these approaches. To address a large-scale scene with a huge number of points and partial overlap, practical registration pipelines use key-point detectors (e.g., Harris three-dimensional (3D) (Sipiran and Bustos 2011)) to extract interesting points and then use feature descriptors such as fast point feature histograms (FPFH) (Rusu *et al.* 2009) to describe such points; the correspondences can then be established upon a specific rule (e.g., the nearest-neighborhood rule (Besl and McKay 1992)) and then with the iterative model fitting framework such as random sample consensus (RANSAC) (Bolles and Fischler 1981). For each iteration, the program exploits a set of candidate correspondences or its samples, produces an alignment based on those correspondences, and carries out a validation process. If sufficient accuracy is established,

a refined strategy with a local registration algorithm such as iterative closest point (ICP) (Besl and McKay 1992) can be executed to arrive at a local optimal alignment.

Exploitation of key-points to represent the scanning scene is necessary for registration of large-scale point clouds. Most registration methods typically apply general detectors such as intrinsic shape signature (Zhong 2009) and 3D Harris (Sipiran and Bustos 2011), but they have their drawbacks. First, the key-points extracted from such general detectors do not contain specific geometric meaning that reduces the repeatability of the same key-point from various scanning scenes. In addition, the quantity and quality of the key-points obtained from those detectors depend largely upon the window size for searching.

Contextual information is widely concerned in the classification of point clouds (Niemeyer *et al.* 2016; Vosselman *et al.* 2017). One of the most significant properties that supports those applications is a certain spatial continuity shown by most scanned objects, hence the quantified feature also shows a certain degree of homogeneity and continuity. The bottleneck, however, in introducing such strategy to generate a descriptor into point cloud registration is that contextual information is typically supported by a neighborhood. It is distinctiveness for 3D key points in most urban environments which is dominated by planar structure.

For matching of the correspondences candidate, the iterative process is typically based on variants of RANSAC. An optimal strategy typically based on the least-squares (LS) theory is applied to optimize an objective with the selected samples from a set of candidate correspondences. On one hand, because RANSAC is a statistical and probabilistic approach, many iterations are required, which makes estimation and validation both computationally expensive. On the other hand, the use of LS to realize optimization is positively related to the redundancy, and LS does not contain the robust property. That means that the increasing redundancy or observations can improve the quality of the estimations, but with this benefit comes an increased likelihood of risk (i.e., increasing the iterations or trapping the convergence).

To address the aforementioned issues, this paper presents an innovative and powerful global registration method in which the correspondences will be established more effective based on the robust key-points; what is more, a novel iterative strategy is introduced to improve the registration accuracy and the computational cost.

## Related Work

The registration of point clouds has been extensively studied (Salvi *et al.* 2007; Tam *et al.* 2013). The goal of coarse registration is to identify a high-quality initial alignment between adjacent point clouds with arbitrary position and orientation;

Photogrammetric Engineering & Remote Sensing  
Vol. 85, No. 8, August 2019, pp. 559–571.  
0099-1112/19/559–571

© 2019 American Society for Photogrammetry  
and Remote Sensing  
doi: 10.14358/PERS.85.8.559

Department of Land Surveying & Geo-Informatics, The Hong Kong Polytechnic University (bo.wu@polyu.edu.hk).

coarse registration is thus a global strategy (Zhou *et al.* 2016). A common registration method should address the following issues: (1) representation of scanning scenes with necessary points, (2) extraction of key-points and description of points with discriminative features, and (3) establishment of correspondences and application of an iterative model fitting framework to align adjacent point clouds. Each of these stages are reviewed in turn.

Most point cloud registration methods operate by down-sampling point clouds. The common method is to use a filter, such as a voxel-grid, to down-sample the point clouds (Holz *et al.* 2015). The extraction of geometric primitives such as lines (Stamos and Leordeanu 2003) and planes (Dold and Brenner 2006) to represent the scanning scene is also an effective approach to simplify a complex scanning scene. Researchers currently use super-voxels for simplification and regularization of point clouds (Xu *et al.* 2017; Zhu *et al.* 2017) that inherit the reliability and efficiency of the octree. Another method used to simplify a scanning scene is by cross section point clouds (Yang *et al.* 2016; Ge 2017). Two advantages of this method are that the continuous features on an object's surface can be preserved as completely as possible and the number of point clouds can be greatly reduced without a high computation cost.

Generally, most registration methods are used to locate key-points by using various detectors and to describe those key-points with various feature descriptors. Many detectors, including intrinsic shape signature (Zhong 2009), Harris 3D (Sipiran and Bustos 2011), 3D SURF (Knopp *et al.* 2010), and 2.5D SIFT (Lo and Siebert 2009), can be used directly with point clouds to extract the corresponding key-points (Theiler *et al.* 2014; Holz *et al.* 2015). Theiler and Schindler (2012) proposed the detection of virtual tie key-points by intersecting triples of detected planes. Ge (2017) used a local RANSAC framework to locate linear primitives and recorded vertex. Keeping these key-points in mind, various feature descriptors, such as the 3D shape context (Frome *et al.* 2004), FPFH (Rusu *et al.* 2009), and binary shape context (Dong *et al.* 2017), can be used to enrich the information on the points based on their neighborhoods.

RANSAC and its variations (Bolles and Fischler 1981; Chum *et al.* 2003; Schnabel *et al.* 2007) are the most well-known strategies to estimate transformation in coarse registration. For example, Ge (2017) and Theiler *et al.* (2014) carried out their 4-points congruent sets (4PCS) methods based on the RANSAC strategy. Moreover, Holz *et al.* (2015) showed different registration methods with the use of RANSAC. Another strategy used to estimate transformation is based on pose clustering (Drost *et al.* 2010; Yang *et al.* 2016). Normal-distribution transformation (DNT) (Magnusson 2009) is one known coarse registration method for large-scale point clouds that is also based on the consistency theory. Another approach to global registration is based on the branch-and-bound framework, such as Go-ICP (Yang *et al.* 2013), that systematically explores the pose space in search of the optimal solution.

One of the major limitations of those methods are their computational expense and unfavorable repeatability. The large number of points to consider is one of the main factors in the computational cost. Partially overlapping issues will significantly exacerbate the consumption and even trap the convergence. In addition, the strict constraints of those methods have tremendous negative consequences for their repeatability. To overcome these limitations, this paper presents a contextual global registration (CGR) algorithm to fast align large-scale point clouds without initial transformation. Compared with previous works, we highlight the following novel aspects:

- (1) We present an effective and robust voting-based method to extract key-points that will assess each point with two-dimensional (2D) information. The reduced-order processing can accelerate the speed of calculation. And for screening via the voting mechanism, each key-point contains specific geometric information that improves its repeatability from adjacent point clouds.
- (2) We propose a quick and simple approach to apply contextual information in registration such that, apart from the geometric features, contextual information is also used to establish and purify the correspondences between adjacent point clouds.
- (3) We provide a penalization strategy to reduce the costs of calculation in both the iterations and the validations. Moreover, the quality of the estimates can be improved by applying such a strategy with reasonable weighting.
- (4) We present a novel iterative fitting framework to implement the iterative estimation, which improves performance both in registration accuracy and in computational costs by changing the data dimension during the iterations.

## Contextual Global Registration of Point Clouds

### Overview of the Approach

The proposed CGR approach is an efficient and robust global registration method used to solve large-scale point cloud registration issues in photogrammetry. CGR extends the potential of the coarse registration method 4PCS (Aiger *et al.* 2008; Mellado *et al.* 2014; Mohamad *et al.* 2015) from computer vision to photogrammetry issues. Moreover, CGR improves its abilities in terms of registration accuracy, computational costs, and repeatability of the previous 4PCS type of methods in the photogrammetry field, such as Key-4PCS (K4PCS) (Theiler *et al.* 2014; Theiler *et al.* 2015) and Semantic Key-4PCS (Ge 2017). CGR begins with a quick down-sampling representation by cross section. The designed voting-based method is then implemented on each point so that correspondences can be established. A penalization strategy is carried out to weight the candidate correspondences and select a fitting model. CGR is terminated if the obtained transformation parameters pass the validation criteria. The overall strategy of the proposed approach is illustrated in Figure 1.

### Feature Point Extraction with a Robust Voting-Based Strategy

The use of CGR to rapidly represent a scanning scene by similar cross sections was implemented by Yang *et al.* (2016) and Ge (2017). However, CGR does not require identification and extraction of the ground plane, which acts as an extremely important role in those previous works. Although a terrestrial laser scanner is often installed upright in an urban scanning project, this hypothesis is not strictly enforced with CGR. Because we claim that CGR is more suitable to handle urban scanning scenes, the man-made structures, such as buildings, are the main scanned objects and always have a certain continuity. Figure 2 shows samples of key-points obtained from a part of the scanning scene in CGR with nonparallel cross sections. The red line represents a cross section perpendicular to the Z-axis (the scanner coordinate system), and the red points represent the corresponding key-points. This situation is common in that the scanner is (approximately) upright. The black line is a cross section that has a clear angle with the Z-axis, and the black points also represent the corresponding key-points. This simulates an exceptional case in which the scanner should be installed at an angle. However, based on the property of CGR (i.e., the extraction strategy) and the property of the man-made surface (i.e., the continuity), we

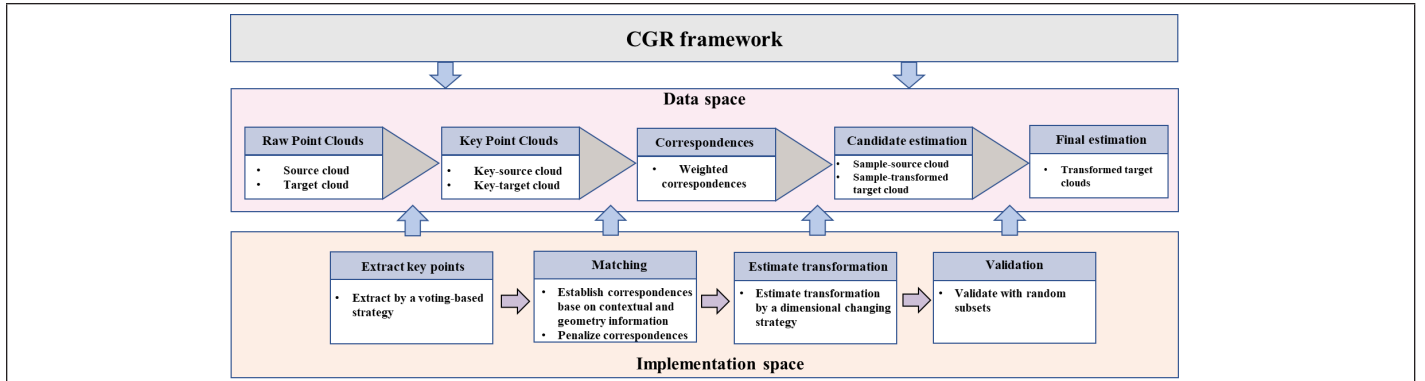


Figure 1. Overview of CGR framework.

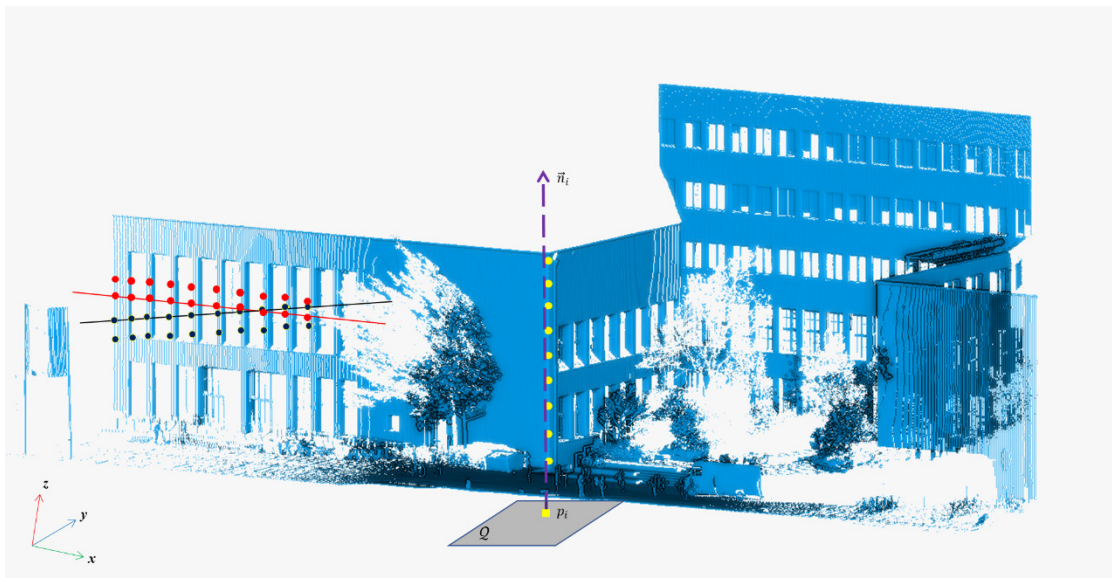


Figure 2. Different types of key-points in CGR. The blue points represent raw point clouds. The red line represents a cross section perpendicular to the Z-axis (the scan coordinate system), and the red points are the corresponding key-points. The black line is a cross section that has a tilt angle with the Z-axis, and the black points are the corresponding key-points. The yellow points represent key-points, and the purple dotted line is their fitting line with a direction  $\vec{n}_i$ . The yellow square is a projection point with the negative direction of  $\vec{n}_i$ .

can see that the key-points, regardless of whether they are red or black, will not affect the performance of CGR.

As mentioned above, in CGR, the obtained key-points have clear geometric information. Because the scanning scene is represented by a series of cross-sections of point clouds, the key-points can be extracted independently from each cross section. One of the main advantages of this method is that the structures in each cross section are simple; this is a 2D treatment, so the computational cost is low. Although the geometric information is simple, the meaning of each key-point is clear. CGR, therefore, can directly divide the points into three categories: 1) the vertexes of lines, 2) the intersection points of two lines, and 3) points in lines. In addition, the implementations for different cross sections are independent, such that CGR allows further acceleration with the multithreading technology of the *OpenMP* application. CGR is used to implement the above classification of points via a robust voting-based method. For each point, CGR executes a voting procedure by direction differences in its  $k$  nearest neighbors. The proposed voting-based method for extracting the key-points is more robust than the previous works, e.g., Yang *et al.* (2016) and Ge (2017) which based on the RANSAC method to fit lines. First of all, the fitting results are sensitive to the setting parameters

when by using RANSAC and to achieve the key-points will heavily depend on those fitting lines, i.e., model-driven. But, in the proposed voting-based method, to achieve the key-points the calculation derives by the physical structural attributes of points themselves, i.e., data-driven. Moreover, the additional robust strategies add in the voting-based method will act directly on the point itself based on the objective physical structural attributes. However, in the fitting-based method, those strategies will act on the fitting process.

In the 2D case (i.e., in a cross section), we can roughly divide the arrangement of points into two categories: straight lines and polylines (see Figures 3 and 4). It is thus convenient to calculate and record direction differences between two points by using a predefined reference. In Figure 3,  $p_1$  is an enquire point, and  $\mathbb{N}_p$  is a local neighborhood point set of  $p_1$  but without  $p_1$ . For  $p_1$ , CGR defines a reference direction by the nearest point of  $p_1$  from  $\mathbb{N}_p$  (i.e., the point  $p_2$ ) and notes it as  $\underline{p_1 p_2}$ . CGR can then calculate all of the direction differences from the reference direction in  $\mathbb{N}_p$  (i.e.,  $\langle \underline{p_1 p_h}, \underline{p_1 p_2} \rangle$ ,  $p_h \in \mathbb{N}_p$  where  $\langle \cdot \rangle$  is an angular operator of two directions). To quickly judge the type of point, CGR restricts the scope between two directions to the interval  $[0, 180]^\circ$  and creates three channels for voting with a linear salient factor  $\alpha$  (see Figures 3 and 4).

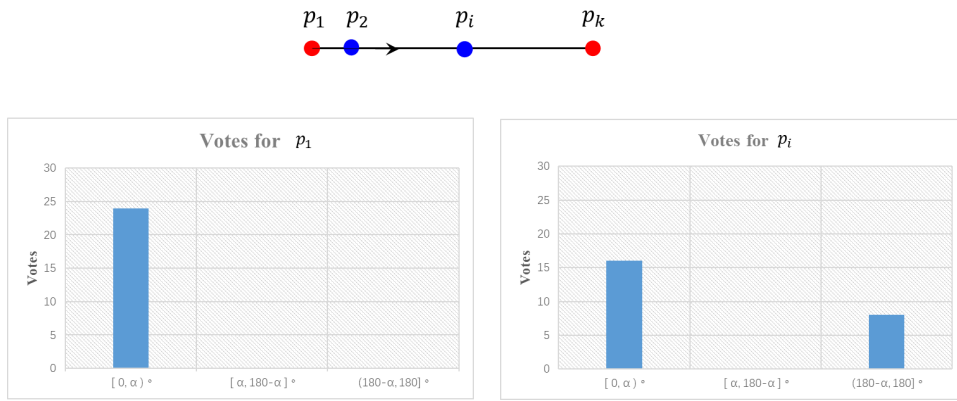


Figure 3. Voting procedure for each point and the voting results in a straight line. The left histogram shows the voting result for a single point, i.e.,  $p_i$  in a local neighborhood and the right one is that for the single point  $p_i$ .

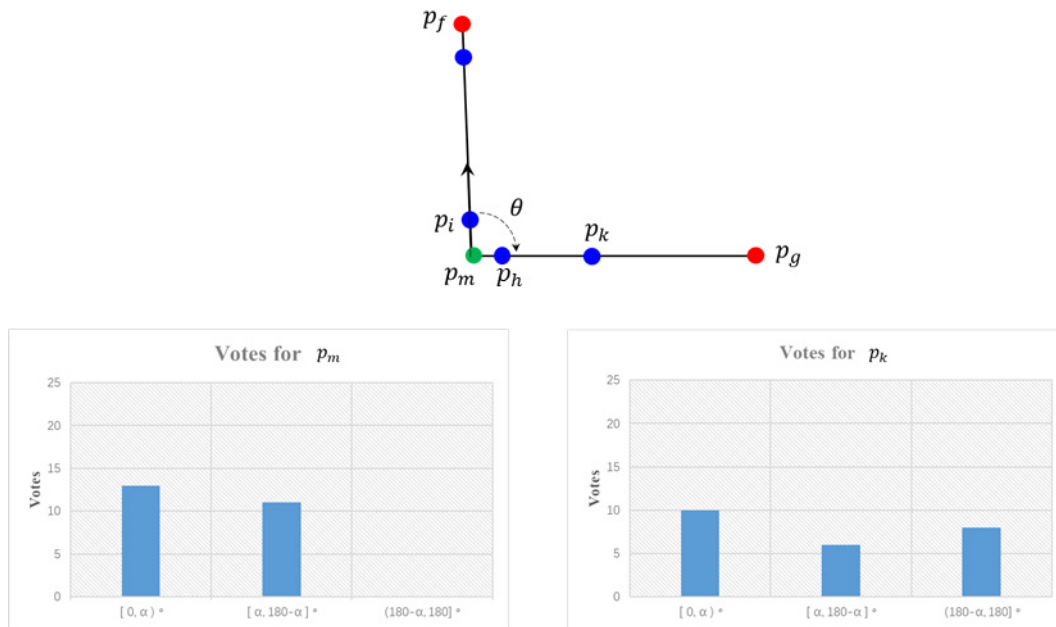


Figure 4. Voting procedure for each point and the voting results in a polyline. The left histogram shows the voting result for a single point, i.e.,  $p_m$  in a local neighborhood and the right one is that for the single point  $p_k$ .

Figures 3 and 4 show three types of points (I, II, and III) in red, green, and blue, respectively. Based on the voting strategy, we can obtain four voting results (i.e., the four histograms in Figures 3 and 4). Clearly, CGR can rapidly find the type I and II points from a cross section by recording the empty votes in the third channel.

It should be noted that although other kinds of lines, such as curves, can be found from a cross section, the presented voting procedure is also effective. Based on this procedure, extreme key-points will clearly be discarded by CGR; for example, the vertexes (the red points) are too close to each other (i.e.,  $\theta < \alpha$  in Figure 4). Taking into account the limited quality of the scanning results, CGR contains some easy yet robust techniques to reduce the influence of scanning errors on the procedure. First, as shown in Figure 4, CGR can quickly determine the two farthest points (i.e.,  $p_f$  and  $p_g$  from two directions of a candidate key-point  $p_m$ ) in its neighborhood. If  $\langle p_m p_f, p_f p_g \rangle < \alpha$  or  $\langle p_m p_g, p_f p_g \rangle < \alpha$ , the point  $p_m$  will move out from the candidate key-point set. In CGR,  $\alpha$  can be defined based on the scanner accuracy. From intensive tests, we find that  $\alpha = 20^\circ$  is a safe selection for most cases. Second, since the laser beam are affected by several factors (Lichti

2007), the position of a laser spot is random (Ge and Wunderlich 2016). Thus, the spots on a structural position are not accurate. For example,  $p_i$  and  $p_h$  are the nearest two points of  $p_m$  (see Figure 4) and will be denoted as two candidate key-points if  $p_m$  is missing. To address this issue, CGR will use one of them to replace  $p_m$ . Take into account that the key-points in CGR have strong structural meanings if two candidate key-points are too close (e.g.,  $d < 10$  cm), CGR will abandon one.  $d$  is a Euler distance threshold that is a soft threshold in CGR and can be predefined depending upon the transformation accuracy. Finally, CGR introduces the difference of normals (Ioannou *et al.* 2012) strategy from 3D to 2D issues and further filters flat key-points from the candidate set. Figure 5 shows an example of a gained candidate key-point set in CGR. Most of the aim structure points can be identified by the proposed method. Some pseudokey-points remain in the candidate set, such as trees and ground. CGR will further purify the candidate set later, and this topic is discussed in the section 3.5.

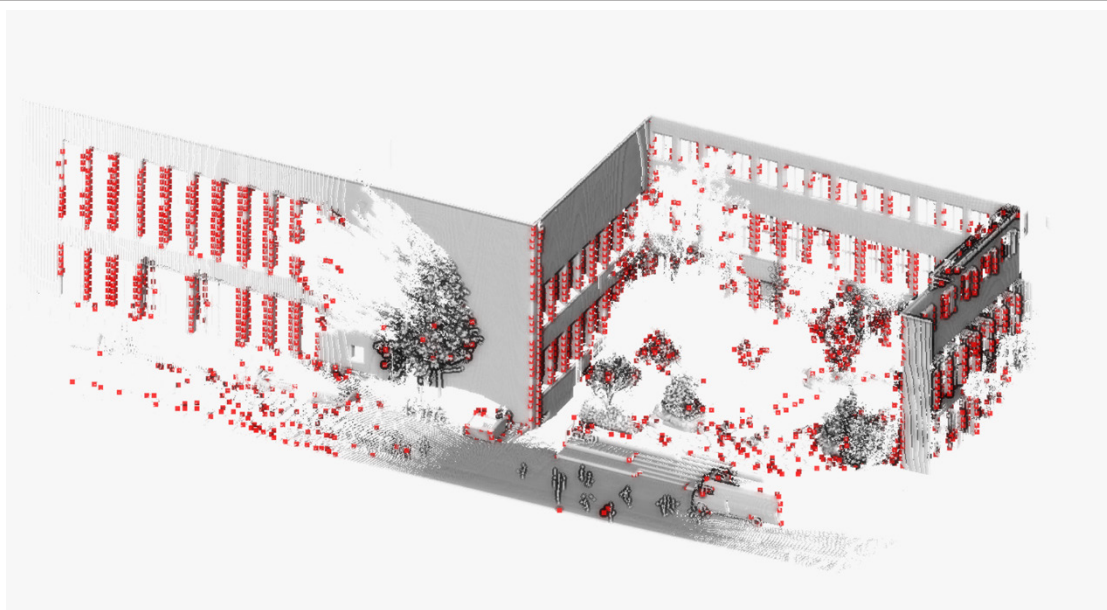


Figure 5. Candidate key-points set by the proposed voting-based strategy in CGR.

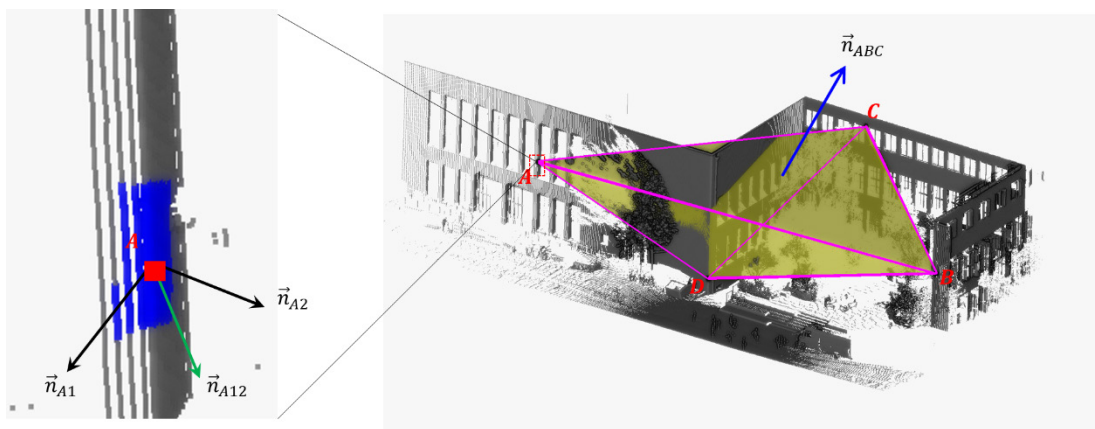


Figure 6. Extended information from a candidate congruent four-point set.

### Correspondence Estimation Based on Contextual and Geometric Information

CGR implements an extended 4PCS approach to detect and establish correspondences between adjacent point clouds in overlapping regions. The 4PCS algorithm (Aiger *et al.* 2008) acts as an efficient global rigid registration algorithm for a linear complementary problem by searching two congruent four-point sets from adjacent point clouds. Those two four-point sets should present some important geometric constraints because of the rigid-body transformation issues. The details of those constraints and the 4PCS principle can be found in the literature (Aiger *et al.* 2008; Theiler *et al.* 2014; Mohamad *et al.* 2015; Ge 2017). In addition to inheriting those constraints, CGR employs a further geometric constraint and contextual information to support and purify the candidate correspondences.

Figure 6 shows a candidate congruent four-point set  $\mathcal{S} = \{A, B, C, D\}$  in the source clouds. We then assume that a candidate corresponding congruent four-point set exists in the target clouds (i.e.,  $\mathcal{T} = \{A', B', C', D'\}$ ). First, based on the rigid-body transformation definition, the volume of these two tetrahedra should satisfy

$$\left| 1 - \frac{V_{ABCD}}{V_{A'B'C'D'}} \right| < \varepsilon_1, \quad (1)$$

where  $V_{ABCD}$  is the volume of the corresponding tetrahedron, and  $\varepsilon_1$  is a differential threshold. Moreover, the angles between two surface normals should further satisfy

$$\begin{aligned} \left| \langle \bar{n}_{ABC}, \bar{n}_{ABD} \rangle - \langle \bar{n}_{A'B'C'}, \bar{n}_{A'B'D'} \rangle \right| &< \varepsilon_2, \\ \left| \langle \bar{n}_{ABC}, \bar{n}_{ACD} \rangle - \langle \bar{n}_{A'B'C'}, \bar{n}_{A'C'D'} \rangle \right| &< \varepsilon_2, \\ \left| \langle \bar{n}_{ABC}, \bar{n}_{BCD} \rangle - \langle \bar{n}_{A'B'C'}, \bar{n}_{B'C'D'} \rangle \right| &< \varepsilon_2, \\ \left| \langle \bar{n}_{ABD}, \bar{n}_{ACD} \rangle - \langle \bar{n}_{A'B'D'}, \bar{n}_{A'C'D'} \rangle \right| &< \varepsilon_2, \\ \left| \langle \bar{n}_{ABD}, \bar{n}_{BCD} \rangle - \langle \bar{n}_{A'B'D'}, \bar{n}_{B'C'D'} \rangle \right| &< \varepsilon_2, \\ \left| \langle \bar{n}_{ACD}, \bar{n}_{BCD} \rangle - \langle \bar{n}_{A'C'D'}, \bar{n}_{B'C'D'} \rangle \right| &< \varepsilon_2, \end{aligned} \quad (2)$$

where  $\bar{n}_{ABCD}$  represents the normal of the surface  $ABC$ , and  $\varepsilon_2$  is an angular threshold. In addition to those constraints, CGR also

considers the contextual information of each point in a candidate congruent four-point set. Figure 6 displays an example with point  $A$ . The blue points represent the near neighborhood of point  $A$ , and CGR can then calculate the statistics of the normal directions around  $A$ .  $\vec{n}_{A1}$  and  $\vec{n}_{A2}$  are the principle normal directions of the surface around  $A$ , and  $\vec{n}_{A12}$  is a mean value direction. Based on the same strategy, CGR calculates those values on each candidate point, and the two candidate correspondence four-point sets should then further satisfy

$$\left| \langle \vec{n}_{M12}, \vec{n}_{N12} \rangle - \langle \vec{n}_{M'12}, \vec{n}_{N'12} \rangle \right| < \varepsilon_2, \quad (3)$$

with  $M, N = A, B, C, D$  but  $M \neq N$ . Due to the different perspectives, we sometimes cannot simultaneously find  $\vec{n}_{M1}$  and  $\vec{n}_{M2}$  on a point. Therefore, according to the overlapping perspectives probability, CGR allows a certain success rate in Equation 3 to establish correspondences.

### Penalization Strategy for Correspondences

After finding a pair of congruent four-point sets  $\{S, T\}$  from  $S$  and  $T$ , respectively, the algorithms under 4PCS strategies normally solve a quadratic minimum optimal problem based on LS. It has the following form:

$$\min_T \sum_{i=1}^4 (\|s_i - Tt_i\|) \quad (4)$$

with  $s_i \in S_i$  and  $t_i \in T_i$ . The goal is to find a pose  $T$  that can pass a validation, i.e.,

$$\sum_n \|s_k - Tt'_k\| < e \quad (5)$$

where  $t'_k \in T' \subseteq T$ .  $T'$  is a subset of  $T$  that depends on the overlap rate.  $\{s_k, t'_k\} \in \Sigma$  is the set of all correspondences that are set up by the nearest point, and  $e$  is a threshold that relates to the overlap rate (Theiler *et al.* 2014). The results of LS problems in terms of the estimated accuracy are known to be positively associated with the redundancy (Hansen *et al.* 2013). Based on this principle, CGR introduces more than one candidate correspondence of the congruent four-point sets into the calculation to implement an LS estimation. A robust penalty  $w(\cdot)$  is used in CGR, and the Equation 4 is rewritten as

$$\min_T \sum_{j=1}^n \left( \sum_{i=1}^4 w(\|s_i - Tt_i\|) \right), \quad (6)$$

CGR uses a scaled Geman-McClure factor to set up  $w(\cdot)$  as

$$w(x) = 1 - \frac{\mu x^2}{\mu + x^2}, \quad (7)$$

where the parameter  $\mu$  controls the range within which residuals have a significant effect on the objective, and  $x$  is a linear function as

$$x = p_i x_i, \quad i = 1, \dots, n. \quad (8)$$

$x_i$  represents the difference of the  $i$ th factor (e.g., the distances) between the correspondences, and  $p_i$  is the weight for such factor. All  $x_i$  values of a single point are normalized into the interval between 0 and 1 to balance the consequence of those factors, and all  $x$  values are normalized into the interval between  $-1$  and  $1$  for the same reason. Figure 7 shows the scaled Geman-McClure factor in CGR for various values

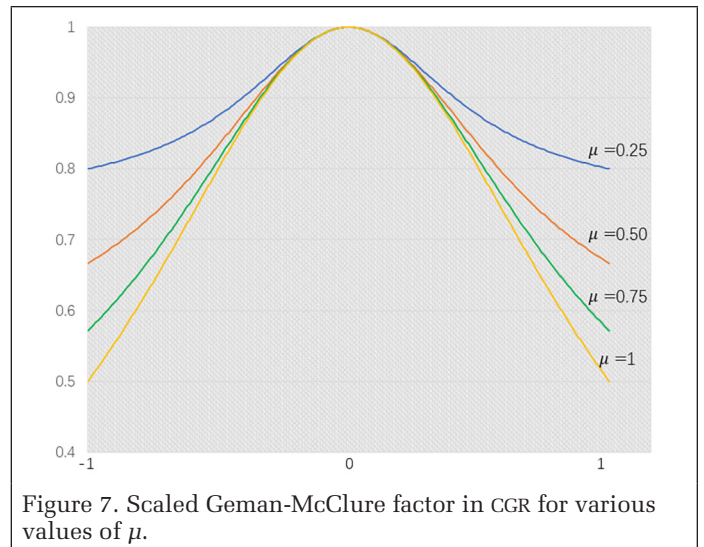


Figure 7. Scaled Geman-McClure factor in CGR for various values of  $\mu$ .

of  $\mu$ . Figure 7 shows that as  $\mu$  increases from 0.25 to 1, the penalization curves become sharper, which means that the poor correspondences will be punished more severely. The setting of  $\mu$  relates to the accuracy of scanning points and to the overlap rate and quality. In CGR, the program controls the quality of the candidate correspondences such that it assumes that very poor correspondences have already been detected and discarded; thus, the proportion of punishment will not exceed two times. The main advantage of this processing step is that the outliers will not pollute the later LS estimation, which is not robust.

### Transformation and Optimization

Estimation of an acceptable transformation set from an extremely large candidate pool is not an economic approach. Although the K4PCS method uses only two key-point sets to implement calculation, the iterative remains computationally expensive. To ensure that the RANSAC framework will work, a large number of key-points is often used—up to tens of thousands. Obtaining an acceptable four-point base set from  $C_N^4$  is very time consuming because  $2C_N^2$  pairs are waiting to be checked for each set. Taking these issues into account, Ge (2017) claimed to project key-points into the ground to further reduce the number of key-points. This strategy works when the ground points are available and when the ground points have reasonable overlapping regions. Clearly, this hypothesis cannot be always satisfied, especially for a large-scale outdoor scanning project. CGR follows this idea and extends to more general cases via a designed three-stage framework.

Figures 2 and 5 show that the key-points in CGR are mostly on the building's characteristic structures and have continuity in a certain direction. For the sake of convenience, we call this the scene's principal direction and mark it as  $\vec{N}$  in this paper. The reliability of  $\vec{N}$  can be guaranteed by the working scenes of CGR. In a key-point set, for each point, CGR uses its  $r$ -radii neighborhood to fit a line with a robust method and gives a direction  $\vec{n}$  (e.g.,  $\vec{n}_i$ ) in Figure 2. CGR then collects all and removes the outliers, and calculates the mean value to express  $\vec{N}$ . Making  $\vec{N}$  a normal vector, CGR creates a virtual plane and projects all key-points on the plane in the negative direction of  $\vec{N}$ . Figure 2 shows an example: if  $\vec{n}_i = \vec{N}$ , then CGR can obtain a virtual key-point, that is,  $p_i$  (the yellow square), from a series of true key-points  $V_i$  (the yellow circles). In addition, the considered surface continuity CGR only preserves the many-to-one relationship (i.e., multiple true key-points to a single virtual key-point). Based on this method, CGR can obtain a set of virtual key-points, and each

virtual key-point ( $p$ ) corresponds to a set of true key-points ( $\mathcal{V}$ ). Therefore, the three-stage approach is as follows.

- (1) Find a pair of congruent four-point sets from the virtual key-point space of two adjacent clouds with the Super-4PCS strategy (Mellado *et al.* 2014).
- (2) Narrow the true key-point space with four sets of true key-points that correspond to four virtual key-points from the first step. Then implement the strategy in the section “Evaluation” to obtain updated correspondences and further estimate the transformation parameters.
- (3) Do a radii search for each corresponding point from the second step, and rapidly set up dense correspondences by the nearest point with the estimated parameters from the second step. We can then further optimize the estimated parameters.

## Experiments and Evaluation

### Description of Datasets and Metric

The performance of the proposed CGR algorithm is evaluated with five datasets captured from various scenes with different challenges. Specifically, the first dataset is an office room that consists of two scans from different points of view. Although the room is not large, the scene is strongly symmetrical, with approximately equal length and width, which could cause the matching process to fail. The quality of this dataset is poor because the point clouds were captured with a red-blue-green-depth (RGB-D) sensor (i.e., Structure Sensor). Although the areas overlap by as much as 66%, a certain distortion in both scans means that the overlapping regions may not necessarily match. The second dataset, which consists of two scans, was captured from the campus of Technische Universität München (TUM) with a Leica HDS7000 terrestrial laser scanner (TLS) system. The main challenges to register this dataset were (1) the enormous amount of data; (2) the large-scale scene; (3) the large amounts of vegetation and numerous artifacts caused by movement of people and traffic; and (4) the relatively low degree of overlap. The third dataset is the TLS point clouds from the ThermalMapper project acquired by Jacobs Universität Bremen (Borrmann *et al.* 2013). This dataset was captured in downtown Bremen, so the scanning scene is even more complex than the TUM campus. The fourth dataset was captured from the campus of Hong Kong Polytechnic University (PolyU) with a Leica BLK 360 portable TLS system. The architectural styles differ completely from the previous two datasets. In addition, this dataset is the most challenging case in our tests because only 19% of the regions overlap. The fifth dataset, which consists of three scans, was also obtained with a Leica ScanStation 2 TLS system. This scene is a large multilevel garden terrace and modern skyscrapers. The main challenge, in this case, is that the horizontal lines of the different scans are distinctly different. In addition, the main overlapping regions in these cases have strong coplanarity. These five datasets are summarized in Table 1.

We evaluate the performance of CGR from two aspects: the registration accuracy and the computational cost. In terms

of the registration accuracy, we investigate the rotation error, translation error, and root mean square (RMS) error. For the computational cost issue, we mainly discuss the CPU runtime and the successful registration (SR) rate. Those indicators are normally used for evaluation of point cloud registration (Guo *et al.* 2014; Theiler *et al.* 2014; Theiler *et al.* 2015; Yang *et al.* 2016; Ge 2017; Dong *et al.* 2018).

The ground truth poses estimate of the datasets obtained before our tests. The initial pose estimates were acquired by manual registration and then refined with an ICP algorithm. We can thus calculate the rotation error and translation error as follows:

$$e_R = \arccos \left( \frac{\text{tr}(\bar{\mathbf{R}} - \mathbf{R}) - 1}{2} \right), \quad (9)$$

$$e_T = \|\bar{\mathbf{T}} - \mathbf{T}\|,$$

where  $(\bar{\mathbf{R}}, \bar{\mathbf{T}})$  and  $(\mathbf{R}, \mathbf{T})$  represent the rotation matrix and translation vector from the ground truth and the estimated parameters, respectively.  $\text{tr}(\cdot)$  denotes the trace of a matrix.  $e_R$ , the rotation error, corresponds to the angle of rotation in the axis-angle representation. To align point clouds  $\mathcal{P}_1$  and  $\mathcal{P}_2$ , we can implement the transformation separately with the ground truth and the estimated parameters to gain  $\mathcal{P}_1^t$  and  $\mathcal{P}_2^e$ , respectively. We then further calculate the RMS error as follows:

$$\text{rms error} = \sqrt{\frac{\sum_{i=1}^n \|p_{1,i}^t - p_{1,i}^e\|^2}{n}}, \quad (10)$$

where  $p_{1,i}^t \in \mathcal{P}_1^t$ ,  $p_{1,i}^e \in \mathcal{P}_1^e$ , and  $p_{1,i}^e$  is the nearest point of  $p_{1,i}^t$  in  $\mathcal{P}_1^e$ . An SR can be defined

$$\text{SR} = \begin{cases} 1 & \max(e_R) < \sigma_1, \max(e_T) < \sigma_2, \text{ and } t_r < \sigma_3 \\ 0 & \text{else} \end{cases}, \quad (11)$$

where  $\sigma_1$  and  $\sigma_2$  are the threshold of rotation and the translation error, and  $\sigma_3$  is the runtime threshold. Those thresholds should be predefined and relate to the real applications. Because the aforementioned 4PCS is a randomized matching strategy, the SR rate should be calculated to evaluate CGR, i.e.,

$$\text{SR rate} = \frac{N_S}{N} \quad (12)$$

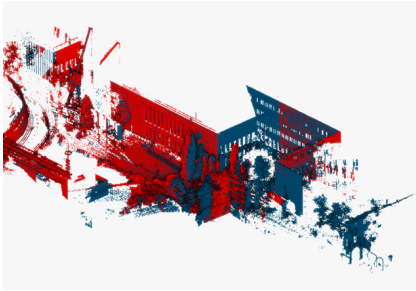
where  $N_S$  and  $N$  are the number of successful registrations and the number of all tasks, respectively. We implemented CGR and other reference methods in C++ with the open-source Point Cloud Library (PCL) (Rusu and Cousins 2011). All experiments were carried out on a standard computer with 16 GB RAM and Inter Core i7-7700HQ @ 2.8 GHz CPU.

Table 1. Detailed information of texted datasets.

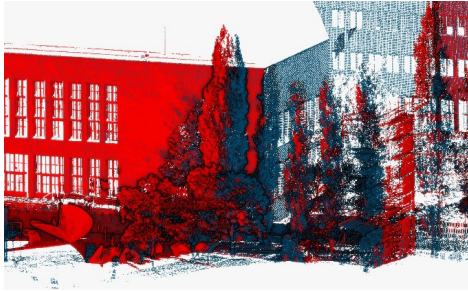
Dataset	Sensor	#Pts (million)	Dimensions (m)	Overlapping (%)
Office room	Structure Sensor	2.5	5 * 5 * 3	66
TUM campus	Leica HDS 7000	23.8	195 * 100 * 28	60
Bremen downtown	Riegl VZ-400	30.3	660 * 451 * 91	51
PolyU campus	Leica BLK 360	25.5	107 * 86 * 47	19
multilevel terrace 1–2	Leica ScanStation 2	20.6	66 * 64 * 45	73
multilevel terrace 2–3	Leica ScanStation 2	17.7	62 * 58 * 45	24



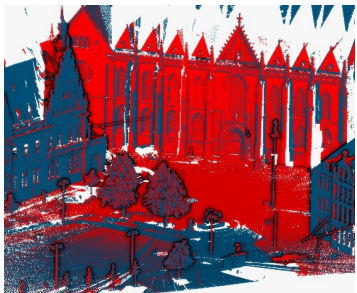
(a) Office room dataset.



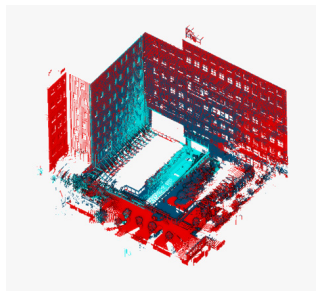
(b) TUM campus dataset.



(c) Bremen downtown dataset.



(d) PolyU campus dataset.



(e) Multilevel terrace dataset.

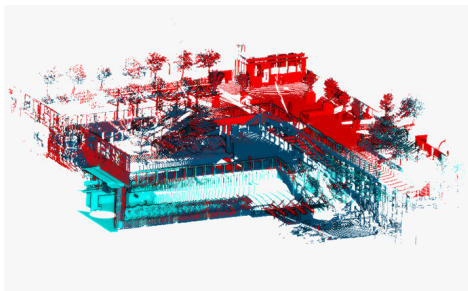


Figure 8. Registered adjacent scans by the proposed method. The figures on the left in (a) to (e) are the whole scenes of each dataset, and the figures on the right are subdetails of each dataset from different perspectives.

## Experimental Results

Figure 8 shows the outcomes of CGR with the five testing datasets and Figure 9 further displays the cloud-to-cloud distances in the overlapping regions after registration. Tables 2 and 3 display in detail the performances of CGR on the experiments in terms of the registration accuracy and the computational cost. Table 4 compares the CGR and the benchmark methods including the K4PCS (Theiler *et al.* 2014), SAC-IA (Holz *et al.* 2015) and DNT (Magnusson 2009). These qualitative experimental results show that the proposed CGR method performs well on all five challenging datasets, thus demonstrating the feasibility and repeatability of CGR for various scenes.

## Evaluation

### Registration Accuracy

Table 2 shows the details of the accuracy performances of CGR in the experiments in terms of the rotation error, translation error, and point RMS error. All scans are obtained from an arbitrary position. Because the goal of coarse registration is to determine an initial value from which to implement fine registration, the thresholds to judge SR should consider whether the results of a coarse registration are sufficient to carry out fine registration. Taking into account the large scanning scales, we set  $\sigma_1 = 10^\circ$  and  $\sigma_2 = 4$  m in our experiments. We should point out that  $\sigma_2$  in the office room dataset is 1 m because the scene is relatively small. We carried out an ICP strategy (Low 2004) with the worst cases in each dataset (i.e., with a rotation error of  $10^\circ$  and a translation error of 4 m to test the validity of the thresholds). The results demonstrate that the thresholds are valid, with rotation error of less than  $0.1^\circ$  and translation error of less than 0.1 m, which can meet the requirements of object extraction and 3D reconstruction. To obtain statistical properties from the experimental results, we implemented CGR 500 times in each dataset. Table 2 shows that CGR performs well in registering point clouds from varying scenes in terms of registration

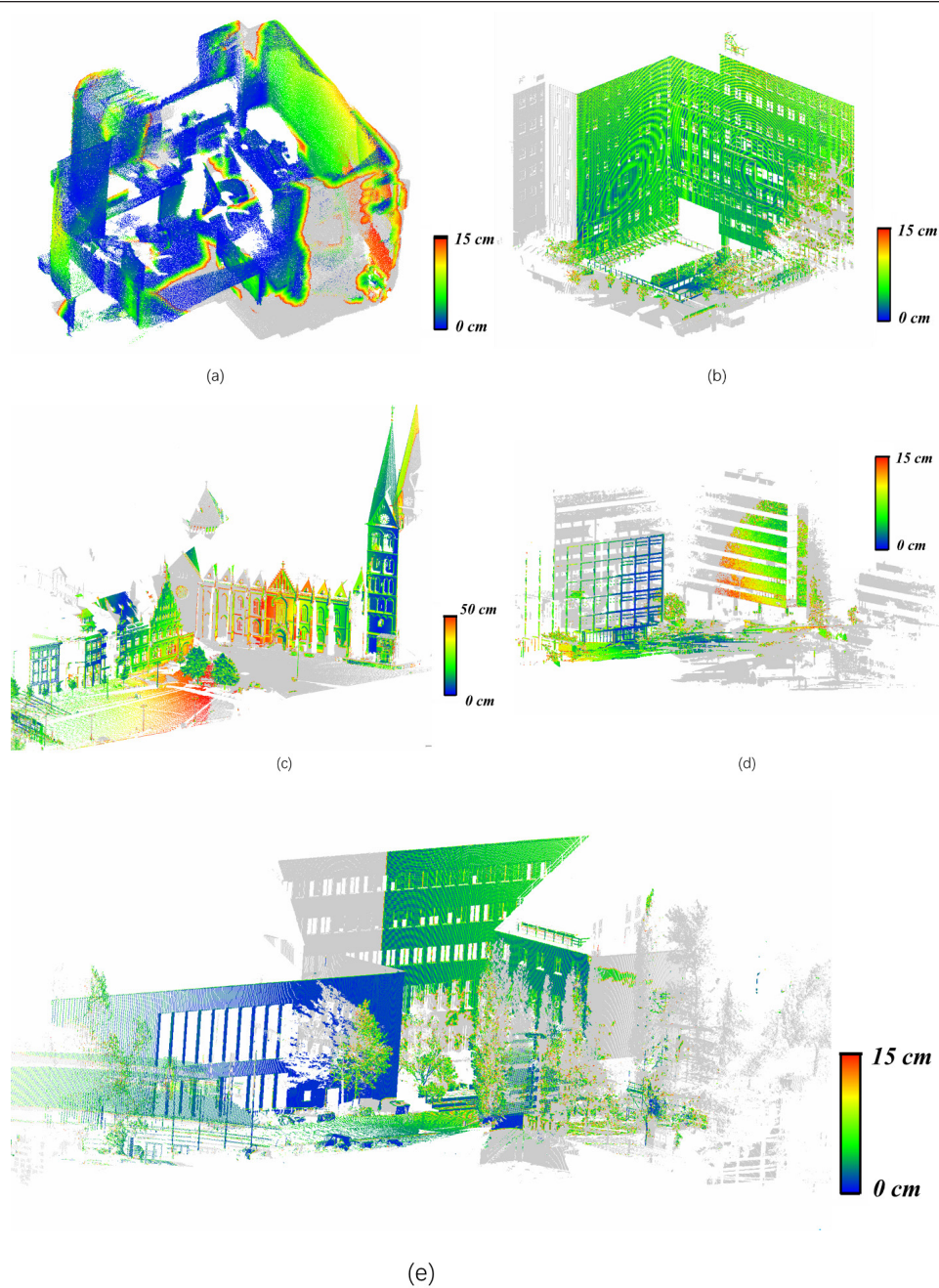


Figure 9. The registration results of CGR colored by the clouds-to-clouds distances in the overlapping regions, where the gray points represent the nonoverlap areas. (a) Office room; (b) Multilevel terrace; (c) Bremen downtown; (d) PolyU campus; (e) TUM campus.

Table 2. Quantitative evaluation of the registration accuracy.

Dataset	Rotation Error (deg)				Translation Error (cm)				Point RMS Error (cm)			
	Max.	Min.	Ave.	RMSE	Max.	Min.	Ave.	RMSE	Max.	Min.	Ave.	RMSE
Office room	9.581	0.002	3.622	3.561	85.5	0.9	26.8	18.8	14.2	0.4	4.0	3.5
TUM campus	3.142	0.001	1.243	1.121	173.1	0.3	32.8	35.6	26.9	0.7	7.4	5.7
Bremen downtown	9.436	0.000	1.010	1.090	459.4	3.7	87.8	88.6	631.7	24.8	92.2	73.8
PolyU campus	10.917	0.108	1.569	1.406	474.1	2.3	111.8	129.5	156.0	2.642	36.3	27.8
Multilevel terrace 1–2	8.606	0.040	2.141	1.560	358.1	1.8	80.7	80.6	220.4	1.9	33.6	32.5
Multilevel terrace 2–3	9.878	0.150	3.330	3.102	367.1	2.1	85.2	85.3	222.1	2.2	35.2	33.4

accuracy. CGR showed only undesirable results in the PolyU campus dataset with an SR rate of 60.4%. One interpretation is that the overlap rate is only 19% in this dataset. This is an extremely low overlap rate for the target-less registration case. Taking into account the size of the scene, the rotation error in the office room dataset is relatively large because of the data distortion resulting from the RGB-D sensor.

Table 4 compares the performances of CGR and the state-of-art benchmark methods in terms of the registration accuracy, computational costs, and SR rate, and Table 5 shows the corresponding improvements in the CGR. We use the corresponding average values in each item of Table 4, and only the SR results contribute to the corresponding average values. To make quantitative comparisons, we set  $\sigma_3 = 600$  s in all experiments. One should first note that we always implemented those methods with good parameter setting. Tables 4 and 5 show that only in the translation error item can K4PCS and DNT perform better

than CGR in the office room dataset and in the multilevel terrace 1–2 dataset, respectively. In other cases, CGR significantly outperforms the other methods. K4PCS can obtain relatively stable results if the calculation is not out of time and does not converge to a local minimal. SAC-IA relies directly on the

Table 3. Time and SR rate performance of the presented method.

Dataset	Runtime (second)			SR Rate %
	Max.	Min.	Ave.	
Office room	21	2	7	100
TUM campus	60	24	30	100
Bremen downtown	405	38	102	99.2
PolyU campus	407	62	221	60.4
Multilevel terrace 1–2	117	4	17	100
Multilevel terrace 2–3	>600	5	20	98.4

Table 4. Performance comparison.

Dataset	Method	Rotation Error (deg)	Translation Error (cm)	Point RMS Error (cm)	Runtime (second)	SR Rate %
Office room	<b>CGR</b>	<b>3.622</b>	26.8	<b>4.0</b>	7	<b>100</b>
	<b>K4PCS</b> (Theiler <i>et al.</i> 2014)	5.922	<b>14.7</b>	11.4	<b>4</b>	45.4
	<b>SAC-IA</b> (Holz <i>et al.</i> 2015)	7.068	70.9	34.9	324	25
	<b>DNT</b> (Magnusson 2009)	4.683	27.3	32.6	111	/
TUM campus	<b>CGR</b>	<b>1.243</b>	<b>32.8</b>	<b>7.4</b>	<b>30</b>	<b>100</b>
	<b>K4PCS</b> (Theiler <i>et al.</i> 2014)	3.317	158	99.5	55	94
	<b>SAC-IA</b> (Holz <i>et al.</i> 2015)	7.354	281.8	171.1	410	11
	<b>DNT</b> (Magnusson 2009)	fail	fail	fail	fail	/
Bremen downtown	<b>CGR</b>	<b>0.910</b>	<b>82.6</b>	<b>90.5</b>	<b>76</b>	<b>99.2</b>
	<b>K4PCS</b> (Theiler <i>et al.</i> 2014)	3.695	241	215.6	303	31.3
	<b>SAC-IA</b> (Holz <i>et al.</i> 2015)	5.014	307	336.9	249	3
	<b>DNT</b> (Magnusson 2009)	fail	fail	fail	fail	/
PolyU campus	<b>CGR</b>	<b>1.462</b>	<b>82.7</b>	<b>35.4</b>	<b>212</b>	<b>60.4</b>
	<b>K4PCS</b> (Theiler <i>et al.</i> 2014)	fail	fail	fail	fail	/
	<b>SAC-IA</b> (Holz <i>et al.</i> 2015)	fail	fail	fail	fail	/
	<b>DNT</b> (Magnusson 2009)	fail	fail	fail	fail	/
Multilevel terrace 1–2	<b>CGR</b>	<b>2.141</b>	<b>80.7</b>	<b>33.6</b>	<b>17</b>	<b>100</b>
	<b>K4PCS</b> (Theiler <i>et al.</i> 2014)	2.627	135.4	63.8	20	88
	<b>SAC-IA</b> (Holz <i>et al.</i> 2015)	5.776	248.7	91.1	90	12
	<b>DNT</b> (Magnusson 2009)	2.564	<b>78.4</b>	<b>46.6</b>	96	/
Multilevel terrace 2–3	<b>CGR</b>	<b>2.630</b>	<b>85.2</b>	<b>35.2</b>	<b>98</b>	<b>98.4</b>
	<b>K4PCS</b> (Theiler <i>et al.</i> 2014)	4.660	198.5	91.5	581	32
	<b>SAC-IA</b> (Holz <i>et al.</i> 2015)	fail	fail	fail	fail	/
	<b>DNT</b> (Magnusson 2009)	fail	fail	fail	fail	/

Table 5. Improvements of CGR.

Percent	Office Room	TUM Campus	Bremen Downtown	PolyU Campus	Multilevel Terrace 1–2	Multilevel Terrace 2–3
<b>K4PCS</b>						
Rotation error (deg)	38.8	62.5	75.4	/	18.5	43.6
Translation error (cm)	-82.3	79.2	65.7	/	40.4	57.1
Point RMS error (cm)	64.9	92.6	58.0	/	47.3	61.5
Runtime (second)	-75.0	45.5	74.9	/	15.0	83.1
SR rate %	54.6	6.0	68.2	/	12.0	66.4
<b>SAC-IA</b>						
Rotation error (deg)	48.8	83.1	81.9	/	62.9	/
Translation error (cm)	62.2	88.4	73.1	/	67.6	/
Point RMS error (cm)	88.5	95.7	73.1	/	63.1	/
Runtime (second)	97.8	92.7	69.5	/	81.1	/
SR rate %	75.0	89	96.2	/	88	/
<b>DNT</b>						
Rotation error (deg)	22.7	/	/	/	16.5	/
Translation error (cm)	1.8	/	/	/	-2.9	/
Point RMS error (cm)	87.7	/	/	/	27.9	/
Runtime (second)	93.7	/	/	/	82.3	/
SR rate %	/	/	/	/	/	/

quality of the results of PPFH, so the registration accuracy is poor if the scanning scene is complex. In our tests, DNT is not a qualified option to address the registration cases if the initial position and attitude show great differences.

**Computational Efficiency**

Table 3 lists the details of the computational costs and SR rates of CGR in our experiments. Generally, CGR shows the best performances in terms of the CPU runtimes and SR rates. Only 1.6% of tests in multilevel terrace 2–3 exceed the runtime threshold. CGR achieves a 100% SR rate in the office room, the TUM campus datasets, and multilevel terrace 1–2; moreover, those tests can be completed in 2 min. For the Bremen downtown dataset, up to 96% of tests can be finished within 4 min., and the SR rate is 99.2%. The loss of 0.8% in the SR rate is due to the translation accuracy. CGR gives a relatively poor outcome in the PolyU campus dataset. It is approximately 95% complete at 6 min. and only about 60% complete at 4 min. because of the poor overlap rate; more efforts should be made in the RANSAC iterations. One of the main attributes support CGR has such good performances in terms of computational efficiency is that the voting-based extraction and the novel iterative framework can effectively reduce the problem size. Figure 10 shows the average number of key-points that were extracted by different methods. Remarkably, the number of key-points in CGR decies exponentially when compared with that be obtained from Harris 3D and SIFT 3D.

Tables 4 and 5 show that CGR has significant advantages over the benchmark methods in terms of the computational cost and the SR rate. Figures 11 and 12 show the comparisons of CGR and the benchmark methods in terms of the runtimes and SR rate. CGR gives the best performances in the SR rate, see Figure 12. Specifically, it can achieve more than 98% SR rate in most cases. For the case with poorly overlapping regions (i.e., the PolyU campus dataset), although CGR arrives at SR

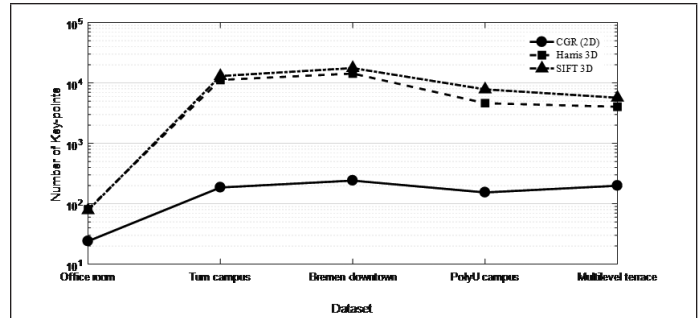


Figure 10. The comparison of the number of key-points by different methods i.e., CGR, Harris 3D, and SIFT 3D, in all tested datasets.

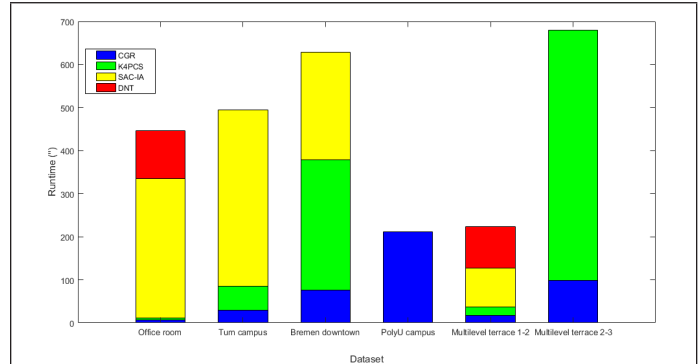


Figure 11. The comparison of the runtime of different methods in all tested datasets. In each dataset, the missing color bar represents the corresponding method cannot achieve convergence, e.g., DNT cannot register Tum Campus dataset.

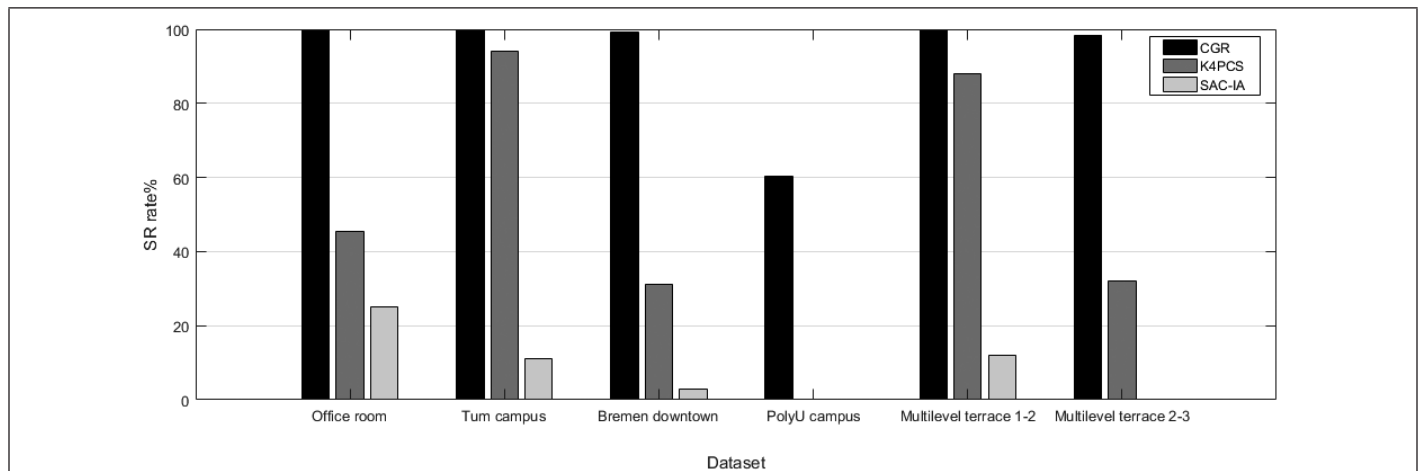


Figure 12. The comparison of the SR rates in all tested datasets.

Table 6. Strategies and their key parameters.

Method	Represent Scene	Feature Descriptor	Key Parameters
CGR	Cross sections	Geometric and contextual	The overlap rate The number of points in the many-to-one projection
K4PCS	Harris 3D	Geometric	The window size for Harris 3D The overlap rate
SAC-IA	SIFT	FPFH	The window size for SIFT The radii for FPFH The convergent threshold
DNT	Voxel grid	Normal distribution	The resolution of the voxel grid The step of More-Thuente The initial values The convergent threshold

rates of only 60.4%, neither K4PCS nor SAC-IA can arrive at an acceptable convergence within 600 s. Figure 11 displays the comparison of the runtime by different methods. We can see that CGR is faster than the other three methods in most cases. We can interpret those performances (i.e., the computational cost and the SR rate) of CGR that the problem size is reduced exponentially by the proposed strategies and the repetition rate of extracted key-points are increased in different point clouds by rich geometric and contextual information.

#### Parameter Setting

Parameter setting is a key step in all coarse registration strategies. The quality of the parameter setting directly affects the performance of a registration algorithm. Table 6 shows the various strategies in the tested methods and their corresponding core parameters in the experiments. We define the core parameters as they relate to various scenes and investigate the parameters in CGR.

In most cases, the parameter setting depends on the scanning scene and the registration accuracy. An overly strict parameter setting scheme, however, will significantly reduce a method's generalization. CGR, therefore, implements a relaxed parameter-setting strategy. Table 6 shows that the overlap rate is a key factor in CGR and K4PCS because it directly affects the search scope and the validation, but it is obvious that we cannot obtain the real overlap rate before registering the adjacent point clouds. Thus, we give an approximate value for this factor. Based on the accumulated experience (Aiger *et al.* 2008; Mellado *et al.* 2014; Theiler *et al.* 2014; Ge 2017), it is reasonable to set this factor to be smaller than the real overlap rate of the adjacent scans. The number of points in the many-to-one projection, discussed in the section "Transformation and Optimization", is important in CGR. This factor can further reduce the number of key-points that relate to the continuity of the surface. From our tests, we suggest setting this factor between 2 and 5 depending on the scanning scene. It is not reasonable to set an overly large factor because it will lead to a dramatic loss of important key-points.

Other parameters should be predefined, including the step of cross sections and the angular threshold for the designed voting-based strategy. Fortunately, there is no need to set those parameters individually in CGR. Reasonable fixed values (e.g., 20° for the voting-based strategy) should be set for those parameters to implement CGR in most urbane cases because CGR is not sensitive to those parameters. The parameter for penalization can be selected between 0.25 and 0.75 based on the local point density. From the tests we know that no obvious change in either the registration accuracy or the computation cost when the value of  $\alpha$  is increased from 0.25 to 0.75 in CGR if the handling point clouds with relatively uniform point density.

## Conclusions and Discussion

We have described a complete framework for registration of pairwise point clouds into a common coordinate system. First, CGR exploits several cross sections to quickly represent the entire scanning scene and then uses the designed voting-based strategy to extract key-points. CGR implements a novel three-step optimal strategy to register adjacent point clouds using the correspondences. In addition to the traditional geometric information used to support the correspondences, the proposed method also exploits novel extended geometric information and reasonable contextual knowledge to purify the correspondences in the proposed method. What is more, a penalization strategy is introduced into CGR to weight various correspondences to improve the registration accuracy and accelerate the calculations.

Comprehensive experiments were carried out to evaluate the capabilities of CGR. The test results show that CGR

performs favorably in terms of the registration accuracy and computational cost in handling various scenes. The comparisons show that CGR performs photogrammetry registration significantly better than the state-of-art baseline methods. CGR can achieve SR rates of nearly 100% in most cases. Although CGR only achieved an SR rate of about 60% in the PolyU campus dataset because of the extremely small overlap regions, it also gave the best performance of all tested methods. CGR carries out a relaxed parameter-setting strategy that allows good generalization. Based on the potentials of CGR, we can implement it on the 3D reconstruction and Simultaneous Localization and Mapping (SLAM).

However, CGR is insufficient in cases with very small overlap regions; therefore, one of the next tasks is to improve the potential of CGR to address those cases, to further investigate and implement CGR in multiview registration, and to handle data from different sensors to register point clouds from airborne LS and TLS.

## Acknowledgments

This work was supported by grants from the Hong Kong Polytechnic University (Project Nos. 1-ZE24, 1-ZEAB, and 1-ZVN6) and a grant from the National Natural Science Foundation of China (Project No: 41471345).

## References

- Aiger, D., N. J. Mitra and D. Cohen-Or. 2008. 4-points congruent sets for robust pairwise surface registration. *Proceedings ACM Transactions on Graphics (TOG)* :85.
- Besl, P. J. and N. D. McKay. 1992. Method for registration of 3-D shapes. Pages 586–607 in *Proceedings Sensor Fusion IV: Control Paradigms and Data Structures, International Society for Optics and Photonics*.
- Bolles, R. C. and M. A. Fischler. 1981. A RANSAC-based approach to model fitting and its application to finding cylinders in range data. Pages 637–643 in *Proceedings IJCAI*.
- Borrmann, D., J. Elseberg and A. Nüchter. 2013. Thermal 3D mapping of building façades. In *Intelligent Autonomous Systems 12*, 173–182. Springer.
- Chum, O., J. Matas and J. Kittler. 2003. Locally optimized RANSAC. Pages 236–243 in *Proceedings Joint Pattern Recognition Symposium*. Springer.
- Dold, C. and C. Brenner. 2006. Registration of terrestrial laser scanning data using planar patches and image data. *International Archives of Photogrammetry, Remote Sensing and Spatial Information Sciences* 36 (5): 78–83.
- Dong, Z., B. Yang, F. Liang, R. Huang and S. Scherer. 2018. Hierarchical registration of unordered TLS point clouds based on binary shape context descriptor. *ISPRS Journal of Photogrammetry and Remote Sensing* 144: 61–79.
- Dong, Z., B. Yang, Y. Liu, F. Liang, B. Li and Y. Zang. 2017. A novel binary shape context for 3D local surface description. *ISPRS Journal of Photogrammetry and Remote Sensing* 130: 431–452.
- Drost, B., M. Ulrich, N. Navab and S. Ilic. 2010. Model globally, match locally: Efficient and robust 3D object recognition. Pages 998–1005 in *Proceedings 2010 IEEE Conference Computer Vision and Pattern Recognition (CVPR)*.
- Frome, A., D. Huber, R. Kolluri, T. Bülow and J. Malik. 2004. Recognizing objects in range data using regional point descriptors. Pages 224–237 in *Proceedings European Conference on Computer Vision*. Springer.
- Ge, X. 2017. Automatic markerless registration of point clouds with semantic-keypoint-based 4-points congruent sets. *ISPRS Journal of Photogrammetry and Remote Sensing* 130: 344–357.
- Ge, X. and T. Wunderlich. 2016. Surface-based matching of 3D point clouds with variable coordinates in source and target system. *ISPRS Journal of Photogrammetry and Remote Sensing* 111: 1–12.

- Gruen, A. and D. Akca. 2005. Least squares 3D surface and curve matching. *ISPRS Journal of Photogrammetry and Remote Sensing* 59 (3): 151–174.
- Guo, Y., F. Sohel, M. Bennamoun, J. Wan and M. Lu. 2014. An accurate and robust range image registration algorithm for 3D object modeling. *IEEE Transactions on Multimedia* 16 (5): 1377–1390.
- Hansen, P. C., V. Pereyra and G. Scherer. 2013. Least squares data fitting with applications. *JHU Press*.
- Holz, D., A. E. Ichim, F. Tombari, R. B. Rusu and S. Behnke. 2015. Registration with the point cloud library: A modular framework for aligning in 3-D. *IEEE Robotics & Automation Magazine* 22 (4): 110–124.
- Ioannou, Y., B. Taati, R. Harrap and M. Greenspan. 2012. Difference of normals as a multi-scale operator in unorganized point clouds. Pages 501–508 in *Proceedings 2012 IEEE Second International Conference on 3D Imaging, Modeling, Processing, Visualization and Transmission (3DIMPVT)*.
- Knopp, J., M. Prasad, G. Willems, R. Timofte and L. Van Gool. 2010. Hough transform and 3D SURF for robust three dimensional classification. Pages 589–602 in *Proceedings European Conference on Computer Vision*. Springer.
- Lo, T. R. and J. P. Siebert. 2009. Local feature extraction and matching on range images: 2.5 D SIFT. *Computer Vision and Image Understanding* 113 (12): 1235–1250.
- Low, K. 2004. Linear least-squares optimization for point-to-plane ICP surface registration. *Chapel Hill, University of North Carolina* 4 (10).
- Lichti, D. D. 2007. Error modelling, calibration and analysis of an AM-CW terrestrial laser scanner system. *ISPRS Journal of Photogrammetry and Remote Sensing* 61: 307–324.
- Magnusson, M. 2009. The three-dimensional normal-distributions transform: an efficient representation for registration, surface analysis, and loop detection. *Örebro Universitet*.
- Mellado, N., D. Aiger and N. J. Mitra. 2014. Super 4pcs fast global point cloud registration via smart indexing. Pages 205–215 in *Proceedings Computer Graphics Forum*. Wiley Online Library.
- Mohamad, M., M. T. Ahmed, D. Rappaport and M. Greenspan. 2015. Super generalized 4pcs for 3d registration. Pages 598–606 in *Proceedings IEEE 2015 International Conference on 3D Vision (3DV)*.
- Niemeyer, J., F. Rottensteiner, U. Sörgel and C. Heipke. 2016. Hierarchical higher order CRF for the classification of airborne lidar point clouds in urban areas. *The International Archives of Photogrammetry, Remote Sensing and Spatial Information Sciences* 41: 655.
- Rusu, R. B., N. Blodow and M. Beetz. 2009. Fast point feature histograms (FPFH) for 3D registration. Pages 3212–3217 in *IEEE 2009 International Conference on Proceedings Robotics and Automation (ICRA'09)*. Citeseer.
- Rusu, R. B. and S. Cousins. 2011. 3d is here: Point cloud library (PCL). Pages 1–4 in *2011 IEEE International Conference on Proceedings Robotics and Automation (ICRA)* Salvi, J., C. Matabosch, D. Fofi and J. Forest. 2007. A review of recent range image registration methods with accuracy evaluation. *Image and Vision Computing* 25 (5): 578–596.
- Schnabel, R., R. Wahl and R. Klein. 2007. Efficient RANSAC for point cloud shape detection. Pages 214–226 in *Proceedings Computer Graphics Forum*. Wiley Online Library.
- Sipiran, I. and B. Bustos. 2011. Harris 3D: A robust extension of the Harris operator for interest point detection on 3D meshes. *Visual Computer* 27 (11): 963.
- Stamos, I. and M. Leordeanu. 2003. Automated feature-based range registration of urban scenes of large scale. Pages 555–561 in *Proceedings CVPR (2)*.
- Tam, G. K., Z. Cheng, Y. Lai, F. C. Langbein, Y. Liu, D. Marshall, R. R. Martin, X. Sun and P. L. Rosin. 2013. Registration of 3D point clouds and meshes: A survey from rigid to nonrigid. *IEEE Transactions on Visualization and Computer Graphics* 19 (7): 1199–1217.
- Theiler, P. W. and K. Schindler. 2012. Automatic registration of terrestrial laser scanner point clouds using natural planar surfaces. *ISPRS Annals of Photogrammetry, Remote Sensing and Spatial Information Sciences* 3: 173–178.
- Theiler, P. W., J. D. Wegner and K. Schindler. 2014. Keypoint-based 4-points congruent sets—Automated marker-less registration of laser scans. *ISPRS Journal of Photogrammetry and Remote Sensing* 96: 149–163.
- Theiler, P. W., J. D. Wegner and K. Schindler. 2015. Globally consistent registration of terrestrial laser scans via graph optimization. *ISPRS Journal of Photogrammetry and Remote Sensing* 109: 126–138.
- Vosselman, G., M. Coenen and F. Rottensteiner. 2017. Contextual segment-based classification of airborne laser scanner data. *ISPRS Journal of Photogrammetry and Remote Sensing* 128: 354–371.
- Xu, Y., R. Boerner, W. Yao, L. Hoegner and U. Stilla. 2017. Automated coarse registration of point clouds in 3d urban scenes using voxel based plane constraint. *ISPRS Annals of the Photogrammetry, Remote Sensing and Spatial Information Sciences* 4: 185.
- Yang, B., Z. Dong, F. Liang and Y. Liu. 2016. Automatic registration of large-scale urban scene point clouds based on semantic feature points. *ISPRS Journal of Photogrammetry and Remote Sensing* 113: 43–58.
- Yang, J., H. Li, D. Campbell and Y. Jia. 2016. Go-ICP: A globally optimal solution to 3D ICP point-set registration. *arXiv preprint arXiv:1605.03344*.
- Yang, J., H. Li and Y. Jia. 2013. Go-ICP: Solving 3d registration efficiently and globally optimally. Pages 1457–1464 in *Proceedings IEEE International Conference on Computer Vision*.
- Zai, D., J. Li, Y. Guo, M. Cheng, P. Huang, X. Cao and C. Wang. 2017. Pairwise registration of TLS point clouds using covariance descriptors and a non-cooperative game. *ISPRS Journal of Photogrammetry and Remote Sensing* 134: 15–29.
- Zhong, Y. 2009. Intrinsic shape signatures: A shape descriptor for 3d object recognition. Pages 689–696 in *Proceedings 2009 IEEE 12th International Conference Computer Vision Workshops (ICCV Workshops)*.
- Zhou, Q., J. Park and V. Koltun. 2016. Fast global registration. Pages 766–782 in *Proceedings European Conference on Computer Vision*. Springer.
- Zhu, Q., Y. Li, H. Hu and B. Wu. 2017. Robust point cloud classification based on multi-level semantic relationships for urban scenes. *ISPRS Journal of Photogrammetry and Remote Sensing* 129: 86–102.

# SUSTAINING MEMBERS

**ACI USA Inc.**

Weston, Florida  
acicorporation.com  
Member Since: 1/2018

**Airbus Defense and Space**

Chantilly, Virginia  
www.intelligence-airbusds.com  
Member Since: 6/2016

**Axis GeoSpatial, LLC**

Easton, Maryland  
www.axisgeospatial.com  
Member Since: 10/2002

**Ayres Associates, Inc.**

Madison, Wisconsin  
www.AyresAssociates.com  
Member Since: 1/1953

**Bohannon Huston, Inc.**

Albuquerque, New Mexico  
www.bhinc.com  
Member Since: 11/1992

**CompassData, Inc.**

Centennial, Colorado  
www.compassdatainc.com  
Member Since: 1/2012

**DAT/EM Systems International**

Anchorage, Alaska  
www.datem.com  
Member Since: 1/1974

**Dewberry**

Fairfax, Virginia  
www.dewberry.com  
Member Since: 1/1985

**DigitalGlobe, Inc.**

Longmont, Colorado  
www.digitalglobe.com  
Member Since: 6/1996

**Environmental Research Incorporated**

Linden, Virginia  
www.eri.us.com  
Member Since: 8/2008

**Esri**

Redlands, California  
www.esri.com  
Member Since: 1/1987

**Extensis**

Seattle, Washington  
www.extensis.com  
Member Since: 1/1997

**GeoBC**

Victoria, Canada  
www.geobc.gov.bc.ca  
Member Since: 12/2008

**GeoCue Group**

Madison, Alabama  
info@geocue.com  
Member Since: 10/2003

**GeoJano**

Pleasanton, California  
https://geojango.com/  
Member Since: 05/2019

**Geomni, Inc.**

Lehi, Utah  
Geomni.net/psm  
Member Since: 03/2018

**Global Science & Technology, Inc.**

Greenbelt, Maryland  
www.gst.com  
Member Since: 10/2010

**GPI Geospatial Inc.**

formerly Aerial Cartographics of America, Inc.  
(ACA)  
Orlando, Florida  
www.aca-net.com  
Member Since: 10/1994

**Harris Corporation**

Broomfield, Colorado  
www.harris.com  
Member Since: 6/2008

**Keystone Aerial Surveys, Inc.**

Philadelphia, Pennsylvania  
www.keystoneaerialsurveys.com  
Member Since: 1/1985

**Kucera International**

Willoughby, Ohio  
www.kucerainternational.com  
Member Since: 1/1992

**Lead'Air, Inc.**

Kissimmee, Florida  
www.trackair.com  
Member Since: 5/2001

**MDA Information Systems LLC**

Gaithersburg, Maryland  
www.mdas.com  
Member Since: 1/1983

**Merrick & Company**

Greenwood Village, Colorado  
www.merrick.com/gis  
Member Since: 4/1995

**Observera, Inc.**

Chantilly, Virginia  
www.observera.com  
Member Since: 8/2002

**PCI Geomatics**

Richmond Hill, Ontario, Canada  
www.pcigeomatics.com  
Member Since: 1/1989

**Pickett and Associates, Inc.**

Bartow, Florida  
www.pickettusa.com  
Member Since: 4/2007

**PixElement**

Columbus, Ohio  
www.pixelement.com  
Member Since: 1/2017

**Quantum Spatial, Inc.**

Sheboygan Falls, Wisconsin  
www.quantumspatial.com  
Member Since 1/1974

**Riegl USA, Inc.**

Orlando, Florida  
www.rieglusa.com  
Member Since: 11/2004

**Robinson Aerial Survey, Inc. (RAS)**

Hackettstown, New Jersey  
www.robinsonaerial.com  
Member Since: 1/1954

**Routescene, Inc.**

Durango, Colorado  
www.routescene.com/  
Member Since: 12/2007

**Sanborn Map Company**

Colorado Springs, Colorado  
www.sanborn.com  
Member Since: 10/1984

**Teledyne Optech**

Toronto, Canada  
www.teledyneoptech.com  
Member Since: 1/1999

**Terra Remote Sensing (USA) Inc.**

Bellevue, Washington  
www.terrareMOTE.com  
Member Since: 10/2016

**The Airborne Sensing Corporation**

Toronto, Canada  
www.airsensing.com  
Member Since: 7/2003

**Towill, Inc.**

San Francisco, California  
www.towill.com  
Member Since: 1/1952

**University of Twente/Faculty ITC**

Enschede, Netherlands  
www.itc.nl  
Member Since: 1/1992

**U.S. Geological Survey**

Reston, Virginia  
www.usgs.gov  
Member Since: 4/2002

**Woolpert LLP**

Dayton, Ohio  
www.woolpert.com  
Member Since: 1/1985

# Pavement Marking Retroreflectivity Estimation and Evaluation using Mobile Lidar Data

Erzhuo Che, Michael J. Olsen, Christopher E. Parrish, and Jaehoon Jung

## Abstract

*Pavement markings are produced with retroreflective materials to enhance visibility for motorists, particularly at night. Retroreflectivity evaluation throughout an extensive highway network for maintenance and asset management purposes is a critical, yet challenging task for transportation agencies because visual evaluation can often be subjective and inconsistent, while field measurement can be time-consuming. Mobile Light Detection and Ranging (Lidar) datasets can potentially provide a safe, cost-effective, and reliable method of performing the required evaluation. This paper presents an empirical model for radiometric calibration of Lidar intensity information from the Leica Pegasus:Two system for pavement marking evaluation. The model was developed using dense handheld retroreflector measurements and mobile Lidar data collected in a variety of geometric configurations on a test site consisting of various markings with varying degrees of wear. The quantitative accuracy assessment of the proposed radiometric calibration model for estimating retroreflectivity was conducted to another independent dataset collected in different lanes and system configurations.*

## Introduction

### Retroreflectivity

Retroreflection plays an important role in increasing nighttime visibility of pavement markings and traffic signs. Specifically, when signs and pavement markings are designed to reflect light from a vehicle's headlights back to the driver, this increases the distances from which the pavement markings and signs can be seen at night and improves clarity (Austin and Schultz 2009). Statistics showing significantly higher fatal crash rates at nighttime, as compared with daytime, are frequently cited as an indication of the importance of retroreflectivity (Carlson and Picha 2009). In the case of pavement marking materials, retroreflectivity is typically achieved through the use of glass beads or microspheres embedded in the paint (Austin and Schultz 2002). Other types of marking materials include waterborne paint, epoxy, polyester, thermoplastic, and tape (Migletz *et al.* 1999). Advanced types of pavement marking materials have been shown to enable savings in pavement marking budgets in various transportation agencies (Saetern 2016).

Unfortunately, the retroreflectivity of traffic control devices degrades over time, as a function of traffic, weather, orientation, and precipitation, among other variables (Kirk *et al.* 2001; Migletz *et al.* 1999). It is for this reason that policies and procedures are in place to assist transportation agencies with the assessment and maintenance of retroreflective markings over time (e.g., the Manual for Uniform Traffic Control Devices, or

MUTCD). Degraded retroreflectivity can adversely affect safety, while premature replacement of signs and pavement markings can unnecessarily increase costs (Austin and Schultz 2002); hence, effective inspection, asset management, and maintenance procedures are critical to transportation agencies.

Current inspection methodologies currently fall into two general types: 1) a visual nighttime inspection using human inspectors and 2) quantitative measurements made with retroreflectometers (Figure 1). While both methods are effective for evaluating the retroreflectance of the signs and pavement markings, there are some challenges concerned in practice. For a visual nighttime inspection method, the result requires an individual to judge the retroreflectivity condition qualitatively, which can be subjective and lack consistency. A retroreflectometer can be used for acquiring an accurate measurement on a pavement marking or sign enabling a quantitative and consistent evaluation. However, it is difficult and costly to achieve a sufficient frequency of data acquisition because it is usually time intensive, resulting in sparse measurements. Furthermore, both methods have associated safety considerations, due to nighttime driving or roadside work. Mobile retroreflectometers mounted to the side of a vehicle provide an alternative to more safely collect the retroreflectivity data, but still pose safety hazards as the retroreflectometer intrudes slightly into the adjacent lane and generally only one line is evaluated at a time. Because of these concerns, as an alternative to retroreflectivity measurements, some transportation agencies have policies of blanket replacement on a set schedule, but the disadvantage is wasted cost of unnecessary replacement.



Figure 1. Handheld retroreflectometer being used to measure retroreflectivity of pavement markings on the Oregon Department of Transportation (ODOT) Pavement Marking Testdeck.

Erzhuo Che, Michael J. Olsen, Christopher E. Parrish, and Jaehoon Jung are with School of Civil and Construction Engineering at Oregon State University.

Photogrammetric Engineering & Remote Sensing  
Vol. 85, No. 8, August 2019, pp. 573–583.  
0099-1112/19/573–583

© 2019 American Society for Photogrammetry  
and Remote Sensing  
doi: 10.14358/PERS.85.8.573

## Mobile Lidar Radiometric Calibration

Mobile Lidar (also called Mobile Laser Scanning or MLS) systems can acquire detailed three-dimensional data efficiently from a moving vehicle at highway speeds with traffic. Mobile Lidar provides several benefits and, as a result, is being widely adopted by Departments of Transportation (DOTs) across the country (Olsen *et al.* 2013). One of the key benefits of Lidar is the fact that the same Lidar dataset can be used by multiple groups for a wide variety of applications, minimizing the need for multiple data collection efforts. As a result, MLS has become a key technology to support transportation asset management programs. Additionally, one can remotely survey a site from safe locations, minimizing the danger to field crews and the travelling logistics. Mobile Lidar also enables a much more efficient and thorough field survey, minimizing the need for costly repeat visits to the site to collect information. Geo-referencing can be completed directly with the combination of components included on the scanner (e.g., Global Navigation Satellite System (GNSS)-aided inertial navigation systems); however, for the highest accuracy applications, survey control points are often established with real time kinematic or static GNSS.

Most Lidar systems provide an attribute called “intensity,” which accompanies each X, Y, Z Lidar point and serves as a measure of return signal strength. These intensity values are a measure of backscattered signal strength and contain information on surface characteristics, including reflectance. However, the raw intensity values are generally provided as uncalibrated digital numbers. In addition to surface reflectance at the laser wavelength, they are also a function of several other variables related to the environment, system and acquisition parameters (e.g., Höfle and Pfeifer 2007; Jutzi and Gross 2009; Kaasalainen *et al.* 2009; Vain *et al.* 2009; Wagner *et al.* 2008). Examples of these variables include laser range, incidence angle, receiver aperture, system transmittance, atmospheric transmittance, beam divergence, and transmitted laser power.

A great number of Lidar intensity correction and radiometric calibration procedures have been developed with the goal of removing the effects of these environmental and system variables to provide values that better represent surface reflectance. (As a side note on terminology, while some authors draw a distinction between reflectance and reflectivity based on surface type, the terms are used interchangeably here.) Depending on the level and type of correction, the output may be referred to calibrated intensity, pseudoreflectance, relative-reflectance, reflectance factor, or true surface reflectance. Kashani *et al.* (2015) provide a comprehensive overview of different types of radiometric calibration and correction routines, which classifies radiometric processing strategies into: 1) theoretical or model-driven approaches and 2) empirical approaches. Those in the first category generally involve inverting the laser range equation to obtain surface reflectance as a function of (known, modeled, or assumed) system, acquisition, and environmental variables. Although many different forms of the laser range equation have been published (e.g., Baltsavias 1999; Höfle and Pfeifer 2007; Jelalian 1980; Kaasalainen *et al.* 2011; Mallet and Bretar 2009; Wagner *et al.* 2008), a common form—under the assumption of a Lambertian, area target is:

$$P_r = \frac{P_t D_r^2 \eta_{atm} \eta_{sys} \rho}{4R^2} \cos \theta_i \quad (1)$$

where  $P_r$  = received optical power (watts),  $P_t$  = transmitted power (watts),  $D_r$  = receiver aperture diameter (meters),  $\eta_{atm}$  = atmospheric transmission factor (dimensionless),  $\eta_{sys}$  = system transmission factor (dimensionless),  $\rho$  = target reflectance at the laser wavelength (dimensionless),  $R$  = range (meters), and

$\theta_i$  = incidence angle. Empirical approaches are generally similar but rely to a greater extent on experimentally-estimated parameters, rather than mathematical models.

Because the transmitter and receiver in a Lidar system are collocated (or nearly so), Lidar intensity inherently measures something akin to retroreflectivity (i.e., the amount of laser light reflected *back in the direction of the source*). In fact, if Lidar intensity data can be appropriately corrected—using, as a basis, the methods presented in the work referenced here—they can provide good estimates of surface retroreflectivity. It is this observation that forms the theoretical basis for this work.

## Mobile Lidar Retroreflectivity Evaluation

### Traffic Signs

Several studies evaluate the geometric state of traffic signs (e.g., flatness, inclination) from Lidar data, which can be directly calculated after extracting the signs from the point cloud (Gonzalez-Jorge *et al.* 2013; Wen *et al.* 2016). However, few studies take advantage of intensity readings from mobile Lidar to assess the retroreflectivity condition of the traffic signs or pavement markings. In one example, (Ai and Tsai 2016) propose a method for automatic sign retroreflectivity condition evaluation using mobile Lidar data with a co-acquired video log. The traffic signs are first extracted from the linked video log such that normalized intensity values corrected by range and incidence angle can be extracted from the point cloud data. The median normalized intensity value of the extracted points is then compared against a threshold to determine if the sign meets specifications. The research shows an important advantage of using Lidar, which is an active sensing technique, in daytime. Several studies using the digital images to evaluate retroreflectivity of traffic signs draw divergent conclusions on their feasibility (e.g., Balali *et al.* 2015; Khalilikhah *et al.* 2015).

As part of a large study investigating a wide range of retroreflectivity evaluation techniques, Carlson *et al.* (2017) perform a preliminary investigation of retroreflectivity evaluation using a Velodyne HDL-32 Lidar sensor operated in static mode to capture various type of retroreflectivity sheeting materials on panels at a variety of orientations. (This scanner has been integrated into several different mobile Lidar units but is operated from a tripod for this study). Initial findings are that the sensor was not sensitive to the colors used for the materials but is somewhat sensitive to the optical design of the material. Using this system poor correlation ( $R^2 = 0.11$ ) is observed between the Lidar intensity and the retroreflectivity values. The authors then investigate the use of hyperspectral imaging technology to capture differences and find distinguishable differences; however, they note that a mobile hyperspectral imaging system does not exist, limiting its efficiency and effectiveness for retroreflectivity evaluation.

### Pavement Markings

While few studies have successfully utilized Lidar for retroreflectivity evaluation, many studies have utilized intensity information for pavement marking extraction and mapping. Most approaches extract the road surface first using local elevation, local intensity, planar feature detection, or detection of curbs while some approaches fuse the mobile Lidar data with other data sources such as video camera logs, airborne Lidar data, road network map, and so on (Guan *et al.* 2016). Once the road surface is extracted from the mobile Lidar data, the road markings can be further segmented based on high radiometric contrast (color and/or intensity) against road pavement through either a two-dimensional (2D) projection or a profile scanline. By projecting the data onto a 2D image, a binary image can be generated to extract the road markings by setting a threshold of intensity (Guo *et al.* 2015; Riveiro *et al.*

al. 2015; Smadja *et al.* 2010; Toth *et al.* 2008; Yang *et al.* 2012; Yang *et al.* 2017; Yao and Hu 2014).

However, in addition to the material, the range and incidence angle will also affect the intensity value from the Lidar data. For example, due to a larger range and incidence angle, the intensity of a point at the edge of the road is usually lower than one at the center. To solve this problem, normalizing the intensity value based on the range and incidence angle from the trajectory can be performed since the scan geometry is relatively consistent (Guan *et al.* 2015; Jaakkola *et al.* 2008; Vosselman 2009; Yan *et al.* 2016; Zhang *et al.* 2016).

### Limitation and Objectives

Given that mobile Lidar data are being routinely collected by many transportation agencies for asset management and other purposes, there is a great opportunity and value in simply utilizing the same information for pavement marking retroreflectivity evaluation without requiring additional sensors or vehicles such as a mobile retroreflectometer. However, although the feasibility of estimating retroreflectivity using Lidar data has been demonstrated for traffic signs, there are two major challenges to overcome for evaluating the pavement markings: (1) unlike traffic signs that can be rotated or repositioned in a test, there is much less flexibility to set up a field test to conduct radiometric calibration for pavement markings that captures a wide range of ranges and incidence angles—these geometric differences need to be completed by varying the sensor orientation; (2) retroreflective objects such as beads can vary substantially in pavement markings compared with consistent patterns used in traffic sign sheeting materials, especially given the highly variable wear from vehicles driving over the markings. These inconsistencies introduce substantial uncertainty in measuring the retroreflectivity.

To take advantage of utilizing the safe, efficient mobile Lidar technology for data acquisition and overcome the aforementioned challenges in retroreflectivity evaluation of pavement markings, the objectives of this manuscript are to:

1. Develop an empirical radiometric calibration model based on the mechanism of a handheld retroreflectometer to convert Lidar intensity to retroreflectivity.
2. Investigate different sampling strategies to relate the mobile Lidar point cloud intensity values to handheld retroreflectometer readings which capture a larger window.
3. Evaluate the accuracy, precision, and lane robustness of the proposed radiometric calibration model quantitatively.
4. Determine potential biases resulting from different system configurations.

To our knowledge, this is the first report in the literature of successful pavement marking retroreflectivity evaluation with mobile Lidar data.

The manuscript is organized as follows. First, we describe the radiometric calibration process, including a description of the field site, the data acquisition process, sampling strategies to relate the mobile Lidar point cloud data to the handheld retroreflectometer, and development of the empirical equation through least squares regression (section “Mobile Lidar Radiometric Calibration”). Next, we describe the validation test setup, data acquisition, comparative analysis, and evaluation in terms of precision and recall capabilities (section “Validation Experiment”). Lastly, overall conclusions, limitations, and future opportunities are discussed in the “Conclusions” section.

## Mobile Lidar Radiometric Calibration

### Test Site “Testdeck”

In order to develop a robust empirical model to calculate retroreflectivity from intensity values, we collected both mobile Lidar data and retroreflectivity data at the “ODOT Pavement Marking Testdeck” (Testdeck). Testdeck is a section of highway containing a number of transverse lines painted in different years with a wide range of materials and colors. Lines are painted transversely across the road so that they wear and degrade much quicker than most of the normal road markings such as longitudinal lines for a performance evaluation (Van Schalkwyk 2010). This site is ideal for developing a radiometric calibration for striping because the wear is highly variable (Figure 2) across the lines with the most significant wear occurring at the locations of the typical wheel paths for vehicles driving in the lane.

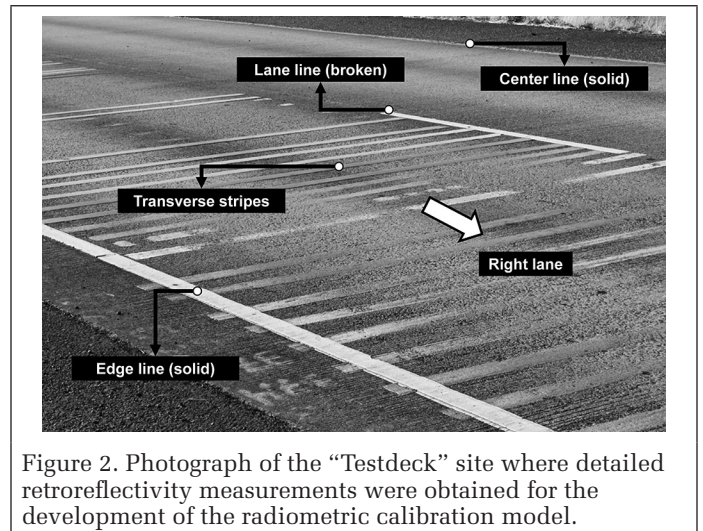


Figure 2. Photograph of the “Testdeck” site where detailed retroreflectivity measurements were obtained for the development of the radiometric calibration model.

Data were captured for a total of 24 lines at this site for the calibration (Table 1). Half of these were located on Asphalt Concrete (AC) and the other half on Portland Cement Concrete (PCC) pavement. These lines cover both yellow and white lines, as well as three common types of marking materials: Methyl Methacrylate (MMA), Thermoplastic (Thermo), and Preformed Thermoplastic (Preformed). For each line of interest, retroreflectometer measurements were sampled every 0.3 m (10–12 samples per line) in order to systematically capture the wide range of wear conditions across the line. To further improve the coverage of lines in different conditions, we repeated the survey of these lines approximately one year after the first acquisition.

Table 1. Summary of the transverse lines with detailed retroreflectivity measurements.

Line ID	Pavement	Color	Material
01–02	AC	Yellow	MMA
03–04	AC	White	MMA
05–06	AC	White	Thermo
07–08	AC	Yellow	Thermo
09–10	AC	White	Preformed
11–12	AC	Yellow	Preformed
13–14	PCC	Yellow	MMA
15–16	PCC	White	MMA
17–18	PCC	White	Thermo
19–20	PCC	Yellow	Thermo
21–22	PCC	White	Preformed
23–24	PCC	Yellow	Preformed

### Mobile Lidar Acquisition

The Leica Pegasus:Two mobile Lidar system owned by Oregon DOT was used for the Lidar data acquisition. In the first survey, the scanner was operated with a single laser profiler that could be adjusted to five operational configurations (+60°, +30°, 0°, -30°, -60°), referring to the orientation of the entire system with respect to the mounting platform. For example, with a 0° configuration, the point distribution of a scanline collected by the mobile Lidar system is perpendicular to the driving direction. Prior to the second survey in July 2017, the scanner had been upgraded to include a second profiler. In this configuration, one scanner is mounted in the -30° configuration while the second is mounted in the +60° configuration. A key benefit of this dual profiler configuration is to increase the point density. In addition, because the profilers are equipped in different orientations, an object can be captured from two different incidence angles and ranges. As a result, this configuration can potentially help balance the impact in the intensity caused by range and incidence angle when we sample the points within a search window to estimate the retroreflectivity.

By altering the orientation as well as the lane of travel, the road markings on the Testdeck (right lane) can be captured from a wide range of distances and incidence angles (Table 2). While more permutations are physically possible, only a select number of combinations were possible due to safety and traffic control requirements. For purposes of the calibration, only passes obtained at 40 kph were included. Note that the rationale for more passes at the -30° orientation was that it was the primary setting used to support several general applications. For example, this orientation enables the front faces of signs to be captured.

### Retroreflectometer Acquisition and Survey Control

A Delta LTL-X Mark II handheld retroreflectometer was used to acquire the ground truth retroreflectivity values at all of the sample points on each line of interest. Sample locations were premarked systematically using a measuring tape such that all measurements could be obtained at the same location. Three retroreflectometer measurements were acquired at each sample location and averaged to ensure a reliable, consistent reading. To reference these retroreflectivity readings to the

point cloud data collected by the mobile Lidar system, we surveyed all the sample points and linked them to ground control points set up on the Testdeck using a Leica Viva TS15 total station. GNSS coordinates were obtained for the ground control points using a Leica GS14 GNSS receiver. Although the mobile Lidar system employs direct geo-referencing from the onboard sensors, additional constraints through the use of ground control points improve the accuracy of the point cloud data, particularly relative to the total station measurements since the same ground control points were used. The typical accuracy (0.03 m horizontal root-mean-squared error (RMSE)) of the direct geo-referencing observed for this dataset can lead to additional errors in linking the retroreflectivity readings to the point cloud, most dramatically in locations with variable wear. Figure 3 shows example figures of the data acquisition as well as an example of the registered point cloud with the sampling points correctly located along the centerline of the 0.1 m wide line.

### Least Squares Regression

#### Sampling Technique

The fundamental concept of a retroreflectometer for road markings is to illuminate a field (active window) at a certain angle and observe the illumination over another field (passive

Table 2. Summary of mobile Lidar data acquisition.

Year	Pass #	Lane	Orientation (deg)	Speed (kph)
2016	01	Left	+30	40
	02	Left	-30	40
	03	Shoulder	+30	40
	04	Shoulder	-30	40
	05	Right	+60	40
	06	Right	+30	40
	07	Right	0	40
	08	Right	-30	40
	09	Right	-60	40
2017	10	Left	-30	40
	11	Shoulder	-30	40
	12	Right	-30	40

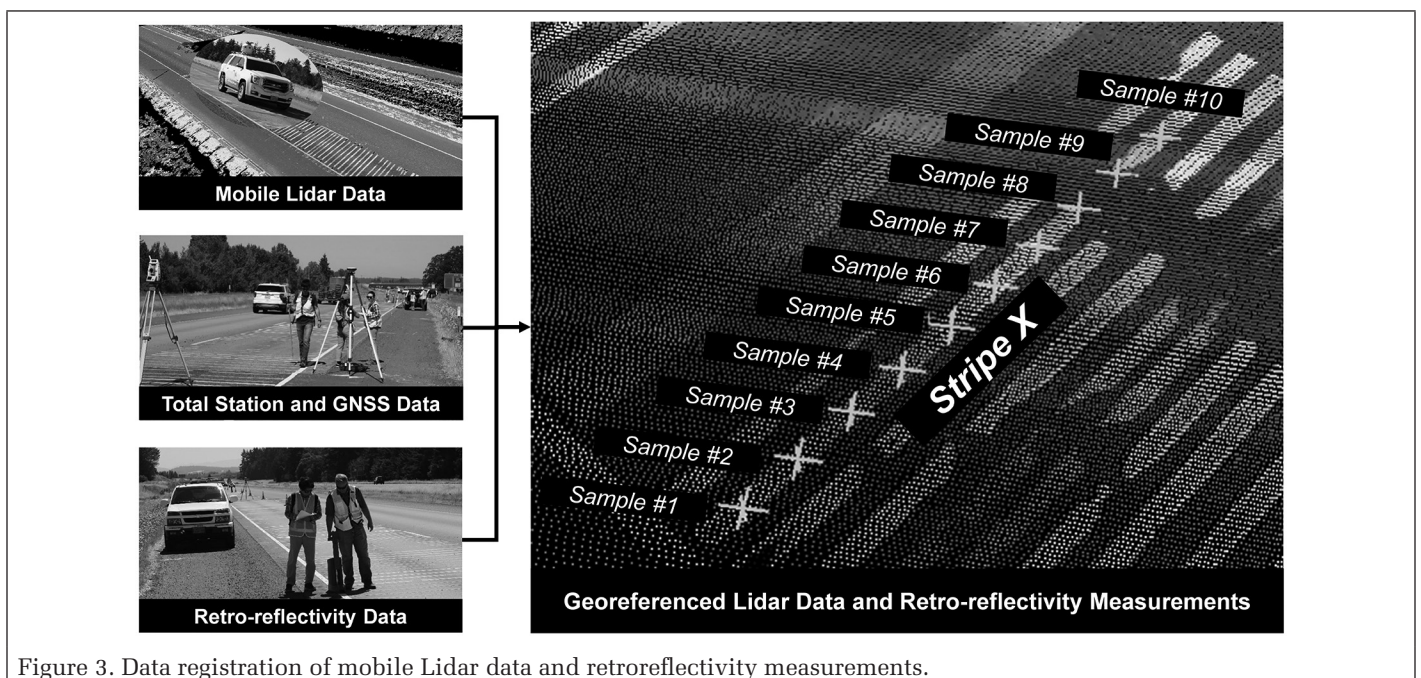


Figure 3. Data registration of mobile Lidar data and retroreflectivity measurements.

window) such that it can simulate the physics of how road markings reflect the light from the headlight of a vehicle to the driver's eyes (Figure 4).

Unlike the retroreflectometer using a fixed active window and passive window, the intensity value of a point in the mobile Lidar data is collected by measuring the energy from a much smaller field (mm to a few cm in size), which is a function of the beam exit diameter, beam divergence, range, and incidence angle. Although a theoretical radiometric calibration model can be developed by converting the measurements of illumination and intensity to reflectance based on the mechanism of the instruments, the manufacturers usually do not provide all the details of their products such as interpolation approach, internal corrections, calibration models, and so forth. Further, there are fundamental differences in terms of operating wavelengths and the window size of illumination between the two data sources rather than attempt to model the underlying physics given the amount of unknown variables. Hence, to develop this empirical model to simulate the retroreflectometer measurement with mobile Lidar data, we tested and evaluated different sampling techniques through regression analysis (Table 3). During the regression analysis, given the position of a sampling reference point and the orientation of the corresponding stripe, we ensure that the search window for extracting Lidar points matches the active or passive footprint of the retroreflectometer, depending on the case.

#### Regression Analysis

In the plots of the retroreflectivity measurements and the intensity values, all sampling techniques tested show a strong correlation between retroreflectivity and intensity (Figure 5). The average point counts for an active and passive window were 15 and 75, respectively. Note that all of the intensity values were scaled to floating point values with a range from 0 to 1, whilst the retroreflectivity readings consist of integer values ranging from 0 to 2000  $mc-d \cdot m^{-2} \cdot lx^{-1}$ , according to the specification of the retroreflectometer. From the distribution of the data points, this correlation tends to be stronger for relatively low values of retroreflectivity and intensity compared with the higher values. The primary reason for such

phenomena results from how pavement markings are made so that they can reflect the incoming light. Typically, glass beads are distributed in the material to provide the retroreflectivity of the road markings. When the road marking is worn, the material is less likely to be even-distributed such that it is impossible to estimate the portion of reflective and nonreflective part within the footprint of a measurement for both Lidar system and retroreflectometer. In addition, for the mobile Lidar system, the intensity value can be saturated (more energy is received than can be recorded with the sensitivity of the sensor) on a road marking with high retroreflectivity. As a result of this information loss, it is impossible to convert these intensity values to reflectance using a radiometric calibration approach. Fortunately, these highly retroreflective markings are not of concern to transportation agencies who are more concerned with evaluating worn markings that may require maintenance or replacement. Hence, it is most important to have a higher quality fit at the lower values of retroreflectivity.

Table 3. Summary of sampling approaches tested in the proposed regression analysis.

Search Window	Interpolation Approach	Definition
N/A	Nearest Neighbor	The intensity of the nearest point to the sampling reference point of the retroreflectometer measurement.
	Mean	Average intensity of all the points within the search window with an equal weight
Both Active & Passive Windows	Inverse Distance Weighting (IDW, $1/d^i$ )	Weighted average intensity of all points within the search window where each point is weighted by the inverse of the distance against the sampling point to the power of $i$ .
	Percentile ( $j\%$ )	The intensity value corresponding to the top $j\%$ of all the points within the search window.

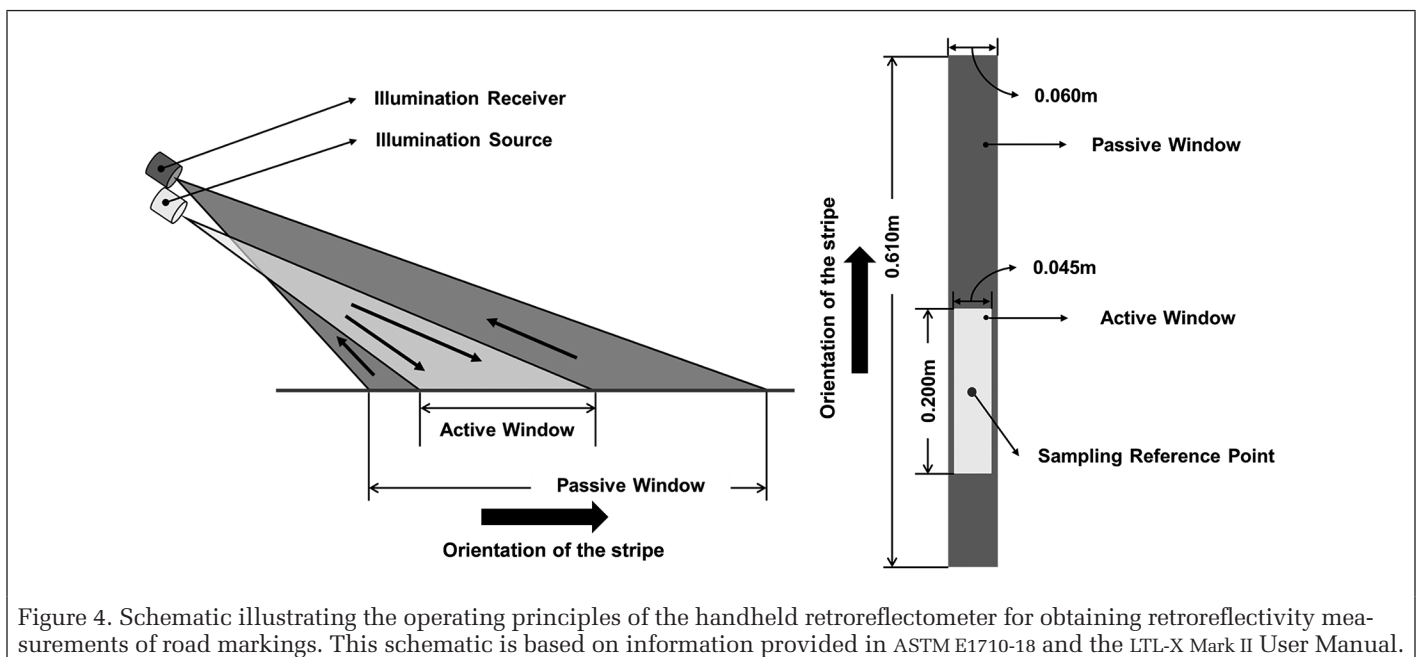


Figure 4. Schematic illustrating the operating principles of the handheld retroreflectometer for obtaining retroreflectivity measurements of road markings. This schematic is based on information provided in ASTM E1710-18 and the LTL-X Mark II User Manual.

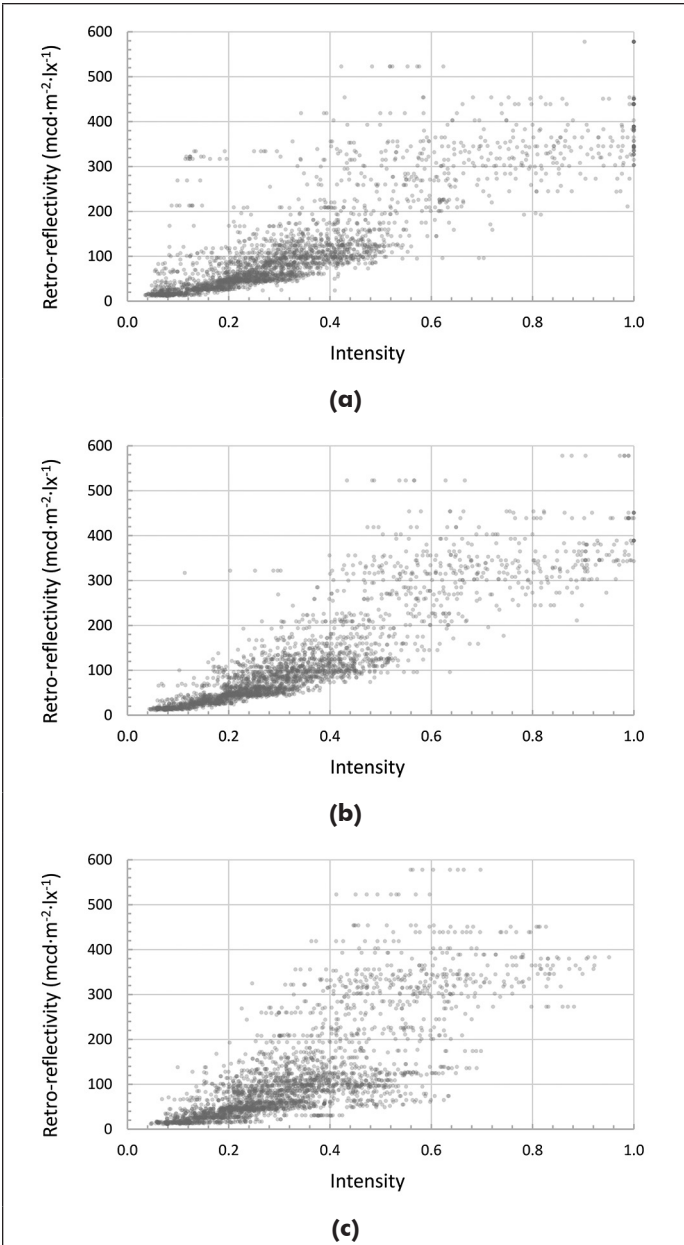


Figure 5. Example correlations between intensity values and retroreflectivity with different sampling approaches. (a) Nearest Neighbor; (b) Active Window Mean; (c) Passive Window Mean.

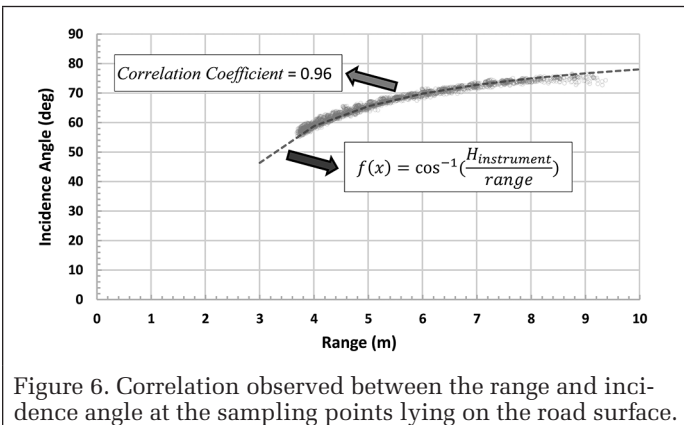


Figure 6. Correlation observed between the range and incidence angle at the sampling points lying on the road surface.

Based on visual analysis of the distribution of the data points, we explored a number of models such as power, linear, and exponential functions for the least squares regression. We also explored a number of models available in the literature to correct the intensity values for range and angle of incidence. The range to a point was obtained by matching each point to the corresponding point on the trajectory based on timestamp and then computing the distance. Given the limited possible geometric configurations of MLS acquisition from the roadway, it was found that the angle of incidence and range were highly correlated (Figure 6) with one another. Consequently, a general radiometric calibration process, which analyzes the range and angle of incidence independently, cannot be performed to estimate the coefficients of a model. Unfortunately, such independent analysis is usually required due to the complexity of such models and limited manufacturer information of the Lidar sensors.

Further, we tested a model applying a range correction to the intensity models as a second order polynomial function, as is common in the literature (e.g., Kashani *et al.* 2015). To evaluate the performance of each sampling technique and model, we calculate not only the correlation coefficient ( $R^2$ ) showing the fitting quality in retrieving retroreflectivity (Table 4) but also the variance of intensity showing the uncertainty of the intensity value in the least squares regression quantitatively (Table 5). Both tables are color coded by the corresponding values where the color ramp from white to black represents the fitting quality from high to low. The variance of intensity from the regression analysis can serve as a reference to help with further analysis of the results in the experiment for validation and accuracy assessment by detecting a potential over-fitting problem, which is critical for a data-driven empirical model. For example, if a validation using an independent dataset is conducted with errors significantly larger than what the variance is shown in the least squares regression, there can be an overfitting problem during the model development, thus indicating that the model is invalid.

Alternatively, one of the principle reasons why corrections remained elusive for the angle of incidence is that the pavement markings themselves do not follow Lambertian reflection, which is the assumption when correcting for angle of incidence in radiometric calibration. Rather, their design is to scatter light back in the direction of the source. Hence, the actual angle of incidence would be closer to zero than the computed angle of incidence based on the local surface orientation since the retroreflective material would be sending most of the light back in the direction from whence it came. In many cases, this retroreflectivity is accomplished through scattering glass beads in the material or paint used for the stripe. Unfortunately, these beads are not uniformly distributed throughout the stripe, resulting in inconsistencies in modeling this effect in a correction.

From this rigorous analysis of model quality shown in Tables 4 and 5, the power function with two coefficients using the 10th percentile of intensity in the active window footprint fits the sampling data better than any other models tested in this work in terms of both  $R^2$  values and variance of intensity values. Because all the sampling points are evenly weighted in the regression process, the points concentrated at lower retroreflectivity and intensity may cause a bias in determining the coefficients of the retroreflectivity estimation model. To compensate the bias in the sampling dataset, we weight a sampling point by its retroreflectivity value in the least squares regression. Then, the final coefficients of the power function for the radiometric calibration can be derived from a weighted least squares regression (Figure 7). The proposed empirical retroreflectivity estimation model is

Table 4. Correlation coefficients ( $R^2$ ) from least squares regression using different sampling approaches and models for retrieving retroreflectivity.

Sampling tech.	Model					
	$a \times Int.^b$	$a \times Int.+b$	$a^{b \times Int.}$	$a \times Int.^2 + b \times Int.+c$	$a \times Int.^b + c$	$(a \times range^2 + b \times range + c) \times Int.^d$
NN	0.7002	0.6963	0.6361	0.6982	0.6930	0.7128
AW Mean	0.7798	0.7815	0.6899	0.7817	0.7597	0.7795
AW IDW^1	0.7670	0.7682	0.6802	0.7684	0.7500	0.7708
AW IDW^2	0.7479	0.7474	0.6680	0.7478	0.7340	0.7553
AW 05%	0.8357	0.8273	0.7980	0.8348	0.8006	0.8191
AW 10%	<b>0.8360</b>	0.8306	0.7870	0.8352	0.8009	0.8190
AW 15%	0.8277	0.8248	0.7694	0.8273	0.7933	0.8147
AW 20%	0.8186	0.8173	0.7526	0.8187	0.7870	0.8094
AW 30%	0.8043	0.8041	0.7275	0.8048	0.7777	0.8006
AW 40%	0.7779	0.7786	0.6940	0.7788	0.7555	0.7779
AW Median	0.7436	0.7438	0.6543	0.7439	0.7283	0.7484
PW Mean	0.5913	0.5856	0.5422	0.5905	0.5536	0.5764
PW IDW^1	0.7552	0.7537	0.6771	0.7556	0.7296	0.7516
PW IDW^2	0.7527	0.7525	0.6714	0.7530	0.7351	0.7571
PW 05%	0.5412	0.5388	0.5242	0.5411	0.5349	0.5583
PW 10%	0.5598	0.5591	0.5333	0.5600	0.5549	0.5819
PW 15%	0.5677	0.5675	0.5353	0.5680	0.5624	0.5919
PW 20%	0.5797	0.5787	0.5457	0.5798	0.5701	0.5988
PW 30%	0.5839	0.5825	0.5387	0.5836	0.5662	0.5882
PW 40%	0.5674	0.5664	0.5105	0.5670	0.5324	0.5490
PW Median	0.5219	0.5200	0.4593	0.5207	0.4691	0.4832

(NN: Nearest Neighbor; AW/PW: Active/Passive Window).

Table 5. Variance of intensity values in least squares regression using different sampling approaches and empirical models for estimating retroreflectivity.

Sampling tech.	Model					
	$a \times Int.^b$	$a \times Int.+b$	$a^{b \times Int.}$	$a \times Int.^2 + b \times Int.+c$	$a \times Int.^b + c$	$(a \times range^2 + b \times range + c) \times Int.^d$
NN	0.0249	0.0265	0.0269	0.0316	0.0367	0.0355
AW Mean	0.0213	0.0226	0.0248	0.0269	0.0324	0.0311
AW IDW^1	0.0219	0.0232	0.0252	0.0277	0.0331	0.0317
AW IDW^2	0.0228	0.0242	0.0257	0.0289	0.0342	0.0328
AW 05%	0.0189	0.0203	0.0209	0.0241	0.0304	0.0287
AW 10%	0.0188	0.0200	0.0213	0.0239	0.0302	0.0286
AW 15%	0.0192	0.0203	0.0221	0.0244	0.0306	0.0289
AW 20%	0.0196	0.0207	0.0227	0.0249	0.0310	0.0292
AW 30%	0.0202	0.0214	0.0236	0.0257	0.0315	0.0297
AW 40%	0.0214	0.0227	0.0248	0.0272	0.0328	0.0313
AW Median	0.0229	0.0244	0.0261	0.0290	0.0344	0.0332
PW Mean	0.0294	0.0314	0.0300	0.0366	0.0440	0.0448
PW IDW^1	0.0224	0.0240	0.0252	0.0284	0.0344	0.0332
PW IDW^2	0.0226	0.0240	0.0255	0.0286	0.0341	0.0327
PW 05%	0.0330	0.0336	0.0333	0.0408	0.0472	0.0476
PW 10%	0.0319	0.0327	0.0325	0.0396	0.0456	0.0456
PW 15%	0.0313	0.0322	0.0320	0.0389	0.0449	0.0446
PW 20%	0.0305	0.0317	0.0312	0.0380	0.0441	0.0438
PW 30%	0.0298	0.0313	0.0307	0.0373	0.0436	0.0437
PW 40%	0.0300	0.0317	0.0310	0.0374	0.0448	0.0457
PW Median	0.0312	0.0333	0.0320	0.0389	0.0472	0.0492

(NN: Nearest Neighbor; AW/PW: Active/Passive Window).

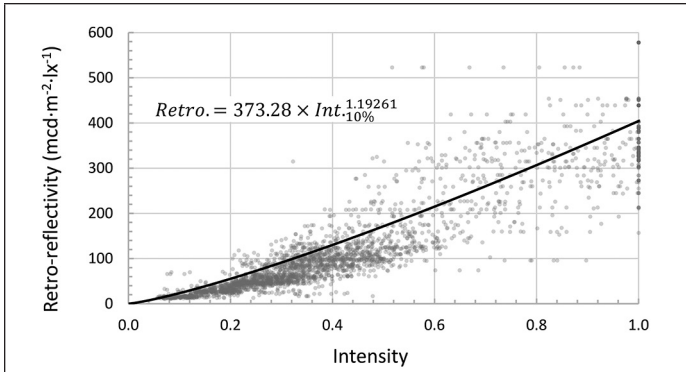


Figure 7. Resulting retroreflectivity prediction model derived from the weighted least squares regression using the 10<sup>th</sup> percentile of intensity values within the active window. The equation shows the coefficients of the proposed empirical model and is plotted as a black line.

further validated and evaluated quantitatively in the following experiment section with an independent data source.

## Validation Experiment

### Validation Dataset

To validate the proposed retroreflectivity estimation model, we collect data from a 75 m section of urban highway in Philomath, Oregon in July 2017 (Figure 8). The condition of the longitudinal line on this site is satisfactory on both ends of the section but poor due to significant degradation in the center area, enabling us to validate the proposed radiometric calibration model across a wide range of road marking conditions. We obtained dense measurements with the retroreflectometer along the longitudinal line every 0.5 m. The mobile Lidar data and retroreflectivity measurements are registered into the same coordinate system following the same approach used in the model development stage at the Testdeck site.

For this test, the mobile Lidar unit was operated in the dual profiler configuration with the scanners fixed at the -30° and 60° orientations. We obtained 4 passes on each lane (left

and right) in a speed of 40 kph. In the following sections, the validation, accuracy, and repeatability of the proposed model is evaluated quantitatively with using both the single profiler (-30°) and dual profiler (-30°/60°) configurations (Table 6). Note that the software does not allow the +60° configuration to be evaluated by itself.

Table 6. Summary of the mobile Lidar settings used in data collection for the validation testing.

Pass #	Lane	Orientation (deg)	Speed (kph)
01	Left	-30/+60	40
02	Left	-30/+60	40
03	Left	-30/+60	40
04	Left	-30/+60	40
05	Right	-30/+60	40
06	Right	-30/+60	40
07	Right	-30/+60	40
08	Right	-30/+60	40

### Validation of the Proposed Radiometric Calibration Model

The calculated retroreflectivity values from the mobile Lidar data are compared against the retroreflectometer measurements as ground truth (Table 7) to quantitatively validate the proposed radiometric calibration model. For each pass, we compute the mean error (ME) and RMSE for all the retroreflectometer data points collected where the ME and the RMSE represent the accuracy and the precision of the proposed model in estimating the retroreflectivity ( $mcd \cdot m^{-2} \cdot lx^{-1}$ ). For each lane, we combine all the results of the passes on this lane to obtain an overall accuracy and precision.

Then we compare the ME and RMSE under different system configurations and lane selections (Table 8). With the same profiler configuration, the passes from the left lane constantly provide better results compared to passes in the right lane for both ME and RMSE. This improvement likely occurs because the longitudinal line is closer to the mobile Lidar system for the right lane passes compared with the left lane passes, resulting in larger incidence angles for the left lane passes. Because the retroreflectometer simulates retroreflectivity at a range of 30 meters with an incidence angle of 88.76° (ASTM International 2018), the scan geometry on the left lane is more similar to that of the retroreflectometer. As a result, the left

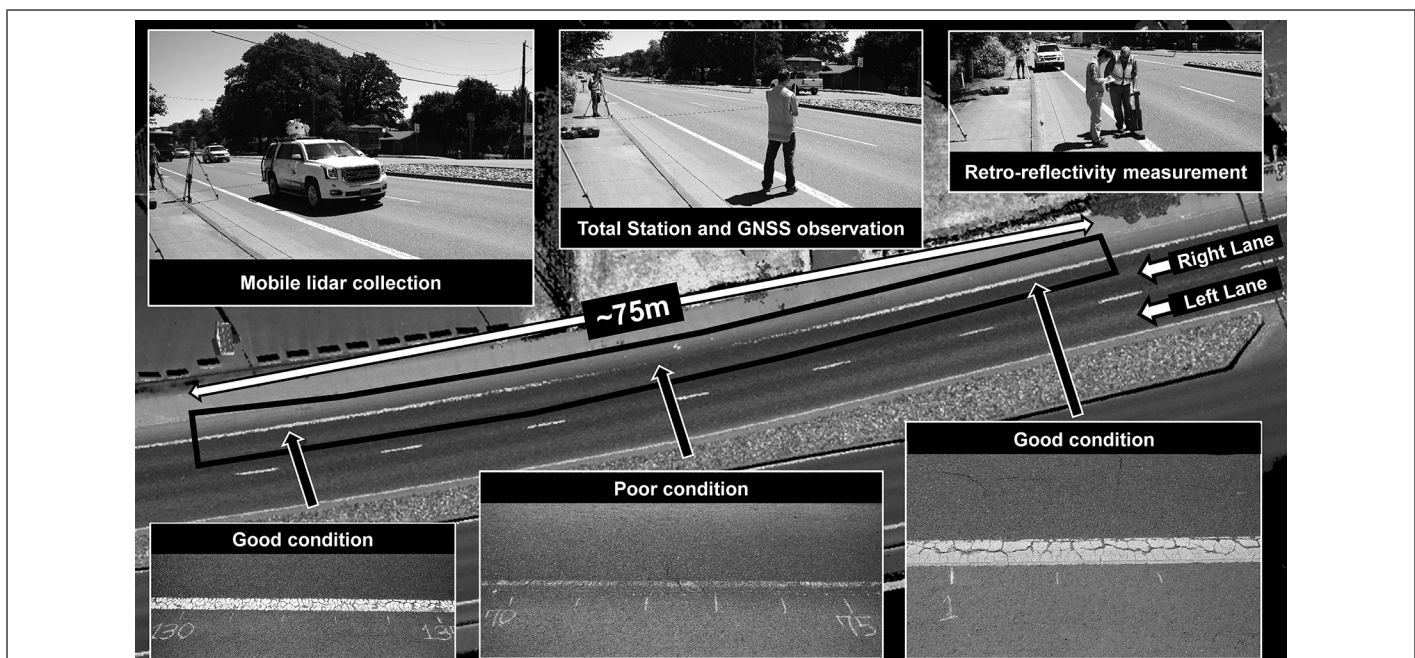


Figure 8. Data collection at the test site for validating the proposed radiometric calibration model.

Table 7. Accuracy assessment to the retroreflectivity estimation. (unit:  $mcd \cdot m^{-2} \cdot lx^{-1}$ ).

Lane & Pass #	Single profiler ( $-30^\circ$ )		Dual Profiler ( $-30^\circ/+60^\circ$ )	
	Mean Error	RMSE	Mean Error	RMSE
Left Lane				
01	-0.1	22.9	-0.5	21.4
02	-3.4	24.1	-4.0	23.0
03	-3.3	25.5	-4.0	23.9
04	-5.3	24.4	-4.6	23.4
01-04	-3.0	24.2	-3.3	22.9
Right Lane				
05	-21.8	35.8	-7.1	25.1
06	-21.1	35.1	-8.1	25.2
07	-20.9	35.2	-5.4	24.4
08	-24.0	37.4	-9.1	25.4
05-08	-22.0	35.9	-7.4	25.0
All Passes	-12.5	30.6	-5.4	24.0

Table 8. Accuracy comparison under different system configurations and lane selections. (unit:  $mcd \cdot m^{-2} \cdot lx^{-1}$ ).

Lane & Pass	$d_{abs}(ME)$	$d_{RMSE}$
Single profiler → Dual profiler		
Left 01-04	0.2	-1.3
Right 05-08	-14.5	-10.9
All passes	-7.1	-6.6
Right lane → Left lane		
Single Profiler	-18.9	-11.6
Dual Profiler	-4.2	-2.1

lane provides a more accurate and precise result in estimating retroreflectivity with the proposed method that essentially simulates the retroreflectometer measurements. Fortunately, by utilizing the dual-profiler, the results on the right lane are significantly improved and similar to those of the lane. The primary reason for this improvement is that the  $+60^\circ$  profiler collects data on the longitudinal line at a larger range and incidence angle. Hence, the dual configuration helps balance the effects of acquisition geometry when capturing information for lines across the roadway.

We further demonstrate the repeatability of the proposed model by plotting the average retroreflectivity values extracted from data acquired from the left lane and right lane (Figure 9). Although both the single and dual profiler data show a same trend with the ground truth retroreflectivity measurements overall, the dual profiler provides a more robust result regardless of the lane driven. The dual profiler not only increases the point density, which may help improve the overall repeatability, acquiring points at a different incidence angle helps provide additional data at a geometric configuration more consistent to the physics that are being modeled by the retroreflectometer. Thus, to some extent, it overcomes the limitation of the proposed model lacking intensity corrections with respect to the parameters of range or angle of incidence without compromising the overall accuracy and precision.

Comparison against the precision testing result tests on the retroreflectometer (ASTM International 2018), the proposed model is almost compatible with a manual retroreflectivity measurement in terms of repeatability and reproducibility. Nevertheless, we also notice that all of the mean errors are negative, which indicates that the proposed method tends to slightly under-predict the retroreflectivity. Hence, the next section will explore this influence on the determination of a pass/fail rating for the strip.

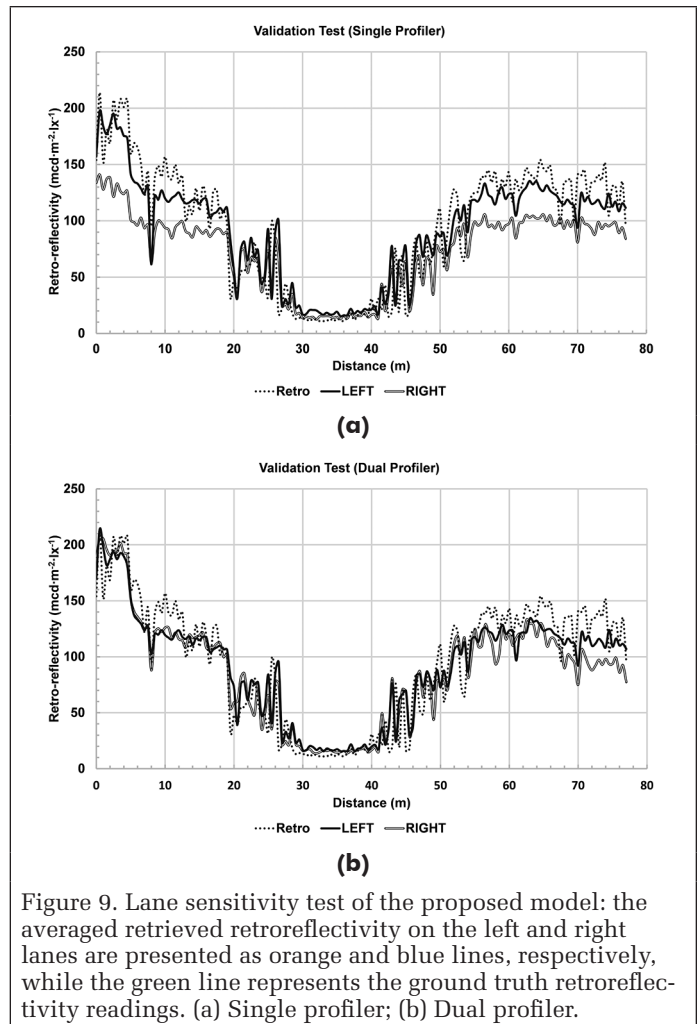


Figure 9. Lane sensitivity test of the proposed model: the averaged retrieved retroreflectivity on the left and right lanes are presented as orange and blue lines, respectively, while the green line represents the ground truth retroreflectivity readings. (a) Single profiler; (b) Dual profiler.

### Validation of the Road Marking Condition Assessment

Because there is no strict requirement of the minimum retroreflectivity for maintenance at this site given that it is a slow, urban road, we chose a pass/fail threshold of  $90 mcd \cdot m^{-2} \cdot lx^{-1}$ , recommended by (Debaillon *et al.* 2007), to evaluate the retroreflectivity of a sampling point. This threshold separates the 155 ground-truth samples into pass and fail categories with a proportion of 59% and 41%, respectively (Figure 10).

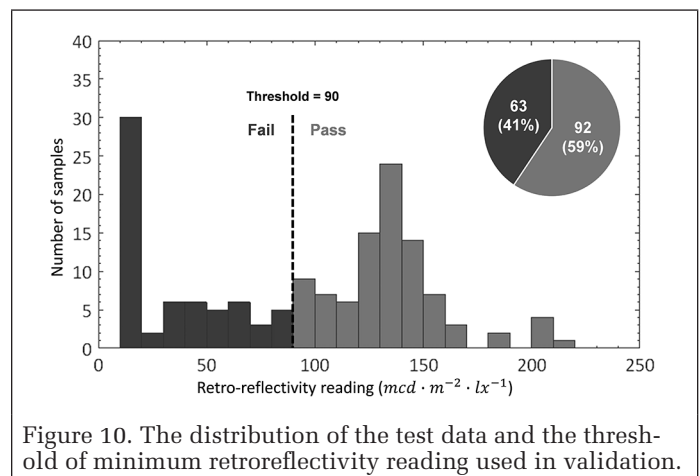


Figure 10. The distribution of the test data and the threshold of minimum retroreflectivity reading used in validation.

The precision, recall, and F1-score are then computed and compared to quantitatively evaluate the performance of the pass/fail decision and compact of lane selection and system configuration using the proposed method (Table 9 and Table

10). Irrespective of the various combinations of lane, pass, and configuration, the precision is consistently over 90%, which indicates that the proposed method is conservative in detecting the line in good condition. Further, these results agree with the analysis in the previous section that the proposed model exhibits better performance from the left lane compared with the right lane. Moreover, notice that the precision percentage is generally more consistent and higher than the recall percentage, especially for the right lane with a single profiler. This proves that estimates from the proposed model are improved by using the dual profiler configuration. It also supports the finding that improved results can be achieved by collecting data from the lane (left in this example) next to the adjacent lane next to the line (right in this example). Lastly, the F1-score quantifies the accuracy of the proposed model by considering both precision and recall. Similarly, the F1-score indicates that the left lane passes and/or utilizing the dual profiler configuration can improve the results.

## Conclusions

In this work, we propose an approach of radiometric calibration that reliably converts intensity values from mobile Lidar data to retroreflectivity measurements. Through several field tests, a strong correlation between intensity and retroreflectivity was observed despite the difference between a mobile Lidar system and a handheld retroreflectometer including measuring range, wavelength, angle, and so forth. Based on the operating principles of a handheld retroreflectometer, we compare multiple sampling approaches for developing an empirical radiometric calibration model. In the experiment, a dataset independent from the one for radiometric calibration is used to validate the proposed radiometric calibration model. We compare the handheld retroreflectometer readings against the retroreflectivity estimated from the mobile Lidar data collected in different lanes, system configurations (i.e., single profiler and dual profilers). Based on the accuracy assessment, it can be concluded that the proposed method using the data collected by dual profilers is more robust to lane selection and provides more accurate estimation than a single profiler. The proposed radiometric calibration model is demonstrated to be able to evaluate the retroreflectivity accurately, which can be further applied to assess the condition of the pavement markings.

Nevertheless, we also notice some limitations of the proposed empirical radiometric calibration model: (1) Due to the limited range of intensity, the proposed model is only capable to estimate the retroreflectivity in a range from 0 to  $373 \text{ mcd}\cdot\text{m}^{-2}\cdot\text{lx}^{-1}$ . Thus, the proposed method is more suitable for assessing the existing pavement markings with wear; (2) The radiometric calibration is conducted to a specific mobile Lidar system, hence the versatility needs to be evaluated by implementing the radiometric calibration process on other systems; (3) Just like a handheld retroreflectometer, the retroreflectivity readings can vary dramatically between wet and dry conditions, and this work only considers dry conditions; (4) All of the data analyzed were collected with a constant speed of 40 kph, thus more tests are required to further demonstrate the robustness and accuracy to a higher speed during data acquisition.

In the future work, we will continue to: (1) conduct additional case studies (e.g., on larger test sites) to further test the proposed radiometric calibration model; (2) explore the impact of weather conditions to the proposed method of pavement marking evaluation; (3) apply the proposed procedures to different MLS systems; and (4) generate metrics in GIS (e.g., index of quality level) for evaluating the pavement marking quantitatively based on the retroreflectivity from the mobile Lidar data.

Table 9. Evaluation of the proposed model for a pass-fail assessment of the retroreflectivity condition of the road marking.

Lane & Pass #	Single Profiler ( $-30^\circ$ ), %			Dual Profiler ( $-30^\circ/+60^\circ$ ), %		
	Precision	Recall	F1-score	Precision	Recall	F1-score
Left Lane						
01	91.84	97.83	94.74	94.68	96.74	95.70
02	92.47	93.48	92.97	94.51	93.48	93.99
03	94.57	94.57	94.57	96.67	94.57	95.60
04	94.62	95.65	95.14	95.65	95.65	95.65
01–04	93.35	95.38	94.35	95.37	95.11	95.24
Right Lane						
05	97.18	75.00	84.66	95.29	88.04	91.53
06	98.68	81.52	89.29	97.62	89.13	93.18
07	98.70	82.61	89.94	95.35	89.13	92.13
08	96.92	68.48	80.25	96.34	85.87	90.80
05–08	97.92	76.90	86.15	96.14	88.04	91.91
All Passes	95.34%	86.14	90.51	95.74	91.58	93.61

Table 10. Comparison of pass-fail accuracy under different system configurations and lane selections.

Lane & Pass	Percent		
	$d_{precision}$	$d_{recall}$	$d_{f1-score}$
Single profiler vs. Dual profiler			
Left 01–04	2.02	-0.27	0.89
Right 05–08	-1.78	11.14	5.76
All passes	0.40	5.44	3.10
Right lane vs. Left lane			
Single Profiler	-4.57	18.48	8.20
Dual Profiler	-0.77	7.07	3.33

## Acknowledgments

This research was funded in part, by Oregon DOT (SPR-799) and the National Science Foundation (Award CMMI-1351487). Note that some of the material in this paper has been adapted from a larger final report that have been submitted to the research sponsor Oregon Department of Transportation for SPR-799 "Lidar For Maintenance of Pavement Reflective Markings and Retroreflective Signs". We appreciate the support of Joel Fry, Lloyd Bestdoe, Dan Wright, and Jon Lazarus, from Oregon DOT who assisted with the retroreflectivity measurements, mobile Lidar scanning, mobile Lidar data processing, and research coordination, respectively. Oregon State University students Chase Simpson, Kory Kellum, Nick Wilson, Katherine Shaefer, and Marian Jamieson assisted with data collection. The authors also appreciate the support of Leica Geosystems and David Evans and Associates who provided hardware and software used in this research.

## References

- Ai, C. and Y. J. Tsai. 2016. An automated sign retroreflectivity condition evaluation methodology using mobile LIDAR and computer vision. *Transportation Research Part C: Emerging Technologies* 63: 96–113.
- ASTM International. 2018. *ASTM E1710-18 Standard Test Method for Measurement of Retroreflective Pavement Marking Materials with CEN-Prescribed Geometry Using a Portable Retroreflectometer*. West Conshohocken, PA: ASTM International.
- Austin, R. L. and R. J. Schultz. 2009. *Guide to Retroreflection Safety Principles and Retroreflective Measurements*. Gamma Scientific.

- Balali, V., M. A. Sadeghi and M. Golparvar-Fard. 2015. Image-based retroreflectivity measurement of traffic signs in day time. *Advanced Engineering Informatics* 29 (4): 1028–1040.
- Baltsavias, E. P. 1999. Airborne laser scanning: Basic relations and formulas. *ISPRS Journal of Photogrammetry and Remote Sensing* 54 (2–3): 199–214.
- Carlson, P. and D. Picha. 2009. *Sign Retroreflectivity Guidebook for Small Agencies, Federal Land Management Agencies, and Tribal Governments* (No. FHWA-CFL/TD-09-005).
- Carlson, P., B. Storey, M. Poorsartep, C. Stevens, B. Ettelman, T. E. Lindheimer, M. Dastgiri, A. Khodakarami, J. Miles, D. Song and R. L. Lytton. 2017. *Advancing Innovative High-Speed Remote-Sensing Highway Infrastructure Assessment using Emerging Technologies: Technical Report* (No. FHWA/TX-16/0-6869-1). Texas A&M Transportation Institute.
- Debaillon, C., P. J. Carlson, Y. He, T. Schnell and F. Aktan. 2007. *Updates to Research on Recommended Minimum Levels for Pavement Marking Retroreflectivity to Meet Driver Night Visibility Needs* (No. FHWA-HRT-07-059). Turner-Fairbank Highway Research Center.
- Federal Highway Administration (FHWA). 2009. *Sign Retroreflectivity Guidebook: How to Meet the New National Standard*. U.S. Department of Transportation.
- Gonzalez-Jorge, H., B. Riveiro, J. Armesto and P. Arias. 2013. Evaluation of road signs using radiometric and geometric data from terrestrial LiDAR. *Optica Applicata* 43 (3): 421–433.
- Guan, H., J. Li, S. Cao and Y. Yu. 2016. Use of mobile LiDAR in road information inventory: A review. *International Journal of Image and Data Fusion* 7 (3): 219–242.
- Guan, H., J. Li, Y. Yu, M. Chapman and C. Wang. 2015. Automated road information extraction from mobile laser scanning data. *IEEE Transactions on Intelligent Transportation Systems* 16 (1): 194–205.
- Guo, J., M. J. Tsai and J. Y. Han. 2015. Automatic reconstruction of road surface features by using terrestrial mobile lidar. *Automation in Construction* 58: 165–175.
- Höfle, B. and N. Pfeifer. 2007. Correction of laser scanning intensity data: Data and model-driven approaches. *ISPRS Journal of Photogrammetry and Remote Sensing* 62 (6): 415–433.
- Jaakkola, A., J. Hyyppä, H. Hyyppä and A. Kukko. 2008. Retrieval algorithms for road surface modelling using laser-based mobile mapping. *Sensors* 8 (9): 5238–5249.
- Jelalian, A. V. 1980. Laser radar systems. Pages 546–554 in *EASCON'80: Electronics and Aerospace Systems Conference*.
- Jutzi, B. and H. Gross. 2009. Normalization of LiDAR intensity data based on range and surface incidence angle. *International Archives of the Photogrammetry, Remote Sensing and Spatial Information Sciences* 38: 213–218.
- Kaasalainen, S., A. Jaakkola, M. Kaasalainen, A. Krooks and A. Kukko. 2011. Analysis of incidence angle and distance effects on terrestrial laser scanner intensity: Search for correction methods. *Remote Sensing* 3 (10): 2207–2221.
- Kaasalainen, S., A. Krooks, A. Kukko and H. Kaartinen. 2009. Radiometric calibration of terrestrial laser scanners with external reference targets. *Remote Sensing* 1 (3): 144–158.
- Kashani, A. G., M. J. Olsen, C. E. Parrish and N. Wilson. 2015. A review of LiDAR radiometric processing: From ad hoc intensity correction to rigorous radiometric calibration. *Sensors* 15 (11): 28099–28128.
- Khalilikhah, M., K. Heaslip and Z. Song. 2015. Can daytime digital imaging be used for traffic sign retroreflectivity compliance?. *Measurement* 75: 147–160.
- Kirk, A. R., E. A. Hunt and E. W. Brooks. 2001. *Factors affecting sign retroreflectivity* (No. OR-RD-01-09). Oregon. Dept. of Transportation. Research Group.
- Mallet, C. and F. Bretar. 2009. Full-waveform topographic lidar: State-of-the-art. *ISPRS Journal of Photogrammetry and Remote Sensing* 64 (1): 1–16.
- Migletz, J., J. Graham, K. Bauer and D. Harwood. 1999. Field surveys of pavement-marking retroreflectivity. *Transportation Research Record: Journal of the Transportation Research Board* (1657): 71–78.
- Olsen, M. J., G. V. Roe, C. Glennie, F. Persi, M. Reedy, D. Hurwitz, K. Williams, H. Tuss, A. Squellati and M. Knodler. 2013. *Guidelines for the Use of Mobile LIDAR in Transportation Applications* (No. Project 15-44).
- Riveiro, B., H. González-Jorge, J. Martínez-Sánchez, L. Díaz-Vilariño and P. Arias. 2015. Automatic detection of zebra crossings from mobile LiDAR data. *Optics & Laser Technology* 70: 63–70.
- Saetern, L. T. 2016. *Preliminary Investigation: Commercial Pavement Marking Management Systems* (No. DRISI-20160512).
- Smadja, L., J. Ninot and T. Gavrilovic. 2010. Road extraction and environment interpretation from LiDAR sensors. *IAPRS* 38 (281–286): 1.
- Toth, C., E. Paska and D. Brzezinska. 2008. Using road pavement markings as ground control for LiDAR data. *International Archives of Photogrammetry, Remote Sensing and Spatial Information Sciences* 37: 189–195.
- Vain, A., S. Kaasalainen, U. Pyysalo, A. Krooks and P. Litkey. 2009. Use of naturally available reference targets to calibrate airborne laser scanning intensity data. *Sensors* 9 (4): 2780–2796.
- Van Schalkwyk, I. 2010. *Enhancements to Pavement Marking Testing Procedures* (No. FHWA-OR-RD-11-02).
- Vosselman, G. 2009. Advanced point cloud processing. In *Photogrammetric Week*, Vol. 9: 137–146. University of Stuttgart Stuttgart, Germany.
- Wagner, W., J. Hyyppä, A. Ullrich, H. Lehner, C. Briese and S. Kaasalainen. 2008. Radiometric calibration of full-waveform small-footprint airborne laser scanners. *International Archives of Photogrammetry, Remote Sensing and Spatial Information Sciences* 37 (B1): 163–168.
- Wen, C., J. Li, H. Luo, Y. Yu, Z. Cai, H. Wang and C. Wang. 2016. Spatial-related traffic sign inspection for inventory purposes using mobile laser scanning data. *IEEE Transactions on Intelligent Transportation Systems* 17 (1): 27–37.
- Yan, L., H. Liu, J. Tan, Z. Li, H. Xie and C. Chen. 2016. Scan line based road marking extraction from mobile LiDAR point clouds. *Sensors* 16 (6): 903.
- Yang, B., L. Fang, Q. Li and J. Li. 2012. Automated extraction of road markings from mobile LiDAR point clouds. *Photogrammetric Engineering & Remote Sensing* 78 (4): 331–338.
- Yang, B., Y. Liu, Z. Dong, F. Liang, B. Li and X. Peng. 2017. 3D local feature BKD to extract road information from mobile laser scanning point clouds. *ISPRS Journal of Photogrammetry and Remote Sensing* 130: 329–343.
- Yao, Y. and Q. Hu. 2014. Automatic extraction method study of road marking lines based on projection of point clouds. Pages 1–4 in *2014 22nd IEEE International Conference on Geoinformatics*.
- Zhang, H., J. Li, M. Cheng and C. Wang. 2016. Rapid inspection of pavement markings using mobile Lidar point clouds. *International Archives of the Photogrammetry, Remote Sensing & Spatial Information Sciences* 41.

# WHO'S WHO IN ASPRS

## BOARD OF DIRECTORS

### BOARD OFFICERS

#### President

Thomas Jordan, Ph.D.  
*University of Georgia*

#### President-Elect

Jeff Lovin  
*Woolpert*

#### Vice President

Jason Stoker  
*U.S. Geological Survey*

#### Past President

Anne Hillyer, CP  
*Bonneville Power Administration (USDOE)*

#### Treasurer

Stewart Walker, Ph.D.

#### Secretary

Roberta E. Lenczowski

### BOARD MEMBERS

#### Corporate Members Council – 2019

Chair: Joe Cantz

Vice Chair: TBA

[www.asprs.org/About-Us/Sustaining-Members-Council.html](http://www.asprs.org/About-Us/Sustaining-Members-Council.html)

#### Early-Career Professionals Council – 2020

Chair: Amanda Aragon

Vice Chair: Peng Fu

#### Region Officers Council – 2020

Chair: Lorraine B. Amenda, PLS, CP

Vice Chair: Demetrio Zourarakas

#### Student Advisory Council – 2020

Chair: Victoria Scholl

Vice Chair: TBA

<http://www.asprs.org/Students/Student-Advisory-Council.html>

#### Technical Division Directors Council – 2020

Chair: John McCombs

Vice Chair: Bandana Kar, Ph.D.

### TECHNICAL DIVISION OFFICERS

#### Geographic Information Systems Division – 2021

Director: Xan Fredericks

Assistant Director: Denise G. Theunissen  
[www.asprs.org/Divisions/GIS-Division.html](http://www.asprs.org/Divisions/GIS-Division.html)

#### Lidar Division – 2020

Director: Amar K. Nayegandhi, CP, CMS

Assistant Director: Joshua Nimetz, CMS  
[www.asprs.org/Divisions/Lidar-Division.html](http://www.asprs.org/Divisions/Lidar-Division.html)

#### Photogrammetric Applications Division – 2020

Director: Paul C. Bresnahan

Assistant Director: Kurt Rogers  
[www.asprs.org/Divisions/Photogrammetric-Applications-Division.html](http://www.asprs.org/Divisions/Photogrammetric-Applications-Division.html)

#### Primary Data Acquisition Division – 2021

Director: Jon Christopherson

Assistant Director: J. Chris Ogier  
[www.asprs.org/Divisions/Primary-Data-Aquisition-Division.html](http://www.asprs.org/Divisions/Primary-Data-Aquisition-Division.html)

#### Professional Practice Division – 2022

Director: Harold W. Rempel, III, CP

Assistant Director: TBA  
[www.asprs.org/Divisions/Professional-Practice-Division.html](http://www.asprs.org/Divisions/Professional-Practice-Division.html)

#### Remote Sensing Applications Division – 2020

Director: David W. Kreighbaum

Assistant Director: Raechel A. White, Ph.D.  
[www.asprs.org/Divisions/Remote-Sensing-Applications-Division.html](http://www.asprs.org/Divisions/Remote-Sensing-Applications-Division.html)

#### Unmanned Autonomous Systems (UAS) – 2020

Director: Benjamin Vander Jagt, Ph.D.

Assistant Director: Megan Miller, Ph.D.

### REGION PRESIDENTS

#### Alaska Region

Caitlin Verlund

<http://www.asprsalaska.org/>

#### Cascades Region

Camile Westlake

<http://columbia.asprs.org/CRR/>

#### Central New York Region

John Boland, C.P.

<http://www.esf.edu/asprs/>

#### Eastern Great Lakes Region

Srinivasan Dharmapuri, CP, CMS

<http://egl.asprs.org/>

#### Florida Region

Erin McCormick

<http://florida.asprs.org/>

#### Heartland Region

Paul Manley

<http://heartland.asprs.org/>

#### Intermountain Region

Sowmya Selvarajan, Ph.D.

<http://asprsiintermountain.weebly.com/>

#### Mid-South Region

Demetrio Zourarakis, Ph.D.

<https://www.asprs.org/all-regions/mid-south.html>

#### New England Region

TBA

<http://neweng.asprs.org/>

#### North Atlantic Region

Richard W. Carlson, Jr., P.L.S., C.P.

<http://natlantic.asprs.org/>

#### Pacific Southwest Region

Lorraine B. Amenda, PLS, CP

<https://pswasprs.org/>

#### Potomac Region

Gang Chen, Ph.D.

<http://www.asprspotomac.org/>

#### Rocky Mountain Region

Jeffrey Young

<http://www.asprs-rmr.org/>

#### Western Great Lakes Region

Kirk Contrucci, CP

<http://wgl.asprs.org/>

# Total Vertical Uncertainty (TVU) Modeling for Topo-Bathymetric LIDAR Systems

Firat Eren, Jaehoon Jung, Christopher E. Parrish, Nicholas Sarkozi-Forfinski, and Brian R. Calder

## Abstract

This paper presents a comprehensive total vertical uncertainty (TVU) model for topo-bathymetric Light Detection and Ranging (LIDAR) systems. The TVU model consists of a combination of analytical uncertainty propagation for the subaerial (above water) portion and Monte Carlo simulation models for the subaqueous portion (water surface to seafloor). The TVU model was tested on a topo-bathymetric LIDAR data set collected by National Oceanic and Atmospheric Administration's National Geodetic Survey (NGS) in Southwest Florida, U.S., in May 2016 using a Riegl VQ-880-G topo-bathymetric LIDAR system. The TVU values were compared against the empirical standard deviation and were found to capture the variability of uncertainty with depth while providing (slightly) conservative estimates of uncertainty. The results may be used to inform data acquisition protocols and data processing models. The model implementation is now beginning to be used operationally at NGS for topo-bathymetric LIDAR projects.

## Introduction

The National Oceanic and Atmospheric Administration's (NOAA) National Geodetic Survey (NGS) Remote Sensing Division (RSD) and Joint Airborne Light Detection and Ranging (LIDAR) Bathymetry Technical Center of Expertise (JALBTCX) partner agencies routinely collect topo-bathymetric LIDAR data for large portions of the U.S. coast. The data support applications ranging from mapping the national shoreline to regional sediment management, flood risk management, emergency response, as well as inland water mapping applications such as monitoring river morpho-dynamics and instream habitat modeling (Wozencraft and Lillycrop 2006; Pfennigbauer *et al.* 2011; Mandlbürger *et al.* 2015; Miller-Corbett 2016; Pan *et al.* 2016; Parrish *et al.* 2016). The topo-bathymetric LIDAR data could also be used to advantage in hydrographic surveying programs, providing valuable information in the shallow nearshore (Imahori *et al.* 2013) and supporting the multi-use objective of the Integrated Ocean and Coastal Mapping initiative (NSTC 2013).

To do so, however, requires reliable, quantitative analysis and reporting of the spatial coordinate uncertainty of the data. According to International Hydrographic Organization (IHO) S-44 standards, Total Propagated Uncertainty (TPU) must account for "all contributing measurement uncertainties" using a "statistical method, combining all uncertainty sources, for determining positioning uncertainty at the 95% confidence level" (IHO 2008). TPU models comprise Total

Vertical Uncertainty (TVU) and Total Horizontal Uncertainty (THU) components and are already widely used for acoustic survey systems, such as multibeam echosounders. Semiautomated data processing algorithms such as Combined Uncertainty and Bathymetry Estimator (CUBE) and CUBE with Hierarchical Resolution Techniques are well established and accepted as part of standard hydrographic data processing protocols (Calder and Mayer 2003; Calder and Rice 2017), being used primarily for acoustic echo-sounding data, but require an estimate of uncertainty to be provided with the data for operation. Bathymetric and topo-bathymetric LIDAR have lagged behind acoustic surveying technologies in terms of the development and operational use of TPU models, and therefore also with respect to processing improvements.

Uncertainty propagation in bathymetric LIDAR systems has been a significant research interest in recent years, and several approaches have been proposed. Gonsalves (2010) predicted uncertainties in LIDAR point clouds for the Coastal Zone Mapping and Imaging LIDAR using the general law of propagation of variance (Wolf and Ghilani 1997). However, the challenge in that approach is that the technical details of the LIDAR-processing routines from commercial system providers are typically not available (Kinzel *et al.* 2013), which complicates determining a valid measurement model. Lockhart *et al.* (2008) proposed a depth variance method as a proxy for an analytical TPU model. However, the interaction of the laser beam with the environment, such as the water surface and the water column, is not accounted for in this approach. The effect of the environment on the bathymetric LIDAR measurement uncertainty has been investigated in a few studies. These studies mainly focused on the effect of the water surface on the bathymetric LIDAR measurement accuracy. The laser beam refraction angle standard deviation just below the water surface in along-wind and cross-wind directions has been reported to be in the range of 3–5° (Birkebak *et al.* 2018). Karlsson (2011) also investigated the effect of varying sea-state conditions on the bathymetric LIDAR measurement accuracy. The results showed that increasing wind speeds lead to lower measurement accuracy as demonstrated in simulation and empirical measurements. Westfeld *et al.* (2017) investigated the effect of refraction due to ocean waves on LIDAR bathymetry coordinates. The results suggested that lateral coordinate errors can be up to several decimeters as a result of the refraction pattern. It has been suggested (Steinvall and Kappari 1996) that maximum horizontal and vertical position errors are correlated with depth in strong wind speeds that range between 10–12 m/s. Horizontal errors were estimated to be within 5–10% of depth, and vertical errors were assumed to be 1–2% of depth. Although these studies investigated the effect of the water surface on bathymetric LIDAR measurements, other sources of uncertainty, such as the trajectory

Firat Eren and Brian R. Calder are with the Center for Coastal and Ocean Mapping, University of New Hampshire, 24 Colovos Road, Durham, NH 03824 (firat@ccom.unh.edu).

Jaehoon Jung, Christopher E. Parrish, and Nicholas Sarkozi-Forfinski are with Oregon State University Civil and Construction Engineering, 101 Kearney Hall, Corvallis, OR 97331.

Nicholas Sarkozi-Forfinski is also with the National Oceanic and Atmospheric Administration, National Geodetic Survey, Remote Sensing Division (Data Solutions and Technology Inc.), 1315 East West Highway, Silver Spring, MD 20910.

Photogrammetric Engineering & Remote Sensing  
Vol. 85, No. 8, August 2019, pp. 585–596.  
0099-1112/19/585–596

© 2019 American Society for Photogrammetry  
and Remote Sensing  
doi: 10.14358/PERS.85.8.585

obtained from the Global Navigation Satellite System (GNSS) aided Inertial Navigation System (INS) and the water column, were not included in the analyses. Carr (2016) proposed an analytical TPU model to account for the uncertainties due to the air-water interface and laser path trajectory. Nevertheless, the proposed approach relies on the high resolution Digital Surface Model of the water surface generated from the three-dimensional (3D) infrared (IR) camera device synchronized with the bathymetric LIDAR, and does not take into consideration the uncertainty contribution from the water column.

This study employs a TVU model that accounts for all the main component uncertainties, including those that arise both above and below the water surface, as well as at the air-water interface and the water column. The contributions from the subaerial (above water) and subaqueous (water surface to seafloor) models are computed separately and then combined to produce per-point LIDAR vertical uncertainty values, i.e. TVU values are generated for the LIDAR points that are identified as seafloor points. The prefix “sub” is used here to signify that these portions are two sub-models that compose the TVU model developed in this study. The results provide insight into the spatially-varying seafloor elevation uncertainty and may be useful in informing data acquisition and processing procedures.

## Methodology

### Survey Site and the Data Set

The topo-bathymetric LIDAR data used in this study were collected by NOAA NGS with a Riegl VQ-880-G system in Southwest Florida (vicinity of Cape Romano, Marco Island, and Gullivan Bay) in May 2016 (Figure 1). The nominal operating altitude of the aircraft was 600 m with beam divergence ranging from 0.7 to 2.0 mrad. The field-of-view for the system is  $\pm 20^\circ$ . The bathymetric channel of the LIDAR system (532 nm) employs a rotating prism to provide a circular scanning pattern with scan speed ranging from 10 to 80 rev/s and angular step width ranging from 0.007 to 0.052°. The data were acquired with a pulse repetition frequency of 145 kHz, which corresponds to an average point density of 9 points/m<sup>2</sup>. The flight speed during the survey was approximately 220 km/h. The survey site is approximately 193 km<sup>2</sup>, with a total of 1.5 billion bathymetric data points ranging from -18.7 to -30.5 m ellipsoidal height with depths ranging from 0 to 12 m relative to mean lower low water.

### General Approach

The topo-bathymetric LIDAR TVU model is broken into two main components, as depicted in Figure 2: the subaerial vector from the LIDAR to the water surface and the subaqueous

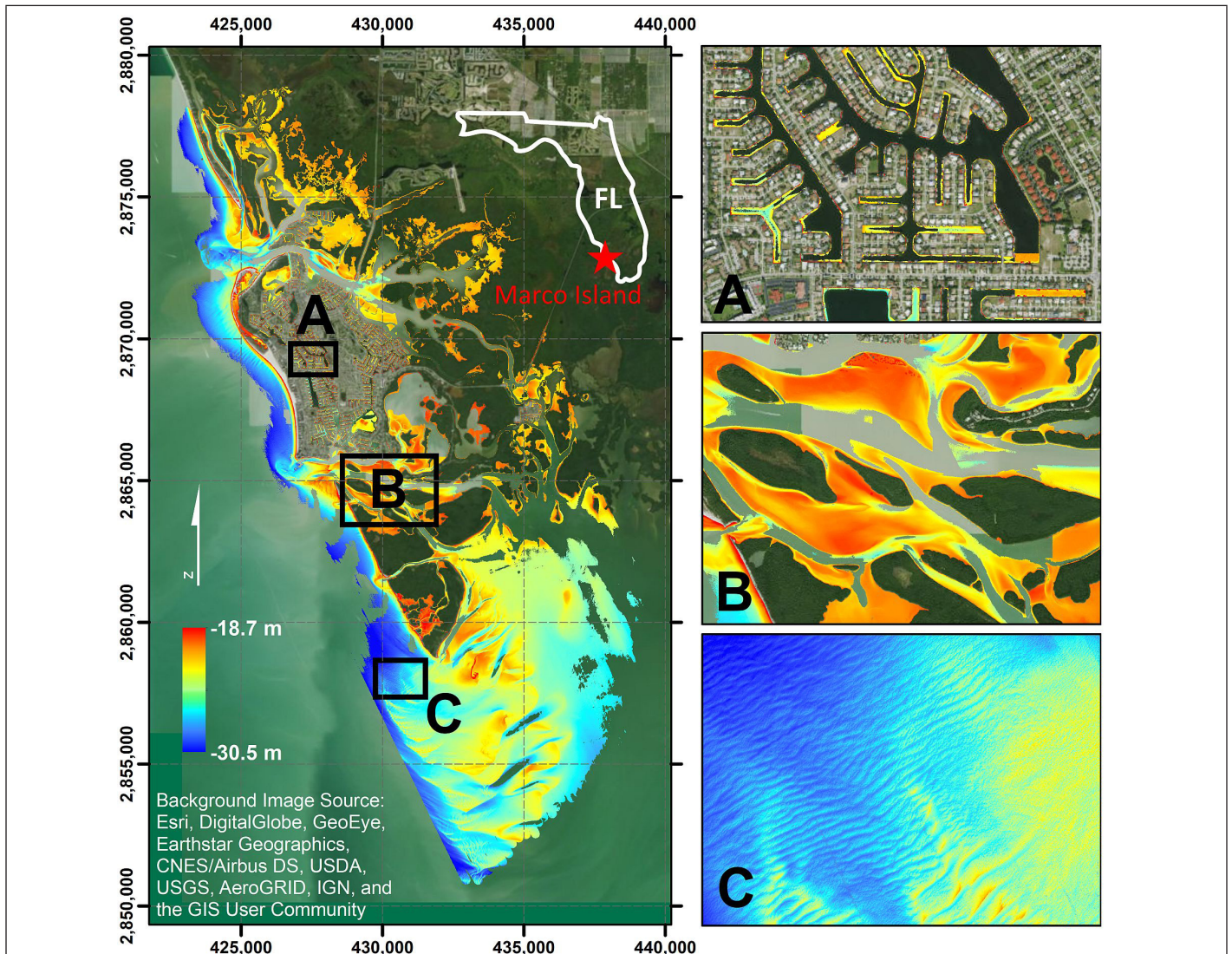


Figure 1. 1 m resolution digital elevation model created from the data points classified as bathymetry (LAS classification code 27): (A) residential area with network of waterways on Marco Island, (B) shallow bathymetry of tidal estuary, and (C) sand waves off the southern tip of Ten Thousand Island. EPSG code:26917: NAD83 / UTM zone 17N.

vector from the water surface to the seafloor. This decomposition reflects the relative complexity of the factors influencing the laser pulse throughout the travel path. The subaerial portion is a well-defined geometric problem that can be tackled using standard geomatics techniques, whereas the subaqueous portion involves complex interactions of light with water that are difficult to model deterministically and are, therefore, more amenable to a Monte Carlo simulation approach.

The workflow of the topo-bathymetric LIDAR TVU model is depicted in Figure 3. The input to the process consists of tiled point clouds in LASer (LAS) file format, version 1.2 (ASPRS 2008), generated from the Riegl VQ-880-G data using Riegl's RiProcess and RiHydro software, trajectory files (from the postprocessed GNSS-aided INS data), including parameter uncertainties, and basic environmental data (wind speed and assumed homogeneous water turbidity conditions). The input LAS tiles consist of 500 × 500 m square blocks, generally composed of data from multiple flightlines, following NOAA NGS protocols. Before analytical error propagation and Monte Carlo simulation are used to model the subaerial and subaqueous uncertainties, respectively, a series of preprocessing steps is performed to isolate the bathymetric data points from the full point cloud and time-match each bathymetric data point with the nearest 200 Hz trajectory data point. The uncertainties output from the subaerial and subaqueous models are then combined in quadrature to produce a final TVU value for each data point. The developed subaerial and subaqueous models are combined as a TVU model and implemented in a software program.

### Subaerial TVU Model

The workflow of the subaerial portion of the TVU model is demonstrated in Figure 4. The input trajectory parameters are the Tait-Bryan roll, pitch, and heading angles ( $r$ ,  $p$ ,  $h$ ), sensor coordinates ( $x_s$ ,  $y_s$ ,  $z_s$ ), and their corresponding standard deviations ( $\sigma_r$ ,  $\sigma_p$ ,  $\sigma_h$ ,  $\sigma_{x_s}$ ,  $\sigma_{y_s}$ ,  $\sigma_{z_s}$ ), all of which are obtained from text smoothed best estimate of trajectory (SBET) files output from Applanix Position and Orientation Systems (POS) Mobile Mapping Suite (MMS) software. Table 1 provides a summary of the input standard deviations for the TVU analysis, where the standard uncertainty of the scan range is obtained from manufacturer specifications. On the other hand, the standard uncertainties of the scan angles are not available in the specifications, but were provided to us by the manufacturer, as part of this research project. Once the geolocation equation and the

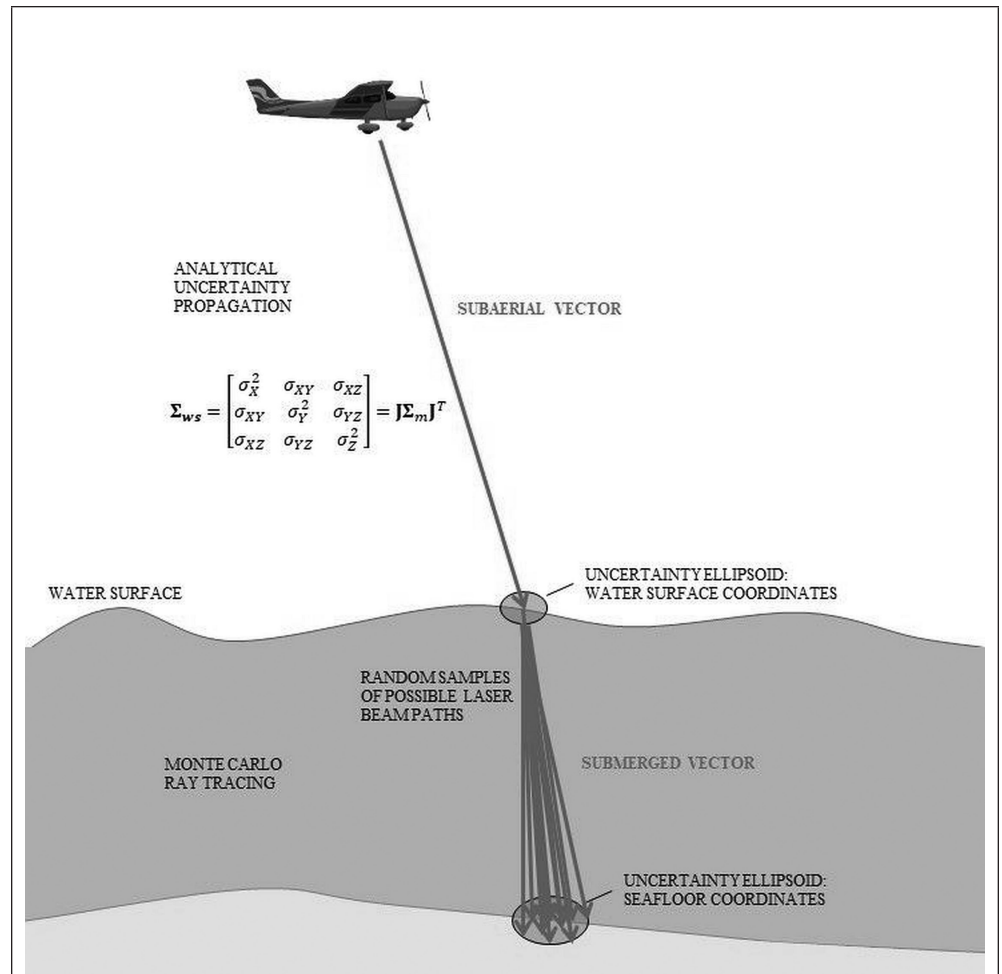


Figure 2. Decomposition of the total vertical uncertainty into subaerial (LIDAR to water) and subaqueous (water to seafloor) components.

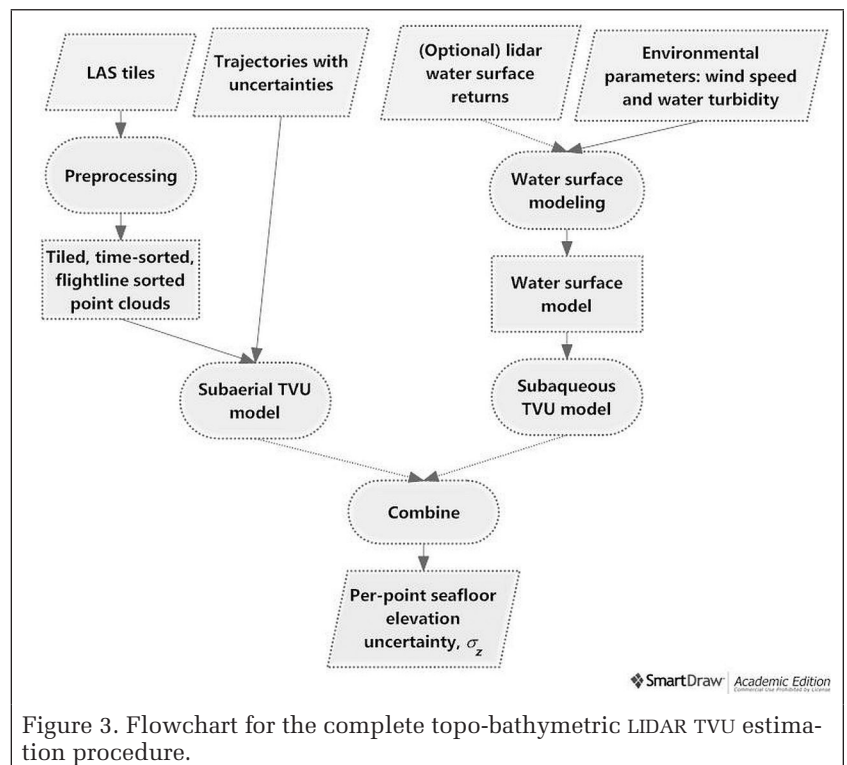


Figure 3. Flowchart for the complete topo-bathymetric LIDAR TVU estimation procedure.

Table 1. Summary of input standard uncertainties.

Component uncertainty	Standard uncertainty symbol	Where Obtained
Attitude angle	$\sigma_{r_t}, \sigma_{p_t}, \sigma_{h_t}$	Trajectory file (custom SBET)
Position	$\sigma_{x_t}, \sigma_{y_t}, \sigma_{z_t}$	Trajectory file (custom SBET)
Scan angle	$\sigma_\alpha, \sigma_\beta$	Discussions with the manufacturer
Range	$\sigma_\rho$	Sensor specification

input standard deviations are defined, the uncertainty of each laser point can be analytically quantified through the special law of propagation of variance.

#### Laser Geolocation Equation

Analytical uncertainty propagation requires a mathematical model expressing computed quantities (e.g., spatial coordinates) as a function of parameters or observations for which estimated uncertainties are known (Hartzell *et al.* 2015). In airborne LIDAR, this mathematical model is provided by the laser geolocation equation and component uncertainties. The version of the laser geolocation equation used in this research differs slightly from the one implemented in the manufacturer's processing software (RiProcess and RiHydro), due to lack of knowledge of proprietary details of the scanner. In particular, the formation of the range vector in the laser-scanner frame differs from the formation used by the manufacturer, which requires additional scan mechanism parameters. However, the version used in this work was confirmed by the manufacturer to provide realistic TVU estimates using scan angle uncertainties,  $\sigma_\alpha$  and  $\sigma_\beta$ , in the range of 0.020° to 0.025°. Figure 5 defines the circular scan geometry and coordinate system conventions adopted in this study. As the aircraft travels along the trajectory, the scan mechanism generates a circular scan pattern on the ground.

The basic geolocation equation with the configuration of Figure 5 can be written as:

$$\begin{bmatrix} x_l \\ y_l \\ z_l \end{bmatrix} = \begin{bmatrix} x_t \\ y_t \\ z_t \end{bmatrix} + \mathbf{R}_b^l \begin{bmatrix} \delta x \\ \delta y \\ \delta z \end{bmatrix} + \mathbf{R}_b^l \mathbf{R}_{ls}^b \mathbf{R}_{lb}^{ls} \begin{bmatrix} 0 \\ 0 \\ -\rho \end{bmatrix} \quad (1)$$

where  $\mathbf{R}_{lb}^{ls}$  is the rotation from the laser beam frame (*lb*), which is defined as in Bang *et al.* (2008), to the laser scanning unit (*ls*),

$$\mathbf{R}_{lb}^{ls} = \begin{bmatrix} 1 & 0 & 0 \\ 0 & \cos\alpha & -\sin\alpha \\ 0 & \sin\alpha & \cos\alpha \end{bmatrix} \begin{bmatrix} \cos\beta & 0 & \sin\beta \\ 0 & 1 & 0 \\ -\sin\beta & 0 & \cos\beta \end{bmatrix} \quad (2)$$

and  $\mathbf{R}_b^l$  is the rotation from the IMU body frame (*b*) to the local level frame (*l*),

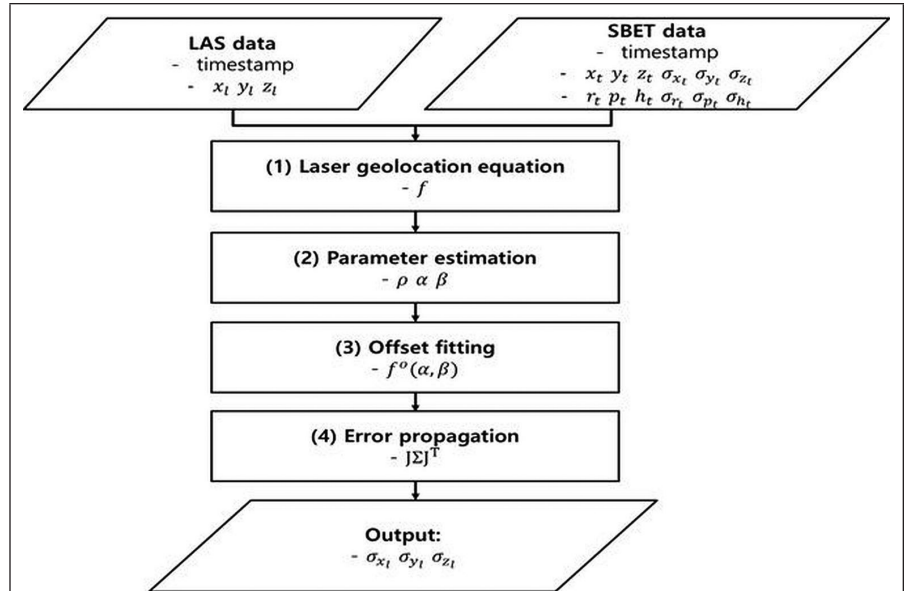


Figure 4. Subaerial TVU modeling workflow.

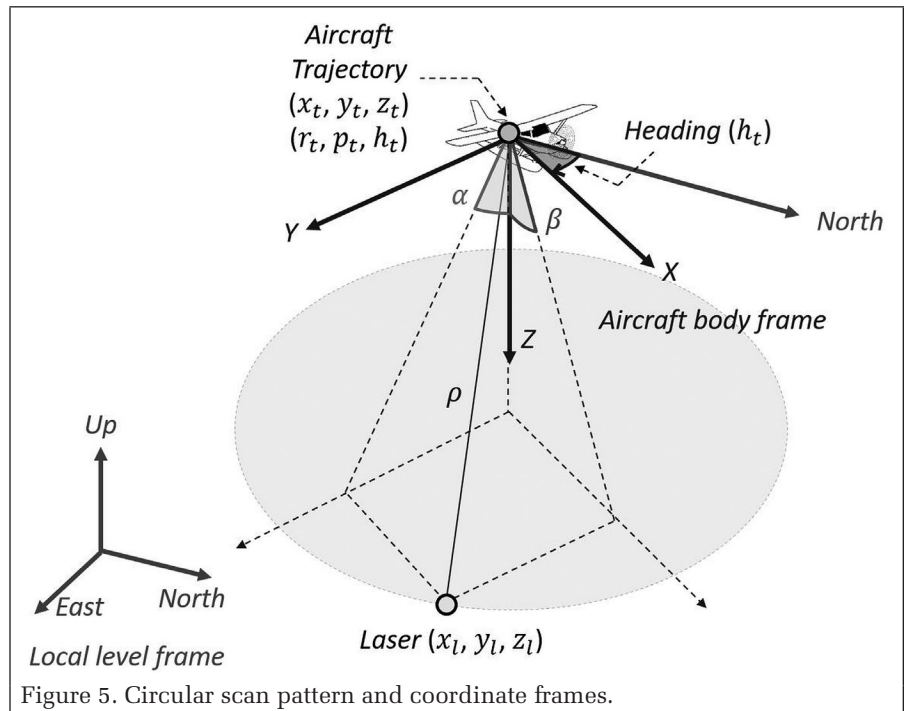


Figure 5. Circular scan pattern and coordinate frames.

$$\mathbf{R}_b^l = \begin{bmatrix} \cosh_t & -\sinh_t & 0 \\ \sinh_t & \cosh_t & 0 \\ 0 & 0 & 1 \end{bmatrix} \begin{bmatrix} \cos p_t & 0 & \sin p_t \\ 0 & 1 & 0 \\ -\sin p_t & 0 & \cos p_t \end{bmatrix} \begin{bmatrix} 1 & 0 & 0 \\ 0 & \cos r_t & -\sin r_t \\ 0 & \sin r_t & \cos r_t \end{bmatrix} \quad (3)$$

and  $\mathbf{R}_b^l$  is the boresight angle misalignment matrix and  $[\delta x, \delta y, \delta z]$  is the lever arms determined in the boresight calibration between the laser scanning unit (*ls*) and the IMU body frame (*b*) (Bang *et al.* 2008). In the present version of the code, we assume both the misalignment angles and lever arms are zero. This assumption, while seemingly dangerous, is actually safe, because: 1) NGS performs a rigorous boresight calibration procedure, and these misalignment angles and offsets are already accounted for in the orientation parameters and sensor coordinates that form the input to our procedures, and 2) the uncertainties associated with any residual misalignment

are negligible in comparison to those in the trajectory parameters and scan angles. However, it should be noted that it is straightforward to modify the tool to include the boresight misalignment angles, when and where available.

**Parameter Estimation**

The trajectory parameters ( $x_t, y_t, z_t, r_t, p_t, h_t$ ) are available from the SBET generated in the Applanix POS MMS software. Because the georeferenced laser points are available from Riegls RiProcess software, the unavailable scan angles ( $\alpha, \beta$ ) and range ( $\rho$ ) can be derived from the inverse of Equation 1. First, the scan range can be estimated by calculating the Euclidean distance

$$\rho = \sqrt{(x_l - x_t)^2 + (y_l - y_t)^2 + (z_l - z_t)^2} \quad (4)$$

Equation 1 can then be simplified, neglecting the first and the second columns of  $R_b^s$ , giving

$$R_b^{JT} \begin{bmatrix} x_l - x_t \\ y_l - y_t \\ z_l - z_t \end{bmatrix} = -\rho \begin{bmatrix} \sin\beta \\ -\sin\alpha\cos\beta \\ \cos\alpha\cos\beta \end{bmatrix} \quad (5)$$

so that  $\alpha$  and  $\beta$  can be calculated by direct substitution from top to bottom.

**Error Propagation**

Once all the input variances and the measurement model are defined, the uncertainty of each laser point can be analytically computed through the mathematical model according to the special law of propagation of variances (Wolf and Ghilani 1997). For each laser shot, the error covariance matrix,  $\Sigma$ , is formed as:

$$\Sigma = \begin{bmatrix} \sigma_X^2 & \sigma_{XY} & \sigma_{XZ} \\ \sigma_{XY} & \sigma_Y^2 & \sigma_{YZ} \\ \sigma_{XZ} & \sigma_{YZ} & \sigma_Z^2 \end{bmatrix} = J \begin{bmatrix} \sigma_\alpha & \dots & 0 \\ \vdots & \ddots & \vdots \\ 0 & \dots & \sigma_\rho \end{bmatrix} J^T \quad (6)$$

where  $J$  is the Jacobian matrix containing partial derivatives of the laser geolocation equation defined in Equation 1 with respect to the nine inputs (i.e., five rotation and four translation parameters) and  $[\sigma_\alpha \dots \sigma_\rho]$  are the input standard uncertainties listed in Table 1.

**Subaqueous TVU Model**

The subaqueous portion of the TVU model is solved via Monte Carlo simulation (Figure 6), where a water surface model either from the survey data or a theoretical wave spectrum is combined with a user-selected diffuse attenuation coefficient, which measures turbidity. Here, a single water surface model is used for the survey data derived water surface model. For the theoretical wave spectrum, separate water surface models are created based on wind speed.

**Water Surface Model Based on 1D Wave Spectrum**

Wave spectrum generated water surface models are used in the subaqueous portion of the TVU model. In this approach, the Elfouhaily, Chapron, Katsaros, and Vandemark (ECKV) spectrum, a one-dimensional (1D) wave model that is typically used to represent capillary gravity waves, is used to model the water surface (Elfouhaily *et al.* 1997). The ECKV spectrum also provides a wave regime that is typically observed in bathymetric LIDAR survey conditions (Karlsson 2011). The inputs to the ECKV wave spectrum model are the wind speed and a dimensionless wave age parameter,  $\Omega$ , which varies from very young ( $\Omega = 5$ ) to fully developed ( $\Omega = 0.84$ ) waves. To reach a surface wave realization, the 1D wave spectrum is combined with a spreading function to obtain the one-sided two-dimensional (2D), directional variance spectrum (Mobley 2016); here, the spreading function chosen is cosine-2s to model the capillary-gravity wave regime (Mitsuyasu *et al.* 1975). The inverse Fourier Transform of the 2D directional wave spectrum results in the generation of a plausible water surface. After the water surface is generated, it is triangulated using Delaunay triangulation and the normal to the water surface is calculated at each point of interest (Delaunay 1934); the normal of the water surface facets are used in simulating the refraction of the laser rays into the water column (De Greve 2006).

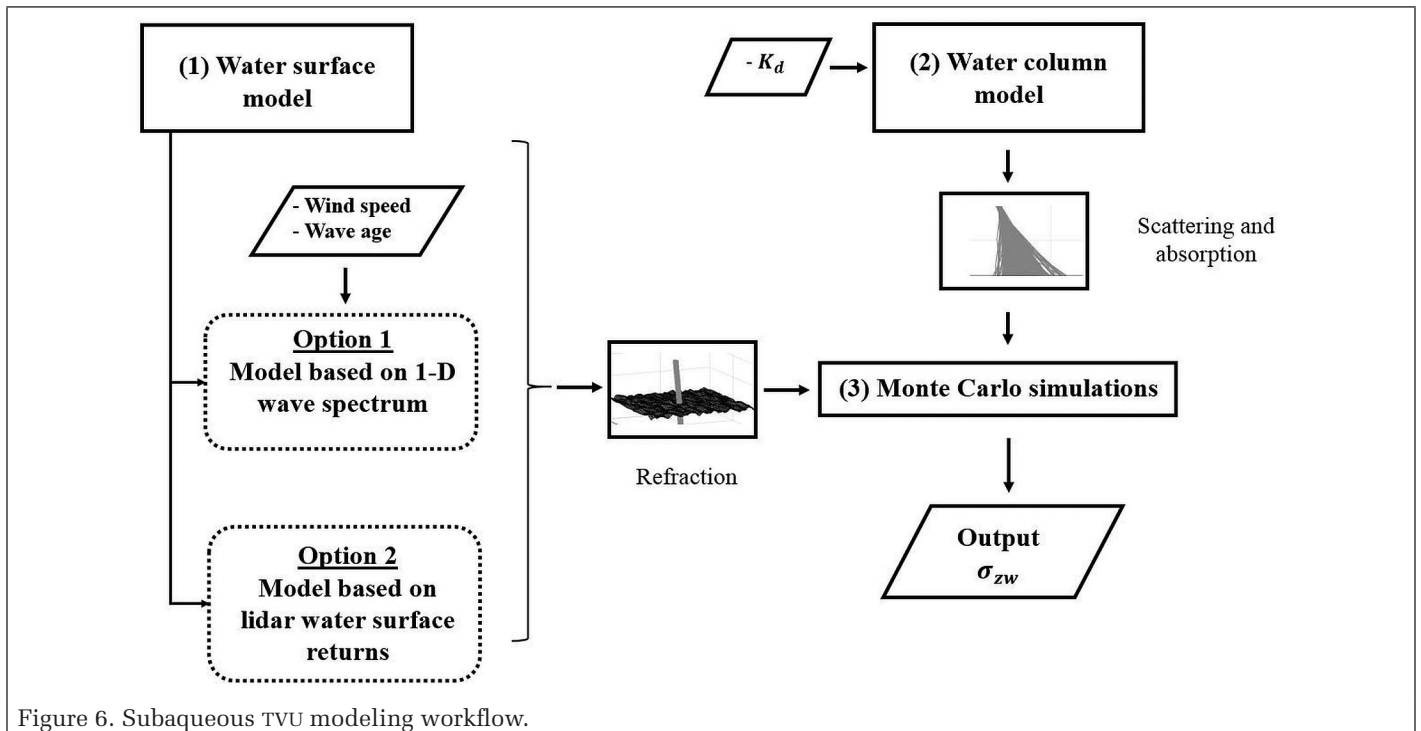


Figure 6. Subaqueous TVU modeling workflow.

### Water Surface Model Based on LIDAR Surface Returns

The second option to model the water surface is by using the LIDAR surface returns obtained during the survey. However, there are two challenges to directly modeling the water surface using the LIDAR point clouds: outliers above the water surface due to sea birds or diffused noisy points, and laser returns from the water column. Here, a two-step approach was taken to model the water surface. First, the outliers above the water surface are filtered out by using an outlier algorithm. Then, the water column data were filtered by using only the first returns as classified by the waveform processing algorithm. The remaining water surface points were then triangulated using Delaunay triangulation (Figure 7).

### Water Column Model

The Monte Carlo simulations within the water column are based on Mobley (1994) and Boss (2013). To model the scattering of the laser beam in the water column, the beam attenuation coefficient,  $c_b$ , is used. However, because it is inherently difficult to empirically measure  $c_b$ , it is instead estimated from the diffuse attenuation coefficient of downwelling irradiance,  $K_d$ . The advantage of this method is that  $K_d$  can be estimated from satellite data through remote sensing algorithms close to the survey time (Adi *et al.* 2003; Stumpf and Pennock 1991; Lee *et al.* 2005; Morel *et al.* 2007). Although there are fundamental physical differences between  $c_b$  and  $K_d$ , there is also correlation between the two. Based on the empirical measurements conducted in a variety of water turbidity conditions, Shannon (1975) proposes

$$c_b \cong \frac{K_d - 0.04}{0.2} \quad (7)$$

which results in a coefficient of determination of  $R^2 = 0.98$ . The empirical model provided in Equation 7 is valid for  $K_d$  in the range  $0.06 \text{ m}^{-1} \leq K_d \leq 0.36 \text{ m}^{-1}$ .

As the laser rays travel through the water column, they encounter potential scattering events every  $q$  meters, where the geometric distance  $q$  is given by:

$$q = -\frac{1}{c_b} \ln R_1 \quad (8)$$

where  $R_1 \sim U(0,1)$ , a uniform random variable. The ray is scattered with probability  $\omega_0 = b/c_b \approx 0.55 - 0.93$  (at 532 nm), where  $\omega_0$  is the single scattering albedo and  $b$  is the scattering coefficient. Here,  $\omega_0 = 0.8$  is used, and the scattering is assumed to be inelastic (Guenther 1985).

One important consideration for the laser ray path modeling in the water column is the scattering direction of the laser ray once it undergoes a scattering event. The photon direction is randomly determined by using a phase function,  $\beta(\psi, \varphi)$ , where  $\psi$  is the scattering angle and  $\varphi$  is the azimuthal angle that is uniformly distributed in the range  $0-2\pi$ , i.e.  $\varphi = 2\pi R_2$  where  $R_2 \sim U(0, 1)$ , a uniform random variable. The phase function,  $\beta$ , used in this study is the Henyey-Greenstein phase function (Boss 2013) with the forward scattering parameter selected as  $g = 0.995$ , which gives a forward scattering angle of

$$\psi = \cos \left[ \frac{1+g^2}{2g} - \frac{1}{2g} \left( \frac{1-g^2}{1+g-2gR_3} \right)^2 \right] \quad (9)$$

where  $R_3 \sim U(0, 1)$ , a uniform random variable. The laser ray path within the water column is simulated by taking into account the scattering angle and the mean free path length. The Monte Carlo simulations in the water column continue until the laser rays intersect with the reference seafloor elevation. The parameters  $K_d$ ,  $\omega_0$ , and  $g$  are input to the water column portion of the Monte Carlo simulations.

Another consideration taken into account in the Monte Carlo simulations is how the energy pattern changed during the laser beam propagation within the water column. During refraction, some portion of the incident light reflects from the water surface and results in  $\sim 2\%$  energy loss as described by Fresnel's law. Within the water column, as the laser beam propagates, the laser ray undergo absorption which result in energy loss and scattering which determines the laser ray

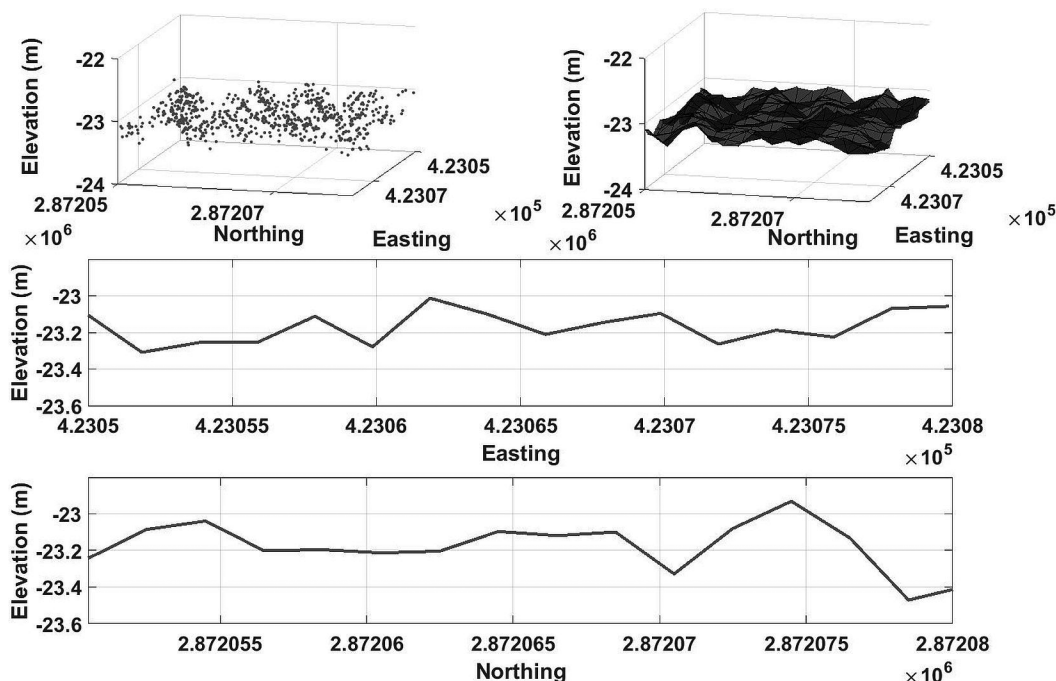


Figure 7. 3D water surface model obtained from the LIDAR surface returns obtained during the survey. (a) The first returns from the LAS data. (b) 3D water surface model triangulated by Delaunay triangulation. (c) The profile line of 3D water surface model along Easting. (d) Profile view of 3D water surface model along Northing.

direction. The laser ray energy distribution on the water surface is assumed to be Gaussian and the loss mechanisms, as modeled by Beer's law, are taken into account to calculate the final laser ray energy, as demonstrated in Eren *et al.* (2013).

#### Monte Carlo Simulations

The Monte Carlo simulation parameters are selected based on the manufacturer hydrographic survey parameters (Riegl 2016). A beam divergence angle of 1 mrad was used, which results in a laser beam footprint diameter of ~0.68 m on the water surface (flight altitude of 600 m). The finite laser beam was simulated with 1000 rays whose locations were spaced at equal intervals in a circular pattern within the laser beam footprint. The circular pattern is kept the same at each simulation configuration to eliminate the uncertainty due to the laser ray locations just above the water surface. For modeled water surfaces, the Monte Carlo simulations were repeated 2000 times, with wind speed ranging from 1–10 m/s at 1 m/s increments, diffuse attenuation coefficient,  $K_d$ , varying from very clear to more turbid waters, i.e., 0.06–0.36  $\text{m}^{-1}$  at 0.01  $\text{m}^{-1}$  increments, and water depth from 1–10 m at 0.1 m increments. This results in a total of more than 56 million simulations for the modeled water surface with ECKV spectrum. The same simulation configuration was kept for the LIDAR surface return-generated water surface model. In this case, wind speed was not included in the Monte Carlo simulations as the water surface is directly modeled through the water surface returns. The Monte Carlo simulations conducted for this case resulted in more than 5.6 million simulations. The seafloor elevation calculation in the Monte Carlo simulations was conducted by taking the average of the ray paths that intersect the seafloor. The seafloor elevation is then

$$\Delta z = r \cos \frac{\theta}{n_i} \quad (10)$$

where  $r$  is the ray path length that reaches to the seafloor,  $\theta$  is the laser off-nadir angle ( $\theta = 20^\circ$ ), and  $n_i$  is the index of refraction of the water ( $n_i = 1.33$ ). At each simulation configuration, the variation of the seafloor elevation obtained from the subaqueous portion, i.e.,  $\sigma_{zw}$ , is stored. The final per-pulse uncertainty value is:

$$\sigma_z = \sqrt{\sigma_{z_i}^2 + \sigma_{zw}^2} \quad (11)$$

where  $\sigma_{z_i}$  is the uncertainty of the laser point on the water surface as obtained from the subaerial portion. As a practical matter, the Monte Carlo simulations take approximately a week to run on a quad-core 3.6 GHz computer in MATLAB. Therefore, the results of the simulations were used to construct a look-up table which consists of polynomial fits corresponding to specific wind speed and diffuse attenuation coefficient (see the section "Monte Carlo Simulations").

## Results

### Monte Carlo Simulations

The Monte Carlo simulations conducted in the subaqueous model demonstrate the variation in the seafloor elevation measurement as a result of the variation in the water surface and water column turbidity. Two simulation examples conducted for a water surface modeled with the ECKV spectrum with 2 m/s winds and  $K_d = 0.10 \text{ m}^{-1}$  ( $c_b = 0.3 \text{ m}^{-1}$ ) for seafloor elevation are demonstrated in Figure 8. The reference seafloor elevation in the figures is 5 m, with wave age,  $\Omega = 0.84$ .

The resulting energy patterns on the seafloor obtained from the Monte Carlo simulations are compared with the empirical measurements conducted at the University of New Hampshire Ocean Engineering facilities (Karlson 2011). The experimental setup to observe the laser beam shape consisted of a camera

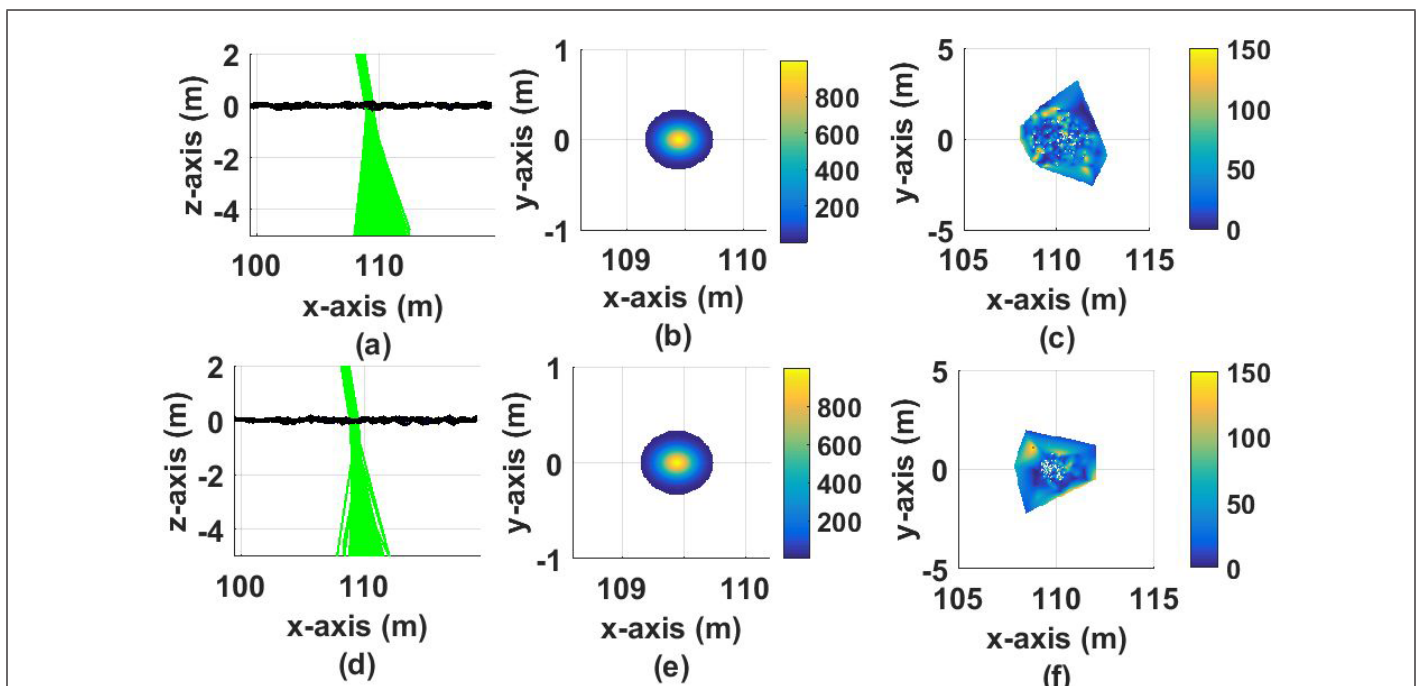


Figure 8. Monte Carlo simulation results for water surface modeled with ECKV spectrum with wind speed of 2 m/s and  $K_d = 0.10 \text{ m}^{-1}$ . The reference seafloor elevation is 5 m. Two different cases at each row result in deep (5.09 m) and shallow bias (4.85 m) in the first and second row, respectively. (a, d) Front view of the laser beam incident on the water surface and the ray paths that refract and scatter within the water column. (b, e) The laser beam footprint on the water surface with a Gaussian energy pattern. The color axis denotes the energy of the laser beam on the water surface in arbitrary units with maximum energy of 1000. (c) The resulting laser beam footprint on the seafloor with deep bias. (f) The resulting laser beam footprint on the seafloor with shallow bias.

placed at the bottom of a wave tank and a white plastic sheet to record the image. The refraction due to the wind waves that are generated by a fan mounted on the wave tank and the scattering within the water column resulted in non-uniform laser beam energy distribution pattern as shown in Figure 9.

Extended Monte Carlo simulations were conducted to calculate the overall contribution of the variation in wind speed,  $K_d$  and depth on the seafloor elevation variation. The simulations conducted for ECKV and LIDAR surface return generated water surface models demonstrate the correlation between the two methods (Figure 10). The LIDAR surface return generated water surface model in Figure 10a is generated with  $K_d = 0.08 \text{ m}^{-1}$ , while the ECKV water surface model in Figure 10b was generated with 1 m/s wind speed with wave age  $\Omega = 0.84$  and  $K_d = 0.08 \text{ m}^{-1}$ .

The results in Figure 10 indicate that the LIDAR surface return generated water surface model is closely approximated

with the ECKV model surface at wind speeds of 1 m/s and  $\Omega = 0.84$ . The second order polynomial fit coefficients for the two methods are close to each other ( $R^2 = 0.997$  and  $R^2 = 0.996$  for LIDAR surface return generated and ECKV surface models, respectively). Further analysis demonstrated that the root mean square error (RMSE) calculated for  $\sigma_{zw}$  between the two methods is 0.001 m.

For efficiency during uncertainty attribution, second-order polynomial fits were made to the simulation results, so that they can be used as look-up tables.  $R^2$  histogram plots and statistics for the simulations conducted for both LIDAR surface return generated and ECKV water surface model are shown in Figure 11 and Table 2.

The results in Figure 11 and Table 2 show that very high  $R^2$  values are obtained for second order polynomial fits in the vertical elevation uncertainty versus depth plots. The mean  $R^2$  value for all configurations is 0.997 for ECKV water surface

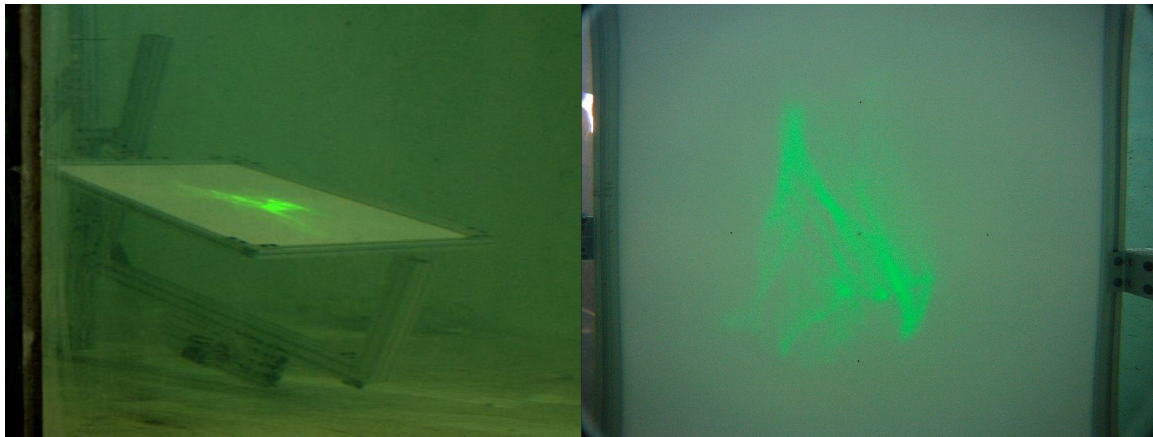


Figure 9. Empirical setup and the resulting laser beam shape images after refraction into the water column (Karlson 2011). Images are courtesy of Dr. Shachak Pe'eri.

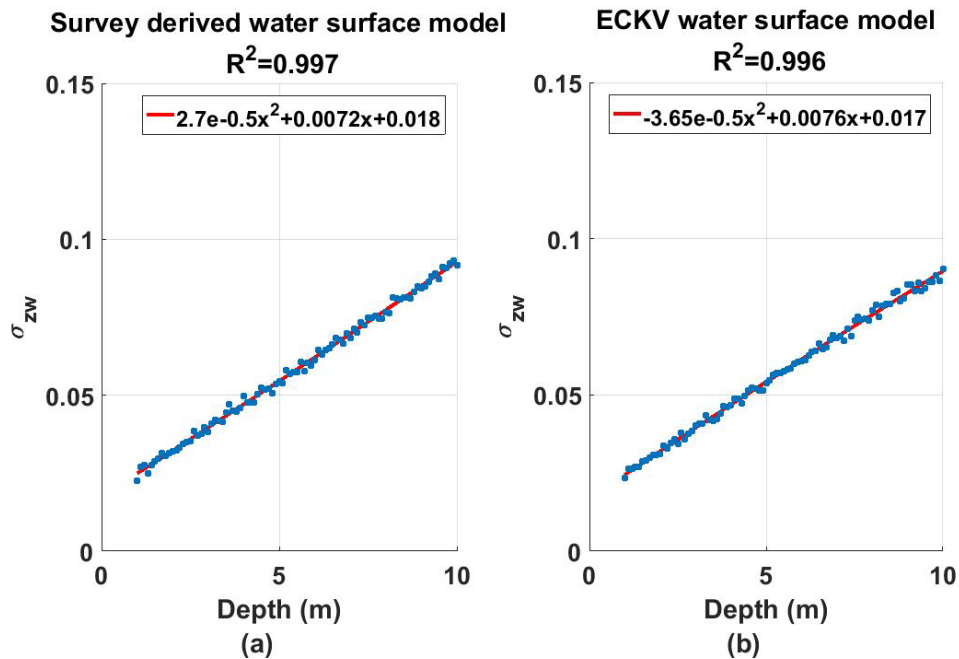


Figure 10. Comparison of the simulated vertical seafloor elevation standard deviation ( $1\sigma$ ) between (a) LIDAR surface return generated water surface model and (b) ECKV water surface model. Blue dots denote the vertical uncertainty data and red line denotes the polynomial fit. (Note that although a linear fit would suffice in the examples shown here, for other combinations of wind speed and  $K_d$ , a quadratic is merited; in no observed cases is a higher-order polynomial required.)

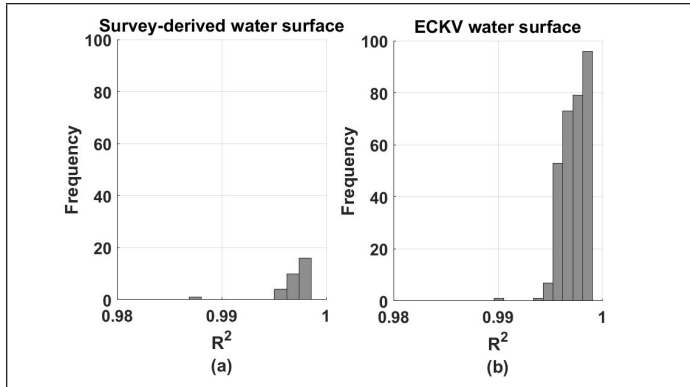


Figure 11.  $R^2$  histograms obtained from the 2nd order polynomial fit approach (a) LIDAR surface return generated water surface model (b) ECKV water surface model.

Table 2.  $R^2$  statistics obtained from the 2nd order polynomial fit approach for the Monte Carlo simulation configurations.

	Water Surface Model	
	Survey	ECKV
Mean	0.997	0.997
Max.	0.999	0.999
Min.	0.987	0.989
Std.	0.002	0.001
Sample size	31	310

and LIDAR surface return derived water surface models with minimum  $R^2$  values is 0.987. These results verify the vertical subaqueous uncertainty values ( $\sigma_{zw}$ ) can be suitably approximated by second order polynomial fits.

**Uncertainty Surface**

The final topo-bathymetric LIDAR TVU is computed from the seafloor elevation standard deviations obtained from subaerial and subaqueous portion on a per-pulse basis. The output is a three-dimensional point cloud containing three vertical elevation uncertainty attributes:  $\sigma_{zi}^2$  (subaerial),  $\sigma_{zw}$  (subaqueous),

and  $\sigma_z$  (total). The corresponding 95% confidence level values are also computed as:

$$U_{95\%CL} = 1.96\sigma_z \tag{12}$$

Purely for visual analysis in this study, the general problem being more complex (Calder 2015), the per-pulse vertical elevation uncertainties were interpolated to a regularly-spaced grid and displayed as an uncertainty surface (Figure 12). The discernable flight lines seen in the TVU surfaces, which would generally indicate an unacceptable artifact in bathymetric surfaces, are entirely plausible in TVU surfaces, as they reflect actual variation in component uncertainties from one flight line to the next. These can be due, for example, to differences in the number of visible GNSS satellites at different headings, or slight differences in flight altitude between adjacent flight lines.

**Comparison with Empirically-Determined Seafloor Elevation Uncertainties**

As a forward predictive model that includes all known uncertainty effects, there is no ready way to verify the uncertainties generated by this method against field observations, since there are no fully repeated observations, and ground control points in the water are difficult to generate. It is of course possible to approximate the uncertainty by, for example, examining the agreement between two passes over the same area, or by examining the empirical standard deviation of observations around a local mean. Both methods, however, measure only repeatability, and therefore will tend to underestimate the true uncertainty since any common-mode effects will not be reflected in the estimates. For example, any uncertainty in the determination of the ellipsoid-datum offset will be common to all data within an area, and therefore unobservable through differencing methods.

Understanding that such methods generally provide a lower bound to the potential observational uncertainty, in this work the empirical standard deviation has been used as a point of comparison. For each area of interest, all of the points marked as “bathymetry” by the NOAA, NGS, RSD in the source data were selected, and a local mean and standard deviation

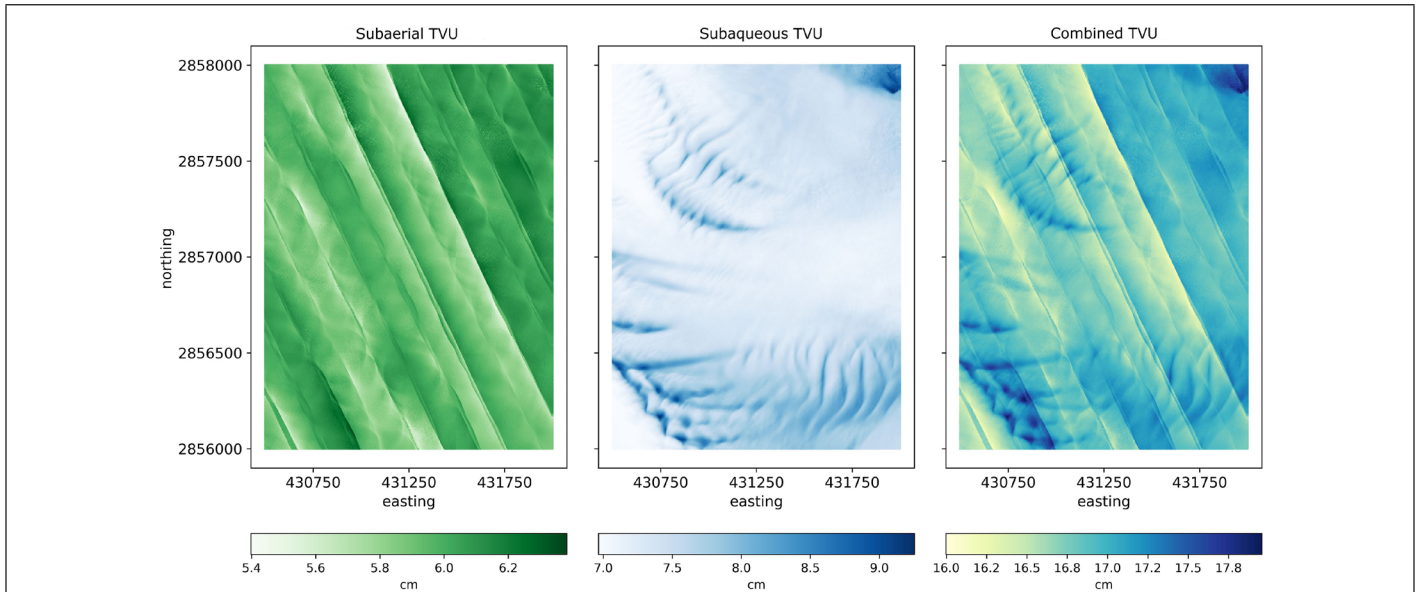


Figure 12. The subaerial and subaqueous TVU components and the combined TVU (subaerial, subaqueous, and vertical transformation TVU combined in quadrature). The TVU values are reported at the 95% confidence level. The grid units represent UTM (NAD83 (2011)) zone 17 eastings and northings in meters.

were computed in hexagonal bins (1 m bin spacing) across the area. Point comparisons of individual observation uncertainty and distributional estimates can then be formed. It should be noted that the water surface model generated from the LIDAR water surface returns is used in this analysis, which included the refraction correction.

The results of this comparison are depicted graphically in Figure 13. The modelled estimates clearly capture the variability of uncertainty as a function of depth, and the left-skewed nature of the empirically observed uncertainty distribution, suggesting that the major features are being modelled effectively. The scale of the distribution of the modelled uncertainties is, as expected, higher than the average empirical estimate due to common-mode effects not being included in the empirical estimates; some significant density in the empirical estimates is observed beyond the upper limit of modelled uncertainty, however. This may be caused either by residual outliers in the processed data, or effects of small bathymetric features in the 1m spatial analysis cells: estimation of standard deviation is sensitive to outliers.

The mean value of the modelled uncertainty is, however, of the same magnitude as the upper reaches of the empirical estimates, which suggests that the modelled uncertainty can be used as a plausible guide to the uncertainty of the observations. The values being generated are conservative, but not overly so, which is typically what is required by users of TPU estimates (Calder and Mayer 2003).

## Discussion

Although the results indicate that the TVU results are plausible, there are several assumptions in the subaqueous portion to address. In the ECKV water surface model, hydrodynamic forces were not taken into account. In the water column simulations, we have adopted an empirical model that expresses the relationship between the beam attenuation coefficient and the diffuse attenuation coefficient as provided by Shannon (1975). However, this model may not be valid for every study site. In addition, the scattering directions in the Monte Carlo simulations in the water column are based on the Henyey-Greenstein phase function. Although not verified

in this study, using different phase functions such as the Fournier-Forand phase function may lead to different results. Similarly, in the water column simulations, inelastic scattering is assumed, i.e., the wavelength is assumed to be constant after interaction with particles. Integration of elastic or Raman scattering may also lead to different results than provided in the study.

Two different surface model representations were used in the subaqueous portion. The main advantage of the ECKV modeled water surface is that the surface waves with wavelengths that are smaller than the laser beam footprint on the water can be modeled. The disadvantage of this method is that the environmental parameters used in the model such as wind speed and wave age may not fully represent the actual water surface during the survey. On the other hand, the advantage of the LIDAR water surface return generated water surface model is that LIDAR surface return data from the survey are used without relying on models and on ancillary environmental data, such as wind speed and wave age. However, the disadvantage of this method is the assumption that the wavelengths are greater than or equal to the laser beam footprint on the surface. With that said, the vertical elevation uncertainty values obtained from these models showed a reasonable correlation, with RMS value of 0.001 m for the data provided in Figure 10. This shows that modeled water surface results can closely approximate the empirical water surface models. This finding is critical in the sense that if the water surface return data from the manufacturer is not available or if it is not possible to generate empirical water surface returns, the modeled water surface return approach can be used as an alternative to calculate the vertical seafloor elevation uncertainty. Another interesting result obtained from the study is that second order polynomial fits performed very well in estimating the vertical seafloor elevation uncertainty as a function of depth for both LIDAR water surface return and ECKV modeled water surface. The statistical analysis of the coefficient of determination values showed that the mean vertical seafloor elevation uncertainty  $R^2$  values for LIDAR water surface return and ECKV modeled water surface models were larger than 0.997. However, it is also observed that at each simulation configuration, the second order polynomial coefficient values are different. This

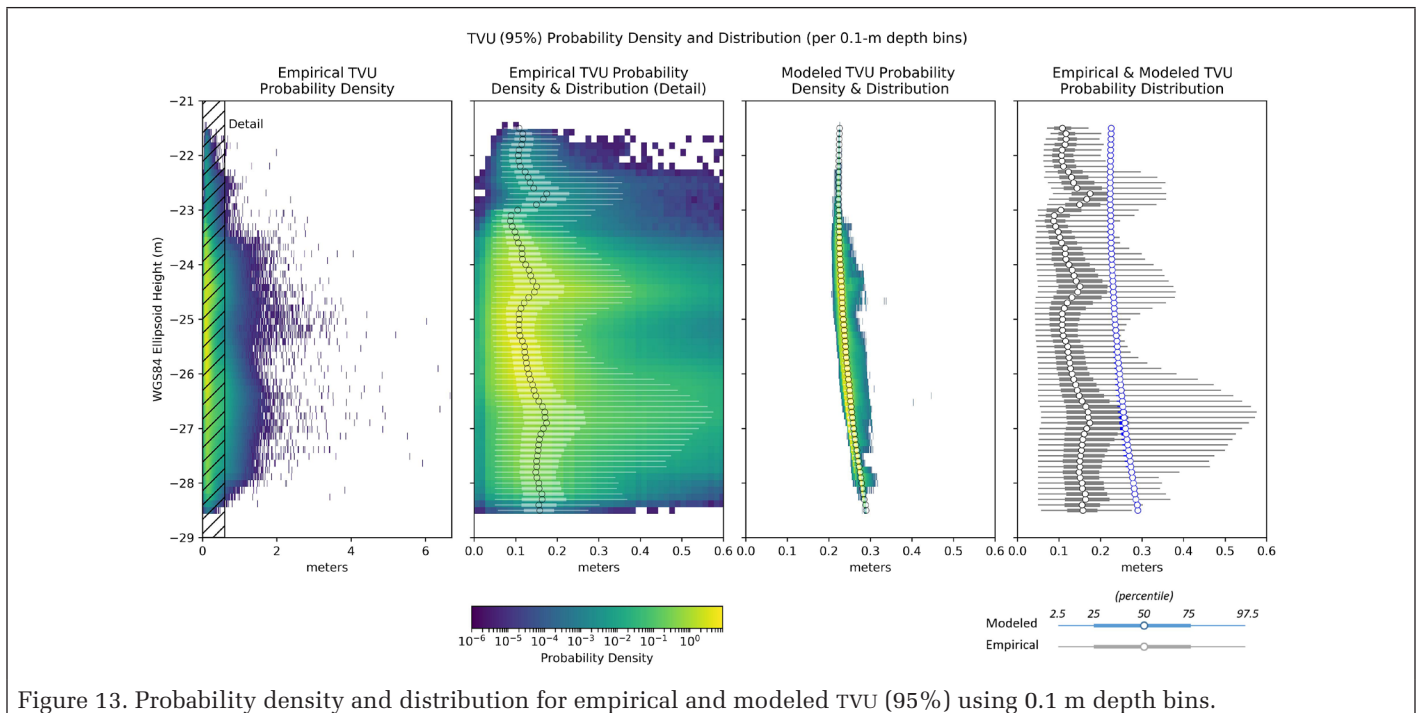


Figure 13. Probability density and distribution for empirical and modeled TVU (95%) using 0.1 m depth bins.

suggests that a single general uncertainty model to estimate vertical seafloor elevation uncertainty for every environmental condition is not sufficient. Instead, water surface characteristics and water turbidity should be taken into account to estimate the vertical seafloor elevation uncertainty more accurately.

Another component of the overall TVU model that has been identified for enhancement is the subaerial ranging uncertainty. Currently, the subaerial TVU model uses the constant ranging precision provided by the manufacturer as an estimate of the in-air ranging uncertainty. However, it is recognized that the ranging uncertainty is, in general, not constant, but rather, a function of a number of environmental and acquisition variables. Ongoing work by the project team includes developing, testing and implementing a more robust in-air ranging uncertainty model.

Although variations in the environment such as the water surface and the water column turbidity are taken into account in this paper, there are other sources of uncertainty that may be significant. The variation in the seafloor material type is also reported to have a potential impact on the vertical uncertainty (Eren *et al.* 2018). Therefore, contribution from the seafloor reflection such as bottom roughness should also be investigated in the future.

## Conclusions

This study involved development, implementation and testing of a comprehensive TVU model for topo-bathymetric LIDAR, accounting for uncertainties in the subaerial and subaqueous portions. The subaerial portion uses analytical uncertainty propagation (special law of propagation of variances), along with a custom laser geolocation equation and trajectory uncertainties output from the post-processed GNSS-aided INS solution. In the subaqueous portion, Monte Carlo simulations are conducted to analyze the effect of water surface and the water column turbidity on the seafloor elevation uncertainty. The computational efficiency can be greatly enhanced by running the Monte Carlo simulations for various combinations of wind speed and turbidity in advance and computing and storing parameters of a quadratic fit of subaqueous depth uncertainty to depth for each pair of the two independent variables. The results from the subaerial and subaqueous portions are combined to generate a final seafloor elevation uncertainty value on per-pulse basis. A comparison between the modelled uncertainty and an empirical estimate of variability showed that the model is a conservative estimate, as expected, but not overly so. These results indicate a strong potential to use the developed TVU model for ingestion of the topo-bathymetric LIDAR data into hydrographic workflows. A Python implementation of the TVU model is currently being transitioned into operational use for topo-bathymetric LIDAR projects in NOAA's NGS. Future work will entail adapting the TVU model to additional topo-bathymetric LIDAR systems operated by partner agencies of the JALBTCX.

## Acknowledgments

This study was supported by the University of New Hampshire/National Oceanic and Atmospheric Administration (NOAA) Joint Hydrographic Center Award Number NA15NOS4000200. The authors would like to acknowledge Mike Aslaksen, Gretchen Imahori, and Stephen White from NOAA Remote Sensing Division. The authors would also like to acknowledge Dr. Shachak Pe'eri from NOAA Office of Coast Survey for providing the experimental laser beam images.

## References

- Adi, N. S., S. Phinn and C. Roelfsema. 2013. Estimating the diffuse attenuation coefficient from moderate spatial resolution, multi-spectral satellite data in a seagrass environment. Pages 310–313 in *IEEE International Geoscience and Remote Sensing Symposium (IGARSS)*.
- ASPRS Board. 2008. LAS specification version 1.2. Proc. ASPRS Board Meeting.
- Bang, K. I., A. F. Habib, K. Kusevic and P. Mrstik. 2008. Integration of terrestrial and airborne LiDAR data for system calibration. Pages 391–398 in *Proceedings International Archives of the Photogrammetry, Remote Sensing and Spatial Information Sciences*.
- Birkebak, M., F. Eren, S. Pe'eri and N. Weston. 2018. The effect of surface waves on airborne lidar bathymetry (ALB) measurement uncertainties. *Remote Sensing* 10:453.
- Boss, E. 2013. Scattering. <<http://www.oceanopticsbook.info/view/scattering/definitions>> Accessed 10 January 2018.
- Calder, B. R. and L. A. Mayer. 2003. Automatic processing of high-rate, high-density multibeam echosounder data. *Geochemistry, Geophysics, Geosystems* 4(6):1048–1064.
- Calder, B. R. 2015. On Risk-based expression of hydrographic uncertainty. *Marine Geodesy* 38(2):99–127.
- Calder, B. R. and G. Rice. 2017. Computationally efficient variable resolution depth estimation. *Computers & Geosciences* 106:49–59.
- Carr, D. A. 2016. *A Shift-Variant Restoration Technique Leveraging High-Resolution Interface Modeling in LIDAR-Based Seafloor Imaging*. Ph.D. Dissertation, Georgia Institute of Technology, Atlanta, Ga., 188.
- De Greve, B. 2016. Reflections and refractions in ray tracing. <[http://graphics.stanford.edu/courses/cs148-10-summer/docs/2006--degreve-reflection\\_refraction.pdf](http://graphics.stanford.edu/courses/cs148-10-summer/docs/2006--degreve-reflection_refraction.pdf)> Accessed 15 November 2017.
- Delaunay, B. N. 1934. Sur la sphère vide. *Izvestia Akademii Nauk SSSR, Otdelenie Matematicheskikh i Estestvennykh Nauk* 7:793–800.
- Elfouhaily, T., B. Chapron, B. K. Katsaros and D. Vandemark. 1997. A unified directional spectrum for long and short wind-driven waves. *Journal of Geophysical Research: Oceans* 102:15781–15796. doi:10.1029/97JC00467.
- Eren, F., S. Pe'eri and M. Thein. 2013. Characterization of optical communication in a leader-follower unmanned underwater vehicle formation. Pages 8724–872406 in *Proceedings of International Society for Optics and Photonics Ocean Sensing and Monitoring V*.
- Eren, F., S. Pe'eri, Y. Rzhanov and L. Ward. 2018. Bottom characterization by using airborne LIDAR bathymetry (ALB) waveform features obtained from bottom return residual analysis. *Remote Sensing Environment* (206):260–274. doi:10.1016/j.rse.2017.12.035.en.
- Gonsalves, M. O. 2010. *A Comprehensive Uncertainty Analysis and Method of Geometric Calibration for a Circular Scanning Airborne LIDAR*. Ph.D. Dissertation, The University of Southern Mississippi, Hattiesburg, Miss. 416.
- Guenther, G. 1985. Airborne laser hydrography: System design and performance factors In *NOAA Professional Paper Series*. Silver Spring, Md.: NOAA.
- Hartzell, P. J., P. J. Gadowski, C. L. Glennie, D. C. Finnegan and J. S. Deems. 2015. Rigorous error propagation for terrestrial laser scanning with application to snow volume uncertainty. *Journal of Glaciology* 61(230):1147–1158.
- Imahori, G., J. Ferguson, T. Wozumi, D. Scharff, S. Pe'eri, C. E. Parrish, S. A. White, I. Jeong, J. Sellars and M. Aslaksen. 2013. A procedure for developing an acceptance test for airborne bathymetric Lidar data application to NOAA charts in Shallow Waters. In *National Oceanic and Atmospheric Administration (NOAA) National Ocean Survey (NOS) Technical Memorandum CS 32*. Silver Spring, Md.: NOAA.
- International Hydrographic Organization. 2008. *IHO Standards for Hydrographic Surveys: Special Publication No. 44*, 5th ed. Monaco.
- Karlsson, T. 2011. *Uncertainties Introduced by the Ocean Surface when Conducting Airborne LIDAR Bathymetry Surveys*, Master's Thesis, Lund Institute of Technology, Lund, Sweden, 81.

- Kinzel, P. J., C. J. Legleiter and J. M. Nelson. 2013. Mapping river bathymetry with a small footprint green LiDAR: Applications and challenges. *JAWRA Journal of the American Water Resources Association* 49(1):183–204.
- Lee, Z. P. K., P. Du and R. Arnone. 2005. A model for the diffuse attenuation coefficient of downwelling irradiance. *Journal of Geophysical Research: Oceans* 110(2).
- Lockhart, C., D. Lockhart and J. Martinez. 2008. Total Propagated Uncertainty (TPU) for hydrographic LIDAR to aid objective comparison to acoustic datasets. *International Hydrographic Review* 9:19–27.
- Mandlburger, G., C. Hauer, M. Wieser and N. Pfeifer. 2015. Topobathymetric LiDAR for monitoring river morphodynamics and instream habitats—A case study at the Pielach River. *Remote Sensing* 7(5):6160–6195.
- Miller-Corbett, C. 2016. Evaluating integration of inland bathymetry in the US Geological Survey 3D Elevation Program, 2014 (No. 2016–1126). U.S. Geological Survey.
- Mitsuyasu, H., F. Tasai, T. Suhara, S. Mizuno, M. Ohkusu, T. Honda and K. Rikiishi. 1975. Observations of the directional spectrum of ocean waves using a coverleaf buoy. *Journal of Physical Oceanography* 5:750–760.
- Mobley, C. D. 1994. *Light and Water: Radiative Transfer in Natural Waters*, 592. Cambridge, Mass.: Academic Press.
- Mobley, C. D. 2016. Modeling Sea Surfaces: A Tutorial on Fourier Transform Techniques. <[http://www.oceanopticsbook.info/view/references/publications#mobley\\_2016](http://www.oceanopticsbook.info/view/references/publications#mobley_2016)> Accessed 15 November 2017.
- Morel, A., Y. Huot, B. Gentili, P. J. Werdell, S. B. Hooker and B. A. Franz. 2007. Examining the consistency of products derived from various ocean color sensors in open ocean (Case 1) waters in the perspective of a multi-sensor approach. *Remote Sensing of Environment* 111(1):69–88.
- National Science and Technology Council (NSTC). 2013. *Progress Made in Implementing the Ocean and Coastal Mapping Integration Act: 2009-2010. Biennial Report to Congress*. Silver Spring, Md.: National Oceanic and Atmospheric Administration.
- Parrish, C., J. A. Dijkstra, J. P. M. O'Neill-Dunne, L. McKenna and S. Pe'eri. 2016. Post-sandy benthic habitat mapping using new topobathymetric LIDAR technology and object based image classification. *Journal of Coastal Research* 76 (sp1):200–208.
- Pan, Z., C. L. Glennie, J. C. F. Diaz, C. J. Legleiter and B. Overstreet. 2016. Fusion of LiDAR orthowaveforms and hyperspectral imagery for shallow river bathymetry and turbidity estimation. *IEEE Transactions on Geoscience and Remote Sensing* 54(7):4165–4177.
- Pfennigbauer, M., A. Ullrich, F. Steinbacher and M. Aufleger. 2011. High-resolution hydrographic airborne laser scanner for surveying inland waters and shallow coastal zones. In *Laser Radar Technology and Applications XVI (8037: 803706)*. International Society for Optics and Photonics.
- Riegl VQ-880-G (2016). <[http://www.riegl.com/uploads/tx\\_pxpriegl/downloads/Infosheet\\_VQ-880-G\\_2016-05-23.pdf](http://www.riegl.com/uploads/tx_pxpriegl/downloads/Infosheet_VQ-880-G_2016-05-23.pdf)> Accessed 17 April 2017.
- Shannon, J. G. 1975. Correlation of beam and diffuse attenuation coefficients measured in selected ocean waters. *International Society for Optics and Photonics in Ocean Optics IV* 63:3–12.
- Steinval, O. V. and E. K. Koppari. 1996. Depth sounding LIDAR performance and models. In *Proceedings of SPIE 2748, Laser Radar Technology and Applications*, 26 June 1996. doi: 10.1117/12.243551.
- Stumpf, R. P. and J. R. Pennock. 1991. Remote estimation of the diffuse attenuation coefficient in a moderately turbid estuary. *Remote Sensing of Environment* 38(3):183–191.
- Westfeld, P. H., G. Maas, K. Richter and R. Weiss. 2017. Analysis and correction of ocean wave pattern induced systematic coordinate errors in airborne LiDAR bathymetry. *ISPRS Journal of Photogrammetry and Remote Sensing* 128:314–325. doi:10.1016/j.isprsjprs.2017.04.008.
- Wolf, P. R. and C. D. Ghilani. 1997. *Adjustment Computations: Statistics and Least Squares in Surveying and GIS*, 584. Hoboken, N.J.: Wiley-Interscience.
- Wozencraft, J. M. and W. J. Lillycrop. 2006. JALBTCX coastal mapping for the USACE. *The International Hydrographic Review* 7(2).

# Exploiting Cosegmentation and Geo-Eco Zoning for Land Cover Product Updating

Ling Zhu, Yang Sun, Ruoming Shi, Yixuan La, and Shu Peng

## Abstract

Land cover is a commonly used index for characterizing land surface and the corresponding human or natural processes. Remote sensing-based land cover maps must be continuously updated to satisfy the requirements of their users. An incremental updating method for land cover maps based on image cosegmentation and a geo-eco zoning-rule database is presented. First, cosegmentation of multitemporal satellite images is used to extract incremental (land cover change) pixels. Then the reliability of the change-detection results is improved by using the geo-eco zoning-rule database to detect and remove spurious changes. Finally, old land cover maps are updated to create new land cover maps. A test data set of 1200×1200 pixels from GlobeLand30 2000 land cover maps are updated to GlobeLand30 2010 land cover maps with an overall accuracy of 84.6%.

## Introduction

Land cover is the synthesis of the natural attributes and characteristics of the earth's surface. Remote sensing is the only effective means for mapping and monitoring land cover and land cover change in large areas (Chen, Chen, and Liao 2016). Remote sensing-based land cover mapping refers to the use of the rich spectra, textural features, and spatial and temporal relationships contained in remote sensing images, combined with various reference materials and related professional knowledge, and applying mathematical statistics and interactive interpretation methods to extract the attribute information and spatial distribution of land cover classes, detect their temporal and spatial changes, and generate corresponding result data sets (Chen, Chen, and Liao 2016). The successful development of remote sensing-based land cover maps significantly facilitates the application of land cover information to the fields of climate-change research, ecological environmental monitoring, and sustainable development planning. Various land cover maps with resolutions of 1 km, 300 m, and 30 m have been developed at the global, regional, and national level from remote sensing data since the 1980s. Sources of global land cover maps include the International Geosphere Biosphere Program Data and Information System (Loveland *et al.* 2000), University of Maryland 1- and 8-km land cover maps (Hansen *et al.* 2000), European Union land cover data GLC2000 (Bartholomé and Belward 2000), and the Global Land Cover 1-km-resolution coverage data set by National Mapping Organizations (Tateishi *et al.* 2011); all four maps were one-time products that did not have updates or new product launches. The current needs of the global community are not only one-time products but also regular and timely delivery of consistent

global land cover maps (Giri 2012a). The land cover maps must be continuously updated to meet the needs of the users.

An incremental updating method was developed and tested on GlobeLand30 land cover maps in this study. The methods and results described were determined by focusing on land cover map updating through double-phase remote sensing imagery. This method first extracts the initial change patches from the images using the cosegmentation algorithm. Then, Geoscience Knowledge, a global geo-eco zoning-rule database, is used to further identify the spurious change patches to improve the accuracy and reliability of the incremental update.

## Background

Some land cover maps have launched multiphase products. The 300-m-resolution products GlobCover 2005 and 2009 (Bontemps *et al.* 2011) were developed by the European Space Agency. The overall accuracy of the GlobCover 2005 Land Cover Map was 73.14% (3167 samples). A quantitative accuracy assessment was also performed for GlobCover 2009 by the same network, and a lower accuracy was found: 67.5% overall, using 2190 samples (Giri 2012b). GlobCover 2005 (V2.2) was considered the main reference when GlobCover 2009 was produced, and GlobCover 2005 and 2009 adopted the same classification algorithm and system. However, a report (Bontemps *et al.* 2011) comparing the two products indicated that their spatial distributions are different. These differences are due not only to changes in land cover but also to the instability of classification. Most of the erroneous changes occur among similar types of objects. The GlobCover 2009 land cover maps cannot be directly compared with the GlobCover 2005 land cover maps, and hence cannot be used for any change-detection purpose. The surface-change rate of the maps is typically lower than the classification-error rate. Therefore, comparison with older land cover maps is unsuitable for determining land cover change.

The time-series analysis method is used on the following maps to improve their results. For the Moderate Resolution Imaging Spectroradiometer Collection 5 annual land cover map (Friedl *et al.* 2010), an algorithm was developed for stabilizing classification results to reduce spurious changes in annual map comparisons. If the pixel-classification result is different from that of the previous year, then the land cover type will change only when the posterior probability value of the new type is higher than that of the previous type. However, this algorithm may yield incorrect transmission types in the land cover change area; thus, the surface cannot be updated. Therefore, such an algorithm must process the data for three consecutive years to accurately update the surface-change map and reduce about 10% of spurious change. However, the results obtained

---

Ling Zhu, Yang Sun, Ruoming Shi, and Yixuan La are with the Beijing University of Civil Engineering and Architecture School of Geomatics and Urban Spatial Information, Beijing, China (zhuling@bucea.edu.cn).

Shu Peng is with the National Geomatics Center of China, Beijing, China.

---

Photogrammetric Engineering & Remote Sensing  
Vol. 85, No. 8, August 2019, pp. 597–611.  
0099-1112/19/597–611

© 2019 American Society for Photogrammetry  
and Remote Sensing  
doi: 10.14358/PERS.85.8.597

by subtracting the annual maps remain higher than the real change. The set of European Space Agency Climate Change Initiative (CCI) second-stage land cover maps currently includes the global annual 300-m-resolution land cover map from 1992 to 2015 (CCI product user guide version 2.0, 2017). The key feature of the CCI Land Cover map is its consistency over time. The annual classification results are derived from a unique base land cover map that is generated from the images of the entire 2003–2012 MERIS FR and RR data set. The time-series images from 1992–2015 are used independently of the base land cover map to detect land cover change. Each pixel is considered a change pixel only when it appears in the classification time series for at least two consecutive years. The annual land cover map is generated from the base land cover map and the change map using backward and forward formulas.

Owing to the continuous development of global change and relevant research, 1-km- and 300-m-resolution global land cover maps have been insufficient to satisfy changing requirements. A high spatial resolution and comprehensive coverage of information are required for land cover maps. China has developed a 30-m-resolution global land cover product called GlobeLand30 (Chen *et al.* 2017), which includes the 2000 and 2010 global land cover for 10 main categories. Directly comparing these two maps to determine land cover changes is not recommended, because the maps are classified separately. GlobeLand30 will develop new phase maps by using two-phase images to extract land cover changes and update products—that is, incremental updating. In incremental updating, only the target area that has changed is updated. Incremental updating has the characteristics of minimal processing time and easy data transformation.

In addition to these global land cover maps, several regional or national land cover maps and their updating methods are surveyed. The National Land Cover Database of the United States, which was developed by the USGS (Jin *et al.* 2013), currently undergoes a five-year update cycle to satisfy the requirements of Multi-Resolution Land Characteristics consortium members and domestic users. Generating land cover maps from the 2006 edition is achieved by incremental updating. The algorithm of image-change detection is implemented through the pixel-based method, which combines the differences in four complementary indices (the differenced normalized burn ratio; dNDVI, the differenced normalized difference vegetation index; CV, the change vector; and the relative CV maximum). The European Coordinated Information on the Environment (CORINE) project (Büttner 2014), which includes the land cover map CORINE Land Cover (CLC), uses a bottom-up mode of production, in which each member is responsible for their own national data maps and integrates these maps to generate a land cover map of Europe. In the CLC2000 version, the CORINE Land Cover Change (CLCC) 1990–2000 map was developed to reflect the land cover changes over a period of 10 years. The methods used by most countries at that time were to upgrade from CLCC1990 to CLC2000 and stack two maps to produce CLCC maps. However, the CLCC map contains considerable noise and spurious changes, given the inconsistency of the minimum mapping unit of the two phases of the map. Several countries adopted the incremental updating method, which detects the 1990–2000 land cover changes and generates a new map; this method was later recommended by the European Environment Agency. DeCOVER is a German land cover map (Buck 2010) that utilizes high-resolution satellite images as the original data. The change-detection algorithm uses the object-based multiscale segmentation method. The old DeCOVER map is used as a constraint during the segmentation process, thus maintaining the consistency of map boundaries at different times. The National Carbon Accounting System Land Cover Change Project (Caccetta *et al.* 2007) in

Australia used Landsat's MSS, TM, and ETM+ images to map the perennial vegetation in Australia since 1972 at 25 m resolution. Long-time-series images were used to monitor the classification parameters of different years. Then, spatiotemporal models were utilized to reduce classification errors. Similar to the CCI Land Cover products, a reference map is accurately produced, and the a posteriori probability is used as the basis for classifying other years. The spatiotemporal model is combined to analyze the classification results of a certain pixel in different years. The types of surrounding pixels are also used to improve classification accuracy.

In summary, the updating methods of land cover maps mainly include separate classification of each stage by combining time-series analysis and incremental updating. Practice has confirmed that the incremental updating method can optimize mapping efficiency and has ensured that the maps of each phase can be compared to extract land cover changes, given a global-coverage high-resolution product of 100 m or less (Xian, Homer, and Fry 2009; Jin *et al.* 2013). Incremental updating can drastically reduce the introduction of new errors (Linke *et al.* 2009).

The incremental extraction method is based on the change-detection method. Change detection of remote sensing images mainly involves two kinds of methods—namely, pixel- and object-based methods (Ma and Liu 2014). The use of pixel-based change-detection methods will inevitably produce “salt-and-pepper” noise. Object-based change detection based on the image-segmentation technique results in a vector form. This form avoids the salt-and-pepper noise and has a clear change polygon boundary; thus, several scattered patches are easy to process. Multitemporal image segmentation for object-based change detection can be performed with two kinds of strategies (Bontemps *et al.* 2008). One strategy is to segment the two-phase images and extract the change patches separately. However, the object that is generated by the object-based method is related to the image characteristics of each phase. Therefore, the geometric characteristics of objects will change with time, and the boundary of the two temporal objects will be inconsistent, thereby resulting in difficulty establishing the corresponding relationship among multitemporal objects (Hussain *et al.* 2013). Moreover, accurately reflecting the range of change can be difficult for polygonal map stacking in different periods for several nonartificial and scattered objects, such as forests, shrubs, and grasslands. The other strategy is based on multitemporal images—that is, using a data stack that consists of both images. The change patches can be extracted by using the parameters of the CV or correlation coefficient. For the multiscale segmentation method utilized in eCognition software, which is widely used at present, the core problem is the selection of the best segmentation scale for different classes. Multiscale segmentation uses the method of regional growth to form the object. The heterogeneity of the growth process is determined by the spectral and shape differences of the object. The difference in shape is determined by the smoothness and tightness, so the accuracy of the segmented result is controlled by multiple thresholds (Benz *et al.* 2004). The pixel- and object-based methods must rely on the threshold of a certain index or a characteristic value to evaluate the changing and unchanging areas. The selection of thresholds will directly affect the accuracy of the results. The expression of the patch is more flexible and accurate in pixel-grid form than in vector form. Moreover, a pixel grid can express certain minor changes.

The cosegmentation-based method originating from computer vision provides a new solution to object-based change detection. Cosegmentation adds a constraint to general image segmentation that multiple images contain the same object to be extracted as the foreground. Cosegmentation

simultaneously segments the images and extracts the same object through the interaction of multiple images. The concept of cosegmentation was first proposed in 2006 (Rother *et al.* 2006) and has been continuously improved by many researchers (Joulin, Bach, and Ponce 2010, 2012). Xiao *et al.* (2017) integrated the change information of bitemporal images into the graph-cut-based energy function to combine change detection and image cosegmentation. Image segmentation and change detection are completed simultaneously as the energy function is minimized. This method connects the cosegmentation of moving images to determine the change in land cover and extends the application field of cosegmentation to the foreground as a multitemporal changed object and the background as an unchanged area. A change-detection method based on cosegmentation can directly obtain accurate and spatially corresponding multitemporal objects and address the inconsistent boundaries of multitemporal objects. Compared with the pixel-based and object-based change-detection methods, the results of the cosegmentation method are the same as those of the pixel-based method, but the algorithm considers the surrounding pixels and avoids salt-and-pepper noise.

Remote sensing images reflect only the instantaneous state of the earth's surface and are based on the sampling period. Thus, many errors and uncertainties occur in accordance with the "same objects with different spectra, different objects with the same spectrum" phenomenon and effect of the seasonal phase. Consequently, the outcome of change detection will include incorrectly detected changes. For example, the spectral characteristics of paddy fields will be similar to those of water bodies and are likely to be regarded as changes during the irrigation period. Identification and elimination of the spurious change in the change map after detection are necessary to improve the accuracy of change detection.

Inaccurate classification detection is improved by using auxiliary data or visual interpretation by the operators or experts with the previously produced land cover data sets. However, visual interpretation not only wastes time and consumes numerous resources but also easily causes misinterpretation given the interpreter's lack of identification experience. Auxiliary data, such as digital-elevation-model data, ecological area data, and vegetation and land cover maps of countries or regions are used. The CCI Land Cover map used the data from the World Mangrove Atlas, Global Human Settlement, Global City Data, and Randolph Glacier Inventory. The reference data of GlobeLand30 in the production process include the existing land cover data (global and regional), Moderate Resolution Imaging Spectroradiometer normalized difference vegetation index (NDVI) global data, basic geographic-information data, global digital-elevation-model data, and online high-resolution images (such as Google Earth, OpenStreet, and Tianditu maps). However, the applications of auxiliary data are sporadic and unsystematic. No global comprehensive specialist system has been established to accumulate and summarize the reference data that aid in producing land cover data sets.

The geo-eco zoning, or geo-ecoregion system shows the earth's surface subdivided into identifiable areas based on macroscale patterns of ecosystem areas within which there are associations of interacting biotic and abiotic features (Bailey 1983), reflecting the spatial pattern of natural elements, including climate, topography, water conditions, soil, and vegetation. The geo-ecoregion system also reflects the matching relationship between these conditions and the resources and environment. The popular international geo-ecoregion systems are the life-zone classification global scale (Holdridge model; Holdridge 1967), world biogeographical biomes (Bailey and Hogg 1986; Bailey 1989), world ecosystems (Bailey 1983), continental ecoregions (Bailey 2004), global ecological zones (Bashkin and Bailey 1993), and the World Wildlife

Fund Global Ecological Zone map for nature protection (ecoregions, such as the terrestrial ecoregions of the world; Olson *et al.* 2001). The application of geo-ecoregion information in producing land cover maps is limited to certain areas or to vegetation growth and change information. The knowledge from global geo-eco zoning is rarely summarized and analyzed. A global knowledge base of global geo-ecoregion zoning should be established to identify error changes automatically after change detection. In this study, an object-based four-layer database framework for global geo-eco zoning was established to aid the detection of spurious changes.

## Methods

The incremental updating method of producing land cover maps applied in this study comprises cosegmentation to extract two-phase image-change patches, identification and elimination of spurious changes based on a geo-eco zoning-rule library, and implementation of the land cover map updating procedure.

### Bitemporal Remote Sensing Image Cosegmentation

Cosegmentation aims to obtain changed image patches in bitemporal images. The two phases of the original remote sensing images should be preprocessed through conventional methods (i.e., geometric and radiation preprocessing) to ensure the quality of cosegmentation. In this study, the cosegmentation algorithm mainly refers to the method that was previously presented in the literature (Xiao *et al.* 2017). The workflow of cosegmentation is illustrated in Figure 1.

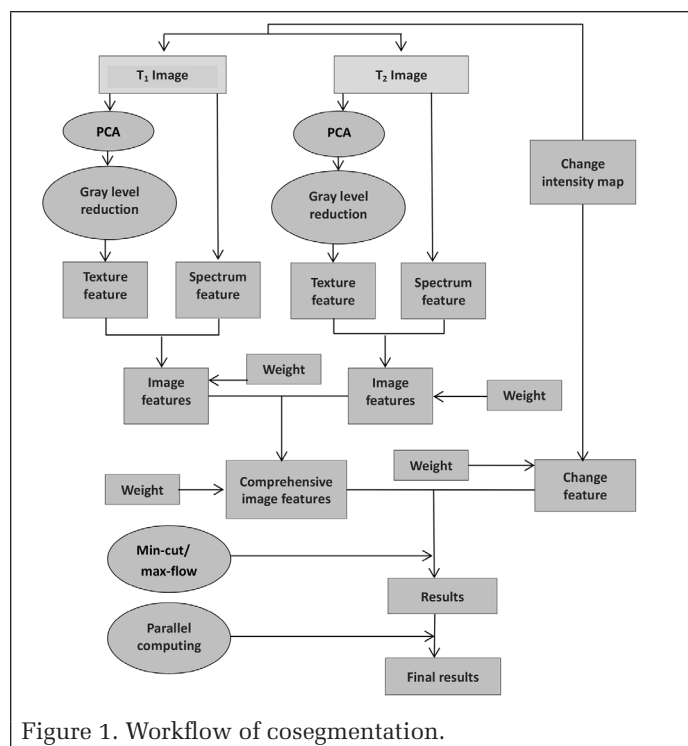


Figure 1. Workflow of cosegmentation.

### Construction of the Energy Function

Each image feature consists of spectral and textural features. The spectral feature is expressed as the mean of all spectral bands:

$$E_S(p) = \frac{1}{N} \sum_{k=1}^N I_k(p), \quad (1)$$

where  $p$  is a pixel in the image,  $I_k(p)$  is the spectral value of the  $k$  band that corresponds to  $p$ , and  $N$  is the total number of

spectral bands. The method for obtaining change and textural features follows that used by Yuan *et al.* (2015). Principal Components Analysis and gray-scale reduction were performed for textural-feature calculation.

In Xiao *et al.* (2017) and Yuan *et al.* (2015), each phase image can produce image features that are cosegmented with the change-intensity map to produce two separate change results corresponding to the two-phase images. In this study, the algorithm was reformed to obtain only one change map by giving a certain weight to image features of each phase image for combining them into a comprehensive one. Then the comprehensive image features and change feature were used to conduct cosegmentation. This method simultaneously considers the characteristics of two images instead of relying solely on one image. The integrated image features  $E_2$  of the two-phase images are expressed as follows:

$$E_2 = \lambda_{t_1} E_{t_1} + (1 - \lambda_{t_1}) E_{t_2}, \quad (2)$$

where  $E_{t_1}$  and  $E_{t_2}$  denote the image features of the  $t_1$  and  $t_2$  phases, respectively, and  $\lambda_{t_1}$  is the weight of the image features of the  $t_1$  phase.

The energy function based on graph theory can be expressed as follows:

$$\text{Energy\_CD}(I) = \lambda E_1 + E_2 \quad (3)$$

where  $E_1$  and  $E_2$  are the change and image features and  $\lambda$  is the weight of the change feature, which is determined by experimental results.

#### Minimum-Cut-and-Maximum-Flow (Min-Cut/Max-Flow) Method

In graph theory, a cut on a graph  $G = (V, E, W)$  consists of a set of nodes  $V$  and directed edges  $E$  that connect the nodes by n- and t-links, where  $W$  is the weight value of each edge. The variable  $V$  is the set of all nodes in the graph, including two additional nodes: foreground ( $t$ ) and background ( $s$ ) terminals. The cost of n-links in accordance with the energy function corresponds to a penalty for discontinuity among the pixels, which are the image-feature items. The cost of a t-link that connects a pixel and a terminal corresponds to a penalty for assigning the corresponding label to the pixel, and is normally derived from the change-feature item.

The outcome of applying the cosegmentation method in change detection is the changed image patches ( $obj$ ), and the background ( $bkg$ ) constitutes the unchanged regions. The min-cut/max-flow method is an optimization approach of the energy function, which optimally segments the image.

The theorem of Ford and Fulkerson (1962) states that the maximum flow from  $s$  to  $t$  saturates a set of edges in the graph and divides the nodes into two disjoint parts ( $\mathbf{O}$  and  $\mathbf{B}$ ) that correspond to the minimum cut. The parts  $\mathbf{O}$  and  $\mathbf{B}$  represent the subsets of pixels and are marked as  $obj$  and  $bkg$ , respectively.

Dinic's algorithm (Dinitz 1970) is used to solve the problems of maximum flow in this study. This algorithm aims to determine the shortest distance that can increase the path length at each step. According to the length of the shortest path from  $s$  to  $t$  in the graph, the breadth-first search method is used to divide the vertices in the graph into different subsets. When the sink  $t$  enters the  $\mathbf{O}$  or  $\mathbf{B}$  subset, the layering ends. Then the algorithm re-layers and determines the path with length +1 until it finds no path from  $s$  to  $t$ .

#### Supervised Classification

The classification of the changed part of the new phase image after extracting land cover change will be the next step in the subsequent processing. The land cover types are determined in accordance with the categories of the GlobeLand30 maps (Table 1); a conventional supervised classification method, the

support vector machine, is used. The selection of the training data and classification are conducted using ENVI software.

Table 1. First class code of the GlobeLand30 land cover product.

No.	Code	Land Cover Class	Legend
1	010	Cultivated land	
2	020	Forest	
3	030	Grassland	
4	040	Shrubland	
5	050	Wetland	
6	060	Water bodies	
7	070	Tundra	
8	080	Artificial surfaces	
9	090	Barren lands	
10	100	Permanent snow and ice	

#### Identification and Elimination of Spurious Change Based on the Geo-Eco Zoning-Rule Database

Cosegmentation can capture all potential land cover change areas rather than areas where only actual land cover change occurred, as only a portion of the potential land cover change is related to actual land cover changes, due to the many spurious changes detected. A geo-eco zoning-rule database is used to identify and eliminate false changes to improve accuracy.

#### Framework Design of Geo-Eco Zoning-Rule Database

The Global Ecological Division established by the World Wildlife Fund (Olson *et al.* 2001) was adopted as the basic framework of the global geo-eco zoning-rule database, which is generally accepted by the international ecological community. Ecological regionalization divides the world into eight eco-geographical zones and 14 biological communities. These two basic layers are combined into 867 geo-eco zones. The shape file of the 867 zones with eco-code can be downloaded from the World Wildlife Fund website (<https://www.worldwildlife.org/publications/terrestrial-ecoregions-of-the-world>).

The spurious change in geo-eco zoning rules considers a large amount of data, given the 867 ecological zones. Summing up the spurious-change rule for every zone is a substantial, time-consuming task. Therefore, this study designed a unique object-oriented approach to establish the geo-eco zoning-rule database. The advantage of object-oriented knowledge representation is that it is a structured knowledge-representation technology and has inheritance and derivation characteristics—that is, subclasses can inherit all of the characteristics of their parents. Thus, this approach significantly reduces workload and solves problems rapidly and efficiently.

The four-layer rule database builds the derivation and inheritance relationship among the different layers from top to bottom, as depicted in Figure 2. On the basis of the eight eco-geographical zones and 14 biological communities, a number

of factors have been considered attribute factors, including temperature, humidity, NDVI, elevation, and slope.

The first layer of the rule base has two parallel branches—namely, the left and right branches—which are designed for ecological-geography class and natural attributes, respectively. The two parallel branches comprise the top layer, whereas all other objects are a subclass of the two parallel branches.

The left branch of the second layer includes eight eco-geographical zones and 14 biological communities; this branch is the subclass of the ecological-geography class of the first layer. The right branch, which includes temperature, humidity, NDVI, elevation, and slope, is the subclass of the natural attributes.

In the third layer, the left branch includes large geographical and ecological zones, namely, the cross-inheritance of geographical areas and biological communities with 64 zones, which are labeled IM01–PA01 (Olson *et al.* 2001). The first two characters in the labels are the codes of the eco-geographical zones. The last two characters are the codes of the biome types. For example, PA01 denotes Palearctic tropical and subtropical moist broadleaf forests. IM01 denotes Indo-Malay tropical and subtropical moist broadleaf forests. In accordance with the different natural conditions of each ecological zone, the right branch of the third layer is subclass of elevation (E), slope (S), NDVI value (N), temperature (T), and humidity (W), depending on their different values, as shown in Figure 2. Because the ecological zone is relatively large and contains multiple regions, it is difficult to use atmospheric temperature to express the temperature. Therefore, temperature is divided into tropical (T1), subtropical (T2), temperate (T3), and cold (T4) zones. The temperature zone is divided according to latitude: 0°–23.5° is tropical, 23.5°–40° is subtropical, 40°–66.5° is temperate, and 66.5°–90° is cold. The average attribute value of the geo-eco zone is considered because each large geographic area corresponds to a large area of the earth. The rule base of this layer stores its corresponding spurious-change rules.

The fourth level is the lowest level and is composed of 867 geo-eco partitions that store specific attribute information, and the spurious-change rule is determined from only this layer.

#### Establishment and Expression of the Rules

The spurious-change rule is expressed in the form of production—that is, the forms of premise and conclusion—and mapped to the table in the object-relational database. A simple spurious-change expression is designed. The representation of the spurious-change rule uses a six-digit code—that is, “XXXXXX”—where the first three digits represent the land cover class of the early phase image and the last three digits represent the class code of the new image. The first class code of GlobeLand30 is used in this study and is displayed in Table 1.

Based on the framework of the geo-eco zoning-rule database, the spurious-change rules are set up layer by layer. The rule base starts with the third level of the frame model. The spurious-change rules of the 64 large geographic ecozones include the general spurious-change rule and the seasonal-phase spurious-change rule. The spurious-change rule that is caused by a seasonal time phase is divided into seven types, as summarized in Table 2. The spurious-change rule caused by the seasonal time phase is related to the zone and land cover type—that is, not every zone or land cover type will be affected by the seasonal time phase—so the spurious-change rule of the seasonal time phase is embedded in the corresponding zone.

The spurious-change rule considering different attributes (i.e., height, slope, NDVI value, temperature, and humidity) is also stored in the production stage.

The fourth layer in the geo-eco zoning-rule base model comprises the spurious-change rules of 867 geo-eco zones, including the rules that were inherited from the upper level and the unique rules that cannot be inherited. This layer mainly includes the spurious-change rules of the small partition and those caused by seasonal effects.

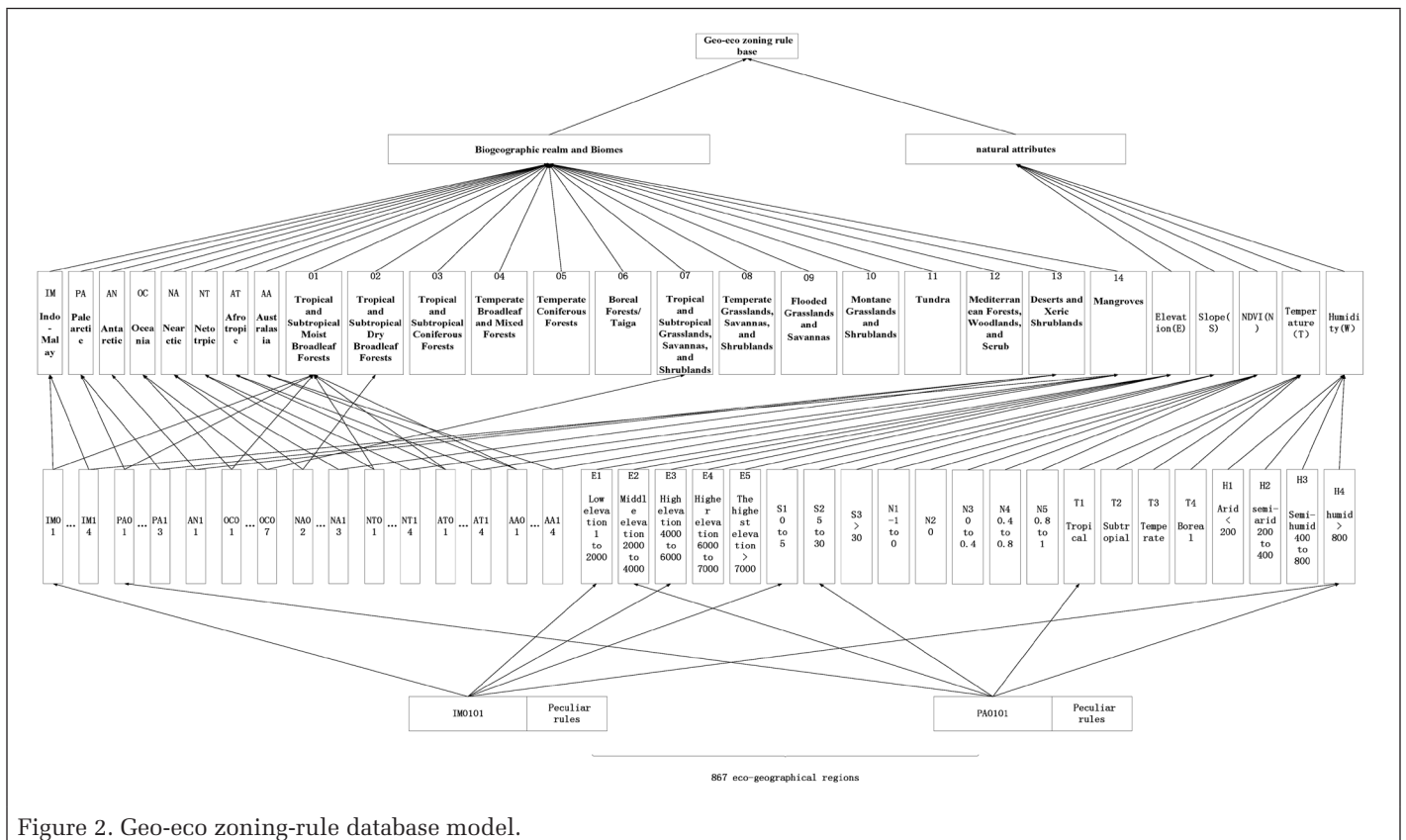


Figure 2. Geo-eco zoning-rule database model.

The specific spurious-change rules of the spurious-change fields of each form—that is, the six-digit code—must be determined based on the expert knowledge of remote sensing interpreters and geographical specialists. Knowledge of the

Table 2. Examples of the spurious-change rules that correspond to season.

<b>ID</b>	<b>Season Time</b>	<b>Name</b>	<b>Spurious Change</b>
1	ST1	Wet season	030060, 030050, 050060, 090060
2	ST2	Dry season	060030, 060090, 060010, 050030
3	ST3	Irrigation season	010060, 010050
4	ST4	Harvest season	010030, 010090
5	ST5	Growing season	050020, 050030, 060030, 090030
6	ST6	Leaf fall season	020030, 020040, 030090
7	ST7	Freeze up	060100

Table 3. Examples of the spurious-change rules that correspond to elevation.

<b>ID</b>	<b>Elevation</b>	<b>Range (m)</b>	<b>Spurious Change</b>
1	E1	<1000	020050, 020080, 030060
2	E2	(1000, 2000)	040050, 020060, 020090
3	E3	(2000, 4000)	030060, 050080
4	E4	(4000, 6000)	020050, 040050, 050070
5	E5	>6000	020050, 050040, 010060

Table 4. Examples of the spurious-change rules that correspond to slope.

<b>ID</b>	<b>Slope</b>	<b>Range (°)</b>	<b>Spurious Change</b>
1	S1	(0, 5)	None
2	S2	(5, 30)	060010, 060030, 060050, 060080, 060090
3	S3	>30	060010, 060030, 060050, 060080, 060090, 010020, 010040, 010060, 010090

Table 5. Examples of the spurious-change rules that correspond to values of normalized difference vegetation index (NDVI).

<b>ID</b>	<b>NDVI</b>	<b>Range</b>	<b>Spurious Change</b>
1	N1	(-1, 0)	020050, 030060, 040080, 050090, 010020, 040070
2	N2	0	050060, 040050, 050080, 020060, 010040, 020050
3	N3	(0, 0.4)	010020, 040050, 080090, 060050, 060020, 060030
4	N4	(0.4, 0.8)	070010, 070050, 070030, 050080, 020090, 080050
5	N5	(0.8, 1)	020050, 040050, 090060, 080040, 070050, 090050

Table 6. Examples of the spurious-change rules that correspond to temperature.

<b>ID</b>	<b>Temperature</b>	<b>Name</b>	<b>Latitude Range (°)</b>	<b>Spurious Change</b>
1	T1	Tropical	(0, 23.5)	070010, 070020, 070030, 070040, 070050, 070060, 070080, 070090, 070100, 100010, 100020, 100030, 100040, 100050, 100060, 100070, 100080, 100090, 050020, 050030, 050060, 050070, 050090, 050100, 090020, 090040, 090050, 090060, 090100
2	T2	Subtropical	(23.5, 40)	070010, 070020, 070030, 070040, 070050, 070060, 070080, 070090, 070100, 100010, 100020, 100030, 100040, 100050, 100060, 100070, 100080, 100090
3	T3	Temperate	(40, 66.5)	070010, 070020, 070030, 070040, 070050, 070060, 070080, 070090, 070100, 100010, 100020, 100030, 100040, 100050, 100060, 100070, 100080, 100090
4	T4	Boreal	(66.5, 90)	020010, 020030, 020040, 020050, 020060, 020070, 020080, 020090, 020100, 030010, 030020, 030040, 030050, 030060, 030070, 030080, 030090, 030100, 040010, 040020, 040030, 040050, 040060, 040070, 040080, 040090, 040100, 050100, 050200, 050030, 050040, 050060, 050070, 050080, 050090, 050100

test area at different levels has been collected and stored in the database. Several examples are presented in Tables 2–8.

#### Rule-Based Management System

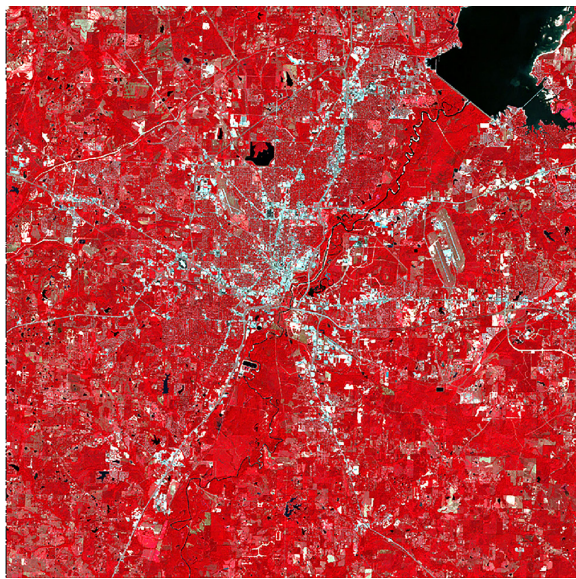
The main functions of the rule-based management system are as follows: to visualize the rule base; to query, add, delete, and modify rule tables in the rule base; and to implement spurious-change recognition, marking, and elimination. The spurious-change judgment method uses forward reasoning. First, the resultant cosegmentation raster data are converted to a polygon, thus keeping the output vector consistent with the input pixel edge, by using commonly available software (such as the raster tool in ArcGIS software). The polygon property must store the code of the land cover type. The land cover types of the patch before and after the change are expressed as a six-digit code, as defined previously. Second, the scope of the changed patch and its geo-eco zone is identified in accordance with the map coordinates. Then the spurious-change rules require the corresponding geo-eco zoning rules—that is, the zoning rules of the fourth layer, including the specific rules and the rules inherited from the third layer. The six-digit code is matched with the rule library; in this library, if this code is marked as a spurious change, then the spurious-change patch is removed. All of the zones that correspond to the patch must be identified, and the rules are merged to identify the spurious change because the changed patch may span different ecological zones. In this article, the final change patches were converted into a pixel format using common software (such as the polygon to raster tool in

Table 7. Examples of the spurious-change rules that correspond to humidity.

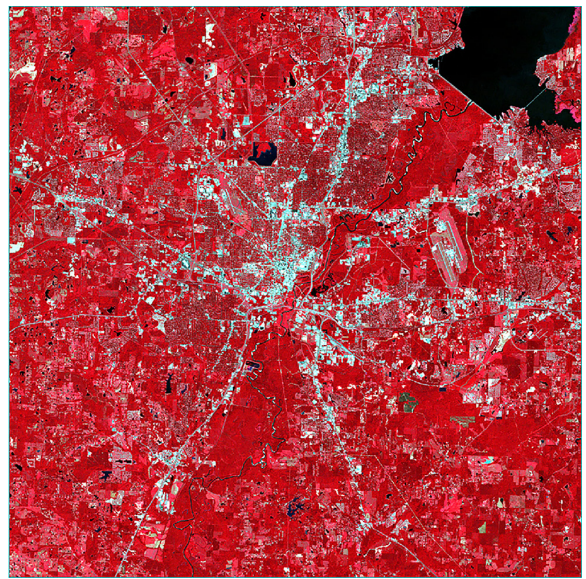
<b>ID</b>	<b>Humidity</b>	<b>Precipitation Range (mm)</b>	<b>Spurious Change</b>
1	W1	<200	010050, 010080, 010090, 020050, 030040, 030090
2	W2	(200, 400)	030060, 020050, 040090, 050080, 060010
3	W3	(400, 800)	060080, 050070, 020050, 030060
4	W4	>800	010050, 010090, 050020, 080060

Table 8. Examples of the specific spurious-change rules that correspond to the test site (NA0413 Zone).

<b>Spurious Change</b>
010070, 010600, 010100, 020050, 020060, 020070, 030100, 030060, 030070, 040060, 040070, 040100, 050070, 050100, 060070, 060100, 070020, 070040, 070030, 070010, 070080, 070050, 070100, 080050, 080070, 080100, 090050, 090100, 100010, 100020, 100030, 100040, 100050, 100070, 100080, 100090

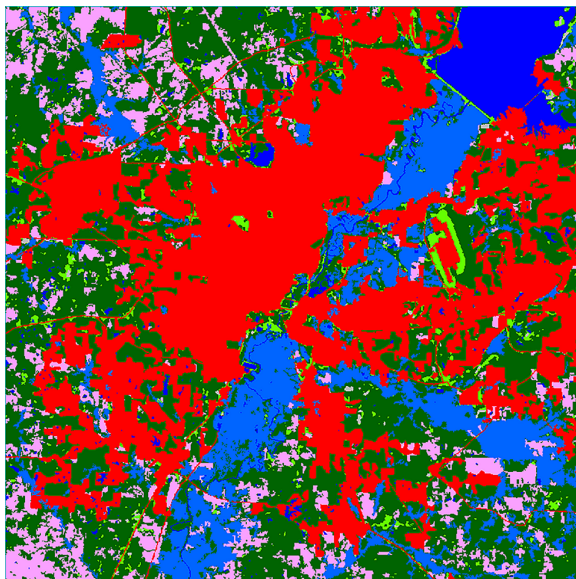


(a)

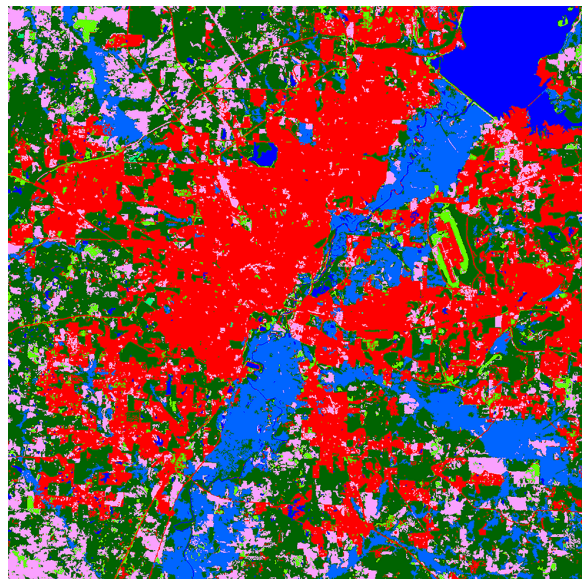


(b)

Figure 3. Test Landsat images acquired in (a) 2000 and (b) 2010.



(a)



(b)

Figure 4. GlobeLand30 (a) land cover maps from 2000 and (b) incremental update results from 2010.

ArcGIS software). The output pixels are consistent with the edge of the input vectors during transformation. The pixels must store the land cover type code.

#### Land Cover Product Updating

The land cover data are generally stored in a raster format. The updating operation is used to replace the corresponding pixels of the t1 (earlier time) map with the new type obtained by the previously presented steps. The small patches can be eliminated in accordance with the minimum mapping unit defined by the land cover map.

### Results

#### Satellite Imagery and Reference Data Set

The land cover change-detection and map-updating test used the 30-m-resolution multispectral Landsat images that cover a 10-year period. A pair of Landsat images acquired on September

17, 2000 (Figure 3a), and September 5, 2010 (Figure 3b), with a time difference of two weeks, was used to reduce the seasonal and phenological differences. Orthorectified level 1T OL1 Landsat 5 images (path/row p122r038) were downloaded from the USGS EarthExplorer site (<http://earthexplorer.usgs.gov/>). A subset of 1200×1200 pixels was selected as the test site, which is located in Jackson City, Mississippi. The label of the geo-ecozoning is NA0413, corresponding to the temperate broad-leaved forest and mixed forest biomes of the 14 possible biomes and the southeastern mixed forest of the 867 possible geographical ecological zones. The Landsat image pair was radiometrically corrected using the ENVI radiometric calibration tool.

Figure 4a demonstrates the GlobeLand30 2000 land cover maps of the same extent, with the legends defined in Table 1.

The results of the 2000–2010 change patches detected by cosegmentation and the spurious change removed by geo-ecozoning were validated by visual inspection of high-resolution images available on the web (Google Earth), because no field data were available.

## Experimental Results

### Cosegmentation Results

The parameter setting of the cosegmentation experiment is that in Equation 3, the weight  $\lambda$  was set to 0.005 according to the experimental result; the variable  $\lambda_{t1}$  in Equation 2 was set to 0.5. The weights of the spectral and textural features when calculating the image feature and weights for four parameters in textural-feature calculation were all set to be the same. The cosegmentation results are exhibited in Figure 5a, where the white and black pixels denote the unchanged and changed parts, respectively.

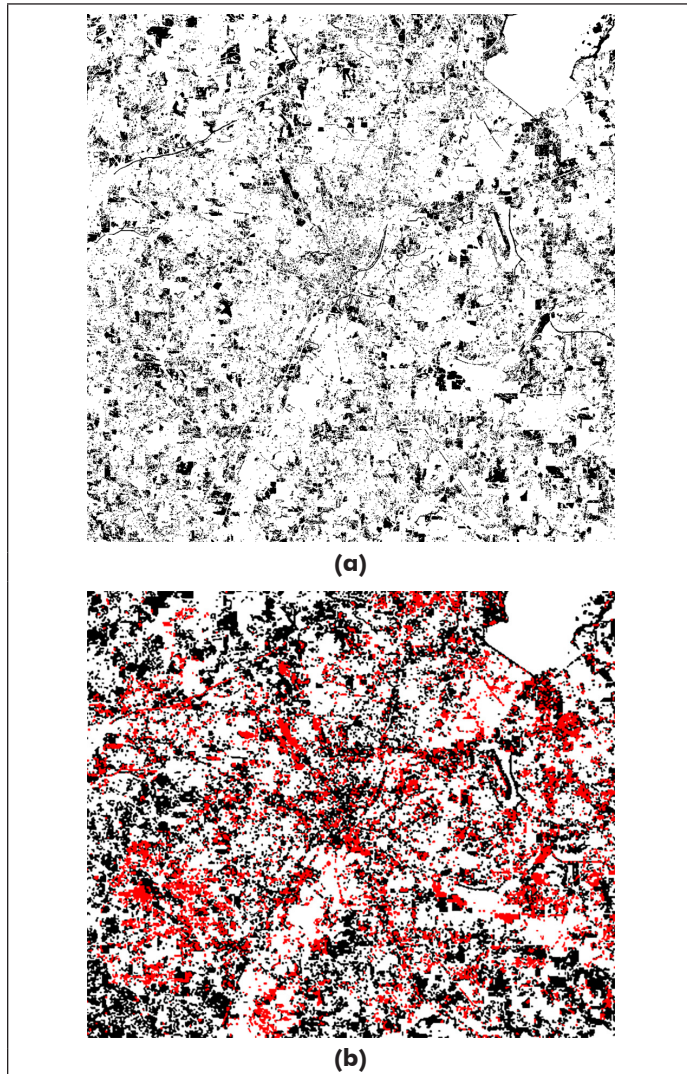


Figure 5. Experimental results of (a) cosegmentation and (b) the change map, where red represents the detected spurious changes.

Table 9. Change-detection results based on cosegmentation.

	Changed	Unchanged	Sum	Producer's Accuracy
Changed	261	49	310	0.988
Unchanged	3	212	215	0.812
Sum	264	261	525	—
User's accuracy	0.842	0.986	—	—
Overall accuracy = 0.901				
$\kappa = 0.801$				

The results are evaluated using the error matrix and kappa coefficient, as summarized in Table 9. The overall accuracy of the results is approximately 90.1%, with  $\kappa = 0.801$ . At the selected sample point, 261 of the 264 changed samples and 212 of the 261 unchanged samples were accurately detected. The producer's accuracy of the changed area was 0.988, and the producer's accuracy of the unchanged area was 0.812. The analysis indicates that the cosegmentation method can identify most of the changes in the two-phase images with high precision. The

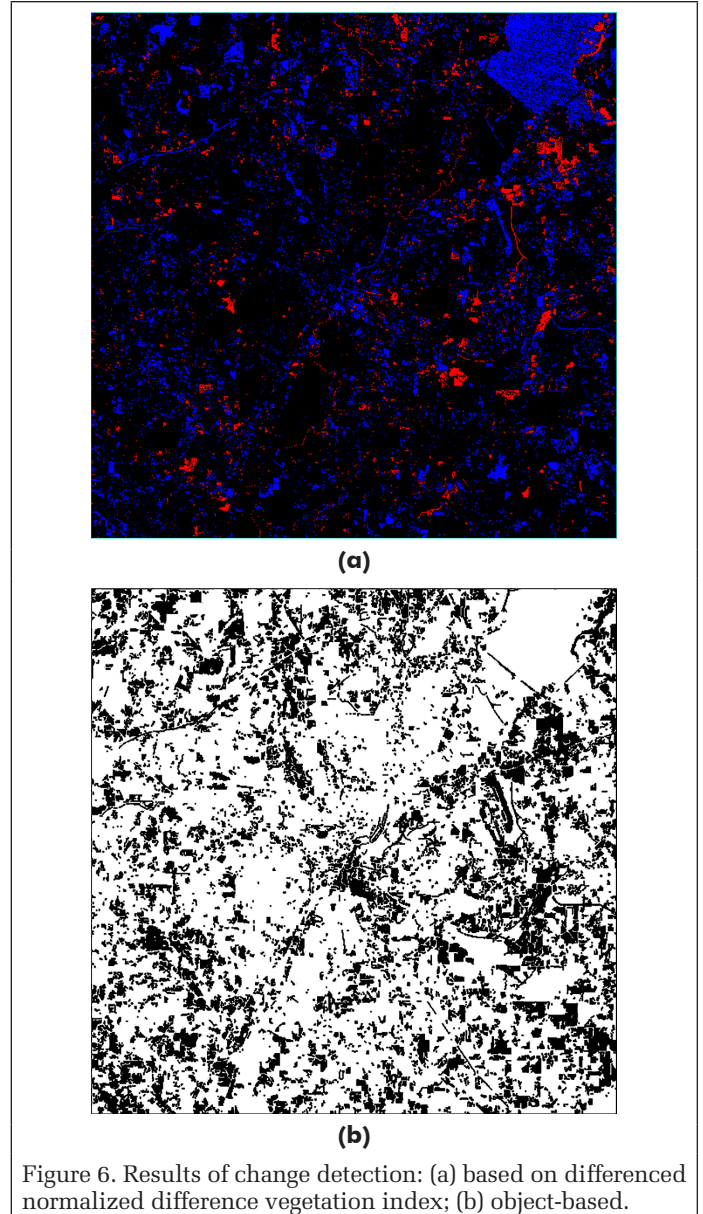


Figure 6. Results of change detection: (a) based on differenced normalized difference vegetation index; (b) object-based.

Table 10. Change-detection results based on pixel differenced normalized difference vegetation index.

	Changed	Unchanged	Sum	Producer's Accuracy
Changed	255	57	312	0.966
Unchanged	9	204	213	0.781
Sum	264	261	525	—
User's accuracy	0.817	0.958	—	—
Overall accuracy = 0.874				
$\kappa = 0.748$				

comprehensive use of spectral and textural features can extract more information than the use of a single feature.

Change-detection methods based on pixels and objects are used to compare and analyze the advantages and weaknesses of the cosegmentation algorithm. Figure 6a demonstrates the change-detection result based on the  $dNDVI$  of each pixel. The detection method uses the image-change workflow tool in the ENVI software (Harris Geospatial Solutions, Broomfield, CO) based on the characteristic index interpolation method in  $NDVI$ . The threshold of  $NDVI$  is obtained by using a histogram-based method (Otsu's method; Otsu 1979) to obtain the optimal value automatically. The red and blue areas in Figure 6a denote the detected change area; the red part indicates an increase in biomass, the blue part a reduction in biomass, and the black part the unchanged part. Table 10 displays the accuracy-evaluation results of  $dNDVI$  change detection. The overall accuracy is 0.874, with  $\kappa = 0.748$ .

Figure 6a demonstrates the pixel-based change-detection methods that identify bits and pieces of pixels. The influence of the "same object with different spectra, different objects with the same spectrum" principle, such as the actual unchanged water body in the upper right corner of the image in Figure 6a, is considerable. The mass area was extracted from the results of the  $dNDVI$ -versus-cosegmentation method, and no change was observed. These results have less overall influence than those of the pixel-based method because the plaque characteristics of the land cover features were considered, although the "same object with different spectra, different objects with the same spectrum" principle also affects the cosegmentation method.

Moreover, the results of the traditional object-based change-detection method are compared. The object-based change-detection experiment is conducted by the multiresolution segmentation process of eCognition Developer 9 (Trimble Geospatial, Munich, Germany). The segmentation scale is set to 30, and the weights of the shape and color (spectrum) are 0.1 and 0.5, respectively. Then, two categories are set in the class hierarchy, "change" and "unchanged," to classify the segmented objects with CV values:

$$CV = \sum_{k=1}^n (I_{t1} - I_{t2})^2 \quad (i = 1, 2), \quad (4)$$

where  $I_i$  is the spectral value of time  $i$  and  $k$  is the number of bands. The total accuracy is the highest when the threshold of CV is  $\mu - 0.2\sigma$  (where  $\mu$  is the mean value of all pixels and  $\sigma$  is the standard deviation).

Figure 6b displays the result of the object-based change-detection method where the white and black parts denote the unchanged and changed areas, respectively. The changed part detected by the object-based method based on CV is more reasonable than that of pixel-based change detection, showing certain plaque characteristics of land cover and rare salt-and-pepper noise. From the error matrix (Table 11), the overall accuracy of the results is 88.8%, with  $\kappa = 0.775$ . The accuracy is better than that of pixel-based change detection. The producer's precision of the changed pixels is 0.882, and that of the unchanged pixels is 0.892. The object-based change-detection method can easily analyze and compare the changed objects and can easily use the spatial information in the algorithm.

The comparison of the accuracy of the object- and pixel-based change-detection methods indicates that the cosegmentation algorithm has the highest accuracy. The cosegmentation method considers image features—that is, neighborhood features of the image pixels. Thus, the results consider the regional characteristics. Compared with the object-based change-detection method, the cosegmentation method considers the spectral and textural features of the pixel, thereby

Table 11. Results of the traditional object-based change-detection method.

	Changed	Unchanged	Sum	Producer's Accuracy
Changed	233	28	261	0.882
Unchanged	31	233	264	0.892
Sum	264	261	525	—
User's accuracy	0.892	0.882	—	—
Overall accuracy = 0.888				
$\kappa = 0.775$				

resulting in improved accuracy. Cosegmentation change detection considers not only the differences among the different phases of the corresponding pixel but also the similarity between the image pixel and the feature information of the surrounding pixels. Cosegmentation change detection also integrates the advantages of pixel- and object-based change-detection methods. In addition, the flexible energy function can be changed in accordance with different research purposes and can be further developed. The change-detection method based on cosegmentation can satisfy the requirements of change detection on the 30-m scale.

#### Results After Removing Spurious Change with the Geo-Eco Zoning-Rule Database

Figure 5b displays a change map in which red represents the spurious changes that have been detected and removed based on the geo-eco zoning-rule database. The map has 59860 change patches, and the number of identified spurious change patches is 11763. The total area of changed patches was 230.876 km<sup>2</sup>, and within this area, 28.99256 km<sup>2</sup> was identified as spurious changes. The area ratio is thus approximately 12.56%. On the one hand, many spurious-change spots were identified, given the spurious change that was caused by instantaneous remote sensing imaging. On the other hand, other spurious-change spots were caused by the image-classification error.

A total of 530 patches were selected in the experimental area to verify the accuracy of spurious-change detection; these sample patches represent approximately 5% of the total spurious changes. A field investigation is infeasible to perform, considering the limited time and capital constraints. Therefore, high-resolution images, such as those from Google Earth, were mainly referred to for manual interpretation of the spurious-change samples. The results are listed in Table 12, and the accuracy of spurious-change detection in the experimentation area is 90.2%.

Table 12. Precision of spurious-change patch removal.

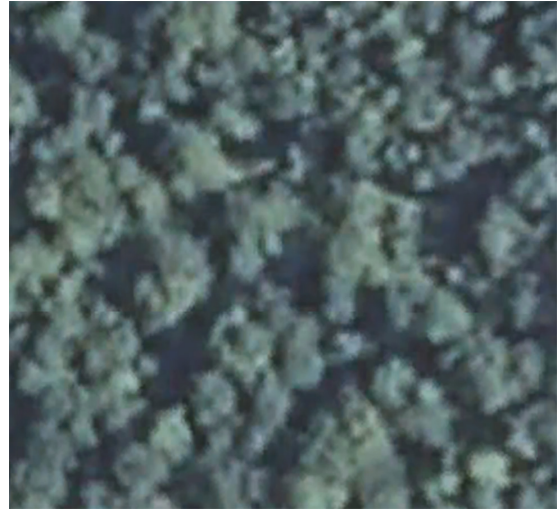
Samples	Correctly Detected Spurious Changes	Correctness
530	478	90.2%

Three change patches were taken at random in the experimental area, and the actual changes were examined. The first patch (Figure 7) was checked and identified as a cultivated land that is converted into a wetland; this conversion is a spurious change in accordance with the rule in the geo-eco zoning-rule database. The two-phase high-resolution images show that in 2002 (since the 2000 Google Earth image could not be found, the 2002 image was used instead) the area was forestland, and it remained unchanged in 2010.

The other example (Figure 8) is identified as a spurious change in which cultivated land is converted into water in accordance with the rule in the geo-eco zoning-rule database. The Google Earth images of the two similar periods show that the area was water in 2002 and remained unchanged in 2010.



**(a)**



**(b)**

Figure 7. Google Earth images acquired in (a) March 2002 and (b) September 2010.



**(a)**



**(b)**

Figure 8. Google Earth images acquired in (a) March 2002 and (b) May 2010.



**(a)**



**(b)**

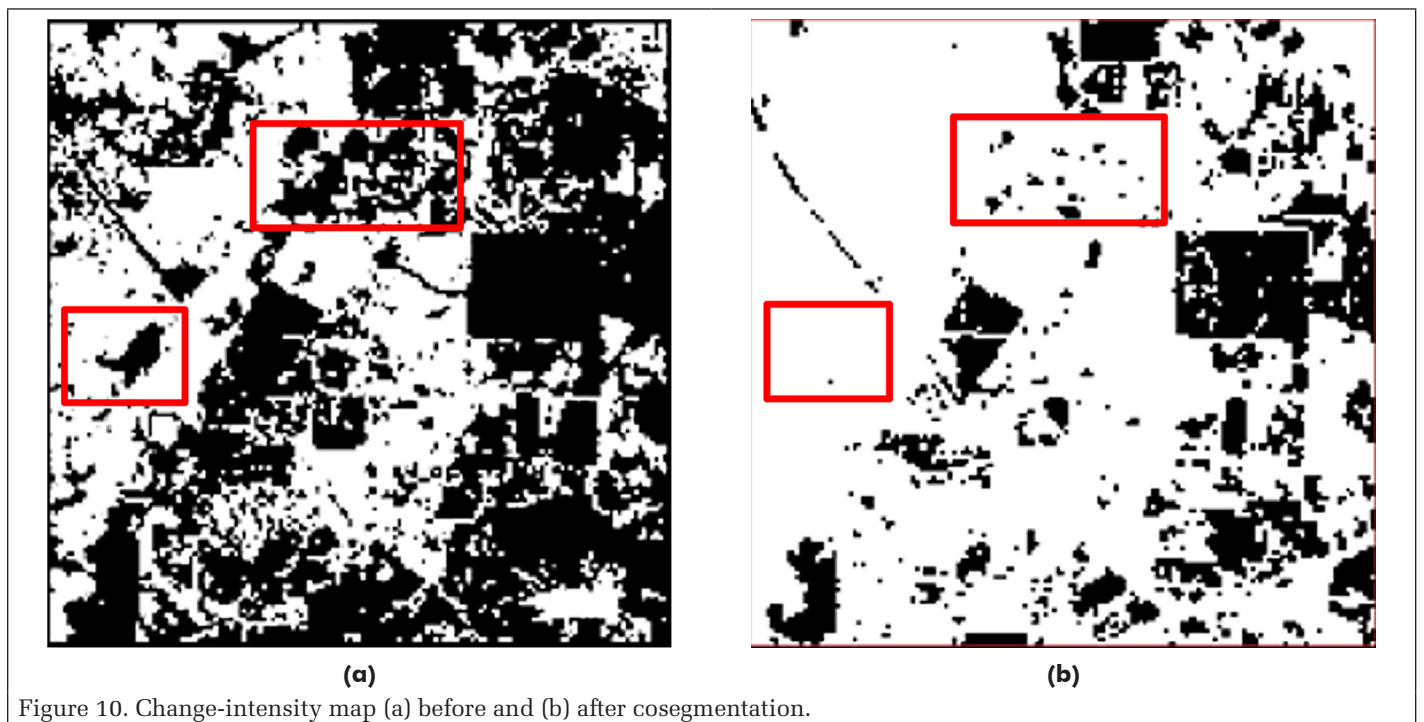
Figure 9. Google Earth images acquired in (a) March 2002 and (b) May 2010.

Table 13. Accuracy analysis of the incremental updating results.

	Forest	Grassland	Shrubland	Wetland	Water Bodies	Artificial Surfaces	Sum	Producer's Accuracy
Cultivated land	0	1	0	2	0	0	43	1
Forest	36	0	0	13	0	0	49	0.818
Grassland	0	17	0	0	0	0	17	0.739
Shrubland	0	0	8	0	0	0	8	0.667
Wetland	8	0	0	21	0	0	29	0.583
Water bodies	0	0	0	0	43	0	43	0.915
Artificial surfaces	0	5	0	0	0	50	55	0.962
Unclassified	0	0	4	0	4	2	10	—
Sum	44	23	12	36	47	52	254	—
User's accuracy	0.930	0.735	1	1	0.724	1	0.909	—

Overall accuracy = 0.846

$\kappa = 0.817$



The third example (Figure 9) is identified as a spurious change from forestland into wetland. The Google Earth images of two similar periods indicate that the region was actually wetland in 2002 and remained unchanged in 2010.

#### Incremental Updating Results

The GlobeLand30 map of the test area is updated to 2010 phase data by replacing the changed pixels using the update tool in the ArcGIS software. The result is shown in Figure 4b. An accuracy evaluation of the products was conducted, and the results are presented in Table 13. Barren lands are excluded from the accuracy evaluation because the sample point of these types of lands is small in the experimental area.

The overall accuracy of the incremental updating results is approximately 84%, with  $\kappa = 0.817$ ; the accuracy for water, cultivated land, and artificial surfaces is the highest, with a mapping accuracy of more than 0.9. The previously presented analysis indicated that the results of the incremental updating of GlobeLand30 data through cosegmentation and a geo-eco zoning-rule database can generally meet the requirements of change detection and incremental updating for 30-m land cover data.

## Discussion

### Influence of the Change-Intensity Map on the Result

Figure 10a illustrates the change-intensity map obtained by the method listed under Construction of the Energy Function; in this figure, the changed pixels that are extracted by the threshold are highlighted in black—that is, these pixels have a large difference in spectral values between the two-phase images. Figure 10b depicts the cosegmentation results. Comparison of the two images indicated that the results of cosegmentation depend on the change-intensity map. Moreover, the change intensity largely determines the results of segmentation. However, certain parts of the intensity map are filtered because the image textural features are also involved in segmentation. Cosegmentation standardizes the extraction of change patches and maintains the integrity of the boundary and interior of the patch.

In each image in Figure 11, the two areas enclosed in boxes are the highlighted areas (changed areas) on the change-intensity map of Figure 10a. However, some parts of these areas were removed after cosegmentation. Comparison with the

high-resolution Google Earth images indicates that the upper right boxed area denotes the unchanged artificial surface from 2002 to 2010, and the lower left box area denotes the woodland. A visual interpretation displays the unchanged vegetation types and textures. These two examples were randomly selected, thereby indicating that the cosegmentation results are reliable. Further analyses verified that the reason these regions were removed was mainly because the image features were involved in cosegmentation. The textural features of the two regions have not changed significantly. Thus, the min-cut/max-flow computation of the energy function flow did not consider the change in the two positions. The change-intensity map provides the potential range of the change for cosegmentation, and the image feature standardizes and aids the process to obtain the final result.

### MATLAB Parallel Computing

The computational complexity of cosegmentation is high, and the speed of operation is slow. The cosegmentation algorithm must calculate the adjacency matrix among the pixels, requiring considerable computation. Currently, the implementation of a 1200×1200-pixel cosegmentation requires many hours to execute. The parallel-computing method was designed using the parallel-computing toolbox in the MATLAB parfor parallel method to enhance computing speed. Large images were cut into several small image blocks, and the parfor statement was used to calculate multiple images simultaneously. Finally, these small image blocks were stitched together to obtain the result.

The 1200×1200-pixel image was divided into 64 blocks for parallel computing, and each image size was 150×150 pixels. After cosegmentation of each block, the result of each block must be pieced back together to form the final result image. Because each small block is relatively independent, the network flow graph constructed in the min-cut/max-flow method is also independent—that is, each block undergoes cosegmentation separately. There is no further processing to ensure that the joints between the blocks will have exactly the same result on either side. In principle, this will cause inconsistency at the joints, so the change map is not consistent at the seams, and some change patches cannot be expressed accurately, affecting the integrity of the segmentation results. However, as we inspect the merging result of each block, the vast majority of the blocks have no such problem. This is seldom seen. Figure 12 shows an example with one or two rows of pixels that were not extracted successfully. Figure 12a shows the cosegmentation results of two adjacent blocks, with the red line in the central region representing the boundary between the two blocks; the changed pixels are highlighted in black. Figure 12b and c shows the corresponding 2000 and 2010 Landsat images. Part of the green rectangle in Figure 12a shows that at the seam, there are one to two rows of changed pixels that are not coherent, in contrast to the Landsat images. Although the parallel-computing method improves the efficiency of the algorithm, it will cause some irregularities or patches of deformation at the seams between the blocks.

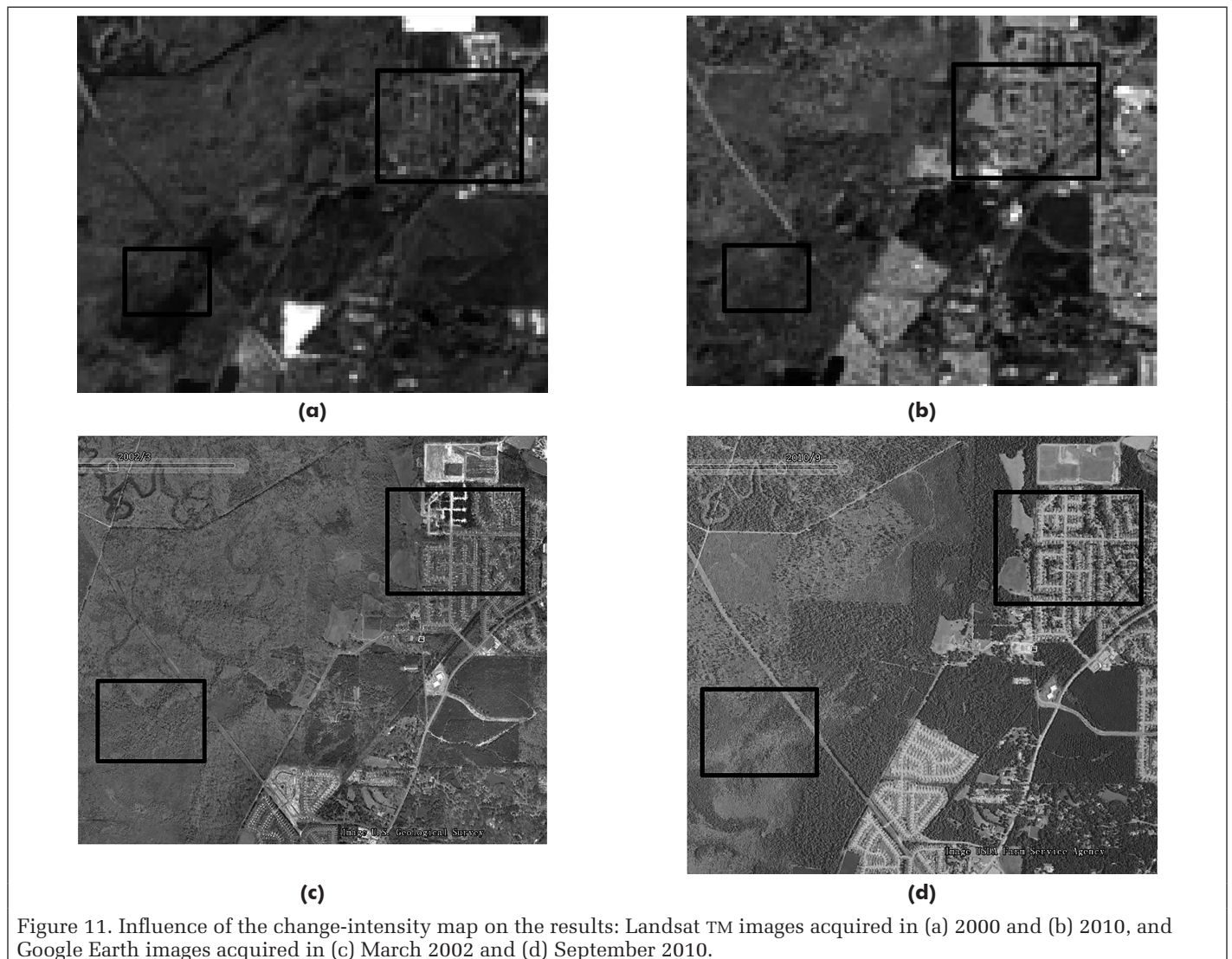


Figure 11. Influence of the change-intensity map on the results: Landsat TM images acquired in (a) 2000 and (b) 2010, and Google Earth images acquired in (c) March 2002 and (d) September 2010.

**Limitations of the Geo-Eco Zoning-Rule Database**

Spurious change identified by the geo-eco zoning-rule database includes the false changes caused by differences in the image spectrum and imaging condition and the changes caused by classification error. At present, the image patches identified as spurious changes are removed directly, which is slightly arbitrary. In some cases, the spurious-change patches identified by the geo-eco zoning rule truly represent a land cover change, although they are detected as spurious change and are hence removed, thereby causing errors in the update. Figure 13 shows two examples of false removal of changed

patches. In Figure 13a, visual interpretation of the Google Earth images shows a plot of cultivated land in 2002 and a water body in 2010 (shown in Figure 13b). However, this changed patch was identified as a spurious change (wetland to artificial surface) and removed due to incorrect classification by the GlobeLand30 2000 product as wetland and incorrect classification by the cosegmentation as an artificial surface. In Figure 13c, a Google Earth image shows a plot of land that was a water body in 2002 but changed to cultivated land in 2010 (shown in Figure 13d). However, this changed patch was identified as a spurious change and removed due to

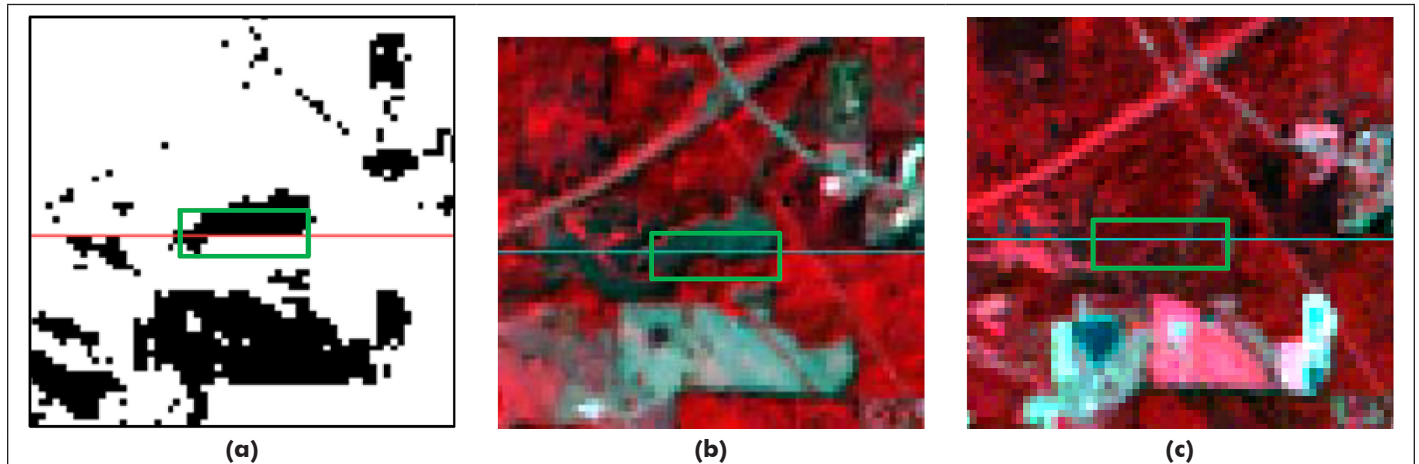


Figure 12. Influence of parallel computing: (a) Cosegmentation result of two adjacent blocks with red line denoting the boundary, and Landsat images acquired in (b) 2000 and (c) 2010, taken from the experimental area.

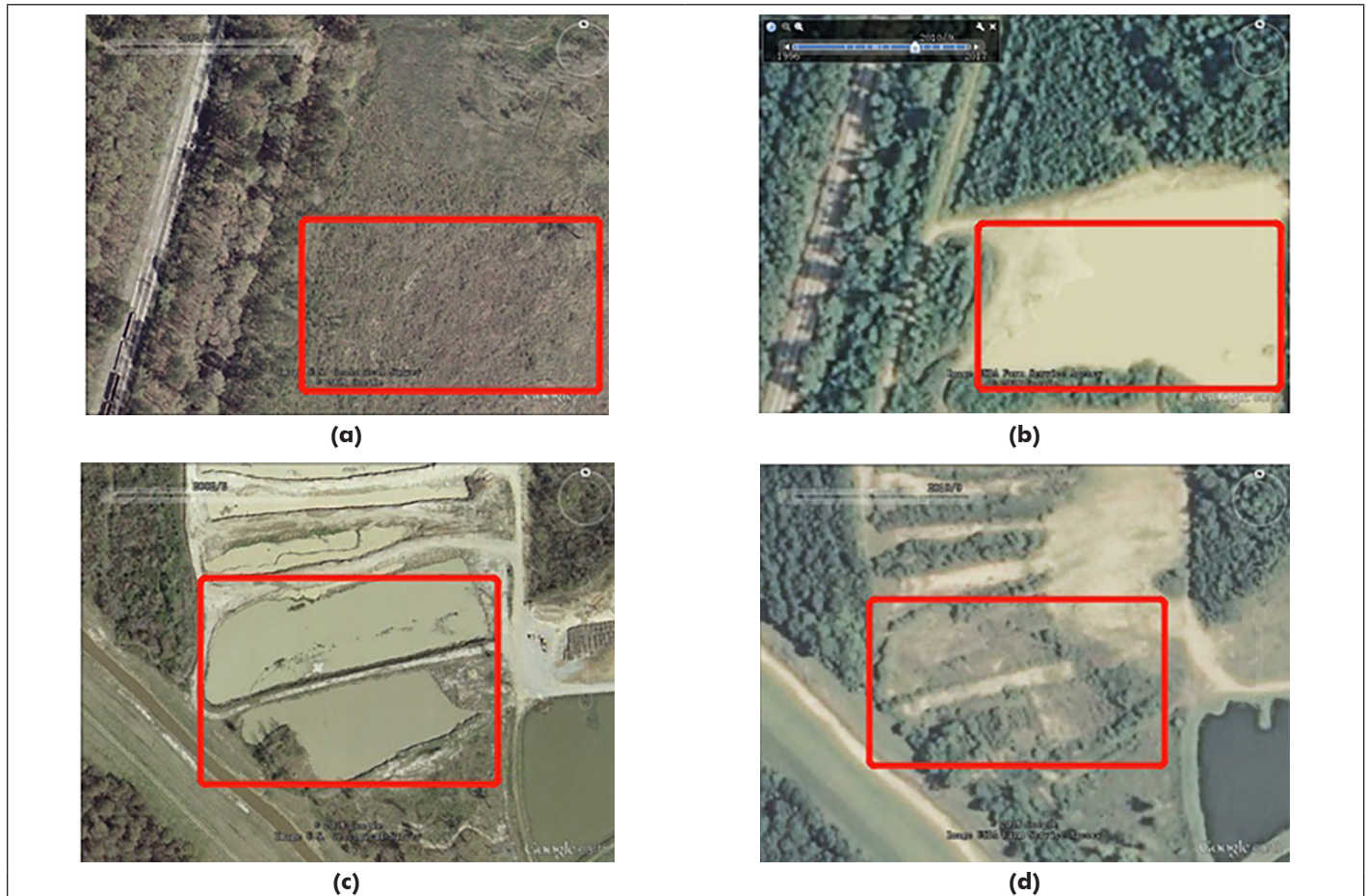


Figure 13. Example of the false removal of changed patches: Google Earth images acquired in (a) March 2002, (b) September 2010, (c) March 2002, and (d) September 2010.

incorrect classification by the GlobeLand30 2000 product as an artificial surface; artificial surface to cultivated land is one of the spurious-change rules.

Experimental discovery shows that the spurious-change problem of incorrect classification does exist and has a little influence on the result. Table 13 shows that of the 530 spurious-change patches inspected, among the 52 wrongly detected patches were a total of 40 such cases. This occurs not because the rules are inappropriate or the geo-eco zoning-rule base causes incorrect recognition, but because of the inappropriate classification result. The spurious changes identified are correct, indicating the validity of the geo-eco zoning-rule database. However, the operation of direct removal of spurious-change patches decreases the accuracy. On the other hand, this is also a way to identify misclassification. The 40 patches are all misclassified either on the t1 phase image or on the cosegmentation result, and need further checking rather than removing. A better method needs to be developed to take advantage of this result.

## Conclusions

This study presents a new method for land cover product updating based on cosegmentation and a geo-eco zoning-rule database. First, incremental updating of two-phase remote sensing images was achieved by cosegmentation. The land cover classification was then conducted only on the incrementally updated parts. Moreover, the geo-eco zoning rules were used to identify and remove spurious changes. Incremental updating was also optimized. Finally, incremental updating of old land cover maps was performed to acquire new land cover maps. This method was verified by experiments, and the accuracy was reliable. The incremental updating method of the subsequent land cover product has the advantages of maintaining continuity with previous and follow-up data production and can ensure that the products among different phases can be easily analyzed and correlated.

Some work will be improved in the future. First, the computational cost of cosegmentation is high. Parallel computing will cause discontinuity at the block boundaries. To solve this problem, the method of superpixel segmentation can be introduced in later research. As the number of nodes decreases, the network flow-graph algorithm becomes feasible in practical applications. Second, the framework of the knowledge-based geo-eco zoning-rule base and the rule of the demonstration area have been established. The next step is to collect the corresponding rules based on geographical elements, such as digital elevation model, humidity, and temperature. Manual collection is required for the special rules within each subarea. Thus, the geo-eco zoning-rule database can be globally feasible. The current rule expression in the geo-eco zoning-rule base is relatively arbitrary and will be adjusted by combining the fuzzy membership degree in the future. Third, the updating operation is simply a replacement of changed pixels of the t1 phase map. When the boundaries of incremental patches do not precisely match with the shared boundaries in the existing t1 phase map, a sliver polygon—for example, an overshoot (wherein the boundary of the changed patches extends slightly past the boundary of a feature on the t1 phase map) or an undershoot (wherein the boundary of the changed patch falls slightly short of a feature existing in the t1 phase map)—can limit the quality of the finished product. Further steps, such as using the method of Linke *et al.* (2009), should be considered.

## Acknowledgments

This research has been funded by the National Key Research and Development Program of China (NO.2016YFB0501404).

## References

- Bailey, R. G. 1983. Delineation of ecosystem regions. *Environmental Management* 7 (4):365–373.
- Bailey, R. G. 1989. Explanatory supplement to ecoregions map of the continents. *Environmental Conservation* 16 (4):307–309.
- Bailey, R. G. 2004. Identifying ecoregion boundaries. *Environmental Management* 34 (Suppl. 1):S14–S26.
- Bailey, R. G. and H. C. Hogg. 1986. World ecoregions map for resource reporting. *Environmental Conservation* 13 (3):195–202.
- Bartholomé, E. and A. S. Belward. 2005. GLC2000: A new approach to global land cover mapping from Earth observation data. *International Journal of Remote Sensing* 26 (9):1959–1977.
- Bashkin, V. N. and R. G. Bailey. 1993. Revision of map of ecoregions of the world (1992–95). *Environmental Conservation* 20 (1):75–76.
- Benz, U. C., P. Hofmann, G. Willhauck, I. Lingenfelder and M. Heynen. 2004. Multi-resolution, object-oriented fuzzy analysis of remote sensing data for GIS-ready information. *ISPRS Journal of Photogrammetry and Remote Sensing* 58 (3–4):239–258.
- Bontemps, S., P. Bogaert, N. Titeux and P. Defourny. 2008. An object-based change detection method accounting for temporal dependences in time series with medium to coarse spatial resolution. *Remote Sensing of Environment* 112 (6):3181–3191.
- Bontemps, S., P. Defourny, E. Van Bogaert, V. Kalogirou and O. Arino. 2011. *GlobCover 2009 Products Description and Validation Report* (Version 2.0). City, Country: Publisher. <<http://ionia1.esrin.esa.int/>> Accessed DD Month YYYY.
- Buck, O. 2010. DeCOVER 2—The German GMES extension to support land cover data systems: Status and outlook. Pages PP–PP in *Proceedings of ESA Living Planet Symposium*, held in Bergen, Norway, 28 June–2 July 2010. Edited by H. Lacoste-Francis. City, St./Country: Publisher.
- Büttner, G. 2014. CORINE Land Cover and Land Cover Change products. In *Land Use and Land Cover Mapping in Europe: Practices & Trends*, edited by I. Manakos and M. Braun, 55–74. Dordrecht, the Netherlands: Springer.
- Caccetta, P., S. Furby, J. O’Connell, J. Wallace and X. Wu. 2007. Continental monitoring: 34 years of land cover change using Landsat imagery. Pages PP–PP in *Proceedings of 32nd International Symposium on Remote Sensing of Environment*, held in City, Costa Rica, 25–29 June 2007. Edited by J. Editor. City, St./Country: Publisher.
- Chen, J., X. Cao, S. Peng and H. Ren. 2017. Analysis and applications of GlobeLand30: A review. *ISPRS International Journal of Geo-Information* 6 (8):230.
- Chen, J., J. Chen and A. Liao. 2016. *Global Land Cover Mapping Based on Remote Sensing*. Beijing, China: Science China Press.
- Dinitz, E. A. 1970. Algorithm for solution of a problem of maximum flow in networks with power estimation. *Soviet Mathematics Doklady* 11:1277–1280.
- Ford Jr, L. R. and D. R. Fulkerson. 1962. *Flows in Networks*. Santa Monica, Calif.: RAND Corporation.
- Friedl, M. A., D. Sulla-Menashe, B. Tan, A. Schneider, N. Ramankutty, A. Sibley and X. Huang. 2010. MODIS Collection 5 global land cover: Algorithm refinements and characterization of new datasets. *Remote Sensing of Environment* 114 (1):168–182.
- Giri, C. P. (Ed.). 2012. *Remote Sensing of Land Use and Land Cover: Principles and Applications*. Boca Raton, Fla.: CRC Press. pp245.
- Giri, C. P. (Ed.). 2012. *Remote Sensing of Land Use and Land Cover: Principles and Applications*. Boca Raton, Fla.: CRC Press. pp254–255.
- Hansen, M. C., R. S. Defries, J.R.G. Townshend and R. Sohlberg. 2000. Global land cover classification at 1 km spatial resolution using a classification tree approach. *International Journal of Remote Sensing* 21 (6–7):1331–1364.

- Holdridge, L. R. 1967. *Life Zone Ecology*. San Jose, Costa Rica: Tropical Science Center.
- Hussain, M., D. Chen, A. Cheng, H. Wei and D. Stanley. 2013. Change detection from remotely sensed images: From pixel-based to object-based approaches. *ISPRS Journal of Photogrammetry and Remote Sensing* 80 (2):91–106.
- Jin, S., L. Yang, P. Danielson, C. Homer, J. Fry and G. Xian. 2013. A comprehensive change detection method for updating the National Land Cover Database to circa 2011. *Remote Sensing of Environment* 132:159–175.
- Joulin, A., F. Bach and J. Ponce. 2010. Discriminative clustering for image co-segmentation. Pages 1943–1950 in *2010 IEEE Computer Society Conference on Computer Vision and Pattern Recognition*, held in San Francisco, Calif. Edited by J. Editor. City, St./Country: IEEE.
- Joulin, A., F. Bach and J. Ponce. 2012. Multi-class cosegmentation. Pages 542–549 in *2012 IEEE Conference on Computer Vision and Pattern Recognition*, held in Providence, R.I. Edited by J. Editor. City, St./Country: IEEE.
- Authors, J. 2017. *Land Cover CCI Product User Guide Version 2.0*. <[http://maps.elie.ucl.ac.be/CCI/viewer/download/ESACCI-LC-Ph2-PUGv2\\_2.0.pdf](http://maps.elie.ucl.ac.be/CCI/viewer/download/ESACCI-LC-Ph2-PUGv2_2.0.pdf)> Accessed 16 August 2018.
- Linke, J., G. J. Mcdermid, D. N. Laskin, A. J. McLane, A. Pape, J. Cranston, M. Hall-Beyer and S. E. Franklin. 2009. A disturbance-inventory framework for flexible and reliable landscape monitoring. *Photogrammetric Engineering and Remote Sensing* 75 (8):981–995.
- Loveland, T. R., B. C. Reed, J. F. Brown, D. O. Ohlen, Z. Zhu, L. Yang and J. W. Merchant. 2000. Development of a global land cover characteristics database and IGBP DISCover from 1 km AVHRR data. *International Journal of Remote Sensing* 21 (6–7):1303–1330.
- Ma, Y., & Liu, Z., 2014. Review on the methods of change detection techniques using remotely-sensed data. *Geomatics & Spatial Information Technology*.
- Olson, D. M., E. Dinerstein, E. D. Wikramanayake, N. D. Burgess, GVN Powell, E. C. Underwood, J. A. D'amico, I. Itoua, H. E. Strand, J. C. Morrison, C. J. Loucks, T. F. Allnutt, T. H. Ricketts, Y. Kura, J. F. Lamoreux, W. W. Wettengel, P. Hedao and K. R. Kassem. 2001. Terrestrial ecoregions of the world: A new map of life on Earth—A new global map of terrestrial ecoregions provides an innovative tool for conserving biodiversity. *BioScience* 51 (11):933–938.
- Otsu, N. 1979. A threshold selection method from gray-level histograms. *IEEE Transactions on Systems, Man, and Cybernetics* 9 (1):62–66.
- Rother, C., T. Minka, A. Blake and V. Kolmogorov. 2006. Cosegmentation of image pairs by histogram matching—Incorporating a global constraint into MRFs. Pages 993–1000 in *2006 IEEE Computer Society Conference on Computer Vision and Pattern Recognition*, Vol. 1, held in New York, N.Y., 17–22 June 2006. Edited by A. Fitzgibbon, C. J. Taylor and Y. LeCun. Los Alamitos, Calif.: IEEE Computer Society.
- Tateishi, R., B. Uriyangqai, H. Al-Bilbisi, M. A. Ghar, J. Tsend-Ayush, T. Kobayashi, A. Kasimu, N. T. Hoan, A. Shalaby, B. Alsaaidh, T. Enkhzaya, G. Tana and H. P. Sato. 2011 Production of global land cover data—GLCNMO. *International Journal of Digital Earth* 4 (1):22–49.
- Terrestrial Ecoregions of the World, URL: <https://www.worldwildlife.org/publications/terrestrial-ecoregions-of-the-world>,
- World Wildlife Fund, Washington, DC (last date accessed: 16 August 2018).
- Xian, G., C. Homer and J. Fry. 2009. Updating the 2001 National Land Cover Database land cover classification to 2006 by using Landsat imagery change detection methods. *Remote Sensing of Environment* 113 (6):1133–1147.
- Xiao, P., M. Yuan, X. Zhang, X. Feng and Y. Guo. 2017. Cosegmentation for object-based building change detection from high-resolution remotely sensed images. *IEEE Transactions on Geoscience and Remote Sensing* 55 (3):1587–1603.
- Yuan M., P. Xiao, X. Feng, X. Zhang and Y. Hu. 2015. High resolution remote sensing image change detection by cosegmentation. *Journal of Nanjing University (Natural Science)* 51 (5):1039–1048.

Advertise in the #1 publication in the imaging and geospatial information industry!



### Impact Factor (2018): 3.15

PE&RS (*Photogrammetric Engineering & Remote Sensing*) is the official journal of the American Society for Photogrammetry and Remote Sensing—the Imaging and Geospatial Information Society (ASPRS). This highly respected publication is the #1 publication in the industry by a wide margin. Advertisers with a desire to reach this market can do no better than PE&RS. It delivers the right audience of professionals who are loyal and engaged readers, and who have the purchasing power to do business with you.

### PE&RS Readership Highlights

Circulation: 3,000

Total audience: 6,400\*

Founded in 1934, the American Society for Photogrammetry and Remote Sensing (ASPRS) is a scientific association serving professional members throughout the world. Our mission is to advance knowledge and improve understanding of mapping sciences to promote the responsible applications of photogrammetry, remote sensing, geographic information systems (GIS), and supporting technologies.

Our members are analysts/specialists, educators, engineers, managers/administrators, manufacturers/ product developers, operators, technicians, trainees, marketers, and scientists/researchers. Employed in the disciplines of the mapping sciences, they work in the fields of Agriculture/Soils, Archeology, Biology, Cartography, Ecology, Environment, Forestry/Range, Geodesy, Geography, Geology, Hydrology/Water Resources, Land Appraisal/ Real Estate, Medicine, Transportation, and Urban Planning/Development.

### RESERVE YOUR SPACE TODAY!

Bill Spilman, ASPRS Advertising, Exhibit Sales & Sponsorships  
 (877) 878-3260 toll-free  
 (309) 483-6467 direct  
 (309) 483-2371 fax  
 bill@innovativemediasolutions.com

	Corporate Member Exhibiting at a 2019 ASPRS Conference	Corporate Member	Exhibitor	Non Member
<i>All rates below are for four-color advertisements</i>				
Cover 1	\$1,850	\$2,000	\$2,350	\$2,500
<i>In addition to the cover image, the cover sponsor receives a half-page area to include a description of the cover (maximum 500 words). The cover sponsor also has the opportunity to write a highlight article for the journal. Highlight articles are scientific articles designed to appeal to a broad audience and are subject to editorial review before publishing. The cover sponsor fee includes 50 copies of the journal for distribution to their clients. More copies can be ordered at cost.</i>				
Cover 2	\$1,500	\$1,850	\$2,000	\$2,350
Cover 3	\$1,500	\$1,850	\$2,000	\$2,350
Cover 4	\$1,850	\$2,000	\$2,350	\$2,500
Advertorial	1 Complimentary Per Year	1 Complimentary Per Year	\$2,150	\$2,500
Full Page	\$1,000	\$1,175	\$2,000	\$2,350
2 page spread	\$1,500	\$1,800	\$3,200	\$3,600
2/3 Page	\$1,100	\$1,160	\$1,450	\$1,450
1/2 Page	\$900	\$960	\$1,200	\$1,200
1/3 Page	\$800	\$800	\$1,000	\$1,000
1/4 Page	\$600	\$600	\$750	\$750
1/6 Page	\$400	\$400	\$500	\$500
1/8 Page	\$200	\$200	\$250	\$250
Other Advertising Opportunities				
Wednesday Member Newsletter Email Blast	1 Complimentary Per Year	1 Complimentary Per Year	\$600	\$600

A 15% commission is allowed to recognized advertising agencies

**THE MORE YOU ADVERTISE THE MORE YOU SAVE!** PE&RS offers frequency discounts. Invest in a three-times per year advertising package and receive a 5% discount, six-times per year and receive a 10% discount, 12-times per year and receive a 15% discount off the cost of the package.

\*Based on 2 readers per copy as well as online views | Source: PE&RS Readership Survey, Fall 2012

LEARN  
DO  
GIVE  
BELONG

**ASPRS Offers**

- » Cutting-edge conference programs
- » Professional development workshops
- » Accredited professional certifications
- » Scholarships and awards
- » Career advancing mentoring programs
- » *PE&RS*, the scientific journal of ASPRS

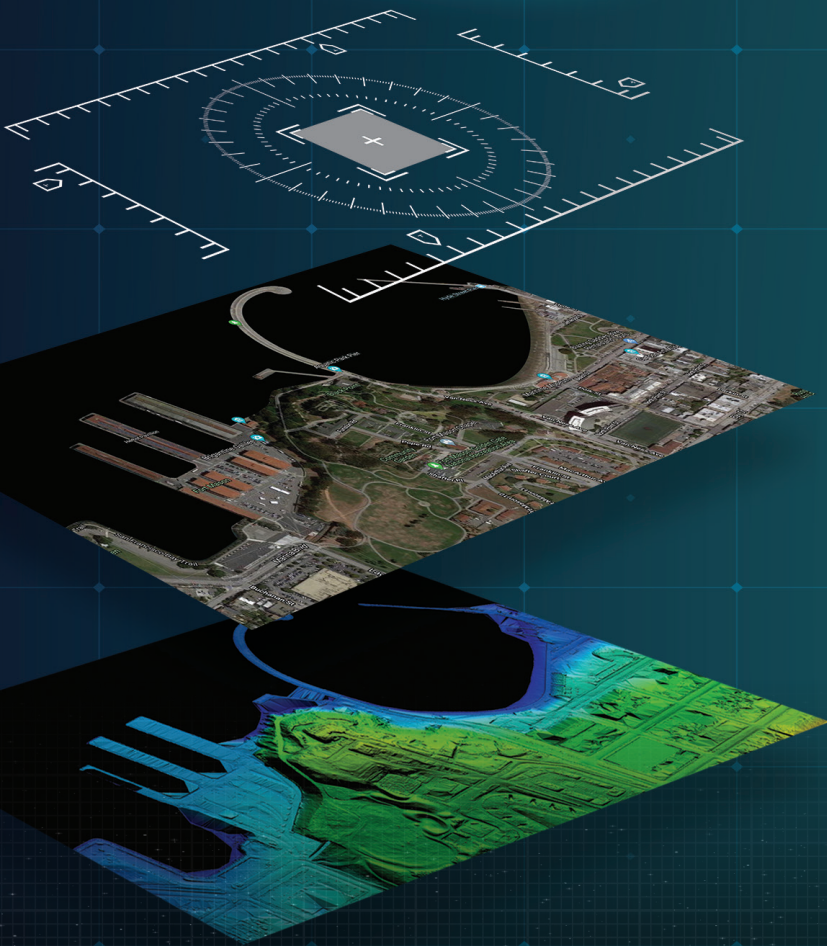
[asprs.org](http://asprs.org)

ASPRS

# AT GEOMNI, WE MAP FOR SUCCESS



When you have Geomni collect imagery and data for your next project you will be harnessing the power of one of the largest Geo-spatial companies in the United States. With 14 hubs nationally, we are local to your next planned job site. Helping you map for success is our mission. We achieve that goal by providing access to our extensive data library, and offering custom imaging flights, while our fleet provides the regional knowledge, resolution, accuracy, and timeliness to deliver the critical information precision mappers need, at a price point fit for your project budgets.



HAWAII

NORCAL

SOCAL

OREGON

IDAHO

HEADQUARTERS

ARIZONA

NEW MEXICO

COLORADO

TEXAS

KANSAS

INDIANA

FLORIDA

SOUTH CAROLINA

MARYLAND

MAINE



[WWW.GEOMNI.COM/PSM](http://WWW.GEOMNI.COM/PSM)